Montgomery, Rachel Ann (2013) *A position sensitive photon detector for the CLAS12 ring imaging Čerenkov application.*
PhD thesis.

A Position Sensitive Photon Detector for the CLAS12 Ring Imaging Čerenkov Application

Rachel Ann Montgomery, M.Sci.

Submitted in fulfilment of the requirements for the
Degree of Doctor of Philosophy

Nuclear Physics Group
School of Physics and Astronomy
College of Science and Engineering
University of Glasgow
September 2013

This thesis is dedicated to my parents.

Abstract

The upgrade of the Continuous Electron Beam Accelerator Facility (CEBAF) Large Acceptance Spectrometer (CLAS) to CLAS12 will offer unique possibilities to study the strong interaction and the internal nucleon dynamics. For this, excellent hadron identification over its full kinematic range is essential and a Ring Imaging CHerenkov detector (RICH) has been proposed for installation into CLAS12 to achieve this. This thesis describes studies performed towards the selection of a photon detector for use in the CLAS12 RICH, which will be a crucial component for the success of the RICH performance.

MultiAnode PhotoMultiplier Tubes (MAPMTs) have been selected as the most promising photon detectors for the CLAS12 RICH. A high-precision laser test-stand was developed to characterise candidate MAPMTs and the results were used to determine the Hamamatsu H8500 MAPMT as the optimal device. Throughout the laser tests the H8500 MAPMT proved to be single photon sensitive as demanded, the spatial resolution was found to satisfy the required value of $< 1\,\mathrm{cm} \times 1\,\mathrm{cm}$ and the device exhibited sufficiently low crosstalk levels of $< 3\,\%$. The response and crosstalk of the device showed a dependency upon the MAPMT construction, the magnitude of which was shown to be negligible and overall the H8500 provides a plane of suitable uniformity to satisfy the imaging functionality of the CLAS12 RICH.

To further confirm the H8500 MAPMT choice, its performance in response to Čerenkov light within two prototype setups was evaluated. First a small-scale prototype was designed and constructed, incorporating one H8500 MAPMT to image Čerenkov rings created by cosmic muons traversing aerogel radiators. Extraction of the results required full understanding of the device based upon calibrations made with the laser tests. The prototype was also simulated in detail, allowing for a model description of the MAPMT to be validated. Secondly, 28 H8500 MAPMTs were used in a large-scale prototype to image Čerenkov rings produced by mixed hadrons traversing aerogel radiators, to evaluate their performance in a geometry and an environment similar to that expected in the CLAS12 RICH. Both prototypes revealed that the H8500 MAPMT can be used to successfully detect the required 7 photons per Čerenkov event to achieve π/K separation in the CLAS12 RICH. Furthermore, a π/K separation of $> 3\,\sigma$ at $6\,\mathrm{GeV/c}$ was observed through a preliminary analysis of data extracted with the large-scale prototype. The prototype studies also confirmed the low-noise behaviour of the H8500 MAPMT. As a result of the laser test-stand and prototype tests, the choice of the H8500 MAPMT as the photon detector for the CLAS12 RICH was validated.

Declaration

I hereby declare that the composition of this thesis, along with the work contained and described within it are my own. Where input/results from others have been given or collaboration with others has been made this is stated or referenced appropriately throughout the thesis. This work has not previously been submitted for any other degree to any institution.

Rachel Ann Montgomery

September 2013

Acknowledgements

I would like to express my appreciation to all my colleagues within the Nuclear Physics Group for the support and many interesting opportunities which I have received throughout my time here. In particular my sincere gratitude is extended to my supervisors, both past and present, including: Dr. Bjoern Seitz, Dr. Matthias Hoek, Dr. Ken Livingston and Prof. Ralf Kaiser. It is important that I acknowledge the role that their supervision has played in the completion of this thesis, through a combination of robust backing, help and advice. I am grateful to have received this assistance not only through the duration of my Ph.D., but also from both nearby and overseas. I am also thankful to Prof. David Ireland and Prof. Guenther Rosner for their endorsement in me through their roles as head of group. There are several other members of the group who were always available to provide me with advice and assistance, to whom I also say thank you: Dr. David Hamilton, Dr. Tibor Keri and Dr. Bryan McKinnon. Furthermore, I am indebted to Mr. Scott Lumsden and Mr. Tony Clarkson for the extensive technical and engineering support which they provided me. I would like to acknowledge the help which I received from my colleagues within the CLAS12 RICH Collaboration and express my thanks to all those I have worked with within this project, especially to Dr. Patrizia Rossi, Dr. Marco Mirazita and Dr. Marco Contalbrigo. I also had opportunities to partake in several interesting test-beam studies during my Ph.D. (ALPHA-X, ATLAS Forward Proton, $\bar{\text{P}}$ANDA Focusing Disc DIRC), which equipped me with many useful skills, therefore I extend a thank you to my colleagues from those projects too. To my fellow students, peers and NPE coffee club card members within the research group, I say a big thanks for your friendship and wish you all success in your future endeavours - in particular to all my office-mates throughout the years, with whom I have had the pleasure of sharing Room 407. These acknowledgements would be nowhere near complete without expressing my heartfelt gratitude to my friends and family - especially Ian and my parents, Ann and Archie. To my wonderful parents: your love, encouragement, guidance and support have always been absolutely endless - this would not have been possible without you and there are no words strong enough to express my appreciation.

Contents

List of Figures

List of Tables

Chapter 1

Introduction

Studies of the extremely complex nucleon sub-structure, hadronic matter and Quantum ChromoDynamics (QCD) are absolutely essential to further and complete our understanding of the description of nuclei, which represent the building blocks of all matter surrounding us. Since the electron-proton scattering experiments of Hofstadter in the 1950's [1], until the current day, many important discoveries concerning these topics have been made through the use of leptons as an electromagnetic probe to study the nucleon and its constituent components. Through lepton-nucleon scattering reactions one may successfully determine how the properties of the nucleon, such as its structure, mass and spin, are generated by the quarks and gluons within it (see for example Fig. 1.1). This therefore allows one to gain a deeper insight into the mechanisms of QCD, which describes the interactions between quarks and gluons. Hadron spectroscopy studies may also be used to investigate QCD and the processes of strongly in-

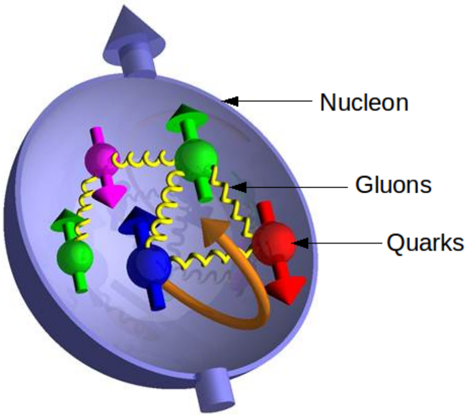

Figure 1.1: Quarks (different colours) and gluons within a nucleon. Spins of the nucleon and quarks are indicated by their arrows and orbital angular momentum of the quarks and gluons is indicated by the orange arrow. Study of the nucleon structure will enlighten our knowledge on the spin puzzle, where only a fraction of the nucleon's spin is attributed to its constituent quarks and gluons. Image from [2].

teracting matter. These studies can be used to understand further issues such as quark and gluon confinement within hadrons and the existence of exotic hadrons, for example, through the mapping of measured hadronic states.

Such challenging topics are currently subject to intense scrutiny within various experimental programs world-wide. In particular, the current upgrade of the Continuous Electron Beam Accelerator Facility (CEBAF) at Jefferson Lab (JLab) (Virginia, USA), in combination with its concurrent upgrade of the CEBAF Large Acceptance Spectrometer (CLAS) to CLAS12, will provide unique opportunities to further explore the nucleon structure in-depth, QCD and hadronic matter, with unprecedented precision. This will be achieved through lepton-nucleon scattering experiments with polarised beams of maximum energy of 11 GeV, high luminosities of $> 10^{35}\,\mathrm{m}^{-2}s^{-1}$ and close to full angular coverage. For the achievement of its physics program, efficient Particle IDentification (PID) over the entire kinematic range of CLAS12 is absolutely essential, and to achieve this the installation a Ring Imaging CHerenkov (RICH) detector into the forward region of CLAS12 has been proposed.

One of the key components determining the success of the RICH detector will be its photon detectors, which must provide both efficient detection of the low yield Čerenkov photons and the imaging functionality of the RICH detector. The work contained in this thesis describes several detailed studies which have significantly contributed to the choice of the Hamamatsu H8500 MultiAnode PhotoMultiplier Tube (MAPMT) as the photon detector for application to the CLAS12 RICH.

The thesis begins with an introduction to CLAS12, its baseline equipment and the requirement for a RICH detector. Following this a description of Čerenkov radiation, RICH detectors and the CLAS12 RICH design is given and in the succeeding chapter the available photon detection technologies which would be suitable are discussed. The outcome of the discussion indicates that MAPMTs are a promising technology for study and hence the next two chapters are devoted to experimental work dedicated to validating the choice of MAPMTs for application to the CLAS12 RICH, and in particular confirm the selection of the H8500 MAPMT. The experimental studies include a full characterisation of the H8500 MAPMT, and two additional MAPMTs for comparison, through laser scanning measurements. Further to the laser tests, the performance of the H8500 MAPMT within small- and large-scale prototypes in response to Čerenkov light produced by cosmic muons and mixed hadron beams respectively is described and studied. The final discussion, based upon the results, validates the choice of the H8500 MAPMT as the most suitable photon detector for the CLAS12 RICH application.

1.1 Jefferson Lab and the 12 GeV Upgrade

CEBAF [3, 4] has provided high intensity and continuous wave electron beams, of energies reaching 6 GeV, for nuclear and hadronic physics research since 1995. Currently JLab is undergoing an upgrade program, resulting in the increase in energy of its electron accelerator from 6 GeV to 12 GeV, as well as yielding increased beam intensities. The upgrade will include the enhancement of detector capabilities in the existing experimental halls, Halls A, B and C, and the addition of a new experimental hall, Hall D, which is under construction. The 12 GeV upgrade plan [5, 6] is illustrated in Fig. 1.2. As shown several new elements will be added to the existing CEBAF framework with no required alteration to its baseline footprint.

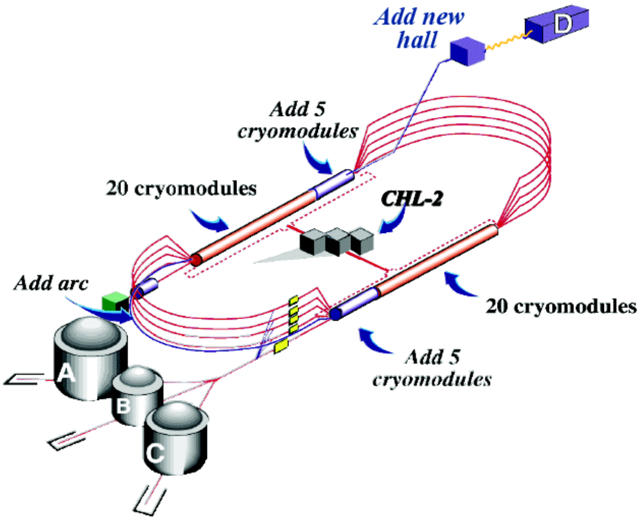

Figure 1.2: The upgrade plan of Jefferson Lab's continuous wave electron beam accelerator facility, resulting in the energy increase of the accelerator from 6 GeV to 12 GeV. Image taken from [6].

CEBAF [3,4] consists of two parallel continuous wave LINear ACcelerators (LINACs) which are based upon Superconducting RadioFrequency (SRF) technology and joined by several magnetic re-circulation arcs to form a racetrack design. The re-circulation arcs reduce the required length of the LINACs to 1.33 km each and the acceleration in the LINACs is performed by multiple cryogenic SRF cavities. Each LINAC is constructed from 20 *cryomodules*, which comprise 8 hermetically-sealed SRF cavities each. A Central Helium Liquefier (CHL) supplies the liquid helium for cooling of the cavities. The longitudinally polarised electron beam is injected and circulated up to a maximum of five times through both LINACs and the re-circulation arcs before extraction. Each time the beam passes through a LINAC, it gains 0.6 GeV of energy. The electron beam is generated by three independent lasers which strike a photocathode material, allowing for interlaced electron beams where three bunched trains are separated by 120°

phase and each third bunch shares common properties which differ from its preceding and succeeding neighbours. After acceleration, the appropriate electron bunches are extracted to each of the end stations simultaneously with energies of either $\frac{1}{5}, \frac{2}{5}, \ldots, \frac{5}{5}$ of the maximum energy of 6 GeV, depending upon the experimental requirements of each experimental hall. CEBAF is capable of delivering continuous wave beams of up to 200 μA to each of the experimental halls simultaneously, however due to the occupancy capabilities of the corresponding detectors typical beam currents delivered to the halls are 10 nA for Hall B and 100 μA for Halls A and C.

In the summer of 2012 CEBAF was switched off to start accelerator work for the 12 GeV upgrade project. The 12 GeV upgrade [5, 6] (see Fig. 1.2) will result in deliveries of beam energies up to 11 GeV for Halls A, B and C and 12 GeV for Hall D. The upgraded LINACs will each provide 1.1 GeV/pass and therefore one complete circulation through both LINACs will yield an acceleration of 2.2 GeV/pass. To meet these ends a total of ten new higher voltage cryomodules, with four times higher gradients per unit length, will be added to the LINACs (5/LINAC). To accommodate this, the CHL capacity will be roughly doubled. The beam transport system will also be upgraded, including the installation of a tenth re-circulation arc. The original 9 arcs may be re-used since they were originally designed with generous bend radii to allow for minimal beam degradation by synchrotron radiation effects in the 12 GeV upgrade project. The bending and focussing strength of their magnet systems and the strength of their power supplies will however have to be increased. At the end stations, the beam separators will also have to be modified to accommodate for the higher energies.

The upgrade will enhance the experimental equipment in Halls A, B and C, including the installation of new detector components. The remainder of this thesis is related to the upgrade of CLAS [7] to CLAS12 [8], which is a magnetic spectrometer housed in Hall B and used for lepton - fixed target [1] scattering experiments. First the physics program for CLAS12 is discussed, followed by a description of the apparatus and the resulting requirement for the installation of a RICH detector to enhance charged hadron identification.

1.2 CLAS12 Physics Program

The upgrade of CLAS to CLAS12 will allow for an abundance of nuclear physics and QCD topics to be studied further, significantly contributing to our understanding of strongly interacting

---

[1] Typically polarised solid-state cryogenic targets are used which are either proton or deuteron rich compounds, depending upon the experimental requirements.

matter. Only a very small subset of the physics program will be summarised here and therefore the interested reader is referred to the extensive overviews of the physics program fully detailed in [6,8,9,10,11]. The CLAS12 physics program will focus upon the internal nucleon dynamics, three-dimensional imaging of the nucleon and quark hadronisation processes. Additional topics will include hadron spectroscopy and the search for exotic mesons. The physics program is designed around the high beam energies, high luminosities and close to full angular coverage provided by CLAS12. Efficient PID in CLAS12 will be fundamental to successfully achieve its proposed physics goals.

1.2.1 The Structure of the Nucleon

Inclusive Deep Inelastic Scattering (DIS) experiments have been the subject of intense study at CLAS, and the results have already provided valuable insights into the structure of nucleons in terms of their constituent partons (i.e. quarks and gluons) [12, 13]. These experiments study the reactions $l\,N \rightarrow l'\,X$, where l and l' denote the initial and final lepton after the scattering process from one bound quark inside the nucleon. N represents the initial nucleon and X describes the resulting hadrons from the fragmentations which occur after the scattering process. The scattering process is further described in Fig. 1.3. The DIS measurements are inclusive, meaning that only the scattered electron is reconstructed and this therefore requires extremely efficient electron identification, which will be provided in CLAS12.

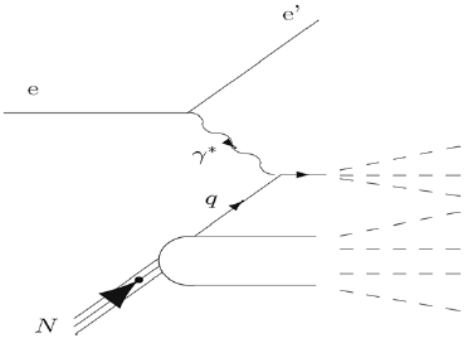

Figure 1.3: The process of deep inelastic scattering of a lepton from a nucleon N [14]. In this case the lepton is an electron, denoted by e and e' in the initial and final states. In the scattering process a high energy photon $\gamma*$ is exchanged between the electron and nucleon, through its interaction with a single quark q of the nucleon. In the final state the struck quark leaves the nucleon, and both the quark and nucleon fragment into hadrons. Image taken from [14].

DIS studies are useful to study the longitudinal structure of the nucleon in terms of the momentum and spin distributions of its partons. Within a perturbative (i.e. calculable) QCD framework and at large momentum transfers from the electron to the quark, the cross-sections for DIS processes provide access to parton distribution functions. Parton distribution functions describe the number density of partons with a certain longitudinal momentum fraction of the parent hadron's [11,12]. In addition to extraction of the longitudinal momentum distributions of partons inside the nucleon, polarised DIS measurements provide information related to the spin content of the nucleon and, through a combination of polarised beams and targets, the helicity [2] density distributions of the nucleon's constituent partons may be obtained, providing data which can reveal further information concerning the nucleon spin puzzle (see Fig. 1.1). Polarised DIS experiments will continue to be studied at CLAS12 [6, 8], and will include large-statistic measurements in kinematic regions where world data is sparse and statistical uncertainties are large.

Nucleon structure studies will be further pursued at CLAS12, going beyond the longitudinal degree of freedom, with experiments devoted to the acquisition of a 3-dimensional image of the nucleon. The core of this program, and indeed one of the major experimental goals of CLAS12, is concerned with the mapping of Generalised Parton Distribution (GPD) functions and Transverse Momentum Dependent (TMD) distribution functions [6,8,11]. Results obtained from GPDs and TMDs are complimentary and when combined allow for the determination of a 3-dimensional image of the nucleon in terms of transverse spatial coordinates, and both the longitudinal and transverse momentum components of the nucleon's constituent partons. These GPD and TMD functions therefore represent extremely powerful and quantitative methods of describing the quark and gluon structure of the nucleon, and their study is achievable through measurements such as Deeply Virtual Compton Scattering (DVCS) [15] and Semi Inclusive Deep Inelastic Scattering (SIDIS) [13]. Therefore a complete program for these measurements is proposed in CLAS12, with unprecedented luminosity and precision.

The GPD functions [6, 8, 9, 10, 11, 15, 16] describe the simultaneous distribution of nucleons with respect to both the transverse position and longitudinal momentum of their constituent quarks and gluons, and may be studied through the exclusive measurements of DVCS and Deeply Virtual Meson Production (DVMP) from the proton. Feynman diagrams, termed "handbag" diagrams, illustrating DVCS and DVMP from the proton p are shown in Fig. 1.4 on the left and right respectively. DVCS measures the electron e scattering process $\mathrm{e\,p} \rightarrow \mathrm{e'\,p'}\,\gamma$, where a virtual photon γ^* is absorbed by one quark inside the nucleon, which in turn emits a real photon γ before returning to the nucleon with a different momentum. This consists of a hard-calculable process describing the scattering of the virtual photon from the proton and the

---

[2] Helicity describes the projection of a parton's spin vector onto the direction of its momentum vector.

so-called soft processes occurring inside the nucleon which are non-calculable and described by the GPDs. In the case of the DVMP measurements, in place of a real photon, meson/s are produced by the struck quark. If the produced meson is successfully detected and identified, its quark content then allows the flavour of the struck quark to be deduced, and hence provide information about the flavour composition of the nucleon. Since GPD measurements performed through DVCS and DVMP are exclusive processes, they require full reconstruction of all final state particles and therefore demand extremely efficient PID for electrons, photons, protons and charged hadrons such as kaons. This will be essential across the entire kinematic range of CLAS12 and a RICH detector will play a crucial role in the full reconstruction of such reactions.

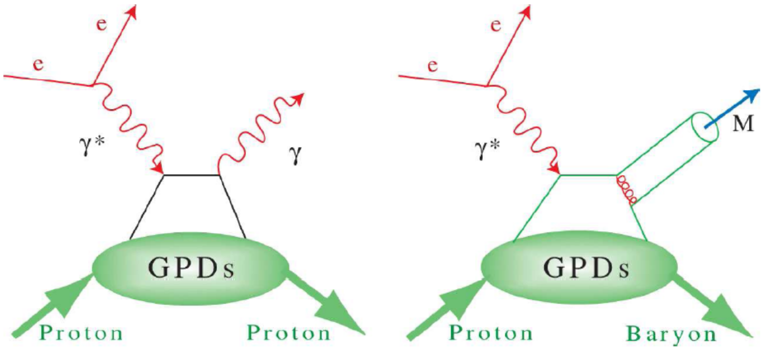

Figure 1.4: The so-called handbag diagrams, illustrating deeply virtual Compton scattering (left) and meson production (right) processes, which are measured to extract information relating to Generalised Parton Distributions. All final state particles are detected in the process, requiring efficient hadron identification. Image taken from [8].

TMD distributions [6,8,9,10,11,13,17] describe the transitions of a nucleon with a certain polarisation in the initial state to a quark with another polarisation in the final state and are connected to the orbital angular momentum of the nucleon wave function, giving access to the transverse spin structure of the nucleon. TMDs may be measured through scattering processes such as SIDIS, and an extremely significant portion of the CLAS12 experimental program in the first five years of its run-time will concentrate upon SIDIS measurements from the nucleon.

SIDIS measurements may be described by $l+N \rightarrow l'+h+X$, where: l and l' denote the initial and scattered lepton respectively; N represents the initial nucleon; h and X describe measured and un-detected final-state hadrons from fragmentation of the proton/struck quark. Both the scattered lepton and initial nucleon may be polarised, and different polarisation states are an important degree of freedom in SIDIS studies. An example diagram of a SIDIS measurement is illustrated in Fig. 1.5, where a virtual photon γ^* is absorbed from a scattered electron e by a quark u inside the nucleon N (proton). As opposed to DVCS measurements

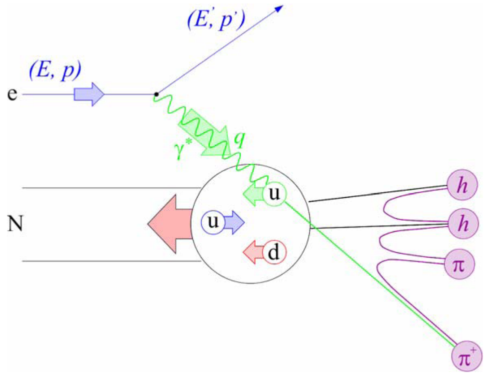

Figure 1.5: Diagram illustrating an example of semi inclusive deep inelastic scattering of an electron from a proton. A virtual photon is exchanged to one quark inside the proton, resulting in the fragmentation of both the initial nucleon and the struck quark. Only the scattered electron and the leading high-momentum produced hadron are coincidently detected in the final state. Image taken from [18].

where the nucleon stays intact, in SIDIS both the struck quark and the nucleon fragment into hadrons. Through such measurements the resulting TMD distributions provide access to the average fraction of the nucleon's transverse momentum which is carried by the struck quark. The measurement is termed semi-inclusive since both the scattered lepton and at least one of the leading high-momentum produced hadrons are coincidently detected in the final state. Similar to the case for DVMP, the detected hadron allows for flavour tagging and hence directly yields information concerning different quark contributions to nucleon properties. Polarised SIDIS measurements may be used to compliment and further DIS measurements, by providing a flavour decomposition of the spin contributions inside the nucleon. For a full flavour decomposition of these effects efficient identification of the scattered leptons and produced hadrons across a wide kinematic range are required in CLAS12, as final-state hadrons mis-identified as electrons usually exist as the most severe source of backgrounds in inclusive measurements [13]. In particular, for the proposed SIDIS program at CLAS12, there is a significant demand for the efficient separation of pions from kaons [11]. SIDIS measurements with strange hadrons will be essential and the efficient detection of kaons over a kinematic range from ∼1 - 11 GeV will allow the study of the contribution of strange sea quarks to the nucleon's transverse momentum and spin structure [11]. SIDIS studies therefore present extremely strong demands for excellent charged hadron identification in CLAS12.

1.2.2 Quark Hadronisation Processes

Further to the procurement of a 3-dimensional image of the nucleon structure, the physics program of CLAS12 will also tackle the study of quark hadronisation processes [6,8,11], especially within the nuclear medium. Experiments concerned with quark hadronisation processes will allow for investigations into the transformation of coloured [3] quarks into colourless hadrons, and features of this which will be probed in more detail include the time it takes to form the colour field of a hadron and how long a coloured quark may remain unconfined before fragmentation [6]. Through such investigations the space-time characteristics of QCD may be studied, and gaining further understanding of quark propagation in the nuclear medium is also crucial for the interpretation of high energy proton-nucleus interactions and ultra relativistic heavy ion collisions, which allow study of the quark-gluon plasma [11]. These studies will typically examine hadron production in nuclear DIS or SIDIS experiments. One observable planned to be analysed in-depth is the hadron attenuation ratio, equivalent to the ratio of the number of hadrons of a certain type produced per DIS event on a nuclear target of a certain mass to the equivalent from a deuterium target [6, 11]. Therefore, efficient hadron PID across the entire anticipated kinematic range, which may be provided by a RICH detector, will be crucial to fully explore these measurements.

1.2.3 Hadron Spectroscopy and the Search for Exotic Mesons

Measuring the spectrum of hadrons, studying their inner structure and mass nature in terms of quarks and gluons, is a crucial component to any physics program aiming to further the understanding of QCD [11]. Hadron spectroscopy studies therefore, where the non-perturbative QCD region may be probed through the electro-production of hadrons and the corresponding study of their properties such as excitation resonances and decays, have played a major role in the previous CLAS physics program and will continue to be studied at CLAS12 as discussed fully in [6, 8, 11, 19].

In the 1950's and 1960's hadron spectroscopy studies led to the development of the *Quark Model*, whereby mesons are bound states of a quark-antiquark pair, and baryons are bound states of 3 quark and antiquark mixtures. QCD theories however also predict the existence of states beyond the standard quark model, such as glueballs (different combinations of gluons coupled together), hybrids (the bound states of 1 quark, 1 antiquark and 1 gluon) and tetraquarks (consisting of 2 quarks and 2 antiquarks). The proposed CLAS12 meson spectroscopy program, or *MesonEx*, will include searches for these exotic states. In particular strangeness-rich final

---

[3] In QCD, quarks carry the quantum number colour charge (r, g, b) and anti-quarks carry anti-colour charge ($\bar{\text{r}}$, $\bar{\text{g}}$, $\bar{\text{b}}$). The colour degree of freedom must be conserved in strong interactions, where the mediating gluons may carry both colour and anticolour.

states will be used in these searches. One such example lies in the possible decay modes to $\phi\pi$ final state particles [11], where the ϕ meson may then decay to the K^+K^- strange hadrons. The proposed hadron spectroscopy program also plans to probe exotic hadrons through the study of strangeonia ($s\bar{s}$), and these states will be identified by their corresponding decays into kaons with momenta ranging up to 7 GeV/c [11]. The ability to detect kaons therefore, over a wide kinematic range, will be crucial for the MesonEx program, in addition to the excellent PID in general required for reconstructing multi-particle final-states.

Such a broad physics program demands efficient hadron identification across its entire kinematic range and therefore the physics program will take full advantage of the CLAS12 apparatus, which is subsequently described below.

1.3 CLAS12 Apparatus

CLAS12 [8] will be optimised to study both exclusive and semi-inclusive reactions with: high beam energies, reaching 11 GeV; maximum beam currents of $90\,\mu$A; high longitudinal beam polarisation of 75 - 85 %; longitudinally and transversely polarised proton and neutron targets; large acceptance; high statistics and luminosities of $>10^{35}\,\mathrm{cm}^{-2}\mathrm{s}^{-2}$, which provide access to reactions with small cross-sections. CLAS12 will therefore be the optimal detector to study the nucleon structure through the topics described above in Section 1.2.

A 3-dimensional model of the CLAS12 apparatus is shown in Fig. 1.6, where the maximum diameter of the detector is ~ 10 m. CLAS12 will consist of two sections: the Central Detector (CD), dedicated for lower momenta particles and a polar angular acceptance range of $35° < \theta < 125°$, and the Forward Detector (FD) which is designed for higher momenta particles and to cover polar angles $5° < \theta < 35°$. Both the FD and CD provide almost complete $2\,\pi$ azimuthal angular coverage.

Sub-components of both the CD and FD are used coincidently for reconstruction of energy (E) and momentum (p) of final state particles, and also for PID, which will be crucial for the success of CLAS12. Typically either the determination of how a particle interacts with matter or the extraction of both its mass and charge is required for successful PID. Some overviews of PID techniques in multi-purpose particle detectors may be found in [20,21,22]. If a particle's momentum p and velocity v are known, then its mass m may be determined through manipulation of the relation $p = \gamma\, m\, v$, where γ is the relativistic Lorentz factor. The charge and momentum of a particle may be deduced from its travel in a magnetic field, of strength B, where the charge of the particle may be extracted from direction of travel and the bending

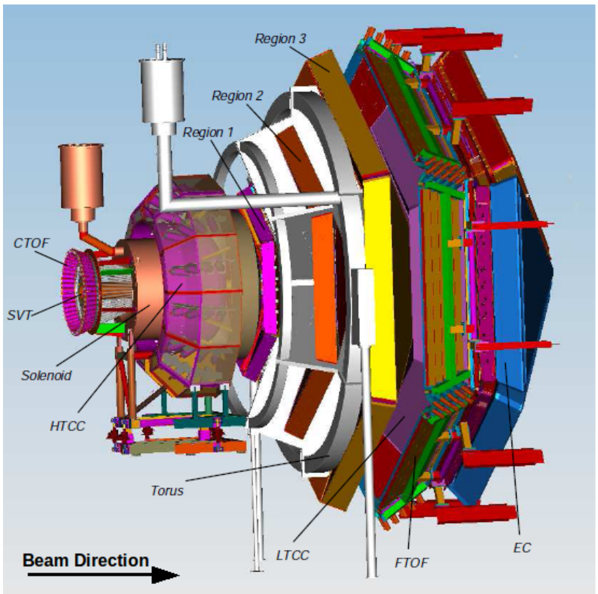

Figure 1.6: 3-D view of CLAS12, indicating detector sub-components of both the central and forward detectors which are used for particle tracking and identification. Image taken from [8].

radius of its track (ρ) is directly proportional to its momentum, with $\rho = \frac{p}{0.3B}$. In CLAS12, which is a magnetic spectrometer [20], tracking detectors will measure the bending of charged tracks in the magnetic field, providing momentum analyses. Measurements of the particle velocities in CLAS12 are then provided by Time-Of-Flight (TOF) measurements. Threshold Čerenkov counters are also used in addition for enhanced identification, and in particular they were designed for electron identification and charged pion rejection. Electromagnetic calorimeters (ECs) are also used in CLAS12, mainly to detect electrons and neutral particles, and to allow for the energy reconstruction of particles through missing mass techniques. The sub-components of the CLAS12 CD and FD providing these functionalities are described below.

1.3.1 The Central Detector

The CD [8, 23] will be a completely new installation to Hall B and will occupy the region immediately surrounding the fixed target. It is primarily used for the tracking and identification of backward scattered recoil particles. The design of the CD is based around a 200 cm - diameter and 180 cm - length superconducting solenoid magnet, which provides a maximum central field strength of B = 5 T. A Silicon Vertex Tracker (SVT) [8, 23], which is used for charged particle tracking, is located inside the magnetic solenoid and comprised from several single-sided silicon strip detectors [24]. The SVT will provide track resolutions of $\sigma_\theta < 20\,\text{mrad}$ and $\sigma_\phi \sim 5\,\text{mrad}$ for polar and azimuthal angles respectively and a fractional momentum resolution of $\sigma_p/p =$

5% [8]. However, it has been suggested that a significant improvement in tracking resolution may be obtained by replacing a subsection of the SVT with layers of micromegas detectors [23, 25, 26]. Central TOF (CTOF) detectors [8, 23] will also be placed inside the solenoid and are used to measure the flight time of particles over a known distance relative to the stable RF signal from the accelerator. The CTOF system consists of strips of plastic scintillators, with dual-readout at both ends by PhotoMultiplier Tubes (PMTs). The design goal of the CTOF system is a timing resolution of $\sigma_{CTOF} \sim 50\,ps$, which would allow for $4\,\sigma$ π/K and π/p separations for momenta ranging up to 0.64 GeV/c and 1.25 GeV/c respectively. A central EC [8] is also included in the CD, primarily for the reconstruction of π^0 and η^0 mesons by their subsequent decays into two photons. There is a limited radial space of ~10 cm available for the central EC and a sampling design is therefore selected, which is composed of plastic scintillating fibres interleaved with metal tungsten powder. The fibres are coupled via light guides to PMTs, providing single-ended readout for energy and timing analysis of signals. Through the combination of information from all of the CD sub-components, efficient identification of charged recoil hadrons is achievable.

1.3.2 The Forward Detector

The FD [7, 8, 23] comprises six superconducting pancake magnetic coils. The magnetic coils create a field in the ϕ azimuthal direction and correspondingly produce a toroidal field, of maximum magnitude 2 T, around the beam axis. This allows for the magnetic analysis of charged particles in the θ polar direction, with the magnetic field always acting transverse to the particle trajectory and leaving the ϕ track angle unaltered. A field-free region is maintained around the fixed target, accommodating for the use of polarised targets. The magnetic torus defines the six-sector symmetrical geometry of CLAS12, surrounding the beamline, and is responsible for the characteristic in-bending or out-bending of charged particles in the forward direction of the spectrometer.

Each sector covers a polar angular acceptance for forward scattered charged and neutral particles from at least 5° - 35° and 2° - 35° respectively and, as may be observed in Fig. 1.7, comprises the following components for PID: High and Low Threshold Čerenkov Counters (HTCC and LTCC); EC detectors; Drift Chambers (DCs) and Forward TOF counters (FTOF). The FD [7,8,23] will be built upon the existing CLAS [7] layout and re-use several elements such as the FTOF counters [27], the LTCC [28] and EC components, but upgraded with improved resolution capabilities. Completely new installations will comprise the HTCC, three regions of new DCs and the torus magnet components. Brief descriptions of these detectors and their PID roles are given below.

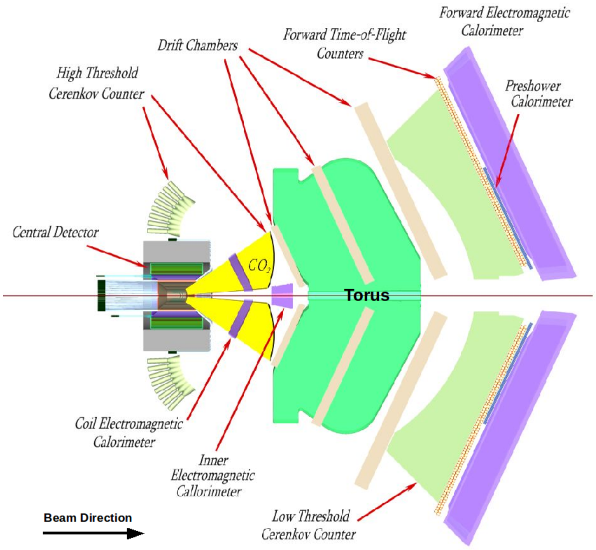

Figure 1.7: Cross-sectional view of CLAS12, with labelling of detector components. Image from [5].

Threshold Čerenkov Counters

The LTCC [7, 8, 28] and HTCC [8, 23] are both primarily designed and used for electron identification and separation from charged pions. When used conjunctively they allow for charged pion identification up to a momentum of 5 GeV/c.

The LTCC consists of six sectors, each covering a volume of ~6 m^3. The sectors are filled with perfluorobutane (C_4F_{10}) Čerenkov radiator gas and with this radiator gas the pion Čerenkov threshold, a concept which will subsequently be described in Section 2.1, is 3 GeV/c. A pion with momentum greater than this will produce Čerenkov light in the LTCC. The LTCC detector incorporates a mirror system which focusses and reflects emitted Čerenkov light to PMTs for detection. An analysis on the corresponding number of detected photoelectrons obtained from the PMT signals then allows for electron triggering and charged pion separation, since this number depends upon the fractional velocities $\beta = v/c$ of the particles (where v is the speed of the particle and c is the speed of light in a vacuum).

The HTCC is located upstream from the LTCC, and the radiator material selected is CO_2 gas. This radiator yields Čerenkov thresholds of 15 MeV/c and 4.9 GeV/c for electrons and charged pions respectively, and for momenta below the pion threshold the HTCC electron identification detection efficiency is projected to be 99.99 %. The design of the HTCC is similar to that of the LTCC, however since it is positioned before the magnetic torus it has a stricter material budget to minimise multiple scattering influence on momentum measurement resolutions. The optical design of the HTCC incorporates one reflection only from low density elliptical mirrors, with the PMTs positioned at their focal points as shown in Fig. 1.8. As with the LTCC, an analysis on the number of detected photoelectrons provides the PID.

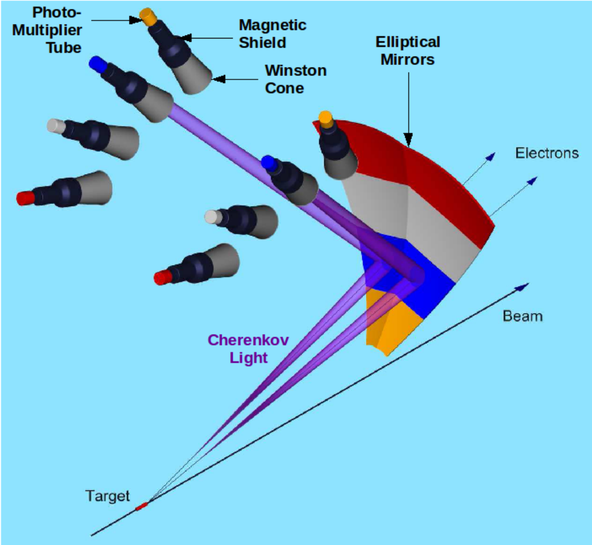

Figure 1.8: Schematic illustrating the detector design principle of the CLAS12 high threshold Čerenkov counter. The photomultiplier tubes are positioned in the focal points of the elliptical mirrors (as matched by colour). Image modified from [8].

Drift Chambers

Three DC regions will be used in CLAS12 [8,23], conforming to the six sector geometry as shown in Fig. 1.9 (a), for the tracking and momentum analysis of charged particles. The three regions (R_1, R_3 and R_3) are located just before, inside and after the torus field volume respectively. DCs are multiwire chambers in which spatial resolution is achieved by measuring the transit time of electrons, from the moment that an initial ionising particle traversed the gaseous detector to their arrival upon the detecting sense wire. A full description of the principles of DCs may be found in [20, 29, 30].

The design of the DCs is similar to the previous CLAS DC design [7,31], but with improved spatial resolution and decreased background sensitivity. Each DC region contains 12 hexagonal-shaped drift cell layers (see Fig. 1.9 (b)), and the DCs therefore yield 36 measurements for individual charged particle tracks. This provides sufficient redundancy for pattern recognition and track reconstruction [23]. The required angular resolutions for the DCs are $\sigma_\theta < 1\,\text{mrad}$ and $\sigma_\phi < 3\,\text{mrad}$ in the θ and ϕ directions respectively, and the required fractional momentum resolution is $\frac{\sigma_p}{p} < 1\%$. The FD tracking system is designed to meet these demands [8].

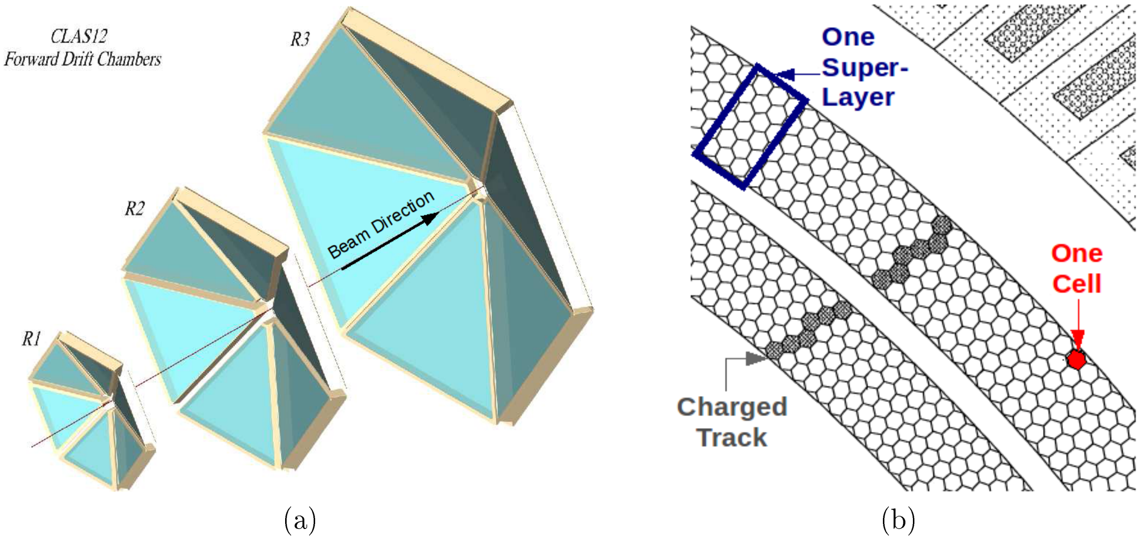

Figure 1.9: (a) The three drift chamber regions for charged particle tracking and momentum measurements in CLAS12. Image modified from [8]. (b) Close-up view of the CLAS drift chamber arrangement, showing two superlayers of hexagonal shaped drift cells (sense wires omitted). Image modified from [31].

Forward Time of Flight System

The FTOF system [8, 23, 27], which is used to measure flight times of charged particles, is located immediately behind the LTCC with an average path length of ∼650 cm from the fixed target. Since the distance (L) and flight time (τ) are both known, this allows retrieval of the particle's velocity ($v = \frac{L}{\tau}$). Combination with the DC measurements then allows for PID. The CLAS12 FTOF was designed to allow for successful π/K separation up to 3 GeV/c.

Each of the six FTOF sectors comprise two panels (Panel 1 and Panel 2) of rectangular plastic scintillator strip arrays, covering different polar angles and offering different time resolutions [8, 23]. Fig. 1.10 gives an example of the FTOF counter design for one sector only, showing the scintillator strips and their dual-ended readout by fast single-channel PMTs. A combined timing resolution of $\sigma_{FTOF} \sim 80$ ps in each sector is obtained from both panels of a sector, which is both required for and projects $4\,\sigma$ π/K and K/p separations up to 3 GeV/c and 4.5 GeV/c respectively for equal π, K and p yields [8, 23].

Electromagnetic Calorimeters

In addition to sufficient charged hadron identification, efficient identification of neutral particles, such as photons, neutrons, K^0 and π^0 hadrons, are also crucial for achievement of the CLAS12 physics program. For these purposes, and for the detection of high energy electrons (with energies >0.2 GeV), the CLAS12 FD will comprise coil, inner, pre-shower and forward ECs [8, 23]. EC components may also be used conjunctively with the DCs for PID, since a

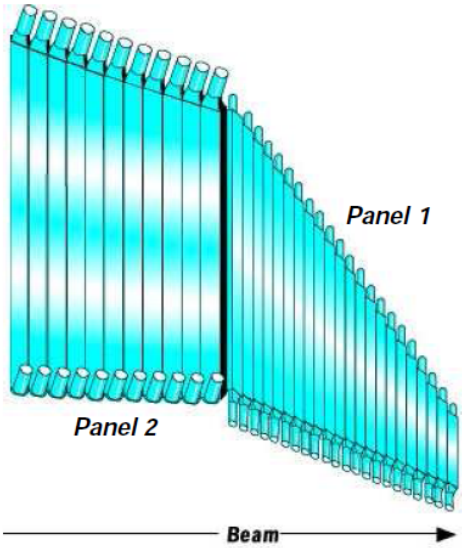

Figure 1.10: One forward time-of-flight sector, comprising two panels of plastic scintillator strip arrays. Image taken from [8].

neutral particle will deposit energy in EC detectors with no tracks in the DCs.

The existing EC from CLAS will be re-used as the CLAS12 forward EC. The design [7, 32] consists of 39 alternating layers of scintillator strips and lead sheets as shown in Fig. 1.11 (a), the scintillator strips are readout using fibre light guides and PMTs and provide a transverse positional resolution of $\sigma_{xy} \sim 2.3\,\text{cm}$ [32]. Six lead-scintillator sandwich calorimeter sectors are used in total, with each sector having a thickness of 16 radiation lengths.

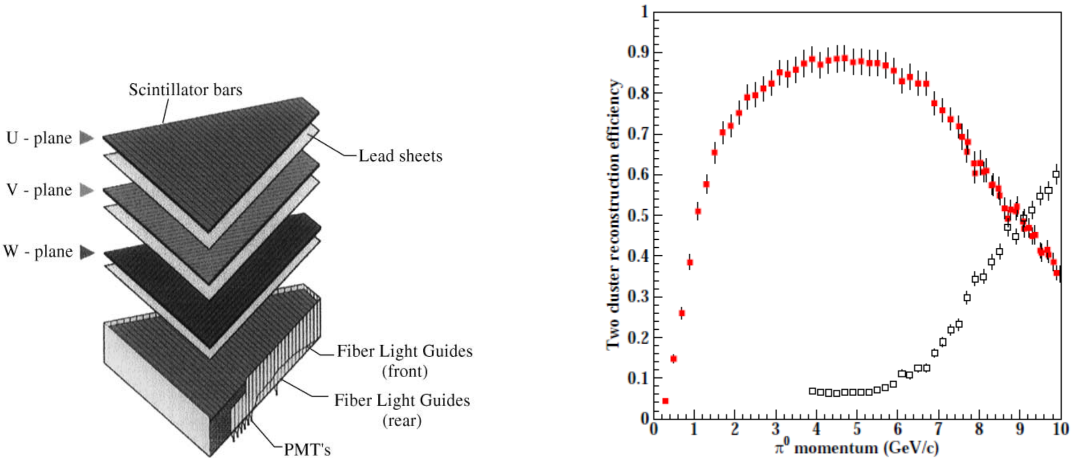

(a) (b)

Figure 1.11: (a) Exploded view of one sector of the CLAS12 forward sandwich calorimeter. The U,V, W labels indicate varying 120 ° rotations of the scintillator planes, providing 2-dimensional position resolution. Image taken from [32]. (b) Simulated efficiency for CLAS12 reconstruction of two photon clusters from the decay $\pi^0 \to \gamma\,\gamma$ (red points). The unfilled points show the probability that one cluster is reconstructed with the same energy as the simulated π^0. The simulation was performed by members of the CLAS collaboration and the result is taken from [8].

The separation of high energy photons from π^0 and η mesons, which decay into two photons, presents a significant requirement for the proposed CLAS12 experiments. As the momentum increases the opening angle between the two decay photons from the π^0 decreases. At the π^0 momenta expected in CLAS12, which range up to 9 - 10 GeV/c, the existing positional granularity of the forward EC will be unable to distinguish the two decay photons from one single high energy photon. This has been subject to simulation studies performed by the CLAS Collaboration (see Fig. 1.11 (b)), and they discovered that beyond 5 GeV/c the efficiency of detecting the two π^0 decay photons as two clusters starts to decrease drastically from almost 90 % to 35 % at 10 GeV/c [8]. Furthermore, the forward EC will be unable to fully absorb the energy of the electromagnetic showers at momenta above 5 GeV/c. For these reasons the pre-shower EC (PCAL) will be placed immediately upstream of the forward EC. The conceptual design for the PCAL is similar to the existing forward EC of CLAS [8, 23], however it will be highly segmented, providing a 2.5 × superior position resolution and allow for a separation of two photons up to momenta > 10 GeV/c [23]. The PCAL is based on a lead-scintillator sandwich design, with 15 alternating scintillator and lead sheet layers, and corresponds to ~ 5.5 radiation lengths. It will cover a reduced polar angular range from 5 ° to 23 ° and aid the forward EC by improving full shower absorption capabilities [8].

The coil EC [8] is placed upstream of the torus and will provide calorimeter acceptance *only* for the regions which are shielded by the torus coils in the PCAL and forward EC components. Arrays of lead tungstate ($PbWO_4$) scintillation crystals are used and readout by avalanche photodiodes. The coil EC concept is based upon the inner EC, which has already been used during the runtime of CLAS for dedicated DVCS experiments. The inner EC [8, 23] is placed immediately upstream of the first DC region, and is used to provide photon and pion calorimetry measurements at extremely forward scattered angles of < 6 °, at momenta of up to 10 GeV/c, and will also be re-used in CLAS12.

Efficient PID across the entire kinematic range is absolutely essential for successful achievement of the CLAS12 physics goals described in Section 1.2, and the various sub-detectors of the CLAS12 baseline apparatus, which have been described above, will be used simultaneously to achieve this.

1.4 Particle Identification in the CLAS12 Forward Detector

The expected PID performance of the CLAS12 FD, in particular for electrons and charged hadrons, has previously been described and commented upon [8, 23, 33, 34, 35].

Electrons are very successfully identified using the combination of LTCC and HTCC measurements for momenta ranging up to 5 GeV/c [8], and at momenta higher than this they are efficiently identified through measurements of deposited energy in the EC components. A further cross-check for electrons, is that the energy deposited in the EC must match the momentum measured in the DCs.

For hadrons, efficient $\pi/K/p$ separations across the entire kinematic range demonstrate crucial benchmark separations for many of the experiments planned for the first five years of runtime with CLAS12. Fig. 1.12 shows which FD components will provide means of separation between these particle species, and across which momenta ranges.

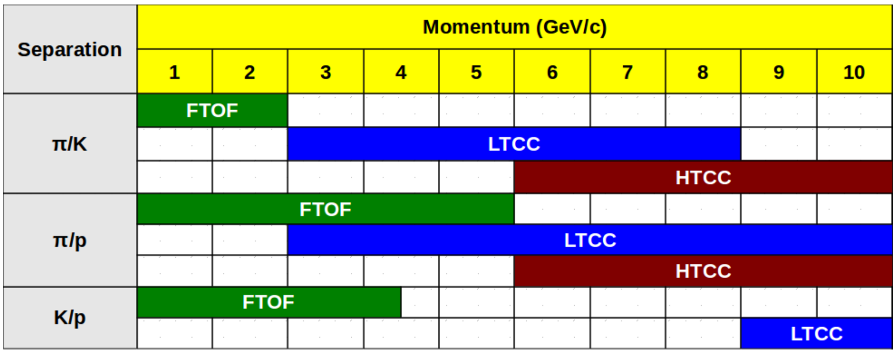

<table>
<tr><th rowspan="2">Separation</th><th colspan="10">Momentum (GeV/c)</th></tr>
<tr><th>1</th><th>2</th><th>3</th><th>4</th><th>5</th><th>6</th><th>7</th><th>8</th><th>9</th><th>10</th></tr>
<tr><td rowspan="3">π/K</td><td colspan="2">FTOF</td><td></td><td></td><td></td><td></td><td></td><td></td><td></td><td></td></tr>
<tr><td></td><td></td><td colspan="6">LTCC</td><td></td><td></td></tr>
<tr><td></td><td></td><td></td><td></td><td></td><td colspan="5">HTCC</td></tr>
<tr><td rowspan="3">π/p</td><td colspan="5">FTOF</td><td></td><td></td><td></td><td></td><td></td></tr>
<tr><td></td><td></td><td colspan="8">LTCC</td></tr>
<tr><td></td><td></td><td></td><td></td><td></td><td colspan="5">HTCC</td></tr>
<tr><td rowspan="2">K/p</td><td colspan="4">FTOF</td><td></td><td></td><td></td><td></td><td></td><td></td></tr>
<tr><td></td><td></td><td></td><td></td><td></td><td></td><td></td><td></td><td colspan="2">LTCC</td></tr>
</table>

Figure 1.12: The momentum coverage of CLAS12 forward detector components used for charged pion (π), kaon (K) and proton (p) separations. Where FTOF, LTCC and HTCC represent the forward time of flight counters and low and high threshold Čerenkov counters respectively. Chart modified from [33].

For π/K separations the FTOF counters will offer reliable $4\,\sigma$ separations for the momentum range 1 - 3 GeV/c. Between 3 GeV/c and 6 GeV/c however, until the HTCC may be used, the separation is significantly less reliable since it relies only upon the veto of K mesons in the LTCC. Furthermore, depending upon the minimum number of photoelectrons detected by the HTCC, it provides a separation power of $3\,\sigma$ only for momenta > 7 GeV/c. The response of the LTCC is very complex and its efficiency is very inhomogeneous across its active area. The LTCC therefore may only be used for PID after strict fiducial cuts are placed, and a $3\,\sigma$ separation for the charged hadron species can only be extracted from the LTCC for momenta > 7.7 GeV/c. The π/K separation could therefore strongly benefit from another direct identification means in the region of 3 - 7 GeV/c. For π/p separations the FTOF counters will again provide sufficient identification at low momenta, covering a range of 1 - 6 GeV/c, and from 3 - 6 GeV/c the LTCC will be used in addition as a proton veto. Beyond this, the LTCC and HTCC may be used simultaneously as two independent vetos for protons, since in both detectors the π mesons will now be above threshold. Unfortunately for K/p separations there exists a large gap in the momentum range where separation will not be possible at all with the base line equipment of CLAS12. The FTOF counters will provide the necessary $4\,\sigma$ separation from 1.0 - 4.5 GeV/c, and from 9 GeV/c onwards the LTCC may be used as a veto for protons, since K mesons will now be above threshold. However, in the range 4.5 - 8.0 GeV/c there are no means by which to perform reliable particle separation.

In summary, as illustrated in Fig. 1.12, there exists an extremely strong argument for the requirement of improved $\pi/K/p$, and most crucially K, identification in the region 3 - 8 GeV/c and π/K separation in the range of 3 - 7 GeV/c. As a further example for this requirement, Fig. 1.13 shows the ratio between semi-inclusive K and π yields as a function of momentum, corresponding to required SIDIS kinematics in CLAS12 and as presented and described in [11]. Over the kinematic range of 3 - 8 GeV/c, for instance, the semi-inclusive K yield is roughly one order of magnitude smaller than the π yield. In the region 3 - 6 GeV/c therefore, where the π/K separation relies solely upon the LTCC performance, the LTCC inefficiency only has to reach values of 10 % or higher before separation will become unreliable, and it has been stated that below 8 GeV/c the LTCC will not provide π rejection factors high enough to achieve a 3σ π/K separation for the expected SIDIS yield ratios [35]. Sufficient K hadron identification over the entire kinematic range of 3 - 8 GeV/c is crucial for the proposed CLAS12 polarised and unpolarised SIDIS experiments, to study for example the contribution of the strange sea to the

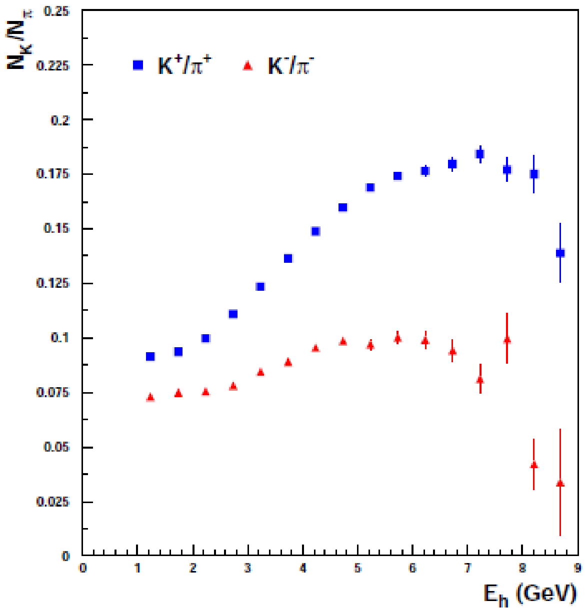

Figure 1.13: A Monte Carlo simulation study, performed by members of the CLAS collaboration, into the ratio between semi-inclusive kaon and pion yields, using an 11 GeV electron beam and as a function of kaon momentum. Image taken from [11].

nucleon spin [8].

Several feasibility simulation studies have been performed [33, 34], which have concluded that the installation of a RICH detector in-place of the LTCC would allow for greatly improved $\pi/K/p$ identification in the momentum range of 3 - 8 GeV/c. The benchmark goal of the RICH detector is to achieve a $\pi/K/p$ separation of $>3\,\sigma$ from momenta of 3 GeV/c up to 8 GeV/c. The addition of a RICH detector into CLAS12 would enhance achievement of the physics program described in Section 1.2, furthering the study of nucleon structure studies at Hall B. The first beam delivery for CLAS12 is expected in 2014 and successful completion of the installation of one of the required RICH sectors is planned for the beginning of CLAS12 data taking in 2016, resulting in a very short time-scale for the detector construction and commissioning project. At least two RICH sectors are currently planned, to provide successful kinematic coverage for experiments studying the scattering of leptons from both longitudinally and transversely polarised targets. However, in the ideal case 6 sectors would be installed eventually for enhanced hadron identification over the entire acceptance of CLAS12. In the following chapter the principles of Čerenkov radiation and RICH detectors, the proposed design of the CLAS12 RICH counter and the corresponding photon detection requirements are described.

Chapter 2

A RICH Detector for CLAS12

The benefit obtained from the installation of a RICH detector into the FD of CLAS12, for improved PID in the momentum range 3 - 8 GeV/c, has been described in the previous Chapter (see Section 1.4). This chapter describes Čerenkov radiation and RICH detectors, along with the foreseen design of the CLAS12 RICH. This section concludes with a discussion concerning the resulting photon detection requirements in the CLAS12 RICH detector, fulfillment of which are crucial for success of the RICH detector.

2.1 Čerenkov Radiation

Čerenkov radiation [20, 29, 36, 37, 38, 39, 40, 41] is defined as characteristic electromagnetic radiation which is emitted when a charged particle traverses a dielectric medium with a velocity greater than the phase velocity of light in the same medium. Inherent to the definition is the existence of a threshold velocity for the charged particle, the Čerenkov threshold β_{thr}, which must be met for Čerenkov radiation to be emitted. For a material of refractive index n, the magnitude of the phase velocity of light in that medium is given by $v_\phi = c/n$, where c is the speed of light in vacuum. In order for a charged particle of velocity v to travel faster than v_ϕ, then its fractional velocity $\beta = v/c$ must be greater than $1/n$. The Čerenkov threshold is therefore given by Equation 2.1 and is directly dependent upon the refractive index of the material.

$$\beta_{thr} = \frac{1}{n} \tag{2.1}$$

The Čerenkov threshold is related to the energy E of the particle through the relation $E = \frac{m_0 c^2}{\sqrt{1-\beta_{thr}^2}}$, where m_0 is the rest mass of the particle. For a fixed energy therefore the threshold velocity will depend upon the particle mass and the Čerenkov effect then already becomes extremely useful as a means for PID through mass discrimination techniques, for example as used in the CLAS12 LTCC and HTCC (see Section 1.3.2).

The Čerenkov radiation phenomenon may be visualised further upon inspection of Fig. 2.1, and as explained comprehensively in [20, 38]. In both cases a charged particle traverses a dielectric material, where the travel of the particle is indicated by the arrow and the atoms of the material are denoted by circles. Close to the passing particle the atoms of the material are polarised by its electric field and therefore form electric dipoles as shown by the polarity signs in Fig. 2.1. If the velocity of the charged particle is less than the phase velocity of light in the material (left-hand case of Fig 2.1), then the dipoles are symmetrically arranged around the particle path and no large-scale dipole field is observed. In other words, if the dipole field is integrated over all constituent dipoles it vanishes and no Čerenkov radiation is emitted in this case. In the right-hand case of Fig 2.1 however, where $v > c/n$, the polarisation field is no longer completely symmetrical since there exists an asymmetrical polarisation of the medium in front of and behind the charged particle. This represents a non-vanishing net electric dipole moment, which also varies with time. The time-variation of the dipole field results in the emission of Čerenkov radiation, since in order for the atoms to return to their ground states a shock-wave of prompt electromagnetic radiation is released.

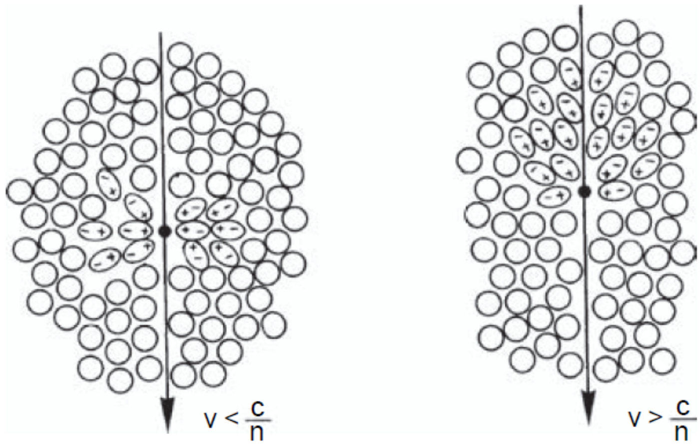

Figure 2.1: The cases of a charged particle traveling through a dielectric material with a velocity (v) less (left) and greater (right) than the phase velocity of light in the material (c/n). The particle travel is indicated by the arrow, and the circles represent atoms of the dielectric. Close to the electric field of the particle, electric dipoles are created. In the case of $v > c/n$ an asymmetric polarisation leads to the emission of Čerenkov radiation. Image taken from [20].

The wavefront of the emitted Čerenkov radiation may be represented by the superposition of spherical Huygens waves, which are produced by the particle as it travels along its trajectory and as illustrated further in Fig. 2.2. As a result the coherent wave-front is conical in shape,

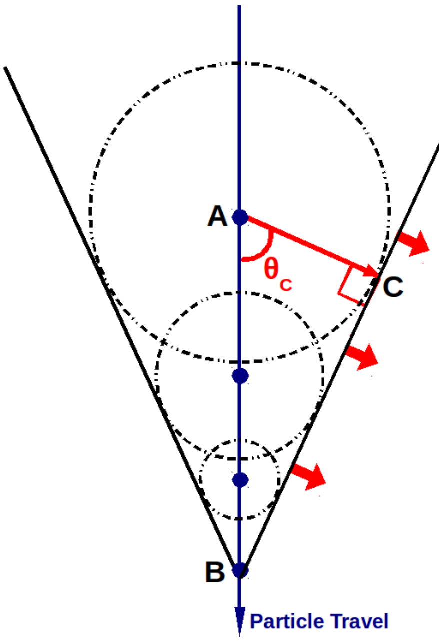

Figure 2.2: The geometry of emitted Čerenkov light and the formation of the characteristic conical shape of its coherent wavefront. Image based upon sources from [20, 40].

with a characteristic polar opening half-angle of θ_C with respect to the particle trajectory. This angle is known as the Čerenkov angle. The emission angle in the azimuthal ϕ direction, with respect to the particle trajectory, has a flat distribution between 0 and 2π. In the case of Fig. 2.2, the distance AB travelled by the particle in time τ is $\tau\beta c$, and the corresponding distance AC travelled in the same time by the emitted Čerenkov radiation is $\tau c/n$. The Čerenkov angle is therefore given by the relation in Equation 2.2.

$$\cos\theta_C = \frac{\tau c/n}{\tau\beta c} = \frac{1}{\beta n} \tag{2.2}$$

Equation 2.2 demonstrates that if the refractive index of the radiating medium is known, then a measurement of θ_C allows for extraction of the velocity of the traversing particle. For values of β close to β_{thr}, the Čerenkov radiation is emitted in the forward direction and will increase with β until a maximum value at the ultra-relativistic case of $\beta = 1$, where the Čerenkov angle saturates at $\theta_C = \arccos(1/n)$. In addition, increasing refractive index of the radiating medium will also yield larger values of θ_C. In reality practical Čerenkov radiators are dispersive materials, and so the refractive index ($n(\lambda)$) is written as a function of the Čerenkov radiation wavelength (λ). In principle dispersion effects therefore, which are proportional to λ^{-2}, will also yield θ_C values which vary with the Čerenkov radiation λ.

The intensity and spectrum of the Čerenkov radiation is governed by the Frank-Tamm relation [38], and for example is expressed in terms of the number of Čerenkov photons emitted per unit path length dN/dx, with wavelengths λ between λ_1 and λ_2, in Equation 2.3 [20, 39].

$$\frac{dN}{dx} = 2\pi\alpha z^2 \int_{\lambda_1}^{\lambda_2} \left(1 - \frac{1}{(n(\lambda)\beta)^2}\right) \frac{d\lambda}{\lambda^2} = 2\pi\alpha z^2 \int_{\lambda_1}^{\lambda_2} \sin^2\theta_C \frac{d\lambda}{\lambda^2} \tag{2.3}$$

The parameters α and z represent the fine structure constant and the electric charge of the traversing particle, in units of the electron charge $[e]$.

In principle there is no spectral cut off in this relation, however due to the dispersion effects of real media the radiation emission is restricted to ranges where $n(\lambda) > 1/\beta$. Furthermore, absorption bands in media tend to limit the Čerenkov spectrum to a range lying between the Ultra-Violet (UV) and near infra-red wavelengths. Also, in the X-ray wavelength regions the index of refraction typically becomes <1 and so Equation 2.1 can no longer be fulfilled, resulting in no emission of Čerenkov radiation. It is interesting to note the dependence upon $1/\lambda^2$ in Equation 2.3 and the dispersive behaviour of the refractive index of a material, which implies that although the Čerenkov spectrum is continuous across a wide wavelength range, a larger intensity of Čerenkov photons are produced for shorter wavelengths. To give an example of the expected order of magnitude of the number of Čerenkov photons emitted per unit length, if one integrates Equation 2.3 over a visible wavelength range only, so for instance between $\lambda_1 = 400\,\text{nm}$ and $\lambda_2 = 700\,\text{nm}$, and for a value of $z = 1$, then the result shown in Equation 2.4 is obtained.

$$\frac{dN}{dx} \approx 490 \sin^2\theta_C \; photons/cm \tag{2.4}$$

However, it has been stated that inclusion of the UV-wavelengths will increase this yield by a factor of 2 - 3 [20, 39]. It is also important to note, upon inspection of Equation 2.3, that the number of Čerenkov photons produced will increase with both the refractive index and length of the radiator material, in addition to the velocity of the charged particle.

For practical use, Equation 2.3 must be integrated over the wavelength region for which $\beta n(\lambda) > 1$. Moreover, to calculate the expected number of Čerenkov photons actually recorded by a particular detector of Čerenkov light, Equation 2.3 must be convoluted with the detector response [37]. For instance, the wavelength range of the integration will be limited by the overall spectral sensitivity of the Čerenkov detector. Other detector efficiencies such as the quantum efficiency of the photon detector, along with Čerenkov light transmissions through detector windows and radiator materials, or reflections from any focussing mirrors will also affect the number of detected photons recorded over a certain wavelength range [37]. In general Čerenkov radiation is a weak source of photons [20, 29], for example scintillation light is approximately 100 times more intense [20], and so to maximise the number of detected Čerenkov photons the light collection and detection methods must be as efficient as possible.

Further and more comprehensive descriptions concerning the history, discovery and theory of Čerenkov radiation may be readily found in literature, along with several interesting reports on the evolution of Čerenkov light detection and different detector designs [20, 36, 37, 38, 39, 42, 43, 44, 45]. There are several existing Čerenkov detector designs which all exploit at least one of the characteristic properties of Čerenkov radiation [41], including: its extremely prompt light emission, the existence of a threshold velocity, or its angular and yield dependence upon both the velocity of the traversing particle and the refractive index of the radiating medium. Some of the different traditional Čerenkov detector designs may be classified into threshold, differential and RICH types [29]. Threshold counters detect and sum all Čerenkov photons produced by particles with $v > \beta_{thr}$, whereas differential counters are designed to detect Čerenkov light originating from only a narrow range of θ_C angles and therefore detect only particles lying within a narrow velocity interval. In a RICH detector the angular dependence of Čerenkov light is exploited, and θ_C is measured directly through imaging of the Čerenkov light cone. There are several modern-day RICH counter designs and variations on the RICH technique [44, 45]. In the following section an overview of the general design and properties of RICH detectors which are relevant to the CLAS12 RICH only will be introduced and discussed.

2.2 Ring Imaging Čerenkov Detectors

RICH detectors [20, 37, 42, 43, 44, 45, 46] offer extremely powerful PID over relatively wide momentum ranges, combining the good phase space acceptance of threshold Čerenkov counters with the superior β resolution of differential Čerenkov counters, as described in [37]. The main components of a RICH detector incorporate a Čerenkov radiator and a position sensitive photon detection plane, with the use of focussing optics and mirrors also optionally included. The aim of a RICH detector is to transform the correlated directional information of individual Čerenkov photons, arising from the conical form of Čerenkov light, into spatial coordinates onto a photon detection plane and subsequently allow for the reconstruction of the Čerenkov angle θ_C. Or in other words, since typically used photon detectors determine position directly rather than angles, the Čerenkov angles must be derived from a spatial image [44]. The reconstruction of θ_C allows for an indirect measurement of the particle velocity (see Equation 2.2) and so when combined with a separate momentum measurement, such as track bending in a magnetic field for example, allows for extraction of the particle mass. To allow for this RICH functionality, the photon detector is a crucial element of such a system and it must provide efficient detection of single photons, with high signal to noise ratios, and sufficient spatial resolution. Fast photon detection is also favourable in order to reject background hits and correlate coincident photons arising from the same Čerenkov events [46]. Two types of RICH setups will be discussed further: the proximity and focussing RICH methods.

A proximity RICH detector images the projection of a Čerenkov light cone onto the photon detection plane directly, with no focussing or reflection of the Čerenkov light involved. A schematic of the principle is shown in fig. 2.3 and further comprehensive descriptions of the technique may be found in [37, 44, 45, 46, 47]. The detector consists of a radiator material, an expansion gap and a plane of position sensitive photon detectors which allow for two spatial coordinates of each detected photon to be recorded, and perhaps the time of each photon hit in addition. Since the distance of the the photon emission point from the photon detection plane is known, the resulting ring image allows an extraction of the Čerenkov angle θ_C. In a proximity RICH detector it is important to keep the thickness of the radiator as thin as possible, in order to reduce the uncertainty on the emission point of the Čerenkov light, which may smear the Čerenkov angle resolution. However, the radiator must be thick enough to produce a large enough yield of Čerenkov photons for the measurement, since this depends on the length of the radiator (see Equation 2.3). It is worth noting that typically knowledge of the position of the particle input track and the path of the photon to the detector surface is required in addition [44]. Examples of previously implemented and successful proximity RICH detectors include the RICH detectors of CLEO [45, 48] and ALICE [45, 49].

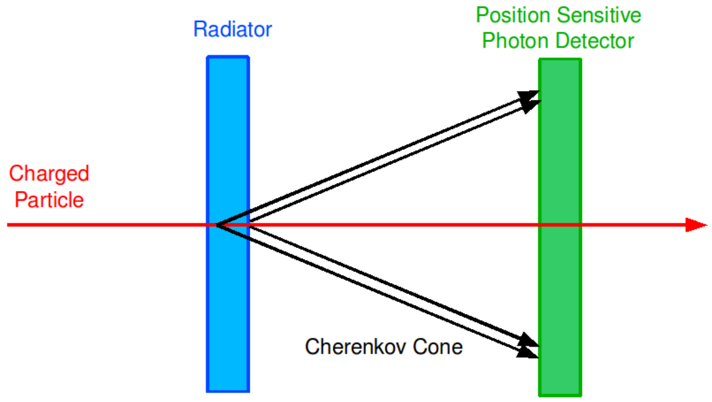

Figure 2.3: Schematic illustrating the principle of a proximity RICH detector. The Čerenkov ring produced by a particle traversing a radiator material is imaged directly by a position sensitive photon detection plane, with no focussing optics or mirrors involved.

In the focussing imaging method [20, 37, 42, 44, 45, 46] the Čerenkov ring image is focused by a lens or mirror and the Čerenkov emission angle is determined from prior knowledge of the detector geometry and focussing optics. Examples of focussing RICH geometries are shown in Fig. 2.4 [47]. Advantages of the focussing method include that one can either magnify or de-magnify the image to match the the spatial resolution of the photon detection plane [44], or comply with complicated detector geometries by, for example, transporting the Čerenkov light to a more suitable location of the imaging plane for detection. Examples of successful previous implementation of focussing RICH detectors may be found in the HERA-B [45, 52], HERMES [45, 53], COMPASS [45, 54] and LHCb [45, 55] detectors.

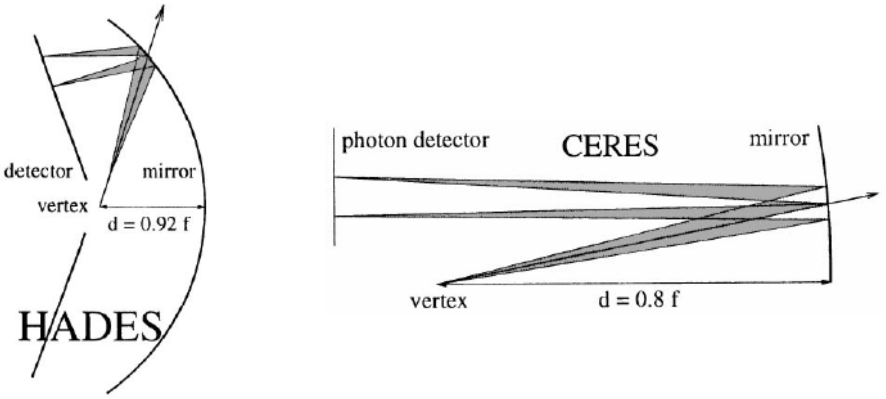

Figure 2.4: Schematics illustrating the principle of focussing RICH detectors. The examples are taken from the HADES [50] and CERES [51] RICH geometries, where d and f denote the distance of the emission point from the optics and the focal length of the mirrors respectively. Images taken from [47].

In general, a RICH detector measures the space directions of N Čerenkov photons for each charged particle above the threshold velocity which traverses the radiator [47]. However, in reality the expected number of photons actually detected by a RICH system ($N_{detected}$), as previously mentioned, is less than the number produced and may be described by the convolution of the Frank Tamm relation with several detector efficiencies. $N_{detected}$ is therefore sometimes written as shown in Equation 2.5 [37, 42, 44, 46, 47], where L is the radiator length [cm], z is the charge of the traversing particle [e] and E is the energy of the emitted Čerenkov radiation [eV].

$$N_{detected} = N_0 \, L \, z^2 \, \sin^2 \theta_C \tag{2.5}$$

The parameter N_0 is referred to as the *figure of merit* of a RICH detector and may be written as $N_0 = (\alpha/\hbar c) \int (Q \, T \, R) \; dE$, where α and $\hbar$ are the fine structure and reduced Planck constants respectively. The parameters Q, T and R are all functions of energy and represent the quantum efficiency of the photon detector (a concept which will subsequently be described in Chapter 3, Section 3.1), the total transmission of the radiator and photon detector entrance window, and the reflectivity of any mirrors used respectively. Typical values of N_0 for practical RICH detectors are $> 1\, N_{detected}/cm$ and vary from $\sim$20 - 100 $N_{detected}/cm$ [46].

The PID performance of a RICH detector is linked to its Čerenkov angle resolution σ_{θ_C} [47], which in general is dependent upon the single photon Čerenkov angle resolution of the RICH detector $\sigma_{single\ photon}$ and the total number of photons detected per event $N_{detected}$, as shown in Equation 2.6.

$$\sigma_{\theta_C} = \frac{\sigma_{single\ photon}}{\sqrt{N_{detected}}} \tag{2.6}$$

If the photon hits are used to determine the ring centre, without external tracking, the $\sqrt{N_{detected}}$ parameter of Equation 2.6 is replaced by the term $\sqrt{N_{detected} - 1}$. In order to minimise the Čerenkov angle resolution, as large a value as possible for $N_{detected}$ is desired and $\sigma_{single\ photon}$ should be minimised. There are several contributions to the single photon Čerenkov angle resolution of a RICH detector, including:

- Optical uncertainties arising in focussing RICH detectors from mirror qualities.
- Spherical aberrations and the approximation of curved focalising surfaces by flat photon detectors.
- Emission point uncertainties caused by finite radiator thicknesses.
- Readout accuracy arising from the granularity of the photon detection plane.
- Multiple scattering of the charged particle within the radiator material.
- Track bending due to stray magnetic fields (if applicable) and uncertainties in particle track parameters.
- Chromatic aberrations caused by the wavelength dependence of radiator refractive indices (dispersion).

Each of these contributions are independent and therefore may be summed in quadrature [47]. Further descriptions and quantifications of such resolution smearing effects may be found in [37,47]. It has been stated that theoretically the dominant contribution to the single photon Čerenkov angle resolution arises from chromatic effects [42,47], which represent very fundamental limitations and are difficult to overcome. The most successful way to improve the limit on $\sigma_{single\ photon}$ set by chromatic aberrations is to maximise $N_{detected}$ [47]. Typically in practical

RICH counters the attainable angular resolution varies from $\sim 0.1\,\mathrm{mrad}$ to $\sim 5\,\mathrm{mrad}$, depending upon the size and type of radiator medium [46]. The Čerenkov angle resolution may then be used to describe the particle species separation power of a RICH detector, in terms of the number of σ separation between different particles N_σ. For example, for a $\beta \approx 1$ particle, of momentum p and entering a radiator of refractive index n, the N_σ separation between particles of mass m_1 and m_2 is then given approximately by the relation shown in Equation 2.7 and as described further in [37,44,46,47]:

$$N_\sigma \approx \frac{|m_1^2 - m_2^2|}{2p^2 \sigma_{\theta_C} \sqrt{n^2 - 1}} \tag{2.7}$$

The momentum coverage of a RICH counter is largely governed by the radiator refractive index selected [46]. Low refractive indices are required to provide PID for high momenta particles, however the disadvantage of this is that the radiators must be relatively long to maximise $N_{detected}$ and correspondingly the multiple scattering contribution to the single photon resolution is increased. For low momenta particles, higher refractive index radiators are used. Typically the momentum range covered by a radiator, given in terms of the ratio between the maximum and minimum momenta values which allow for $\sim 3\,\sigma$ particle separations for a given refractive index, is ~ 4 - 7 and for larger momenta ranges two or more different radiators are required [47].

RICH detectors offer several advantages for PID over alternative techniques such as TOF, dE/dx, or threshold Čerenkov counters, as described fully in [46]. For example RICH counters provide excellent separation powers, with positive PID for the desired particles and outstanding background rejection over very wide momentum ranges [46]. In principle the design of a RICH detector is very versatile and may be tuned to precisely meet the PID and geometrical demands of the experiment [46]. Some disadvantages include their relatively high cost and in some cases complicated imaging optics. The overall PID power and performance of a RICH detector is determined by its design and experimental constraints, and in practice there are many limits imposed by, for example, photon detector availability and performance, geometrical and radiator length considerations, attainable radiator sizes, production specifications, and cost [44].

2.3 CLAS12 RICH Detector Design

There are several challenges influencing the design of the CLAS12 RICH detector, including its allowed geometry, the high background rate environment caused by a CLAS12 design luminosity of $10^{35}\mathrm{cm}^{-2}\mathrm{s}^{-1}$, overall cost, and the wide kinematic range of 3 - 8 GeV/c over which the detector must function. Ultimately all factors must be taken into consideration and impact the final design of the detector [33, 34, 56, 57].

Since the CLAS12 RICH detector [33,34,56,57] must fit into the original space occupied by CLAS12 there are strict constraints imposed upon its geometry. There is also restricted space available for the RICH counter as it will be positioned in the location previously assigned to the LTCC, which is sandwiched between the final DC region and the FTOF counters. Further to this the RICH counter must provide detection over large areas and at least two out of six radial sectors in total are required, each with a projective geometry. The large areas arise from the projective geometry and the fact that the RICH detector is located $\sim$5.4 m from the interaction point. The allowed geometry is illustrated in Fig. 2.5, which shows the baseline CLAS12 LTCC equipment and frame, with the space allocated to one RICH sector highlighted. Each sector has a limited gap depth of $\sim$1.2 m, an opening window area of $\sim 4.5\,\mathrm{m}^2$ and is expected to cover polar scattering angles from 5 ° - 35 °. The external frame for each sector is roughly triangular

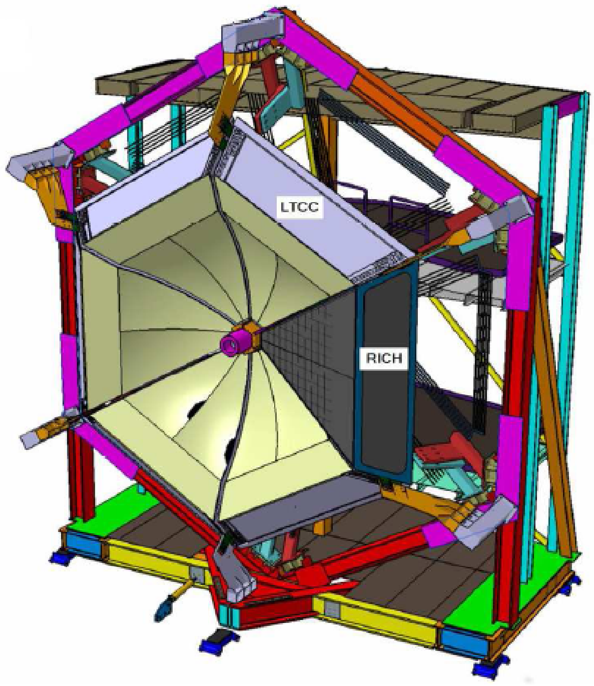

Figure 2.5: The existing CLAS12 LTCC geometry and frame, which represents the geometry and space allowed for the RICH. Each of the triangular shaped sectors have base and height dimensions of $\sim$4.3 m and $\sim$3.8 m respectively and cover polar angles from $\sim$5 ° - 35 °. Image taken from [58].

in shape with a base of $\sim 4.3\,\mathrm{m}$ and a height of $\sim 3.8\,\mathrm{m}$, and it is tilted with respect to the vertical by $\sim 65\,^{\circ}$.

There is also a low material budget for the CLAS12 RICH counter, to minimise influence on the measurements of the FTOF detectors and calorimeters which are placed immediately behind the detector. The previous LTCC from CLAS has a radiation thickness of $3.2\,\%$ of one radiation length, and the aim is that the RICH detector material thickness is comparable.

Several simulation studies have been performed to investigate which design of RICH detector, for example which overall combination of geometry, radiator material and photon detectors, will both meet the construction constraints and provide the necessary Čerenkov angle resolution to allow for the desired particle species separation power over the entire required kinematic range (see Section 1.4) [33, 34]. The benchmark design goal of the CLAS12 RICH detector is a $> 3\,\sigma$ π/K separation up to $8\,\mathrm{GeV/c}$ and ultimately to achieve this the simulation studies favour a novel hybrid imaging Čerenkov detector design, incorporating aerogel radiators, visible light photon detectors, and a focussing mirror system [33, 34].

A schematic illustrating the concept of the proposed CLAS12 RICH design is shown in Fig. 2.6. The imaging design is termed hybrid since a combination of techniques will be used. For forward scattered particles ($\theta < 12\,^{\circ}$) with momenta $\mathrm{p} = 3$ - $8\,\mathrm{GeV/c}$ a proximity imaging method will be used, where the Čerenkov cone is imaged directly. From now on this may be referred to as the direct light case. The expansion gap between the aerogel and the photon detection plane is aimed to be $\sim 1\,\mathrm{m}$. Whereas for particles incident with larger angles of $12\,^{\circ} < \theta < 35\,^{\circ}$ and intermediate momenta of $\mathrm{p} = 3$ - $6\,\mathrm{GeV/c}$ the Čerenkov light will be focussed by an elliptical mirror, followed by two further passes through the radiator material and a reflection from planar mirrors before detection. The mirror has a focal length of $\sim 1\,\mathrm{m}$ and this case is known as the reflected light case. In this case the Čerenkov light will be radiated from a thicker amount of aerogel material than it will be reflected through, to compensate yield losses whilst obtaining a focussed ring. The aerogel thicknesses will range from $2\,\mathrm{cm}$ in the proximity imaging case up to a maximum of $6\,\mathrm{cm}$ in the focussing mirror setup and slabs of aerogel tiles will be used. The reflected light configuration represents the most challenging case for the CLAS12 RICH detector, since the Čerenkov yield may be greatly reduced as a result of the double reflections and absorptions caused by double passes through the aerogel material. Furthermore effects resulting from mirror misalignments and scattering of the Čerenkov light as it passes through the aerogel are likely to degrade the Čerenkov angle resolution of the detector, in comparison with the direct light imaging case. It is important to note also that the

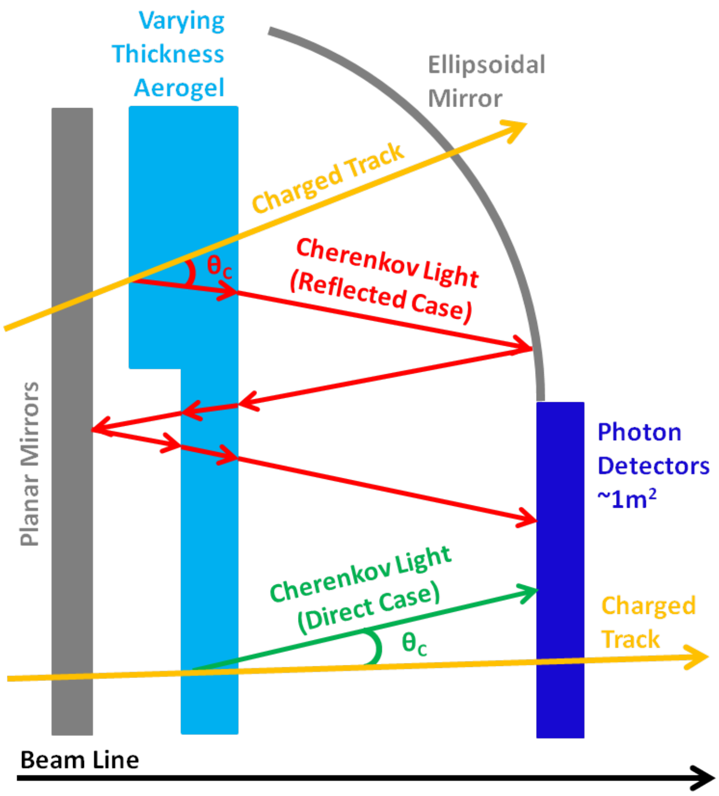

Figure 2.6: The CLAS12 hybrid RICH design concept - Čerenkov light is imaged directly for incident particle tracks of angles $<12^\circ$, and after two reflections and passes through the aerogel radiator for particle tracks with incident angles between 12° and 35° (not to scale).

case will also exist whereby Čerenkov rings are imaged partly by both the direct and reflected light cases simultaneously.

Considering the two imaging cases of the RICH detector design, the projected hadron PID for the kinematics of the CLAS12 forward detector are summarised in Fig. 2.7, which shows simulated hadron scattering angle versus momentum obtained from SIDIS processes [34]. For momenta below 3 GeV/c the FTOF system will provide the necessary π/K identification for polar angles up to 40°, whereas for momenta ranging from 3 - 8 GeV/c the RICH counter will be used. Either the proximity or focussing mirror imaging techniques are incorporated, for both high-momenta regions at forward scattering angles and intermediate momenta and large scattering angles respectively. The boundaries in scattering angle shown in Fig. 2.7 are not currently definitive and are drawn mainly for illustration purposes only [34]. Although the diagram only shows the appropriate regions corresponding to the FTOF system and the RICH detector, in reality the HTCC is expected to aid the RICH measurements for π/K separation at the higher momenta values of $\sim$6 - 8 GeV/c and across all scattering angles.

The entire RICH detector geometry is currently simulated by members of the CLAS12 RICH

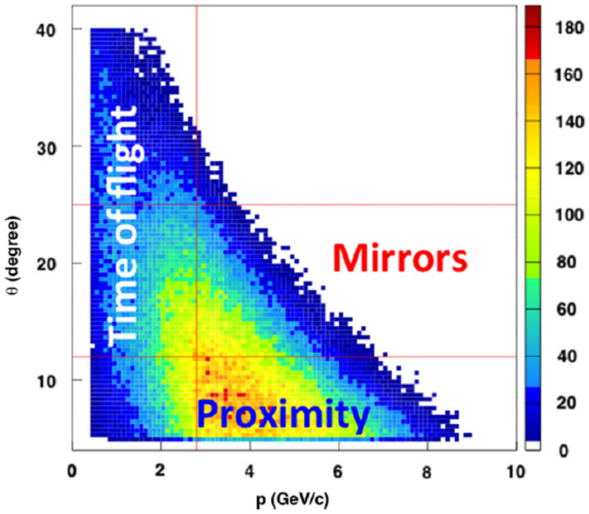

Figure 2.7: Simulated hadron scattering angle versus momentum in the CLAS12 forward detector for semi-inclusive deep inelastic scattering processes, where the colour fill indicates frequency. Time of flight counters will provide particle identification in the low momentum region and across all scattering angles. Whereas for momenta from 3 - 8 GeV/c particle detection will be provided by a RICH counter used in either a proximity or focussing mirror imaging mode. A high threshold Čerenkov counter will also aid in particle identification for momenta > 6 GeV/c, across all scattering angles. Image from [34].

Collaboration within the CLAS12 Geant4 framework. This includes simulation of the expected background rates and radiation loads for the CLAS12 RICH detector components, which is underway. Unlike previous focussing RICH detectors, such as in the HERMES experiment where the reflection was away from the beam line [53], in CLAS12 the direction of the reflection in the focussing imaging case will be towards the beam line, where the expected background rates are relatively high. The flux of background particles close to the beam line can not only cause radiation damage to the RICH detector components, but will also increase the level of background hits resulting from the creation of Čerenkov light as background particles pass through the aerogel radiators or photon detector windows, for example. In CLAS12 the main background source will be caused by the production of secondary neutrons, and from simulation studies an upper limit of $\sim 5 \times 10^9$ neutrons/cm^2/year is expected in the region of the CLAS12 RICH photon detection plane close to the beam line, when CLAS12 is operated at maximum design luminosity [56, 57].

The overall expected performance is studied through the simulations, which also allows for the development of high level pattern recognition algorithms. The algorithms involve both maximum likelihood methods and the inclusion of ray tracing ansätze, and must be able to cope with the varying ring patterns expected where in some cases only partial rings are imaged. Results from simulations [33,34,59] imply that, to achieve the $>3\,\sigma$ π/K goal up to a momentum of 8 GeV/c a minimum of around 7 detected photons per ring are required in the direct light imaging case. The performance of the radiator material and photon detectors will play crucial roles in achieving this goal.

2.3.1 Aerogel as a Radiator Material

Silica aerogel is a unique material which successfully fills the refractive index gap between gas and liquid Čerenkov radiators, allowing for successful PID and Čerenkov radiation emission in the momentum range on the order of a few GeV/c [60]. For example heavy gases such as C_4F_{10} maintained at atmospheric pressure, which have been traditionally used in previous RICH detectors, are useful for momenta above 10 GeV/c [53]. Additionally, clear liquid radiators, such as liquid C_6F_{14}, are suited to hadron identification below ∼2 or 3 GeV/c because of their very low Čerenkov thresholds [53]. The momentum gap between these two radiator types may be successfully bridged by the refractive indices offered by aerogel. This is illustrated further in Fig. 2.8, which shows simulation results obtained by the CLAS12 RICH Collaboration for the expected Čerenkov angles for charged π, K and p as a function of particle momentum. The Čerenkov angle separation between the hadrons for liquid and aerogel radiator types are also marked at a momentum of 8 GeV/c, the upper value of the CLAS12 RICH kinematic range, indicating that a larger separation may be extracted through the use of aerogel. Another advantage of silica aerogel is that it is a solid, and therefore successfully eliminates any corre-

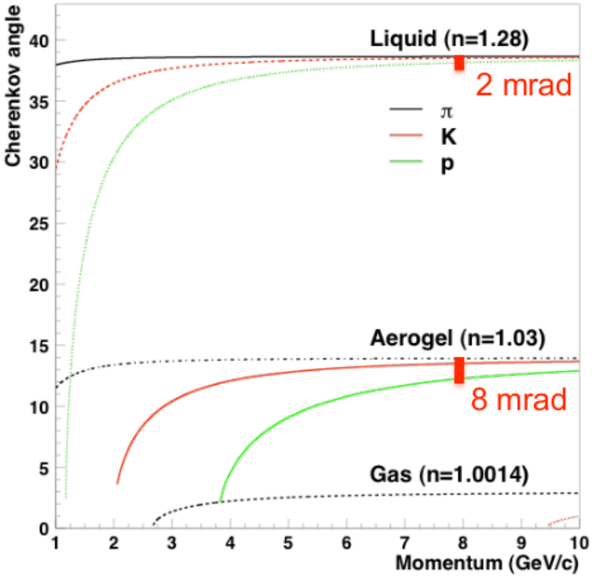

Figure 2.8: Čerenkov angle in [mrad] versus momentum for typical gaseous, aerogel and liquid radiator materials obtained with π, K and p. The expected Čerenkov angle separations at 8 GeV/c are also indicated. Result obtained by members of the CLAS12 RICH Collaboration and image taken from [33].

sponding problems associated with the containment and maintenance of liquids or gases under pressure.

Silica aerogel [20, 29, 60, 61, 62, 63, 64, 65] is a transparent and highly porous material of very low density, ranging from ~0.05 - 0.60 g/cm^3. It is a 3-dimensional network consisting of amorphous grains of silica (SiO_2), which have typical diameters of 4 - 10 nm, interspersed with pockets of air [29]. The sizes of the air pockets are on the order of 60 nm and the porosity (air content) of the aerogel can reach values as high as 95 - 98 % [29]. Since the diameters of the air bubbles are small compared to the typical wavelength of the traversing light, the medium appears to have a refractive index which is an average between the air pockets and the solid SiO_2 of the aerogel structure [20]. In general the refractive index n of an aerogel may be described in terms of its density ρ as is shown in Equation 2.8, where ρ is in units of $[g/cm^3]$.

$$n = 1 + (0.210 \pm 0.001) \times \rho \tag{2.8}$$

Typically aerogels with indices of refraction varying between 1.01 and 1.13 are available, depending upon the production technique [20, 29].

The aerogel production process is a complicated one, which has evolved significantly over recent years. Generally speaking, silica aerogel is produced by the hydrolysis of Silane ($Si(OCH_3)_4$) in the presence of an alcohol solvent. The alcohol solvent is subsequently evaporated at high temperature and under pressure, resulting in its replacement with air pockets [29]. Further descriptions of the aerogel production process may be found in [60, 63, 64, 65, 66, 67]. The amount of solvent used in the process is tuned to produce the required aerogel refractive index (n), since the refractive index is dependent upon the ratio of the volumes occupied by the air (V_{Pores}) and SiO_2 (V_{Silica}) components, as shown in Equation 2.9 [29].

$$\frac{V_{Pores}}{V_{Silica}} = \frac{0.41}{n-1} - 1 \tag{2.9}$$

The aerogel production process ultimately determines not only the refractive index but also the optical quality of the resulting aerogel. The method of aerogel production will also define how hygroscopic the resulting aerogel material is.

The optical quality of aerogel radiators may be described in terms of its transmittance T, which is typically parameterised as a function of wavelength λ and radiator thickness t by the

Hunt formula in the wavelength range of ~200 - 800 nm [55, 62, 68], as given in Equation 2.10.

$$T(\lambda) = Ae^{-Ct/\lambda^4} \tag{2.10}$$

A is a constant for the material and is dependent upon the absorption length (Λ_A), where $\Lambda_A = -t/\ln A$. The parameter C is termed the clarity factor and is inversely proportional to the scattering length of the aerogel (Λ_S), where $\Lambda_S = \frac{\lambda^4}{Ct}t$. In aerogel the absorption length is typically relatively high in the visible wavelengths, and it is the scattering length which dominates the transport of the produced Čerenkov light and limits its performance as a Čerenkov radiator. The dominant contribution arises from Rayleigh scattering effects, the cross-section for which is proportional to λ^{-4} and hence its occurrence in Equation 2.10. Rayleigh scattering therefore smears the directionality of the radiated Čerenkov light at small wavelengths, such as in the UV-region, and so the emission of useful Čerenkov photons from aerogel material is limited to the visible wavelengths.

Following the initial proposal of aerogel as a Čerenkov radiator for PID by Cantin [60], the major obstacle in its application to imaging Čerenkov detectors was caused by rather low optical qualities and poor long-term stabilities of the quality, and in general its use was restricted to threshold counters, such as the threshold counter of the TASSO experiment [67]. However, subsequent improvements in its production [66, 69] resulted in greater uniformity of its substructure and consequently reduced Rayleigh scattering effects and higher transmittances. This led to its maintained successful use in threshold counters, such as the aerogel threshold Čerenkov counter of the Belle spectrometer [66, 70], but also its large scale application to RICH detectors, such as the RICH detector of the HERMES experiment [53, 62, 71, 72]. The aerogel tiles used by the HERMES collaboration were obtained from Matsushita Electronic Works (Japan) and had typical T values of around 0.67 in the range of 200 - 900 nm. Since then aerogel has also been used successfully, for example, in the LHCb RICH detector system [55, 73, 74, 75], the RICH detector of AMS [75, 76, 77, 78] and is planned for future use in a proximity RICH detector for the upgraded Belle II spectrometer [64, 79].

The radiation hardness of aerogel radiators has been studied [80, 81, 82], and is accepted as being sufficient for their use in high-radiation accelerator environments. For example, it is selected as the radiator for the proximity RICH of the upgraded Belle II spectrometer, despite an expected neutron fluence of $\sim 1\times 10^{11}$ neutrons/cm^2/year [83, 84]. This is higher than that expected for the CLAS12 RICH detector. Radiation is most likely to affect aerogel clarity and refractive index, through the development of colour centres and changes in density respectively.

In summary, due to its refractive index match with the kinematic range of 3 - 8 GeV/c, recently improved transparency, ease of use in comparison with gases and liquids, and its reported success in previous RICH counters, aerogel has been selected as the Čerenkov radiator material in the CLAS12 RICH detector. The selected refractive index value is currently not finalised, however nominally a value of $n = 1.05$ is chosen, with the option of moving to either 1.04 or 1.06 depending upon whether any significant performance enhancement is expected. The performance of the photon detectors selected for the CLAS12 RICH will be extremely important in maximising the detected Čerenkov yield and angular resolution, and the corresponding requirements are discussed in the following section.

2.4 CLAS12 RICH Photon Detector Requirements

In general the demands of a RICH counter on its photon detector are very challenging and typically limit the available photon detector choices. The CLAS12 RICH detector is no exception and for successful performance of the entire RICH counter there are several strict requirements which must be fulfilled by the selected photon detector.

Due to the low-intensity light-yield of Čerenkov radiation, it is absolutely vital that the chosen photon detectors are sensitive to single photons and also provide a sufficient detection efficiency for such measurements. The photon detector must therefore offer a high gain performance, a concept which will be discussed further in Section 3.1, with values on the order of $\sim 10^6$ or higher favourable. Again, due to the mandatory detection of such low photon levels, the chosen photon detector must also be a very low noise device and preferably exhibit minimal dark count rates and crosstalk effects. Crosstalk in a position sensitive photon detector may be observed if a certain channel is illuminated with light and false signals are obtained from non-illuminated channels. Since the crosstalk signals are extracted from channels with no light incident upon them, as a result of noise mechanisms, the term *false* is used. Crosstalk may therefore compromise the position sensitivity of a photon detector and essentially the obtainable Čerenkov ring reconstruction.

Detection in the visible light wavelength range is also crucial for the CLAS12 RICH and the photon detector must have sufficient spectral sensitivity and high quantum efficiency in this wavelength region (quantum efficiency is a concept which will be further described in Section 3.1). The aim of this is to minimise chromatic error contributions to the Čerenkov angle resolution, arising from Rayleigh scattering of UV-wavelength photons travelling through the aerogel radiator material, and dispersion effects occurring inside the aerogel material.

Position sensitivity of the photon detector is also essential to obtain the location of photon hits and the resulting images of the Čerenkov rings. In order to achieve the required Čerenkov angle resolutions and hence the benchmark π/K separation values, simulation studies have shown that a photon detector with a spatial resolution of $< 1\,\mathrm{cm} \times 1\,\mathrm{cm}$ is necessary [34], indicating a need for multi-channel position sensitive devices. Due to the imaging aspect of the CLAS12 RICH it is also important that the chosen photon detector provides an active area with minimal deadspace. Further to this, since large photon detection areas of $\sim 1\,\mathrm{m}^2$ are required in each of the RICH sectors it is likely that multiple photon detector units will be tiled into arrays, and therefore the photon detector must provide as high a packing fraction [1] as possible for these purposes. The photon detectors must have compact form factors, with small depths, since the gap-depth of the RICH detector is limited to $\sim 1.2\,\mathrm{m}$ and there should be sufficient room for the readout electronics. Since the photon detection plane should provide as homogeneous a detection plane as possible, the uniformity of both inter-channel and inter-photon detector gain and single photon signal efficiencies will be crucial. This factor is also important in defining the required dynamic range of the readout electronics. Moreover, the photon detection plane should uphold the same geometrical efficiency and homogeneity for a combination of both the relatively large Čerenkov angles produced in the aerogel radiator material and the demanding geometry of the CLAS RICH counter, which must cover a wide range of polar angles over a large area. For this reason it is also favourable if the photon detector requires no extra focussing optics to increase the geometrical efficiency of the imaging plane, for instance such as the telescope lens systems used in the RICH detectors of COMPASS [54, 85, 86, 87] or HERA-B [52, 88, 89], as it is not clear how such complicated systems would cope with the required wide angular acceptance.

The design luminosity of CLAS12 is high with values on the order of $10^{35}\,\mathrm{cm}^{-2}\mathrm{s}^{-1}$ expected, and the photon detector must provide sufficient rate capabilities to cope with the expected photon and background rates. Data from the CLAS12 RICH detector will be readout using a 20 kHz rate and a maximum occupancy of 8 % of all channels is expected [56]. The majority of modern day fast vacuum and solid state photon detector devices should provide satisfactory capabilities for these purposes. Fast signal times and timing resolutions are also important factors, since the Čerenkov counter will look for coincident Čerenkov hits on the photon detection plane, amongst background and noise, in order to form the ring images from each event. Furthermore it is expected that an overall time resolution of at least $\sim 1\,\mathrm{ns}$ is

---

[1] The packing fraction is defined as the ratio of active to passive areas on the photon detector surface.

required in order to disentangle direct and reflected imaging photons.

The magnetic field behaviour is not a crucial parameter for the photon detector chosen for application to the CLAS12 RICH. The location of the RICH will be downstream from the magnetic torus and, although the detector will lie in the fringe field of the torus, simulation studies have shown that the maximum field strength that the photon detectors are likely to experience is 0.5 mT in the absolute worst case and depending upon their longitudinal position [90]. This is a value which is manageable for most of the considered photon detector technologies.

Such photon detection requirements, combined with, in particular, cost restraints, will ultimately determine the final choice of photon detector for the CLAS12 RICH application. Ideally, since the instrumentation of large areas is required, the photon detector cost should be as low as possible whilst maintaining adequate performance for the RICH detector. The expected lifetimes of the photon detectors should also be as long as possible to minimise replacement costs and this will be a particularly important factor in the CLAS12 RICH due to possible radiation damage caused by the relatively close location of the photon detectors to the beam line. It is required therefore that the photon detectors should be sufficiently radiation hard to cope with the expected neutron fluences of $\sim 5\times10^{9}$ neutrons/cm^2/year.

Finally, it is important to note the short timescale of the CLAS12 RICH project. Currently the first beam delivery in Hall B of JLab is expected in 2014, and the first sector of the RICH detector must be installed into CLAS12 in time for the start of data taking, which is expected in 2016. Therefore, the allowed time for research and development of novel photon detector technologies is strictly limited, and it is preferable to rely upon a mature technology which is readily available. The existing photon detector options for the CLAS12 RICH are discussed further in the next chapter.

Chapter 3

Photon Detection Technologies

Photon detectors [30, 40, 91, 92, 93, 94, 95, 96] are a vital component for numerous nuclear and particle physics experiments, in particular for calorimetry and PID purposes, where they are used as powerful tools to convert incoming photon fluxes into measurable electrical signals which are then extracted and processed for analysis. There are several photon detection technologies which are effective across a varied range of photon wavelengths and incident light-levels, ranging from the extremely sensitive detection of a single photon up to values exceeding hundreds of thousands of photons. It is indeed for these versatilities that they play a crucial role in so many areas of scientific research. Furthermore, the development of fast position sensitive photon detectors, with high granularities, are extremely useful for retrieving spatial and temporal information of photon hits upon a detector face, adding to the performance of a variety of imaging applications.

Photon detectors for single photon counting applications such as the CLAS12 RICH are challenged with providing efficient and position sensitive detection for single photons originating from a broad wavelength range. Candidate photon detector technologies which may provide this in the CLAS12 RICH application are briefly discussed and considered below. The detectors may be divided into two classes, namely vacuum based or solid state technologies [1]. Within these two classes there then exist several interesting detector options to choose from, however, ultimately the requirements of the application and factors such as cost will determine the

---

[1] Gas avalanche photon detectors, or gaseous photomultipliers, which combine a solid photocathode material with a fast gas electron multiplier also exist. Single photon detection is achievable with these detectors, over large surface areas, and their previous use in RICH detectors is widely reported upon [97, 98]. Originally these detectors were constructed with UV-sensitive gases or photocathodes. However, recent progress in different photocathode materials has furthered the sensitivity of these detectors from the far UV, through the visible, and up to the IR wavelength regions. These detectors are not considered and will therefore not be discussed, however, comprehensive introductions to this technology may be found in [99, 100] and the references therein.

choice of photon detector. First a general introduction to the mechanisms of photon detection and useful quantities which allow for the comparisons between different technologies is given below. This is followed by a discussion concerning the suitable photon detection technology for application to the CLAS12 RICH detector, from which the conclusion is drawn that MAPMTs offer the most promising solution.

3.1 General Components of Photon Detection

There are four general steps defining the photon detection process [94]: photon conversion; charge carrier collection; charge carrier multiplication and finally signal readout. The first step describes the process whereby an incident photon produces a resulting primary charge carrier. This charge carrier may be either a PhotoElectron (PE) in the case of vacuum-based detectors, or an Electron - Hole (E - H) pair in the case of solid state photon detectors. The next step describes the process by which the PE / E - H pair is collected by the detector. This is then followed by multiplication, where the primary charge created is amplified to produce a measurable signal [2]. The final stage is readout, where both the primary and secondary charges are collected and extracted for signal processing. Each stage is convoluted with its own noise sources and inefficiencies, which smear the photon detection resolution and influence the performance deviation of the detector from the ideal case.

Photon detection is an indirect process and relies upon the interaction of the photon with the medium of the detector [20]. The main interactions of photons with matter comprise Compton scattering, pair production or the photoelectric effect [20, 29, 30, 40]. Out of these interactions, the photoelectric effect is responsible for the initial photon conversion process in photon detectors. In the photoelectric effect [20, 29, 30, 40] the energy of an incident photon is completely absorbed by an atomic electron, resulting in the ejection of the electron from the atom. The outgoing electron has a maximum kinetic energy equivalent to the energy of the incident photon [3] minus the initial binding energy of the electron. Due to momentum conservation, the recoil momentum of the process is absorbed by the atomic nucleus. This is the reason why $\sim 80\,\%$ of the total photoelectric cross-section corresponds to photon absorption by electrons in the K shell of the atom, due to its close proximity with the atomic nucleus. In the

---

[2] The multiplication step is not always applicable, for example in the cases of Charge Coupled Device (CCD) cameras [20, 29, 30], Complementary Metal-Oxide-Semiconductor (CMOS) sensors [101] or conventional silicon PhotoDiodes (PDs) [29, 30]. These technologies however were not considered for the CLAS12 RICH, which requires single photon detection, and are therefore not discussed further.

[3] The energy of the incident photon is described as $h\nu$, where h is Planck's constant and ν is frequency.

process of filling the vacant shell of the ionised absorber atom, X-ray photons or Auger electrons may also be emitted during the photoelectric process through electronic rearrangement. For the photon detection purposes described below, the photoelectric effect may be distinguished as either external or internal. In the external method, illustrated further in Fig. 3.1, PEs are emitted into the vacuum from a photosensitive material, which is termed the photocathode. This method is incorporated in MAPMTs and MicroChannel Plate PhotoMultiplier Tubes (MCPPMTs) for example. Typically the photocathode is a material with a low work function, since the incident photon must have an energy at least equal to or greater than this work function in order to release an electron. In the internal method, the PEs are excited from the valence band into the conduction band of a semiconductor material, creating an E - H pair, and this process is further termed the photoconductive or photovoltaic effect.

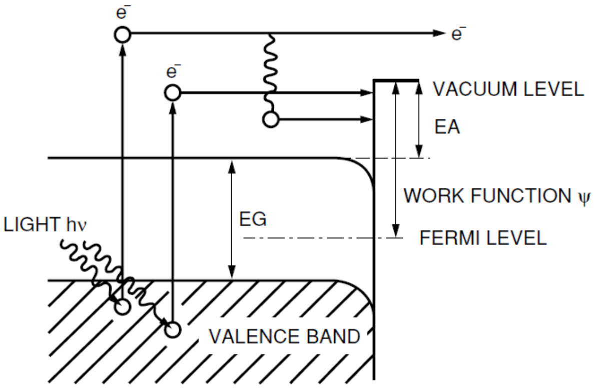

Figure 3.1: The external photoelectric effect: the energy of an incident electron is completely absorbed by an atomic electron, which is then emitted into the vacuum. Image taken from [91].

The photoconversion process varies strongly with the frequency of the incident light and the structure of the photoemissive material. The overall spectral response of the process is described by the Quantum Efficiency (QE) parameter, which is usually expressed in terms of a percentage and is equivalent to the ratio between the number of photoconversions and the incident photons upon the cathode. For vacuum-based photon detectors the QE is typically rather low over the wavelength region of interest for the CLAS12 RICH, at ∼20 %, however, the remainder of the photon detection process is extremely low noise. Whereas for solid-state photon detectors the QE is very high, reaching values of even >90 % depending upon the wavelength of the incident light. Unfortunately, the intrinsic noise of the devices themselves is rather high and limits the detection of low light signals. For such reasons the Photon Detection Efficiency (PDE) is sometimes used in place of the QE to compare photon detector technologies. It is a percentage which relates the probability of photon detection taking into account factors like QE, PE / E - H pair Collection Efficiencies (CEs) and probabilities of successful signal amplifications.

Some other examples of useful performance parameters used to compare photon detector technologies, and assess their advantages and disadvantages for application to detectors such as the CLAS12 RICH, include: signal gain; time resolution and rate capability; crosstalk level; dark count rate; geometrical efficiency and channel-to-channel uniformities; lifetimes and costs. The gain parameter describes the level of multiplication, the method of which differs between vacuum based and solid state devices, and may be calculated as the ratio of the charge collected after multiplication to the initial charge created by the incident light and collected by the photon detector. For a single photon counting application such as the CLAS12 RICH, the gain of the photon detector will be crucial to ensure efficient detection of the low level light signals. A high gain is required to both produce measurable electrical signals from incident single photons and to maximise the signal separation from any baseline noise, hence increasing the signal to noise ratio. The time resolution describes the accuracy to which the detector can determine the arrival time of a photon hit. Environmental conditions will affect a photon detector's performance with respect to the parameters above, and so the response within the baseline CLAS12 apparatus and requirements for additional systems, such as temperature control for example, are also important considerations for the CLAS12 RICH photon detector. In the following section candidate photon detector technologies for application to the RICH are described.

3.2 Candidate Photon Detector Discussion

Several photon detection technologies were initially considered for use in the CLAS12 RICH detector, in response to the requirements set out in Section 2.4. Examples include MCPPMTs, Silicon Photomultipliers (SiPMs) and MAPMTs. For comparison's sake, to give an insight into the selection process, their main advantages and disadvantages are briefly described below.

Microchannel Plate Photomultiplier Tubes

MCPPMTs [30, 40, 91, 92] are vacuum tube devices which offer position sensitive photon detection at the single photon level, with high gains on the order of $\sim 10^6$ - 10^7 available. The devices offer typical peak QE values of $\sim 22\,\%$ at $\sim 380\,\text{nm}$ and are sensitive across the visible wavelength region, which therefore makes them suitable for the detection of Čerenkov photons from aerogel materials in the proposed CLAS12 RICH detector.

Traditionally, lifetime issues exist for MCPPMTs as concerns for their application to the harsh environments of modern-day high-luminosity detectors. One of the main issues affecting the lifetime of MCPPMTs is reduction in photocathode QE values caused by positive ion generation and feedback during the electron multiplication process within the MicroChannel Plate (MCP) structures [102] [4]. There have been several attempts to overcome this, including: the addition of very thin ($\sim$5 - 10 nm) aluminium-oxide protection layers between the MCP stages and photocathode, improved MCP surface treatments, the generation of better vacuums and the coating of MCP surfaces with an atomic layer to reduce any out-gassing effects [102, 103, 104]. Such techniques have increased the lifetimes significantly, up to values of 2 - 3 Ccm^{-2} integrated anode charge [103, 104]. Unfortunately, the addition of aluminium protection layers may reduce the CE of MCPPMTs by as much as $\sim$40 % [104] and in general the MCPPMT lifetime improvements on the mass-market remain in the development stages. Considering the short time-scale of the CLAS12 RICH project and its corresponding requirement for a readily available robust and mature technology, the lifetime properties of MCPPMTs render them unfavourable for the application.

The main advantage of MCPPMTs is their extremely fast timing capabilities, due to the very short collection and multiplication distances involved, the high electric fields used and short mean path lengths experienced by the electrons during multiplication [30, 40, 91, 92]. Signal rise and fall times are usually sub-ns, with pulse widths being on the order of a couple of ns and moreover single photon timing resolutions are typically superior than $\sigma \sim$ 50 ps, with values approaching 30 ps achieved depending upon the MCPPMT [105, 106, 107, 108, 109, 110, 111].

The detection capabilities of MCPPMTs when coupled with Čerenkov radiators have already been widely studied for Čerenkov PID detectors, in particular for those aiming to measure the timing of Čerenkov photons to aid in PID and/or reduce chromatic dispersion effects. For example, members from the Belle collaboration investigating the proposed Time-Of-Propagation (TOP) counter [112] for Belle II have performed several research and development studies into the corresponding use of MCPPMTs [108, 113, 114, 115, 116]. Typically single photon timing resolutions of $\sigma <$ 50 ps are required to record the time of travel of the Čerenkov photons detected in TOP counters, and so MCPPMTs may be well suited to this [20].

---

[4] In an MCPPMT electron multiplication takes place in the MCP stages. An MCP is a lead-glass plate which is perforated by a two dimensional array of parallel and continuous channels. The channels have circular cross-sections of diameters ranging from 2 μm - 25 μm and their inner walls are pre-processed with a highly resistive material. When a PE strikes the inner wall of a channel, further electrons are emitted by secondary emission and this process is then repeated along the entire length of the channel.

The inclusion of timing information to reduce chromatic dispersion effects has also been studied with MCPPMTs to further improve the original Detector of Internally Reflected Čerenkov light (DIRC) principle [117,118]. Moreover, it is also interesting to note that MCPPMTs have been investigated for the future aerogel proximity RICH detector of Belle II, the design of which is similar to the direct-light case of the CLAS12 RICH detector, where one possible justification for their use was to incorporate additional TOF information [113,119,120,121,122].

The CLAS12 RICH however does not plan to use time information for resolution enhancement methods such as those described above. The impressive behaviour of MCPPMTs within magnetic fields, for example as described further within [106, 110], is also not required for the CLAS12 RICH detector. Furthermore, the price per unit of appropriate commercially available MCPPMTs, such as the Photonis 64-channel Planacon MCPPMT [123], is rather high, at ~ £ 5 000 per 53 mm × 53 mm 64-channel device [124], which is roughly double the current price of equivalent MAPMTs [125]. Considering that ~ 356 units would be required for each CLAS12 RICH sector, the price for instrumentation would be prohibitively high and the MCPPMT technology is therefore, due to cost limitations, not considered for the application.

Silicon Photomultipliers

SiPMs [126, 127, 128, 129] offer several advantages for the CLAS12 RICH. In particular they provide remarkable single photon counting capabilities, they are sensitive in the visible wavelengths with QE values of ~ 80 % - 90 % depending upon wavelength, and they may be tiled into position sensitive arrays. However, in their application to a Čerenkov detector, the major drawback of the devices is their high dark count rates, which are indistinguishable from single photon hits. Both of these advantages and disadvantages are described further below.

The SiPM [126, 127, 128, 129] consists of an array of high-gain Geiger-mode Avalanche PhotoDiodes (G-APDs) [126, 127, 129], termed microcells, connected in parallel as shown in Fig. 3.2. A G-APD is similar to a conventional avalanche photodiode [20, 30, 40, 126, 127], however, in a G-APD the depletion zone is biased above its breakdown voltage and it is therefore operated in a non-linear regime. Photon absorption can therefore induce a diverging multiplication avalanche which is self-sustaining, and eventually must be stopped by active quenching circuits or passively by a high ohmic resistor connected in series to the G-APD (see Fig. 3.2). Due to this breakdown and quenching cycle of the G-APD, the signal extracted from a G-APD is independent of the incident photon number and the G-APD acts in a binary way to indicate if there was a hit or not.

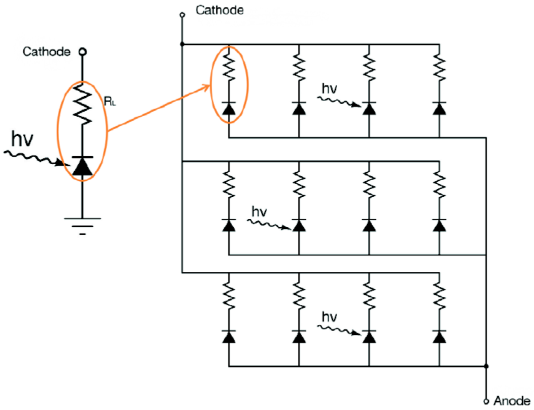

Figure 3.2: The concept of a silicon photomultiplier. A matrix of Geiger-mode avalanche photodiodes, each quenched by its own resistor in series, are connected in parallel. Image taken from [130].

Since all signals from the microcells of the SiPM are summed to provide an analogue output which is proportional to the incident photon level, and due to the highly uniform amount of charge produced every time a microcell undergoes a breakdown [130], the output signal of the SiPM is also quantised depending upon the number of microcells which fire. The SiPM signals therefore offer impressive photon counting capabilities at low light levels, since in the first order the number of microcells undergoing breakdowns will relate directly to the number of incident photons. The SiPM photon counting principle is illustrated further in Fig. 3.3, which gives an overlay of oscilloscope signals extracted from an SiPM in response to low-level [5] laser light of wavelength 634.7 nm [6]. The SiPM used was a SensL SPMMini [131], which has an active area

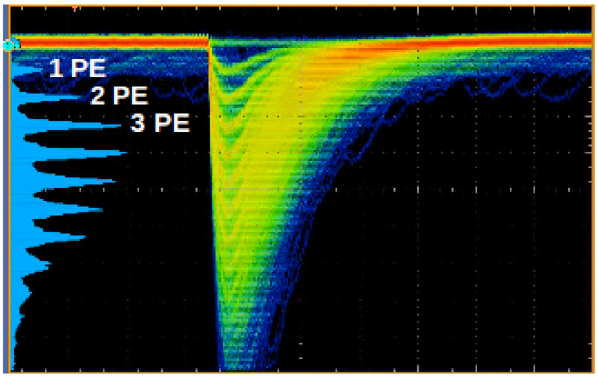

Figure 3.3: A signal extracted from a silicon photomultiplier. The photon counting capabilities are demonstrated by the quantised pulse heights of the signal.

of 1 mm × 1 mm and comprises 848 G-APD microcells. The device has a gain of $\sim 10^6$, and the

---

[5] In this case, the term low-level is used to imply that the incident number of photons per laser pulse is significantly lower than the number of microcells of the SiPM.

[6] PiLas model EIG1000D.

signal was extracted through a $\times 20$ pre-amplifier. The individual pulse heights correspond to an increasing number of microcells firing and therefore increasing incident photon levels, with the baseline value equivalent to 0 PE. The photon counting capability is emphasised by the pulse height histogram which is shown in blue on the left of Fig. 3.3. This impressive feature of the SiPM is particularly attractive for the CLAS12 RICH application, where the efficient detection and counting of single photons will be crucial.

The timing properties of SiPMs are comparable with fast vacuum-based PMTs, and are not a concern for the CLAS12 RICH detector. Signal rise times are dependent upon the SiPM size, and vary from ~ 1 ns to ~ 10 ns for 1 mm× 1 mm and 6 mm× 6 mm devices respectively [130]. Sufficient time resolutions may also be obtained, even down to the single photon level, since the multiplication mechanism is fast and the active multiplication region used is very thin (typically ~ 2 - $4\,\mu$m) [129]. The Root Mean Square (RMS) single photon time resolution is typically on the order of 100 ps or lower, and has been shown to reach values as low as RMS ~ 50 ps, for photons absorbed in the depletion zone and if the result is decoupled from experimental systematic contributions [132]. Another advantage of SiPMs is that their high gains, required to obtain single photon detection and photon counting capabilities, are achievable with low bias voltages of ~ 30 - 50 V and with low power consumptions of $< 50\,\mu$W/mm^2 [126]. This is an attractive feature for a space-constrained and large-area application like the CLAS12 RICH.

The major obstruction in the use of SiPMs for a single photon counting application is their dark count noise rates [126,127,128,129], which pose a severe problem since the majority of the dark noise signals are indistinguishable from single photon hits. In SiPMs the dark counts arise from thermally excited electrons or field assisted generated electrons in the Si, when no incident photons are present [126,127]. One of the main causes of performance degradations arising from dark count noise in SiPMs is its fluctuation, since its occurrence in time follows Poisson statistics and therefore may not simply be subtracted as would be possible for a constant background noise source [130]. Typical dark count rates, measured with a signal amplitude threshold level equal to half that of the single photon amplitude, are expected to vary between 100 kHz and several MHz per mm^2 at 25°C [126, 127, 129]. Table 3.1 gives some examples of the dark count noise rates, obtained at room temperature and measured with a 0.5 PE threshold, quoted for currently commercially available Hamamatsu Photonics SiPMs of various active areas and microcell sizes [133]. As visible in Table 3.1, the dark count rates increase dramatically with both the total surface area of the silicon and the individual microcell sizes. This may be explained by, in first order, the larger silicon areas combined with the proportionality of the

Table 3.1: Expected dark noise rates of commercially available silicon photomultipliers, as provided by the documentation from Hamamatsu Photonics [133].

SiPM Area [mm × mm]	**Microcell Size [μm × μm]**	**Expected Dark Count Rate [MHz]**	**Fill Factor [%]**
1×1	25×25	0.3	30.8
	50×50	0.4	61.5
	100×100	0.6	78.5
3×3	25×25	4	30.8
	50×50	6	61.5
	100×100	8	78.5

thermal generation of carriers, which may cause dark counts, to the depleted volume of all microcells [127]. For the CLAS12 RICH detector, in order to reduce the required number of readout channels whilst fulfilling the spatial resolution requirement, the largest available SiPM dimensions would be the most appropriate. This however yields significantly larger dark count rates. Furthermore, as large a fill factor [7] as possible is desired for the CLAS12 RICH application in order to enhance the imaging performance, however, from Table 3.1 this requires larger microcell sizes, which in turn also increases the dark count rates. The dark noise rates can be decreased - but not eliminated - by cooling of the devices or by operation with smaller bias voltages. Unfortunately, reducing the bias voltage also reduces the gain of the SiPM and is therefore not ideal for single photon counting applications. In general, the dark count rate of an SiPM has been said to reduce by a factor of 2 per every 8 ° cooling, but large-area cooling systems can be difficult to regulate in environments such as the CLAS12 detector and may be bulky, which is not ideal due to the restricted depth available for the RICH detector. The optical crosstalk levels and gains of SiPMs are also extremely sensitive to temperature, and imply the requirement for bulky cooling systems. Optical crosstalk represents a further noise source in SiPMs, which may also be problematic for their use in RICH applications. This crosstalk mechanism occurs as a result of optical photons, created during the avalanche multiplication process in a G-APD, which may travel to neighbouring microcells and initiate subsequent breakdowns there. Typically $\sim 2 \times 10^5$ optical photons are produced per electron crossing a P-N junction [130], and they are emitted isotropically over a $4\,\pi$ solid angle. Although the SiPM QE is high, the PDE [8] for an SiPM is significantly lower than this in reality, due

---

[7] Fill factor is defined as the ratio of active to passive areas on the detector surface.

[8] The SiPM PDE is defined as a product of the QE, the geometric fill factor and the probability that a photon will trigger an avalanche breakdown in the SiPM [126, 129].

to the effects of dark counts, optical crosstalk, afterpulsing [9] and recovery times [10] of the microcells. For example, narrowly peaked values of ~ 30 % and ~ 40 % are obtained for SiPMs from Hamamatsu and Photonique/CPTA at ~ 460 nm and ~ 575 nm respectively [126, 127].

It has been concluded that, despite the coincidence technique employed in RICH detectors, currently dark count noise rates and their associated noise effects are too problematic to allow for the use of SiPMs in the first sector of the CLAS12 RICH, which must be installed for the beginning of CLAS12 data taking. On the other hand the SiPM industry is rapidly evolving, the technology is constantly improving and commercial companies are frequently reducing their quoted dark count rates. Per unit area the current price of SiPMs is not significantly lower than MAPMTs. For instance a typical 64-channel 51 mm × 51 mm area MAPMT today costs ~ £ 2 500 [125], whereas a 16-channel array from Hamamatsu, with outer dimensions 16 mm × 18 mm, will cost ~ £ 1 231 [134]. The prices do drop significantly if the devices are bought in bulk, for example if 100 of these arrays are purchased simultaneously then the price per units becomes ~ £ 800 [134], however they still then remain more expensive than the current MAPMT technology per unit area. The prices of SiPMs are continually lowering in general though and it is predicted that in the future they will offer a relatively cheaper solution than vacuum-tube devices. Furthermore, if the noise levels can be improved in the future, then they may be considered for sectors of the CLAS12 RICH which follow the initially installed one. Since the incident particles' trajectories and momenta will be known by independent measurements from the drift chambers in CLAS12, priors on where to search for rings in the RICH detector will be known. This will be a significant aid in the separation of coincident Čerenkov signals from SiPM dark noise, if the levels are maintained under control. SiPMs therefore remain a candidate technology for any future upgrade plan of the CLAS12 RICH detector.

Candidate Technology

Through comparison with other commercially available photon detection technologies on the market today, such as MCPPMTs or SiPMs, it is proposed that MAPMTs currently offer the most promising solution for the CLAS12 RICH. They are sensitive to single photons across the entire visible wavelength region, making them suitable candidates for the CLAS12 RICH

---

[9] Afterpulsing [126] occurs in SiPMs due to charge carrier trapping, followed by their subsequent delayed release.

[10] The recovery time [126] is the time needed to re-charge a microcell after a breakdown has been quenched.

application. In comparison with MCPPMTs they offer a cost-effective solution, and when compared with SiPMs they are extremely low noise devices ($<2\,$nA dark current per channel [86]). Typically the pixelisation of the devices is in accordance with that required for the RICH detector and moreover the packing fractions of the current flat-panel MAPMTs available from Hamamatsu offer values close to $\sim 90\,\%$, yielding a very efficient imaging plane. The design and performances of MAPMTs are therefore discussed further in the next section.

3.3 Multianode Photomultiplier Tubes

PMT and MAPMT technologies are already somewhat established in the field of RICH detectors. As the luminosities of high energy physics accelerators have in general been rapidly increasing, so too have the several demanding and challenging requests for RICH detector performances. Some examples include high trigger rates, challenging background levels and the ability to handle complex crowded events with high photon and charged particle fluxes [135]. There has therefore been a gradual move away from slower gaseous detectors towards fast vacuum tube devices, such as PMTs or the recently available MAPMTs [135]. This is also a result of the increased requirement for the detection of Čerenkov photons in the visible regions, for example through the increased use of aerogel and quartz radiators [136].

PMTs have therefore played a significant role in providing photon detection for several successful RICH applications, due to their high gains of $\sim 10^6$ to $\sim 10^7$ and resulting single photon detection capabilities, intrinsic low noise behaviour (detector capacitances on the order of 1 pF), their fast signals (on the order of 0.1 ns - 1.0 ns), their ruggedness and ease of use in comparison to complex gas systems, and satisfactory QE values of $\sim 20\,\%$ across broad ranges in the visible wavelength regions [136]. Some examples of instances where single channel PMTs have been used very successfully to provide the required PID in Čerenkov detectors include: the DIRC of BaBar at SLAC [137,138]; the RICH of the SELEX experiment which was performed at Fermilab [139]; the dual-radiator RICH of HERMES at DESY [53,62]; the aerogel threshold Čerenkov counter of the Belle detector at KEKB [88].

The development of MAPMTs offers an attractive position sensitive option of the PMT technology for use in current and future RICH detectors. MAPMTs maintain the same advantages as PMTs but moreover offer pixelised and miniaturised configurations of PMT devices, with high spatial resolutions of typically $< 1\text{cm} \times 1\,\text{cm}$ and compact form factors. This allows for improved imaging performance compared to normally larger diameter and bulkier single channel PMTs for example, and higher rate capabilities due to the increased number of channels available per unit area. MAPMTs have therefore also been used in and studied for several recent RICH detectors.

The first RICH detector to employ MAPMTs was used in the HERA-B detector at DESY [52, 88]. The HERA-B collaboration selected MAPMTs over gaseous photon detectors due to the expected high rates of up to 1 MHz per photon detector channel [88, 89]. Studies before and after installation into HERA-B successfully proved that MAPMTs could be used for single photon detection with high efficiency and low crosstalk [88, 140, 141]. Due to the relatively low packing fraction of the early generations of MAPMTs a two-lens demagnification system was used to optimise the imaging plane efficiency. One disadvantage of optical lens setups, however, is that they may restrict the angular acceptance of a RICH detector. Another RICH detector which used MAPMTs was the so-called RICH-1 detector of COMPASS [54, 85, 86, 87], where again MAPMTs were used in conjunction with lens telescopes to provide efficient detection of single photons with high rates of several MHz/channel [54, 85, 86, 87]. Furthermore, the AMS-02 RICH detector also currently incorporates MAPMTs which are coupled to light guides, to detect Čerenkov rings produced from aerogel radiators [77, 78, 142, 143].

Numerous research and development projects focussed on photon detectors have also confirmed the suitability of MAPMTs for single photon detection in Čerenkov imaging detectors. For example, through studies performed for a BTeV RICH [144], a focussing DIRC for SuperB [117] and the proposed RICH for the Belle II upgrade project [79, 145, 146, 147]. Furthermore, MAPMTs are planned for use in future RICH detectors, for example the Hamamatsu H8500 MAPMT is the current chosen photon detector for the future CBM RICH detector [148, 149].

MAPMTs therefore exist as a very strong candidate for the CLAS12 RICH detector and hence PMT and MAPMT technologies are further described below, followed by a discussion on the MAPMT suitability for application to the CLAS12 RICH.

3.3.1 Description of Single Channel Devices

In order to comprehend the mechanisms of position sensitive MAPMTs, it is first useful to consider the detection process and constituent components of conventional single-channel PMTs [30, 40, 91, 92]. A schematic displaying the main components of a single-channel PMT is shown in Fig. 3.4. PMTs are vacuum tube devices, which consist of: an entrance window, which allows the incident photon to enter the PMT (labeled *faceplate* in Fig. 3.4); a photocathode, which may produce a PE by the photoelectric effect; focussing electrodes to guide and accelerate

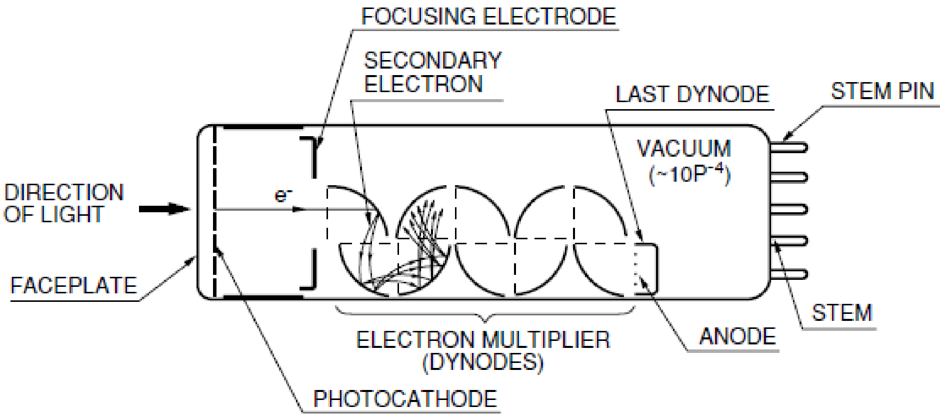

Figure 3.4: Schematic illustrating the main components of a conventional single-channel photomultiplier tube. Image taken from [91].

the PE towards the first dynode; electron multiplying dynodes to amplify the initial PE into a measurable current by secondary emission, and an anode for collection of the amplified signal. The stem pins labeled in Fig. 3.4 are used to connect the PMT to a voltage divider circuit. Typically the components of the PMT are enclosed within an evacuated glass tube. The photon detection stages and constituent components are described in brief below, and for further in-depth and extremely comprehensive discussions the reader is referred to [30, 40, 91, 92].

The input window material will ultimately limit the spectral sensitivity of the PMT in the short wavelength region. Typically borosilicate or lime glasses are used, which have transmission cut-off wavelengths between 250 nm - 300 nm. In addition UV-extended windows also exist, for example fused silica or UV-glass windows, which lower the cut-off wavelengths below 250 nm. Transmission spectra for different window types may be found in [91,92]. The entrance window is usually only a few mm thick.

A photon which passes through the entrance window then strikes the photocathode material. Typically, and for the PMTs which will be discussed further below, semi-transparent cathodes are used, meaning that the photocathode material is directly deposited onto the side of the entrance window which is enclosed in the vacuum [92]. As described previously, if the energy of the photon surpasses the work function of the photocathode then a PE may be emitted into the vacuum by the photoelectric effect. There are several steps to this photoemission process process [92]. First, the absorbed photon imparts its energy to an electron in the material, releasing it. Next, the released PE diffuses through the photocathode, losing a very small fraction of its energy through interactions with mainly the crystal lattice. Finally, when the electron reaches the photocathode-vacuum interface it will escape if it has enough energy remaining to overcome the surface barrier. The photocathode consists of a thin layer of photoemissive material with a low work function, and contributes directly to the QE of the PMT. The compounds are usually formed from alkali metals with low work functions [91] and are typically a few hundredths to a few tenths of a micron thick [92]. There are several photocathode materials to choose from and different photocathode materials show varied spectral sensitivity characteristics as given in the example shown in Fig. 3.5. The spectra show

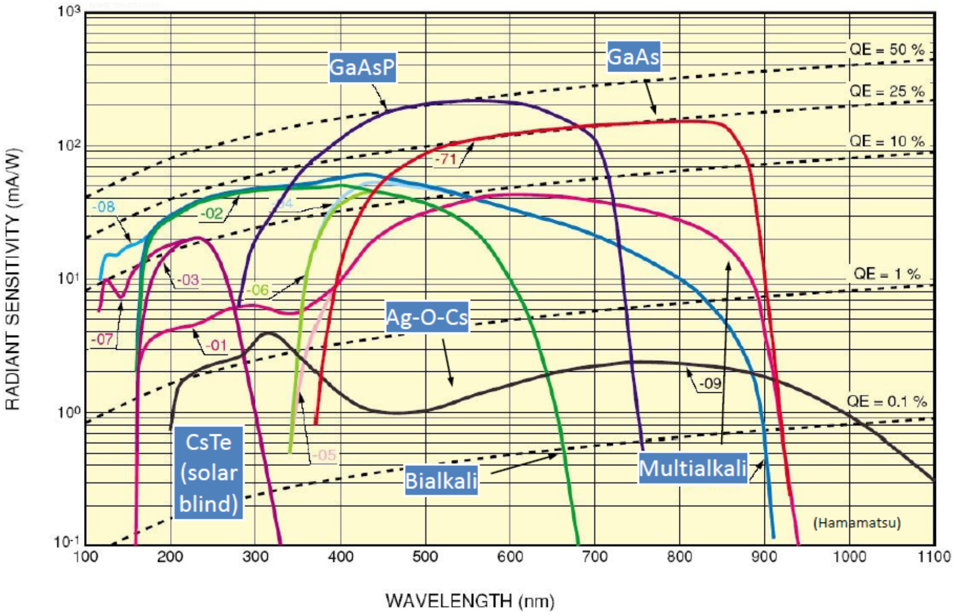

Figure 3.5: Spectral sensitivities of commonly used photocathode materials in photomultiplier tubes. Dashed lines indicate constant quantum efficiency values. Image taken from [150].

the radiant sensitivities [11] of several photocathode materials across different wavelengths and lines of constant QE values are also shown. The most widely used photocathodes are silver-oxygen-caesium (AgOCs), antimony-caesium (SbCs, not shown) and the low work function bi- and multi-alkali compounds SbKCs, SbRbCs and $SbNa_2KCs$. Comprehensive summaries of commonly used photocathode material characteristics can be found in [30, 91, 92].

The emitted PE is then accelerated and focussed to the useful area of the first dynode by the electron optical input system, comprising focussing electrodes which are maintained at the same potential as the first dynode [92]. These components establish the electric field required to collect the PEs. The optical input system aims to minimise the transit time spread of the electron trajectory and to maximise the Collection Efficiency (CE) of the first dynode, regardless of the initial velocity and point of origin of the PE. The electron travel between the

---

[11] The radiant sensitivity is defined as the photoelectric current generated by the photocathode divided by incident radiant flux at a given wavelength [91].

photocathode and the first dynode corresponds to the region in the PMT where the transit time spread has the highest fluctuation. The CE is defined as the ratio between the number of electrons landing on the effective area of the first dynode to the number of PEs emitted from the photocathode. For conventional PMTs the CE varies with wavelength, and is typically greater than 80 % [92].

The electron multiplier system consists of a chain of typically 10 to 14 dynode stages, for multiplication of the initial PE signal. When the initial PE strikes the first dynode, several electrons are released by secondary emission [30, 40, 91, 92]. The energies of the secondary electrons are typically on the order of a few eV. These electrons are then focussed and accelerated to the next dynode in the chain, where further electrons are released, and this process is repeated until the end of the dynode chain where the anode is used to collect and extract the amplified current signal. A series of voltage dropping resistors is used to create the electric fields between the dynodes, which are required for the acceleration and focussing of the electrons. Typically equal voltages are applied between all dynode stages, apart from perhaps the first and the last, which are sometimes higher in order to increase the initial PE collection and signal readout efficiencies. The electric fields between dynodes are tailored to optimise the transit time spread amongst the trajectories of electrons between dynodes and to optimise the chances for secondary emission to occur by ensuring that the electrons emitted by each dynode strike the succeeding dynode with an energy of a few hundred eV. There are three stages to secondary emission [92], which are similar to the photoemission process: absorbed primary electrons impart energy to electrons in the material; energised electrons diffuse through the material and upon reaching the surface escape into the vacuum if they have sufficient excess energy to overcome the potential barrier. The dynode secondary emission coefficient δ defines the ratio of the number of secondary electrons emitted to the number of primary electrons, or in other words describes the gain of each dynode. Example δ curves for some typically used materials, displayed as a function of the accelerating voltage between dynodes, are given in Fig. 3.6 (a). Typically the secondary emissive materials are coated onto a conducting substrate electrode such as nickel, stainless steel or copper-beryllium alloy [91], as shown in Fig. 3.6 (b). The secondary emissive material must have low thermionic emissions, i.e. be low noise, and they must provide stable secondary emission effects under high currents [92]. Several dynode chain arrangements exist, with each arrangement offering advantages tailored for specific applications, such as: size, magnetic field immunity, signal gains, linearity or time responses. Metal channel dynodes will be discussed further below, since they are incorporated for MAPMTs. The

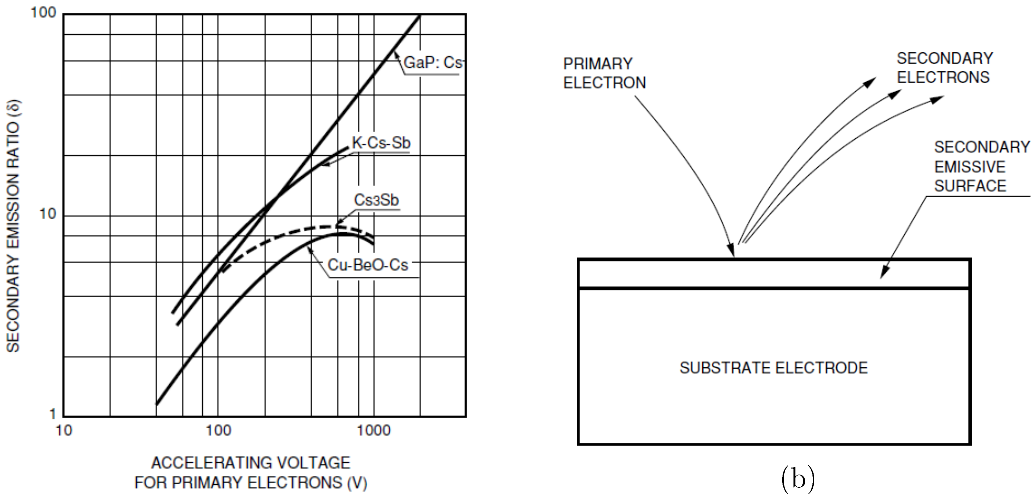

(a) (b)

Figure 3.6: (a) Example dynode secondary emission coefficient curves for typically used materials. (b) Schematic of secondary emission from a dynode in a photomultiplier tube. Images taken from [91].

interested reader is referred to [30, 40, 91, 92] for further descriptions on secondary emission, dynode chain arrangements and extra details on the electron multiplier system of a PMT.

The overall gain of the electron multiplier [30,40,91,92] depends on the number of dynode stages and their corresponding δ values, which essentially is dependent upon the voltage supplied to the multiplier system. The dependence on voltage is very sensitive, for example the supply voltage must be regulated within 0.1 % for a a 1 % gain stability in a conventional single channel PMT with ten dynode stages [40]. Not all electrons emitted by a dynode will reach the next dynode however and so each interdynode space is characterised by a collection efficiency n, which is also a function of the voltage supplied. The gain g_i of each i^{th} dynode, out of a total N dynode stages is therefore given by the relation in Equation 3.1, and the overall gain M of the entire electron multiplier system is given by the product of the individual dynode stage gains as shown in Equation 3.2.

$$g_i = \delta_i n_i \tag{3.1}$$

$$M = \prod_{i=1}^{N} g_i \tag{3.2}$$

The multiplication process in PMTs is extremely low-noise, since the most significant factor influencing the resolution of the PMT and the signal gain is caused by the probabilistic and statistical nature of secondary emission [30,40,92,151]. The gain of each dynode stage fluctuates around a statistical mean and the overall gain of the multiplier system is therefore described by a mean value and a Poisson probability distribution, in the most simple model [30,40,92,151]. Furthermore it may be shown that, due to the increased electron statistics, the relative contribution to the fluctuation of the PMT gain decreases with the proximity of the dynode stage to the end of the chain [30,40,92,151]. In other words, the fluctuations in the δ_1 value of the first dynode, where the total number of electrons is the smallest, has the strongest contribution to the gain fluctuation and therefore the largest influence on the signal to noise ratio of the PMT [30,40,92,151]. The overall gain of the PMT may also be described as the ratio of the anode to photocathode current, which is directly proportional to the incident number of PEs when the PMT is operated in its linear regime. Electron multiplication in PMTs may yield typical gain values higher than $\sim 10^7$, which is large enough to detect single photon and low-level light pulses. The gain of a PMT increases rapidly with the supply voltage, and its absolute value may be calibrated by measuring the charge extracted from a single photon incident on its surface at a particular voltage setting.

In general PMTs exhibit very low noise [30, 40, 92], although some noise sources which do exist include afterpulsing and dark current sources. Afterpulses [30, 40, 92] are spurious pulses that appear after the true output pulses. They are mainly caused by luminous reactions resulting from electrode glow and ionisation of residual gases within the PMT vacuum, and are not considered to be an issue for a RICH application. Dark current [92] in PMTs arises from several sources, including leakage currents, thermionic and field emissions. Thermionic emission effects are the main source of dark noise in PMTs operated at standard room temperature and supply voltages. The noise has a pulsed structure and is caused by thermionic emission from the photocathode or dynodes, which increases with the applied voltage and temperature. Dark counts arising from thermionic emission usually have signal amplitudes corresponding to that of a single PE signal or less. The dark count noise will depend strongly upon the photocathode material, with bialkalis offering relatively low noise solutions. A bialkali photocathode for example yields thermionic emission values between 10 and 100 electrons/cm^2/s. The dark count rates are therefore significantly lower than those observed with SiPMs.

The majority of the principles described here for single channel PMT devices are immediately transferable to MAPMTs, where the main difference lies in the electron multiplication stage and the anode collection space, as described below.

3.3.2 Extension to Position Sensitive Devices

MAPMTs [91, 96, 136, 152, 153, 154], in particular the most recent flat-panel types offered by Hamamatsu Photonics K.K., offer spatial hit information in small fields of view with minimal deadspace. Conceptually MAPMTs may be considered as arrays of miniaturised PMTs, providing high sensitivity detectors with compact form factors. The flat-panel MAPMTs provide high packing fractions, with values approaching 90 %, and therefore offer extremely efficient imaging planes. Current flat-panel MAPMTs are made possible through the development of their metal channel dynode systems, which will be further described below, and their square metal outer packages [152, 154]. The metal outer package is used to enclose the MAPMT, in place of the traditional glass envelope, and is directly coupled to the entrance window. The result of this is minimal peripheral deadspace surrounding the active area. The devices also have minimised curvatures at the corners. Such factors make them ideal for tiling purposes to provide large areas of photon detection in imaging applications, such as will be required in the CLAS12 RICH detector. Several spatial resolutions are currently available with MAPMTs, most of which comply with that required by the CLAS12 RICH. Gain values on the order of 10^6 are attainable and therefore, in combination with their pixelisation, rate capabilities (several MHz) and low dark noise (less than a few Hz/channel) they are deemed suitable for the required detection of single photons in RICH detectors [88, 96, 136, 152, 153].

The design of MAPMTs and the resulting advantages and disadvantages for application to the CLAS12 RICH are discussed below.

Multianode Photomultiplier Tube Design and Performance

The MAPMTs which will be discussed incorporate metal channel dynodes and multi-anode readouts to retain the positional information of the photon hit on the MAPMT face. Each MAPMT combines either a linear or 2-dimensional array of channels, called pixels, into a compact photon detector package which is readout through a matrix anode system. In this way, each channel of an MAPMT consists of an area of photocathode material, a narrow electron-multiplying dynode channel and dedicated anode readout. This is shown in Fig. 3.7, which shows a cross-sectional view of an MAPMT with the metal channel dynode and multi-anode readout structures visible. An example PE electron trajectory is visible in Fig. 3.7. The PE is emitted from the photocathode and focussed by a mesh of focussing electrodes onto the first dynode of the closest channel. The CE values for flat-panel type MAPMTs are rather high and may reach values of ∼80 %, over the active areas of their surfaces [96]. The photocathode is normally a bialkali photocathode, which is well-suited to the wavelength spectrum of the Čerenkov light emitted from the aerogel radiators in the CLAS12 RICH, and is deposited semi-transparently onto the MAPMT window. The window is usually either borosilicate or UV-extended glass. The electron multiplication then occurs in the one narrow dynode channel and the amplified signal is extracted by a dedicated anode at the end of the dynode chain.

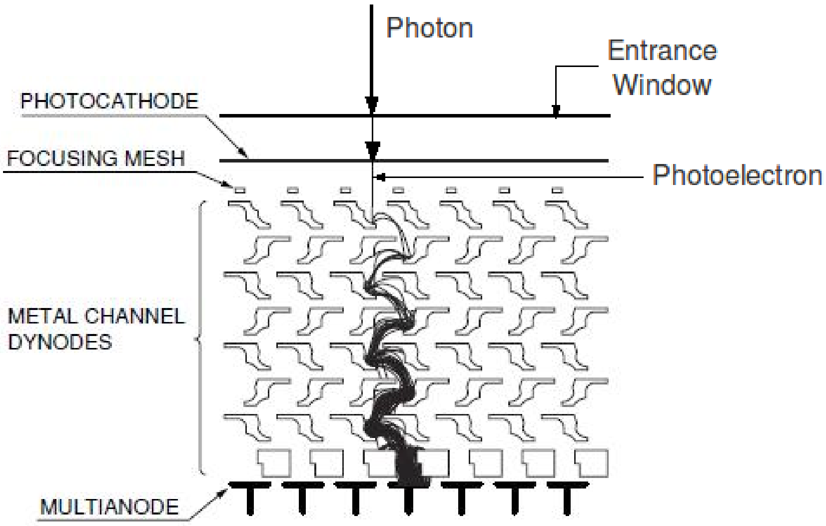

Figure 3.7: 2-Dimensional schematic of the metal channel dynode structure incorporated in the majority of flat-panel multianode photomultiplier tubes (modified from [91]).

In this way the original positional information of the photon hit is maintained, with minimal spatial spread which is defined by the pixel sizes.

The metal-channel dynode system is produced through micro-machining techniques, allowing for the fine structures of the components [154]. The dynodes are typically coated with caesium-antimony (Cs_3Sb) secondary emissive material [96], and normally 8 - 12 dynode stages are incorporated to provide the high gains. The length of the dynode chains is relatively short compared to conventional PMTs, since the metal channel dynodes are very thin and arranged closely to each other [91]. The short distances over which the electrons have to travel results in fast signals, with typical transit times of $\sim$6 ns and signal rise and fall times of $\leq$1 ns [96]. Furthermore single photon timing resolution values as low as $\sigma = 125$ ps have also been reported [153]. The fast timing of the MAPMT signals and corresponding short detector memory make them very suitable for high background and modern-day high trigger rate experiments. For instance, in MAPMT studies performed by the COMPASS collaboration no signal degradations for incident photon rates above 5 MHz/channel were observed [86].

As in conventional single channel PMTs, the gain of a metal channel dynode tube is the product of the average δ values of its dynode stages. The readout electronics noise is, for example, on the order of magnitude of 500 electrons RMS and so is typically much smaller than the $\sim 10^6$ gain of the device. Thus, signal gain fluctuations are dominated by the variance of δ_1 for the first dynode stage [96]. Typically in an MAPMT δ_1 is $\sim$3 - 5, resulting in the single PE photopeak resolution being rather broad and not completely separated from the pedestal noise level. Moreover, unlike for the SiPM, it is normally inseparable from the subsequent photopeaks corresponding to higher numbers of incident photons [96]. An optimal single photon detector would have, for instance, a maximised signal to noise ratio and as large an energy resolution as possible, to allow the single photon charge signal to be clearly separated from the baseline noise. Due to these reasons the MAPMT is not considered as the optimal detector for single photon detection, however it is widely accepted as an adequate solution (see for example some of its previous uses in RICH detectors given by the references above in section 3.3). Consequently, it is therefore crucial to fully assess if the single photon sensitivities of MAPMT devices provide sufficiently efficient detection prior to their application in the CLAS12 RICH application.

MAPMTs have better immunity to magnetic fields than conventional PMTs, due to their metal package construction and the fact that the electron paths are very short [91]. It has been reported that in a magnetic field MAPMT signal gains and efficiencies drop for field values greater than 2 mT - 4 mT, depending on the field direction and MAPMT orientation [96]. The residual magnetic field in CLAS12 is therefore not considered to be a major issue for the use of MAPMTs in the RICH.

The radiation hardness of MAPMTs is also considered to be sufficient for their use in the CLAS12 RICH detector [57]. Radiation may affect the performance of MAPMTs through deterioration of the glass window and other materials, such as metals or insulators, used to construct the MAPMT [91]. The performance degradation is, however, mostly caused by a loss in the transmittance of the glass window, and the photocathode sensitivity and dynode secondary emission ratios typically exhibit little variation in response to radiation [91]. The loss in window transmission is visible as a colouring of the glass, which is caused by the development of colour centres. The upper limit of the neutron background fluence in the CLAS12 RICH ($\sim 5\times10^{9}$ neutrons/cm^2/year) is not considered a concern, since it lies below the orders of magnitudes where typical MAPMT borosilicate and UV-glass window transmission losses are reported to begin [91].

Another important factor for application to the CLAS12 RICH detector will be the channel-to-channel gain uniformity of the device. For MAPMTs the inter-channel uniformity values obtained from literature are slightly worse than SiPM arrays [12], with typical anode gain uniformities of 1 : 3 obtained and values of 1 : 5 reported in the most severe cases [91, 96]. The uniformity issue in MAPMTs is mostly caused by gain variations between the electron multiplier

---

[12] For example, a commercially available 4×4 matrix SiPM array from SensL offers a channel to channel uniformity of 1.00 : 1.18 [156].

channels [30]. The uniformity may also be affected by the difficulty to create an even thickness of photocathode during the deposition process [30], although this is a more severe problem in PMTs with larger diameters than those typical of MAPMTs. An un-even photocathode thickness may directly affect the QE and CE of a PMT, as a function of the incident photon position on the entrance window. During the photoemission process, after the absorption of the initial photon, the released PE must migrate to the photocathode surface. Throughout the migration process the PE will lose energy through electron-electron collisions and, in order to escape into the vacuum at the photocathode surface, the PE must have sufficient energy remaining to overcome the potential barrier (i.e. the work function). Variations in photocathode thickness, fluctuating around the escape depth [13] for instance, will directly influence the number of PEs with energy great enough to escape, and hence produce a variation in the QE across the photocathode. The momentum of the escaped PEs will rely upon the fraction of their energy lost throughout migration. Variations in the thickness of the photocathode will therefore also influence the momentum distribution of the released PEs, which can subsequently affect the CE of the focussing electrode and first dynode.

There are several crosstalk mechanisms present in MAPMTs [91,92,155], which are intrinsic due to their design. For instance optical sources of crosstalk exist whereby the incident light may diverge as it passes through the MAPMT window. This effect is largely dependent upon the window thickness and the characteristics of the incident light such as its angle. Another source of optical crosstalk, which has been quoted as one of the main sources in MAPMTs [91], results from the improper proximity focussing of PEs emitted from the photocathode surface into the wrong dynode channel and the subsequent multiplication in the wrong dynode channel. This source of crosstalk will be dependent upon the momentum of the released PE and the momentum distribution over which the electric fields setup by the focussing electrodes are successful in accelerating the PE towards the correct MAPMT channel. The incident photon wavelength will therefore affect this crosstalk mechanism, since a photon of shorter wavelength will typically produce a PE with a higher kinetic energy than that from a longer wavelength photon and, depending upon the directional component of the PE momentum, this may result in its improper focussing. Crosstalk may also exist through the charge spillover of electrons into neighbouring dynode channels during the multiplication process. This will again be influenced by the momentum distribution of the secondary electrons and the efficiency of the focussing

---

[13] The escape depth is the depth within the photocathode material at which PEs may originate and still reach the surface with sufficient energy to overcome the potential barrier.

from the electric fields setup between each successive dynode stage. Electromagnetic crosstalk effects also exist, due to the unwanted capacitive or inductive coupling of energy from one part of a circuit or signal line to another. This usually takes place in either the readout electronics, or the spaces between the last dynodes and the anodes, or amongst different anodes. Crosstalk magnitudes may be measured by illuminating a single channel only and measuring the charge extracted from non-illuminated channels [91]. Crosstalk magnitudes have been quoted in literature as ranging from the levels of typically 2 % - 5 % [91,94,150,153] and therefore do not exist as a major concern. Through such measurements, it has also been shown that the levels of crosstalk are larger in the immediate 4 neighbouring side-sharing pixels to the illuminated one, than in pixel-cornering channels [91, 152, 154].

Considering the design, advantages and disadvantages, MAPMTs are selected as the most promising candidate photon detector for the CLAS12 RICH. A series of experimental laser characterisation studies were subsequently performed to further confirm their performance and capability, and to select the most appropriate MAPMT for the application from the wide choice available on the market, as is described in the following Chapter.

Chapter 4

MAPMT Characterisation and Selection

This chapter describes in detail a series of photon detector response and characterisation studies which have been performed with several different MAPMTs to confirm their applicability for the CLAS12 RICH detector and, in particular, to select one to be studied further in RICH prototype setups.

For these studies a laser scanning facility was developed to map detector responses across their surfaces, with varying degrees of resolution, and subsequently study properties such as single photon detection capability, spatial resolution, imaging plane homogeneity, noise and crosstalk behaviour. Such studies, performed in a controlled and low-noise laser laboratory environment, were extremely important to allow for fair comparison between different devices and were crucial to understand fully the intrinsic behaviour of the devices. As will be shown, all tested MAPMTs exhibited single photon sensitivity and spatial resolution conforming with the requirements of the CLAS12 RICH detector. A series of high resolution scans revealed that the response and crosstalk noise behaviour of all tested MAPMTs was dependent on the metal channel dynode arrangements, and examples of these results will also be given. The magnitude of such crosstalk effects however was found to be extremely low-level and is not a concern for the CLAS12 RICH application. Based upon the inherent MAPMT designs and measured performance parameters with the laser test-stand, the Hamamatsu H8500 has been selected as the most appropriate photon detector for the CLAS12 RICH application, as is discussed throughout the Chapter.

4.1 Laser Scan Test Facility

To perform the various in-depth characterisation studies and comparisons of MAPMTs an automated, ultra-high precision and extremely stable picosecond laser scanning test-bench was developed. The experimental setup of the test-bench, the laser scan method, analysed quantities extracted from scan data, and the stability of the test-stand are described in the sections below.

4.1.1 Experimental Setup and Laser Scan Method

A schematic of the laser scan test-bench setup is shown in Fig. 4.1. A fast laser pulser [1], of wavelength (634.7 ± 2.5) nm [157] and variable beam diameter, was mounted upon X - Y motorised stages [2] inside a light-tight box. The X - Y stages allowed for scanning in both the horizontal (X) and vertical (Y) directions across the surface of the MAPMT under test in programmable step sizes, with minimum step sizes of 0.1 μm achievable and a 5 % step accuracy [158].

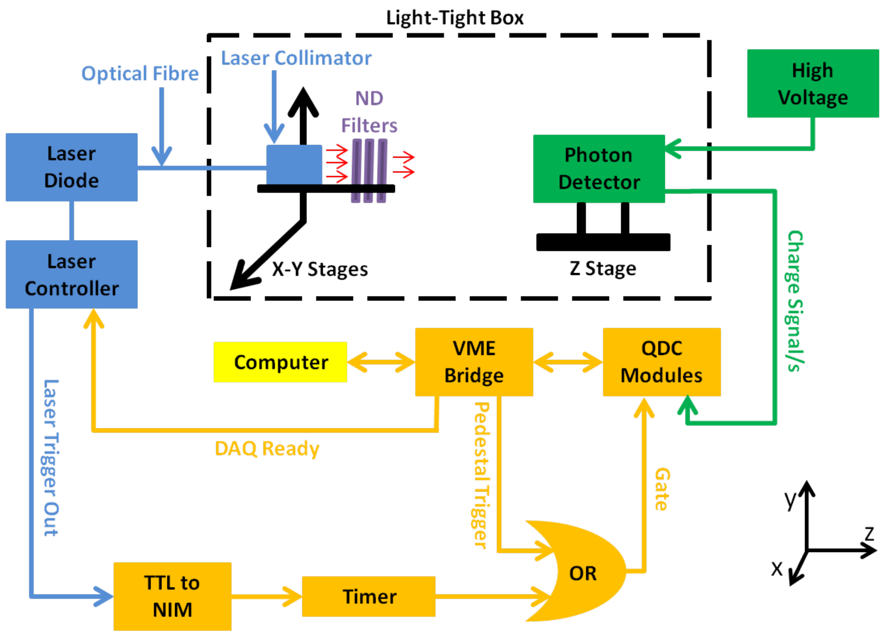

Figure 4.1: Schematic of the laser test-bench setup, consisting of a laser light source mounted upon X - Y motorised stages for scanning of photon detector responses.

Since the MAPMT single photon response represents a crucial property to be assessed prior to detection in the CLAS12 RICH detector, and to therefore aid in the achievement of low PE

---

[1] PiLas model EIG1000D.
[2] Thorlabs NRT150.

level signals, the wavelength of the laser was intentionally matched with the low QE region of the conventional bialkali photocathodes which are typically used in MAPMTs (see Fig. 3.5). The laser system consisted of a laser diode and controller unit, which were positioned outside of the light-tight box for noise reduction purposes. The laser light was then coupled inside the box via a multi-mode fibre optic cable and focussed by a collimator lens, which was mounted on the X - Y stages. The collimator lens was used to vary the beam width and focal length. Prior to laser scans a CCD [3] was used, in place of the MAPMT under test, to image the laser spot. Since the CCD pixels are quoted by Hamamatsu as having dimensions of $6.45\,\mu\text{m} \times 6.45\,\mu\text{m}$, this in turn allowed the Full Width Half Maximum (FWHM) diameter of the laser beam to be measured precisely. An example of such a CCD image is shown in Fig. 4.2 (a), where the diameter for the laser spot shown was extracted as (0.100 ± 0.006) mm. Both coarse and fine level laser scans of the MAPMTs were performed and typically the beam spot was set to 1.0 mm and 0.1 mm for the low and high resolution mapping of detector responses respectively. Imaging of the laser beam with the CCD and subsequent analysis using its accompanying software [4] also allowed for the intensity profile of the laser and the presence of any halo effects, which were negligible, to be examined. For example, the cross-hairs of Fig. 4.2 (a) illustrate how the intensity profile of the beam spot was monitored throughout CCD measurements. Similarly Fig. 4.2 (b) shows a 2-dimensional intensity profile for a different CCD image, where the horizontal and vertical axes denote CCD pixel and the colour fill indicates intensity. The

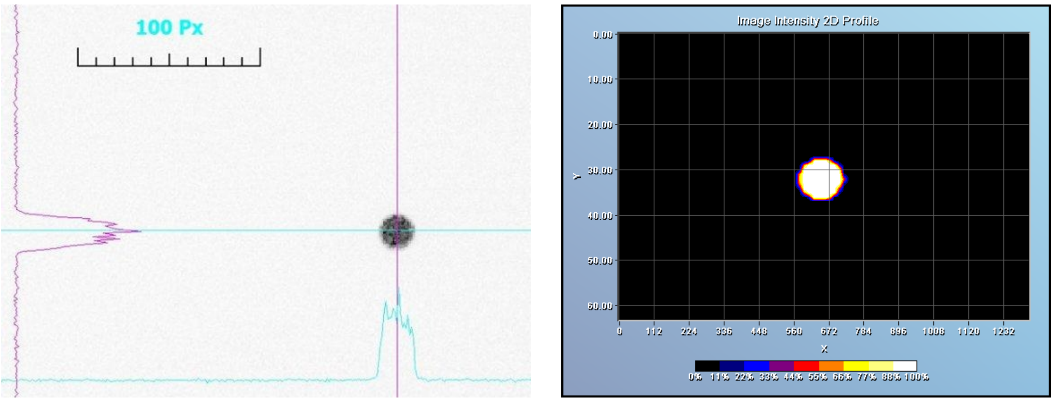

(a) (b)

Figure 4.2: (a) CCD image of a laser spot having a diameter of 0.1 mm, where the cross-hairs illustrate the intensity profile of the laser beam and the grey-scale (from light to dark) indicates increasing signal intensity. (b) 2-Dimensional intensity map from a different laser spot, where colour fill (from black to white) denotes increasing signal intensity.

---

[3] Hamamatsu C9260-901 board camera.

[4] Hamamatsu HCImage software.

image displays a very uniform intensity across its entire area, with a sharp drop off at its edge. Throughout beam imaging the CCD was mounted on a manually-translatable Z-stage, orthogonal to the plane of the motorised stages, allowing for the laser focal length to be finely tuned. The focal length was set to be at the position of the MAPMT photocathode. The laser system is extremely fast and for the typical pulsing frequency (7 - 10 kHz) and relative intensity of the laser controller (50 %) used throughout the measurements, the laser pulses are quoted as having a FWHM of 36 ps and a pulse jitter of 2.0 ps [157]. Absorptive Neutral Density Filters [5] (NDFs) of various Optical Density (OD) values were used to attenuate the laser intensity to the required light level. The relation by which one may convert NDF OD into percentage transmission (T) of the laser light is given in Equation 4.1 [159].

$$T = 10^{-OD} \times 100\% \tag{4.1}$$

The NDFs were attached directly to the laser collimator, in order that the laser light only passed through one area of the NDFs at all times throughout a scan and so that the surface of the MAPMT under test only was scanned.

The MAPMT under test was mounted inside the light-tight box, at the focal length of the laser. All components inside the light-tight box were secured to an optical table for alignment purposes. The High Voltage (HV) for the MAPMTs was supplied by a NIM module [6] and their gains were normally set to $> 10^6$, to allow for the detection of single photons. The analogue signals from the MAPMT under test were typically extracted to custom-made readout boards and then to VME-controlled Charge to Digital Converter (QDC) modules [7], which integrated the charge signals. The charge resolution used for the QDCs was 100 fC per QDC bin.

The trigger signal for reading data from the QDCs was derived through a combination of the Data AcQuisition (DAQ) system being in a ready-state and the arrival of the trigger output signal from the laser. If the DAQ was ready to accept data a signal was sent from the VME bridge [8] to the laser controller unit, which then triggered a laser pulse. The external trigger out signal from the laser controller unit was then used to supply the QDC gate through a timer unit. In this way data was only readout from the MAPMT if the laser fired, reducing any random non-correlated noise effects. The frequency at which the laser pulses fired was ultimately

---

[5] Kodak optical filters.

[6] CAEN N470 4 channel programmable high voltage power supply.

[7] CAEN V792 32 channel QDC.

[8] CAEN V2718 CONET - VME bridge.

determined by the DAQ readout rate capability. Typically, for a multichannel device with 64 channels, this rate was observed on the DAQ system to be stable at ~8 kHz, which exceeds the estimated rate requirements per channel in the CLAS12 RICH detector. The accuracy of the DAQ trigger timing was defined by the jitter of the laser trigger out pulse (2 ps), and this aspect of the experimental setup could be improved through reduction of the jitter value. This would be a particularly interesting option for future MAPMT signal timing resolution studies, for example. Another method of achieving this would be to split the laser beam into two, before it reaches the MAPMT under test, so that one path passes to the MAPMT and the other is sent to an ultra-fast reference detector such as a streak tube. The signal from the reference detector could then be used, in place of the laser trigger out pulse, to provide the signal for the DAQ readout. However, it is unclear if this method would work at the single photon level.

The DAQ readout software was controlled by a computer running Linux and was used to perform automated laser scanning measurements of the MAPMT surfaces. For this a configuration file was supplied which defined the step-size of the scan, the maximum travel of the scan in both directions and the initial offset alignment positions for the laser. In this way either the entire surface, or a selected area of an MAPMT could be scanned. At each laser step of the scan, 10 000 events were taken and the resulting QDC data for all readout channels was extracted. Pedestal readings for all channels were also recorded immediately before and after each laser scan, with no laser light incident upon the MAPMT surface, to monitor electronic noise and stability. This pedestal trigger was supplied by an internal signal from the VME bridge.

4.1.2 Laser Scan Data Analysis

QDC data obtained from laser scans was analysed using the ROOT [9] software framework. An example QDC spectrum obtained from an MAPMT pixel in response to a multi-photon laser signal (red) and the corresponding noise pedestal obtained with no laser light incident (black) are shown for illustration purposes in Fig. 4.3. In the data analysis of such QDC spectra two main quantities, named *signal efficiency* and *signal gain* were extracted. The signal efficiency is calculated as the fraction of the signal spectrum events which are positioned above 95% of the pedestal noise distribution events and the signal gain is calculated as the difference, in QDC

---

[9] http://root.cern.ch

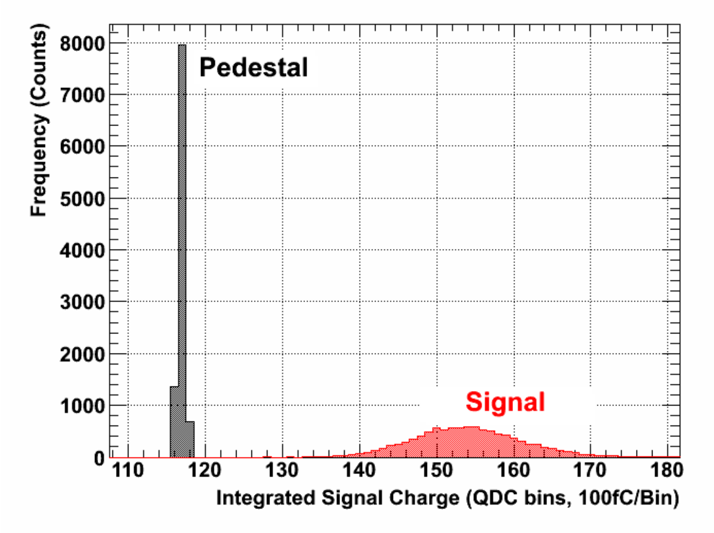

Figure 4.3: An example QDC spectrum obtained from one pixel of an MAPMT in response to a multi-photon light level (red) and the noise pedestal extracted with no light source present (black).

bins, between the mean positions of the pedestal and signal spectra. The pedestal threshold cut for efficiency calculations is selected without the fitting of a Gaussian distribution, for example, due to a combination of the well-defined narrow pedestal widths obtained and to avoid the use of timely fitting regimes during the automated analysis of laser scan data. Typical pedestal RMS widths extracted with the laser test-stand were 0.5 QDC bins. The value of 95% was concluded to be sufficient in order to contain the majority of the pedestal beneath the threshold cut and to avoid the inclusion of any spurious noise events lying outwith the main pedestal distribution in the threshold calculation. The signal efficiency results are applicable to single PE level spectra, where a fraction of the signal is lost to the pedestal distribution. The signal efficiency quantity is very sensitive to the incident light level, and typically for multi-photon levels will be equal to 1. The signal gain results are tailored towards multi-PE level measurements, where noise pedestals and signals are clearly separated, as illustrated in Fig. 4.3. The method used for setting single and multi-PE light levels is described in Section 4.4. For laser scan data, these quantities were calculated both for every MAPMT channel readout and for all laser positions of the scans. This then allowed the plotting of signal efficiency or signal gain maps of the photon detector response across the area of the laser scan.

The signal efficiency and signal gain maps which are shown represent relative measurements of each MAPMT's response across its surface, and were used to investigate the relative uniformity of the imaging planes offered by the tested MAPMTs only. Such measurements are useful to assess both the overall uniformity of the MAPMT imaging plane and the required dynamic range of any amplifiers and front end electronics which are to be employed for MAPMT readout in the CLAS12 RICH detector. The measured signal efficiency and signal gain maps therefore may not be used alone to map such parameters as absolute QE or absolute gain uniformities of the tested MAPMTs individually, since these quantities are convoluted together in the response maps which are plotted.

To measure the absolute QE and gain of an MAPMT's response, a reference detector, such as a calibrated photodiode, should be included into the setup shown in Fig. 4.1. The previously calibrated reference detector may then be used as an absolute measure of the laser light level, and would allow for a calibrated measure of the single photon response of the MAPMT under test. This could involve the use of optical components to split the laser beam into two paths, in order to illuminate both the reference detector and MAPMT under test simultaneously, although it is unclear if this method would work for single photon light levels. Since the signal efficiency and signal gain maps which are shown were measured without the use of a reference detector, the single PE level results cannot be guaranteed to originate from purely single photon events and the calculated efficiency parameter is likely to include events where more than one photon was also recorded by the MAPMT. To measure the absolute QE across the MAPMT face the photocurrent generated by the photocathode could be measured directly, without allowing the PE to be multiplied in the dynode stages and for a known light level determined by the reference detector. This, however, may be practically difficult to achieve with MAPMT assembly units and would require some level of dismantling and modification of the detectors. Furthermore, a calibrated light level would allow for an absolute measure of the MAPMT gain to be extracted. Such a de-convolution of the MAPMT QE and gain would also allow direct measurements of parameters such as CE or PDE, and provide access to an easier de-coupling of the different sources of crosstalk present in the MAPMT.

4.1.3 Stability of the Laser Scan Test Facility

Depending upon the laser scan step size and the number of MAPMT channels readout by the DAQ system, the laser scans took several hours to complete, and in some cases even over 24 hours. The stability of the laser test-stand and its readout electronics was therefore assessed and monitored throughout the experimental studies. The light source was previously shown to be extremely stable over a period longer than 24 hours [160]. Moreover, the pedestal readings performed immediately before and after each laser scan were used directly to monitor any drift in the electronics.

Figs. 4.4 (a) and (b) give an example of the stability of the pedestal distributions obtained from a typical ∼35 hour long scan of a 64-channel MAPMT. In total three 32-channel QDC modules were readout simultaneously, with 65 out of the total 96 QDC channels connected to the MAPMT (QDC channels 0 - 64). Fig. 4.4 (a) shows the difference in the mean positions of the pedestal distributions obtained before and after the scan, whereas in Fig. 4.4 (b) the differences between the pedestal RMS - widths are given. Both the extracted position and widths of the pedestal distributions are extremely stable over the scan period, with the maximum drifts lying below 0.4 QDC bins and 0.2 QDC bins respectively. To further emphasise this Fig. 4.5 shows the mean pedestal position extracted for one of the un-attached QDC channels at every position of the laser scan. The maximum shift in the pedestal distribution is less than 0.5 QDC bins, confirming the strong stability of the experimental setup and readout electronics. The slight striped pattern is likely an artifact of the laser scan path, which moves in vertical strips.

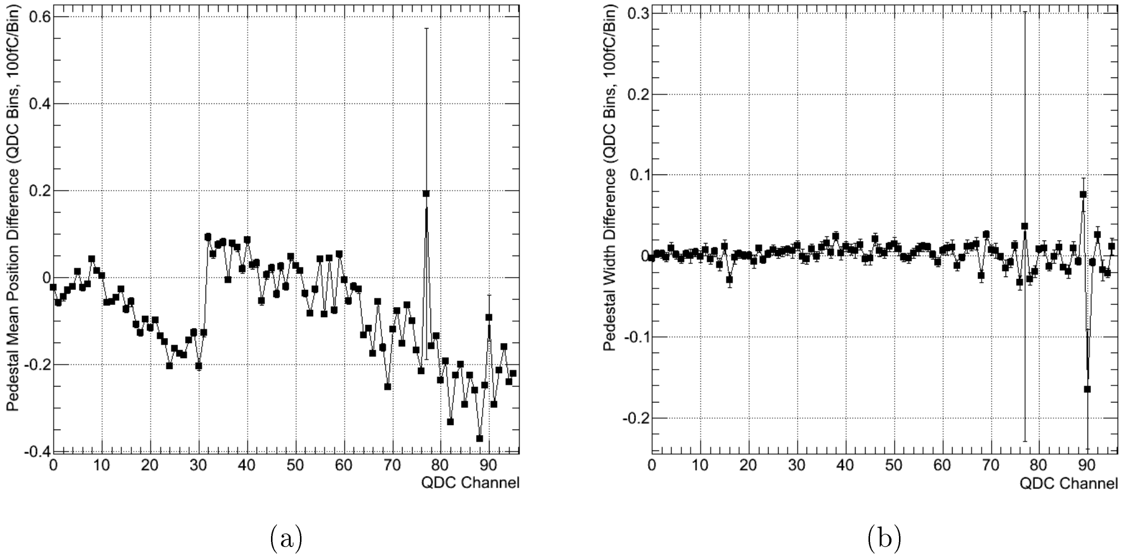

(a) (b)

Figure 4.4: Example differences in pedestal (a) mean positions and (b) RMS - widths obtained immediately before and after a 35 hour long laser scan. 65 out of the 96 QDC channels were connected to the MAPMT.

4.2 Tested Multianode Photomultiplier Tubes

Three different candidate MAPMTs from Hamamatsu have been studied using the laser scan test-bench, and their resulting suitabilities for application to the CLAS12 RICH detector have been assessed. This has involved a selection of investigations into their single photon detection capability, the uniformity of their response, their spatial resolution, any present crosstalk

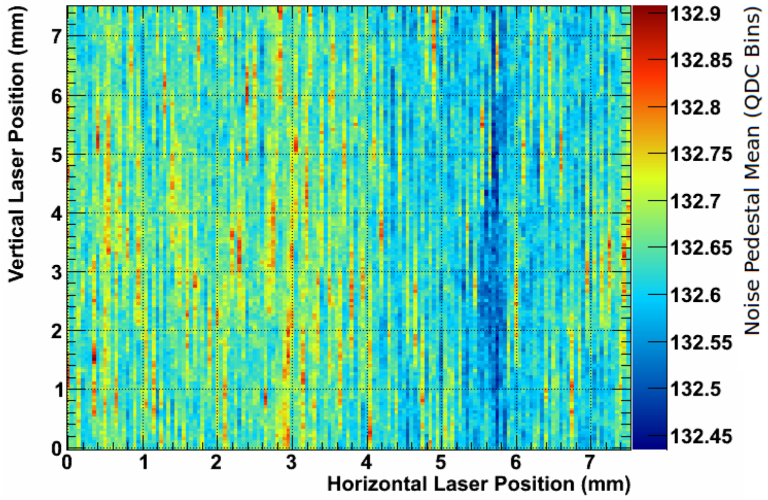

Figure 4.5: The mean noise pedestal position extracted (shown by colour fill) for an empty QDC channel at each laser step of a 35 hour long laser scan. The laser position throughout the scan is indicated by the horizontal and vertical axes.

behaviour and its corresponding origin and magnitude. Each MAPMT also offers a common last dynode output signal, which may act as a common logic OR between the pixels of the MAPMT. The signal strength uniformity and timing properties of this signal for one MAPMT type have also been studied.

The tested MAPMTs were the Hamamatsu H8500, H9500 and H7546 devices, which are shown in Figs. 4.6 (a), (b) and (c) respectively. All MAPMTs comprise metal channel dynode structures with 12 stages. They offer interesting comparison studies for the CLAS12 RICH application since they differ in spatial resolutions, spectral sensitivities and dimensions, as shown by the comparison of their characteristic parameters obtained from Hamamatsu and given in Tab. 4.1. All three MAPMTs provide satisfactory spatial resolutions for application to the


(a) (b) (c)

Figure 4.6: The tested Hamamatsu (a) H8500, (b) H9500 and (c) H7546 (image from [161]) MAPMTs.

Table 4.1: Parameters of the Hamamatsu H8500, H9500 and H7546 MAPMTs.

MAPMT Parameter	**H8500** [162]	**H9500** [163]	**H7546** [161]
Number of Pixels (Matrix)	64 (8×8)	256 (16×16)	64 (8×8)
Pixel Size [mm]	5.80×5.80	2.80×2.80	2.00×2.00
Pixel Pitch at Centre [mm]	6.08×6.08	3.04×3.04	2.30×2.30
Effective Active Area [mm]	49.0×49.0	49.0×49.0	18.1×18.1
Dimensional Outline [mm]	52.0×52.0	52.0×52.0	30.0×30.0
Window Material [Glass]	Borosilicate	Borosilicate	UV
Photocathode Material	Bialkali	Bialkali	Multialkali
Spectral Response [nm]	300 to 650	300 to 650	185 to 880
Peak Wavelength [nm]	400	400	420
QE at 420 nm (%)	24 (typical)	24 (typical)	38 (minimum)
Maximum Supply Voltage [V]	-1100	-1100	-1000
Typical Gain	1.5×10^6 at - 1 000 V	1.5×10^6 at - 1 000 V	0.8×10^5 at - 800 V
Typical Anode Uniformity Maximum Anode Uniformity	1 : 2 1 : 4	1 : 4 1 : 6	1 : 3 1 : 5
Crosstalk [%]	3	5	2
Typical Dark Current [nA/Channel]	0.1	0.05	0.2
Rise Time [ns]	0.8	0.8	1
Transit Time [ns]	6	6	12
Transit Time Spread (FWHM) [ns]	0.4	0.4	0.38

CLAS12 RICH detector, with the H7546 device offering the smallest pixel size. Unfortunately, as seen in Table 4.1, the H7546 suffers severely from a bulky outer packaging and a large area of deadspace in the peripheral region surrounding the active area. The H8500 and H9500 MAPMTs however originate from the flat-panel branch of Hamamatsu MAPMTs, which have been optimised for imaging applications and have minimal deadspace. They both provide very efficient active areas, with extremely high packing fractions of 89 % offered by both devices, and therefore the devices are well-suited to applications where they must be tiled together to provide a large area imaging plane. The H9500 MAPMT offers an interesting comparison to the H8500 MAPMT since it provides the same geometrical efficiency with a four times improvement in spatial resolution. The length of the H7546, H8500 and H9500 MAPMTs are 45 mm, 32.7 mm and 36.4 mm respectively, all of which should comply with the restricted geometry of the CLAS12 RICH detector and allow enough room for readout electronics.

Despite the increased deadspace in the H7546 MAPMT, this MAPMT was selected for tests due to its improved single photon sensitivity, resulting from an increased CE caused by the arrangement and design of its dynode channels [164]. Furthermore, the selected model has an increased spectral sensitivity and QE compared to the H8500 and H9500 MAPMTs, due to a combination of its UV-glass transmission window and multialkali photocathode. The multialkali photocathode however results in increased dark count levels, which is less favourable for a single photon counting application such as the CLAS12 RICH detector. The H9500 MAPMT, from the information provided by Hamamatsu, exhibits larger crosstalk and uniformity mis-match issues between its channels, most likely caused by the increased number of metal channels, and the H8500 device appears to provide the most uniform response. The time responses of all MAPMTs are very fast and acceptable for the CLAS12 RICH application.

From comparisons between the performance parameters listed in Table 4.1, the most appropriate MAPMT for the CLAS12 RICH application appears to be the H8500 device. It offers the most suitable compromise between an optimised efficient active area, its sufficient spatial resolution and the lowest required number of readout channels. It has a fast response, the superior uniformity, moderately low crosstalk levels and low dark noise. In-depth studies and characterisations were performed upon all three MAPMT detector types, however, an emphasis was placed upon the H8500 MAPMT to confirm it as the most suitable candidate for the CLAS12 RICH. The results obtained from the H9500 and H7546 MAPMTs were extremely useful as crosschecks for behaviour observed with the H8500, and to further understand the performance of MAPMTs in general.

4.3 Common Last Dynode Signals

All three MAPMTs investigated feature a common last dynode output signal, which is provided for self triggering purposes. This signal is named the *dynode 12* signal and its derivation within an H8500 MAPMT, for example, may be viewed in Fig. 4.7. The magnitude of the dynode 12 charge signal is $\sim$7 - 10 times smaller than individual channel signals, resulting from charge losses occurring during its simultaneous extraction from all 64 channels using a capacitive coupling technique. The dynode 12 extraction technique also results in a slightly nosier signal than the individual pixel responses collected at the matrix of readout anodes. The dynode 12 signal is common amongst all channels of an MAPMT and therefore may be used as a logic OR between its pixels. Such a signal yields very interesting prospects for the CLAS12 RICH detector, since the photon detectors will be placed close to the beam line and hence be subjected to high background rates. The Čerenkov rings of the CLAS12 RICH will span several MAPMTs, and the dynode 12 signal may be an interesting option for use either online or offline as a coincidence trigger between MAPMTs, for the identification of true Čerenkov ring events.

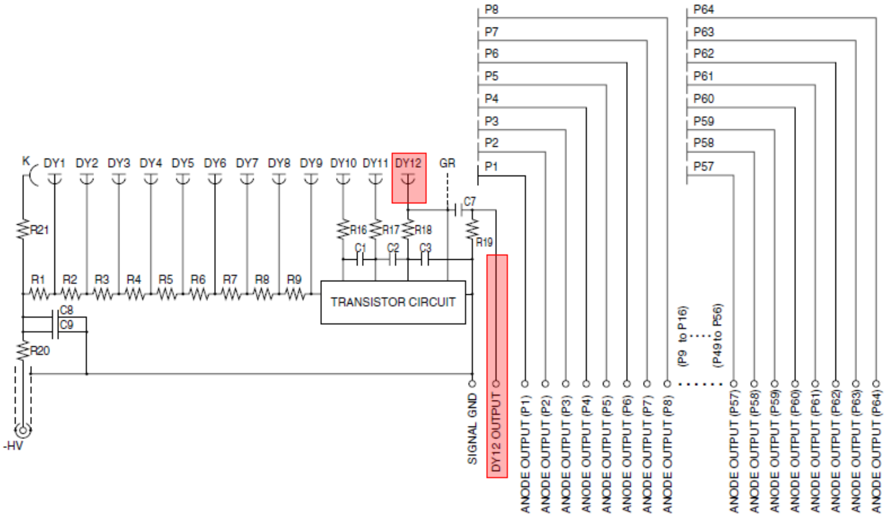

Figure 4.7: Schematic showing the extraction of the Hamamatsu H8500 MAPMT common last dynode, or dynode 12, signal (highlighted by red and labelled *DY12 OUTPUT*). Image taken from [162].

4.3.1 Common Last Dynode Signal Readout

The strength and timing of dynode 12 signals extracted from the H8500 MAPMT have been mapped throughout a subset of the series of MAPMT laser scans. The scheme for the inclusion of dynode 12 signals into the laser test-stand readout electronics is shown in Fig. 4.8. The dynode 12 signal is first amplified by a factor of 200 and then passed through a fan in/fan out unit purely for inversion of its positive signal to negative polarity. The negative output is then discriminated by a Constant Fraction Discriminator (CFD), with the optional analogue output from the CFD sent to a QDC and the ECL digital output sent to a Time to Digital Converter (TDC) for recording of its timing information. A CFD is used, as opposed to a leading edge discriminator, to minimise any time walk effects caused by varying pulse heights, which may deteriorate the dynode 12 signal timing resolution measurement. The trigger signal for readout of the QDC and TDC is the same as that derived for the readout of the analogue MAPMT charge signals as shown previously in Fig. 4.1.

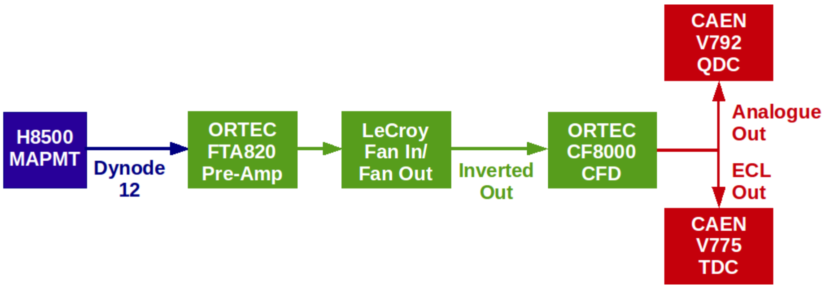

Figure 4.8: The electronics setup used for the readout of H8500 MAPMT common last dynode signals.

4.3.2 Common Last Dynode Signal Analysis

Signal efficiencies from dynode 12 signals were calculated from the charge spectra extracted at each laser position of the scans as described previously in Section 4.1.2. An example of a typical dynode 12 charge spectrum obtained at the single PE light level is shown in Fig. 4.9 (a), where the pedestal is seen on the left and is broadened due to the use of the pre-amplifier. The single PE peak is less separable from the noise pedestal in comparison with typical charge spectra from the pixels of the H8500 MAPMT (which will be shown below) due to the charge losses experienced during the extraction of the dynode 12 signal, and appears as a broadened tail to the pedestal. The TDC spectra were fitted with the sum of two Gaussians (termed G_1, G_2) and a quadratic background, of the form $G_1 + G_2 + a + bx + cx^2$, as described in [153] and previously used successfully for the description of time spectra obtained from the H8500 MAPMT. Examples of TDC spectra acquired at single and ∼8 PE light levels are shown in Fig. 4.9 (b). From the fits to the time distributions, standard deviation σ_1 resolutions of (141.4 ± 12.6) ps and (63.2 ± 2.0) ps are extracted respectively for the narrow components of the double Gaussians.

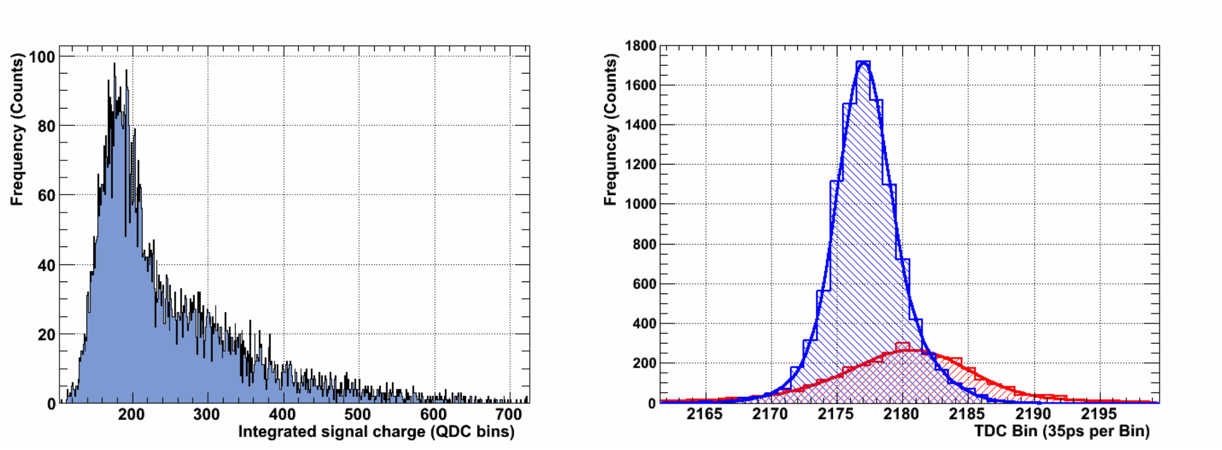

(a) (b)

Figure 4.9: Typical H8500 MAPMT common last dynode (a) charge spectrum obtained at a single photoelectron light level and (b) fitted time spectra obtained at single (red) and 8 (blue) photoelectron light levels.

4.4 Single Photoelectron Levels and Calibration Method

For single photon-level studies of the MAPMTs: NDFs were used to attenuate the laser beam such that the mean of the Poissonian governing the photon statistics per pulse was less than one photon, allowing for the corresponding MAPMT single PE charge spectra to be extracted. Examples of single PE spectra obtained with each of the three MAPMTs are shown in Figs. 4.10 (a), (b) and (c), illustrating that single photon detection is possible with all three MAPMTs. The graphs are shown on logarithmic scales for visualisation purposes. The spectra were selected randomly as examples only and it is important to note that the resulting resolutions may not be fairly compared since the absolute gain of each device, and also each pixel used, was different. However, to describe the spectra which are shown the resolutions of the single PE peaks, which is defined here as the Gaussian σ - width of the single PE peak divided by its mean value, are extracted as 83.22 %, 60.75 % and 52.04 % for the H8500, H9500 and H7546 MAPMTs respectively. These values are also reflected in the visible differences between the peak - to - valley ratios [10] of the spectra.

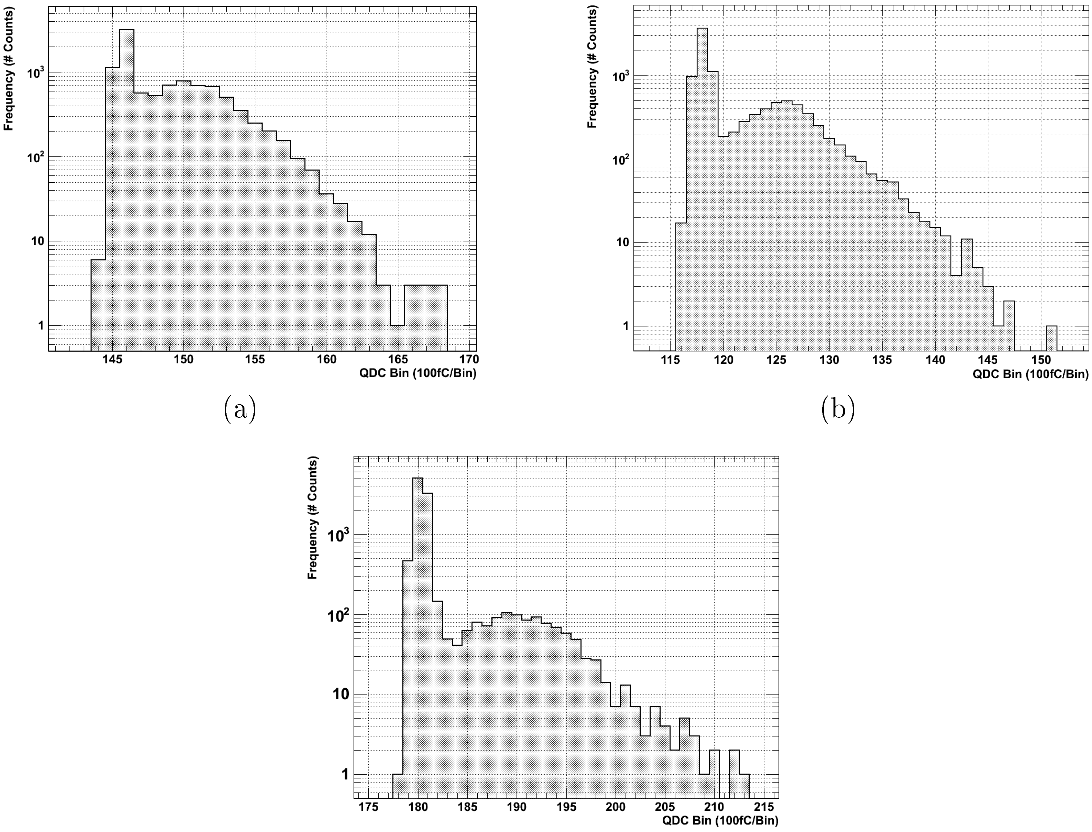

(a)

(b)

(c)

Figure 4.10: Examples of single photoelectron spectra obtained with the Hamamatsu (a) H8500, (b) H9500 and (c) H7546 MAPMTs.

In addition to determining its applicability to the CLAS12 RICH detector, obtaining the single PE spectrum for any MAPMT is also extremely useful for calibrating its gain. For

---

[10] The peak - to - valley ratio is defined as the ratio between the heights of the single PE peak and the valley lying between the pedestal and single PE peaks.

calibration purposes a fit function was used which was developed by M. Mirazita [165] from the mathematical description of the PMT single PE response explained in literature by R. Perrino *et al* [166]. The fit describes single PE charge spectra as a function of QDC bin q, and a corresponding expression for the fitting function is shown in Equation 4.2.

$$f(q) = A \times \left\{ e^{-\mu} Gauss_0(q) + \sum_{k=1}^{N_{Max}} \frac{\mu^k e^{-\mu}}{k!} \times Gauss_k(q) \right\} \tag{4.2}$$

The parameter A is a normalisation factor, μ denotes the mean number of detected PEs and k is representative of PE number up to a maximum value of N_{Max}. The function describes the PMT response as a Poisson weighted Gaussian for the pedestal distribution, corresponding to $k = 0$ and depicted as $e^{-\mu} Gauss_0(q)$, summed with Gaussian smeared Poisson distributions for each of the present PE contributions, $\frac{\mu^k e^{-\mu}}{k!} \times Gauss_k(q)$. The Gaussian distributions have standard deviations $\sigma_k = \sigma_1 \sqrt{k}$ and their mean positions may be described as $m_k = m_1 + d(k-1)$, where d is the inter-peak distance in units of QDC bins. Fitting the charge spectra with such a function allows retrieval of the distance between the single PE and pedestal peaks, or in other words provides a measure of the absolute gain of the device. The fit function also returns the fraction of single PE signal events lost below the noise pedestal distribution, which as observed in Figs. 4.10 (a), (b) and (c) is non-zero. Additionally the mean corresponding PE level of the charge spectrum may also be extracted.

An example of the function fitted to a single PE spectrum obtained with an H8500 [11] MAPMT pixel set to -1 000 V is shown in Fig. 4.11, where the overall fit is shown in black, the pedestal is shown in blue, and the individual PE contributions are shown in red. The result of the fit yields the mean number of PEs as as <1 and equal to (0.6899 ± 0.0203) PE, confirming the suitability of the method described above for successfully finding a light level corresponding to single PE spectra. This fitting procedure was therefore incorporated as a cross-check for the light level settings used throughout single PE level scans of the MAPMTs. However, as described in Section 4.1.2, this method of obtaining single PE spectra was performed without the use of a calibrated reference detector. The spectra are therefore assumed to correspond to that of a low-photon level as opposed to an absolute single photon level, however for the purposes of the results which are shown they are termed single PE spectra. The fraction of single PE contribution events lost below the noise pedestal distribution, which was returned by the output of the calibration fitting function, represents a more accurate description of the tested

---

[11] S/N DA0269.

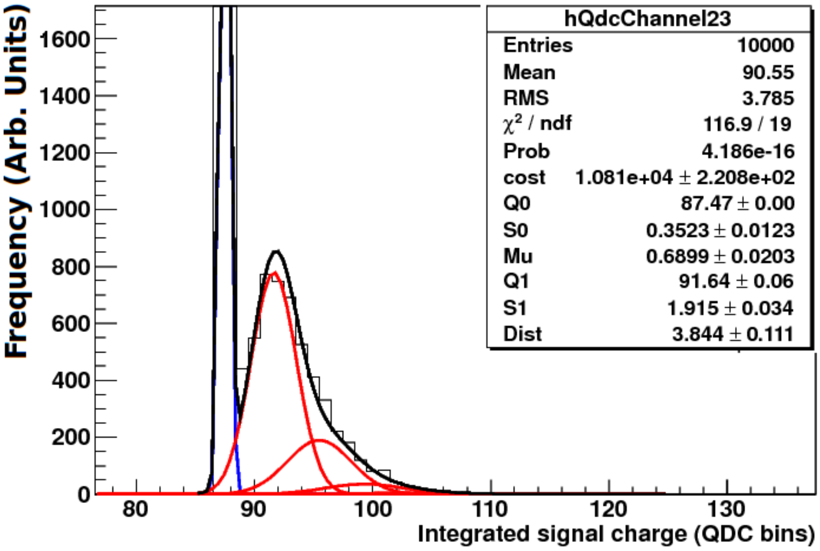

Figure 4.11: An H8500 charge spectrum fitted with a function to describe each photoelectron peak as a Poisson weighted Gaussian. The function allows extraction of the distance between the pedestal and single photoelectron peaks, the fraction of single photoelectron signal lost to the pedestal and the mean number of photoelectrons detected.

MAPMTs' single photon detection capabilities. This parameter was therefore always used for MAPMT response calibration and characterisation purposes, whereas the signal efficiency maps described in Section 4.1.2 were used to assess the relative homogeneity of the MAPMT signal responses. The fit result shown in Fig. 4.11 also returns a distance of (3.844 ± 0.111) QDC bins between the pedestal position and the first PE peak, translating to a gain factor of 2.4×10^6 for this pixel of the MAPMT. The distance between the pedestal and first PE peaks was used to calibrate and set the multi-PE levels used throughout the laser scans. Since the MAPMTs were operated in their linear gain regimes, the pedestal-spectrum distances at multi-PE levels were converted into corresponding mean PE levels through normalisation by the single PE gain factor. To study the relative gain variations between different pixels of the MAPMTs, laser scans were performed, as described in the following sections.

4.5 Low Resolution Laser Scan Studies

For the low resolution laser scan tests the laser spot size was focussed to 1.0 mm. Although the single photon response capability and corresponding uniformity are the most crucial parameters for the CLAS12 RICH application, laser scans were performed at both single- and multi-PE levels. At multi-PE levels the entire charge signal is resolved by the MAPMTs, and scans at these levels may therefore yield a slightly more reliable assessment of the absolute gain uniformity. The multi-PE laser scans also act as a crosscheck to verify behaviour observed at the single PE level, and allow for noise mechanisms which would otherwise be lost at the single PE level to be observed and understood.

For presentation of the scan results which will be shown below, *global* signal efficiency or gain maps are given. The global maps show the response of the pixel with the largest signal at each laser position, by colour fill, for all laser positions and the horizontal and vertical axes denote the relative laser position during the scan. In some cases *single channel* signal efficiency or gain maps are given, which show the response from one individual MAPMT channel only at every position of the laser scan.

4.5.1 Hamamatsu H8500 Results

Results obtained with the Hamamatsu H8500 MAPMT are shown below, including: uniformity ratios, single photoelectron signal loss estimates, spatial resolution, angular uniformity response and crosstalk levels - all of which are extremely important properties to assess before consideration for the CLAS12 RICH detector. For the duration of the H8500 MAPMT scans, the HV of the MAPMT was set to -1 000 V. Several low resolution scans were performed with the 1.0 mm laser beam, including pixel-to-pixel pitch scans, whereby the centre of each pixel only was illuminated, 1 mm step scans of the entire H8500 surface and 0.5 mm step scans of individual pixels.

The resulting single PE level normalised global signal efficiency map from a pixel-to-pixel pitch scan of an H8500 MAPMT [12] is shown in Fig. 4.12, where each channel's signal efficiency is normalised to that of the highest efficiency pixel. The response across the surface of the MAPMT appears rather uniform, apart from a low efficiency portion at the top right corner of the device and right-most column. Such a single PE response should provide an imaging plane of adequate efficiency for the CLAS12 RICH application, with only 5 pixel outs of 63 returning relative signal efficiencies $< 50\,\%$ than that of the leading pixel. A uniformity ratio for the MAPMT of 1.00 : 3.49 is obtained, which is in accordance with the general values quoted by Hamamatsu (see Table 4.1). The most efficient region of this PMT lies in the centre, with the lower efficiency pixels comprising the edge channels of the MAPMT, and moreover the efficiency behaviour of the MAPMT is very localised, for example higher efficiency channels are clustered together and vice versa. The corresponding spectra for the lowest and highest

---

[12] S/N DA0269.

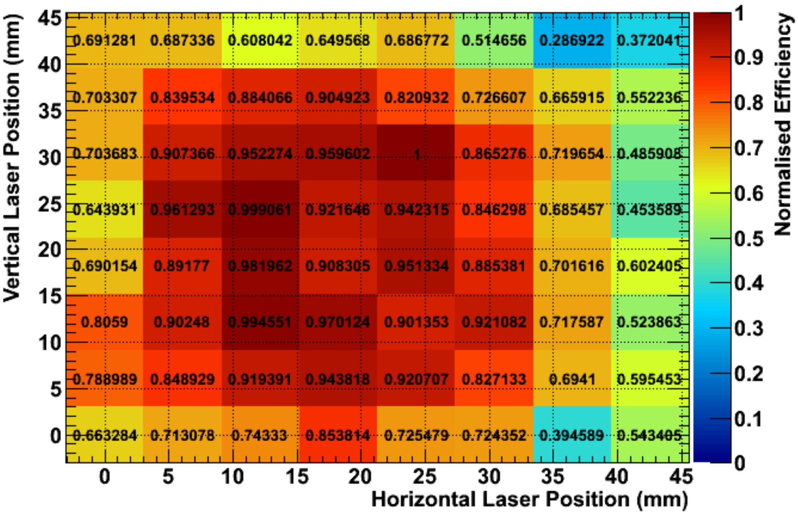

Figure 4.12: Normalised global efficiency map obtained from a single photoelectron pixel - to - pixel pitch scan of an H8500 MAPMT.

signal efficiency pixels are shown in Figs. 4.13 (a) and (b) respectively, where the low-efficiency result appears as a shoulder to the pedestal. A calibration analysis performed on this single PE centre pitch scan data, using Equation 4.2 described above, yielded the mean number of detected PEs as 0.74. The resulting probability of events corresponding to 0 PE from Poisson statistics is then 48 %, leaving a fraction of roughly 52 % assumed for >0 PE level events. This fraction will therefore include both single and > 1 PE level events and agrees well, for example, with the un-normalised signal efficiency value of 55 % extracted from the laser scan analysis

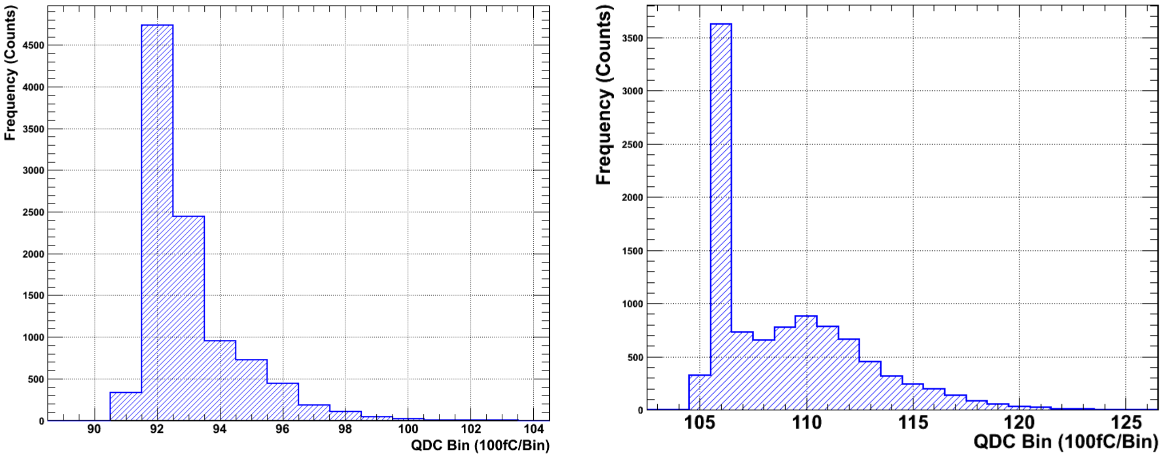

(a) (b)

Figure 4.13: H8500 MAPMT pixels which displayed the (a) lowest and (b) highest fractions of their single photoelectron spectra lying above 95 % the pedestal distribution during a single photoelectron scan of the device.

results for the spectrum shown in Fig. 4.13 (b). The mean gain of the device, averaged over the calibration fit result gain parameters obtained from all 64 channels, was extracted as 2.85 QDC bins and translated to a factor of 1.78×10^6. Fig. 4.14 (a) shows a typical single PE spectrum obtained from a channel with a similar gain to the average value, where the spectrum is clearly separated and identifiable from the pedestal noise. Fig. 4.14 (b) shows the fraction of single

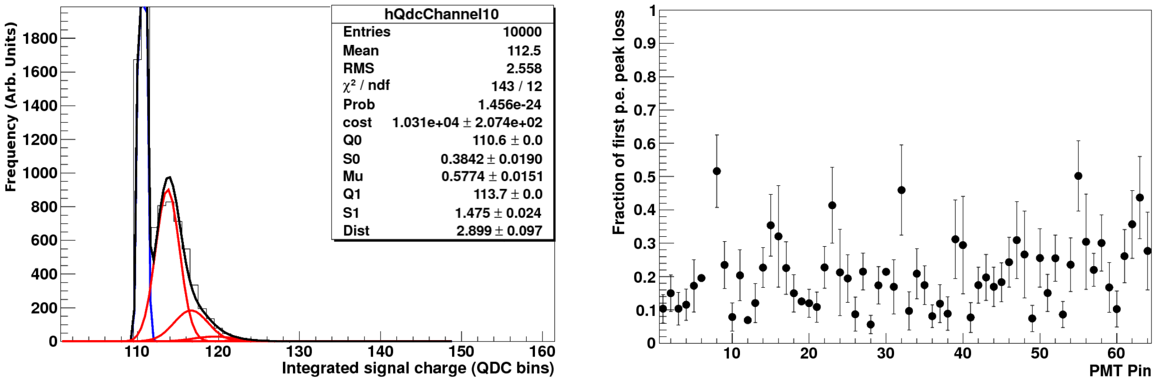

(a) (b)

Figure 4.14: (a) Example single photoelectron charge spectrum obtained from an H8500 pixel with a gain close to the average gain of all MAPMT channels and (b) calculated fraction of single photoelectron events lost beneath the pedestal distribution, for each channel of the H8500 MAPMT.

PE events lost beneath the pedestal distribution for each of the 64 channels of the device. In the worst cases the loss fractions reached values as high as ∼ 50 %, however the majority of channels provided losses much less severe than this and the average loss fraction amongst all 64 channels was calculated as 20.8 %. This loss fraction could be improved by increasing the HV, or in other words the gain, of the MAPMT.

The normalised global signal gain map obtained from a pixel - to - pixel pitch scan performed at a light level corresponding to ∼ 20 PE is shown in Fig. 4.15 (a). The resulting uniformity

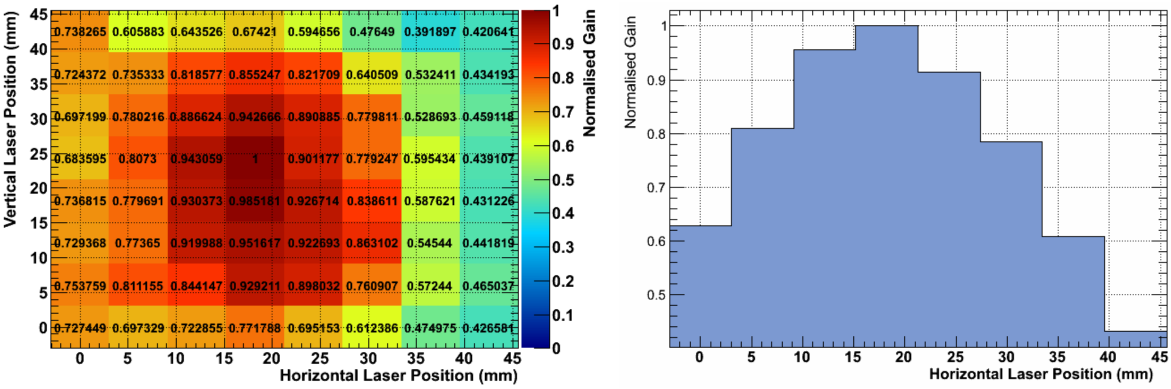

(a) (b)

Figure 4.15: (a) Normalised global signal gain map and (b) corresponding horizontal projection of a central row, obtained from a 20 photoelectron level pixel - to - pixel pitched scan of an H8500 MAPMT.

is similar to the single PE result (see Fig. 4.12) and a uniformity ratio of 1.00 : 2.55 was obtained between the lowest and highest gain channels from the 20 PE normalised result, which is superior to the value obtained with the single PE normalised efficiency map. This is most likely caused by the higher accuracy of the method at the 20 PE level and lower relative signal fluctuation with respect to the single PE level. For example purposes, a horizontal projection taken from the row containing the strongest gain pixel is shown in Fig. 4.15 (b), emphasising that the region of highest gain pixels lies in the centre of the MAPMT.

To cross-check the extent of variations between different MAPMTs, a second H8500 [13] MAPMT was subject to similar laser scans. As an example Fig. 4.16 (a) shows the resulting normalised single PE global signal efficiency map obtained from a pixel - to - pixel step scan. The missing pixel has been removed due to a faulty electronics line in the readout board and data from this channel is excluded from uniformity calculations. Immediately obvious from the single PE result is that the response appears to be more uniform than that shown in Fig. 4.12, and confirming this a uniformity ratio between the lowest and highest efficiency pixels of 1.00 : 1.56 is obtained. Fig. 4.16 (b) displays the corresponding map obtained for a multi-photon light level, which in this case corresponds to ∼ 8 PE and returns a uniformity of 1.00 : 2.04, deviating slightly more from the single PE result than the equivalent uniformity comparisons made between Fig. 4.12 and Fig. 4.15 (a). To understand this conflict in more detail would require further study, which was not performed due to time constraints. The overall pattern of these responses is also different to the results shown previously in Fig. 4.12 and

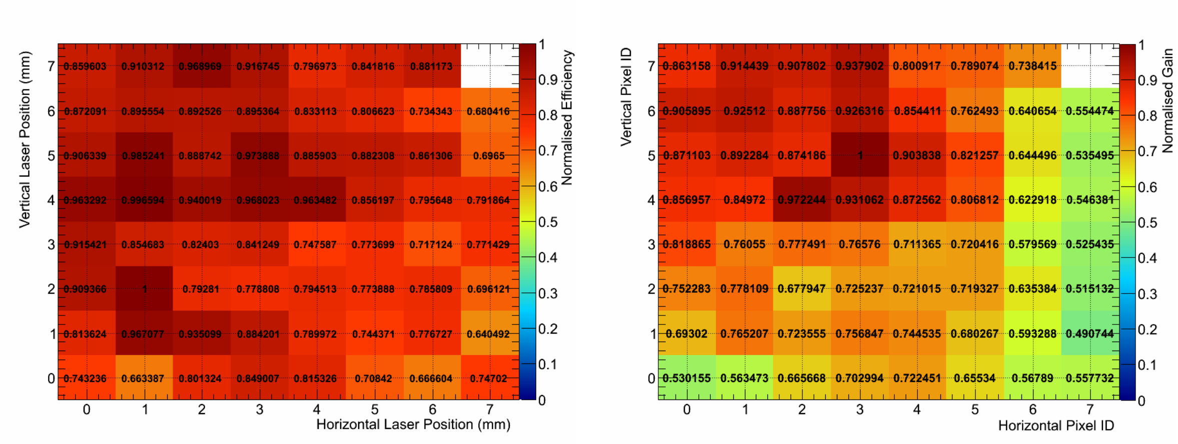

(a) (b)

Figure 4.16: Normalised global signal (a) single photoelectron efficiency and (b) ∼ 8 photoelectron gain maps obtained from pixel - to - pixel pitch scans performed with a second Hamamatsu H8500 MAPMT.

---

[13] S/N CA3906.

Fig. 4.15 (a), and one conclusion drawn from such a comparison is that prior to the procurement of numerous such devices, one should first consider and specify from the manufacturer both the pixel - to - pixel uniformity and the PMT - to - PMT gain variations required for the imaging application. This will, unfortunately, increase the prices of the devices.

The signal charge and time resolution uniformity of dynode 12 signals amongst the H8500 MAPMT pixels and their dependence upon MAPMT channel gain were also mapped through a selection of the pixel - to - pixel pitched scans. For instance the normalised dynode 12 single and 8 PE global signal efficiency and gain maps, which correspond to the pixel uniformity maps shown in Figs. 4.16 (a) and (b), are given in Figs. 4.17 (a) and (b). The agreement between the resulting maps with the previously shown uniformity results for the individual pixel responses of this MAPMT (see Figs. 4.16 (a) and (b)) is extremely close, implying that the dynode 12 signal gain matches very closely that of the MAPMT channel from which the hit originates, as expected. Dynode 12 signal strength uniformities of 1.00 : 1.78 and 1.00 : 2.13 for the single and 20 PE results are obtained from Figs. 4.17 (a) and (b), which are also in strong agreement with the values of 1.00 : 1.56 and 1.00 : 2.04 extracted for the MAPMT pixel responses. The corresponding dynode 12 signal time resolution results obtained at the single and 8 PE levels respectively are shown in Figs. 4.18 (a) and (b). The colour-fill scales given in Figs. 4.18 (a) and (b) may not be directly compared and are bound by different limits, in order that the time resolution variations may be more easily observed. Upon comparison with Figs. 4.17 (a) and (b) it is concluded that variation in time resolution is not exactly, but largely representative of the gain uniformity of the MAPMT. This is particularly visible for the 8 PE level result,

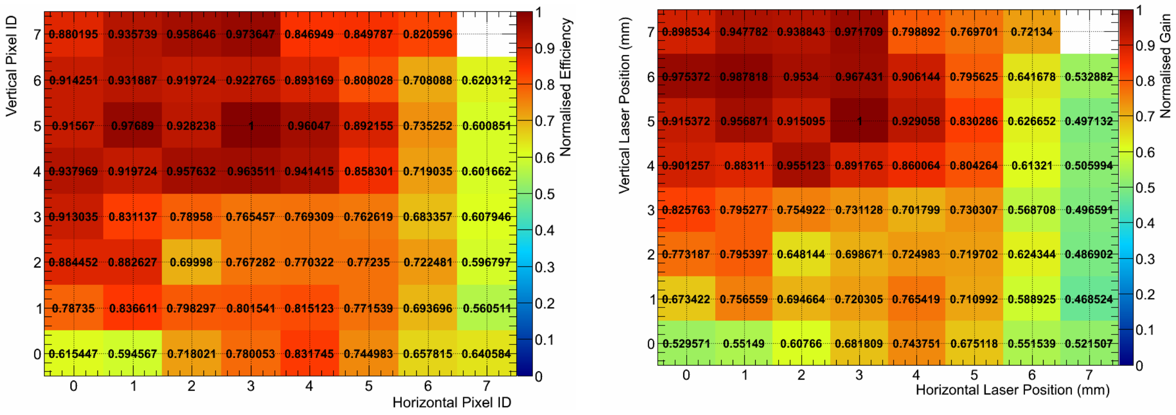

(a) (b)

Figure 4.17: Pixel - to - pixel uniformity of H8500 common last dynode signal (a) single photoelectron signal efficiency and (b) 8 photoelectron signal gain maps.

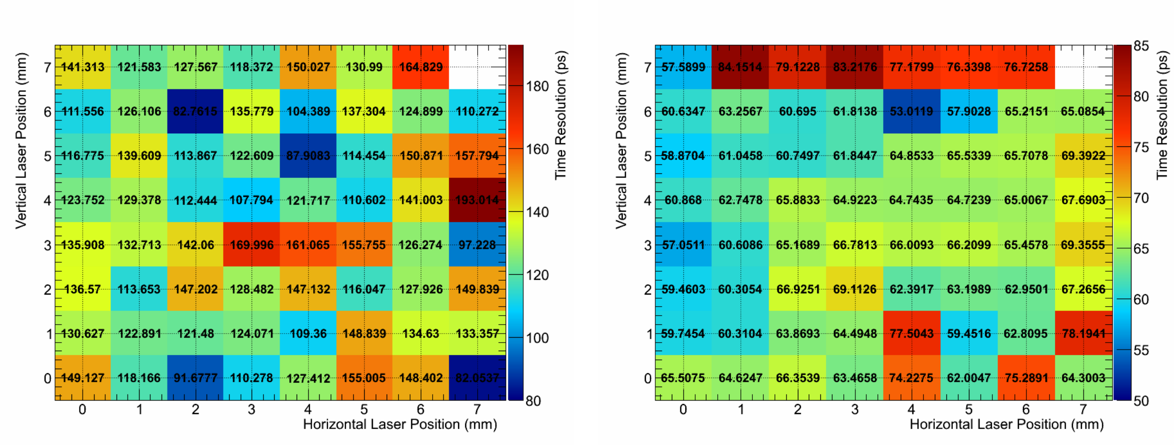

(a) (b)

Figure 4.18: Pixel - to - pixel uniformity of H8500 common last dynode signal time resolutions obtained at (a) single and (b) eight photoelectron light levels.

with smaller σ_1 values typically corresponding to higher gain channels. A few anomalous pixels do exist, however, for example those lying along the upper-most row of the MAPMT at the 8 PE level. The mean σ_1 time resolutions extracted from all 63 included channels at 8 and single PE light levels were (65.67 ± 0.49) ps and (128.99 ± 1.76) ps respectively, with both mean values lying well within the required 1 ns time resolution for distinguishing between direct and reflected light imaging case Čerenkov photons in the CLAS12 RICH detector.

The aim of the finer resolution scans with 1 mm steps was to study both false signals arising in inter-pixel deadspaces and homogeneities within individual pixels. The resulting single PE normalised global efficiency map from a 1 mm step scan across an entire H8500 [14] area is shown in Fig. 4.19, where the matching pixel - to -pixel pitch laser scan result for comparison was shown in Fig. 4.12. The result indicates that for the highest efficiency channels the inner pixel responses are largely uniform, however in lower efficiency pixels their response tends to weaken towards their edges. The level of false signals arising at the boundaries, or deadspace, between pixels is rather high, particularly between higher efficiency channels. Since the laser beam and step sizes are larger than the quoted deadspace distance of 0.28 mm, it is expected that true signals are included at these locations of the scan also. However, it is interesting that the relative signal efficiencies are much larger between side-sharing neighbours lying on the same horizontal row, than between neighbours separated in the vertical direction. This is further emphasised upon comparison of Figs. 4.20 (a) and (b) which show horizontal and vertical projections across the centre of the normalised global efficiency map given in Fig. 4.19

---

[14] S/N DA0269.

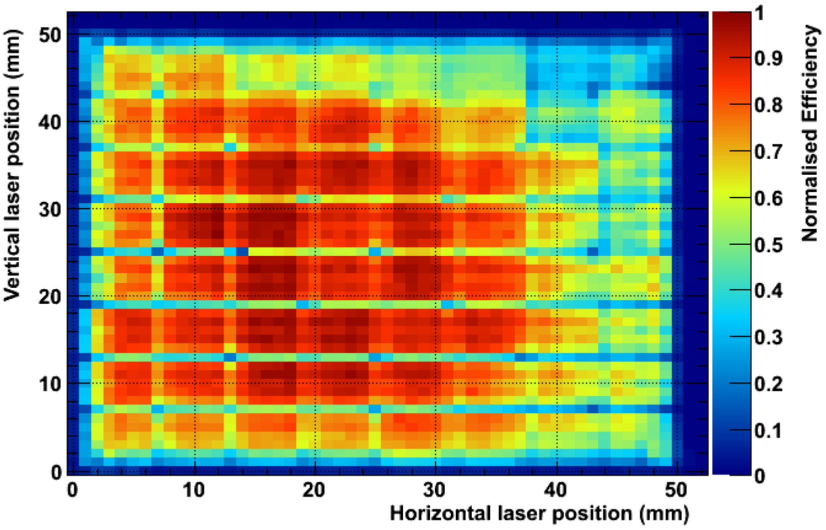

Figure 4.19: Normalised global efficiency map obtained in response to a 1 mm step single photoelectron scan across the entire area of an H8500 MAPMT.

respectively. In the vertical direction the relative single PE signal efficiency drop between individual channels is much sharper than in the horizontal direction. This directional effect

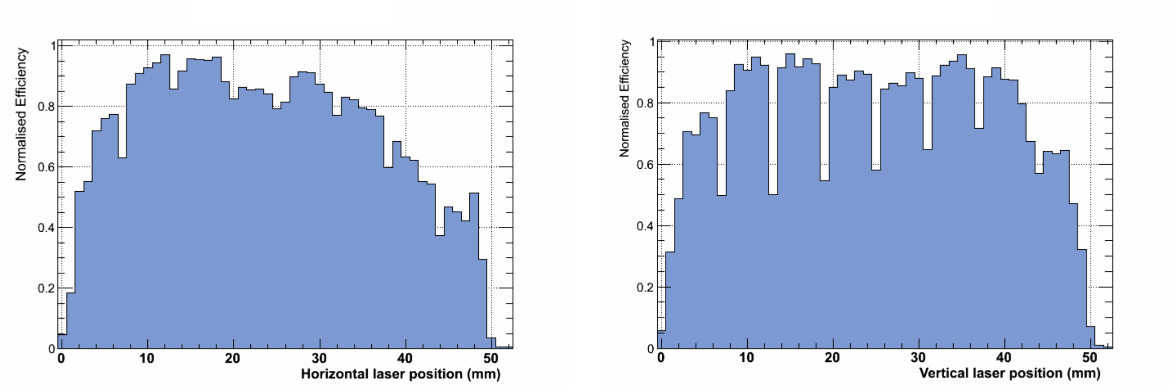

(a)

(b)

Figure 4.20: (a) Horizontal and (b) vertical projections across the centre of the normalised single photoelectron global efficiency map obtained with laser steps of 1 mm across the H8500 surface.

may also be observed on inspection of single channel signal efficiency maps, such as the example shown in Fig. 4.21. Contrary to the global signal efficiency or gain maps shown, the result shows the normalised signal efficiency for one individual channel only at every position of the laser scan. The location of the pixel is visible by the high efficiency area. The area returning efficiency values of $>50\,\%$ corresponds roughly to the quoted $5.8\,\text{mm} \times 5.8\,\text{mm}$ pixel sizes. Relative signal efficiencies lower than $50\,\%$ are also present, which extend beyond the area of $6\,\text{mm} \times 6\,\text{mm}$ marked in Fig 4.21, and likely correspond to a combination of both false signals or crosstalk obtained when the laser strikes the surrounding deadspace areas and true pixel

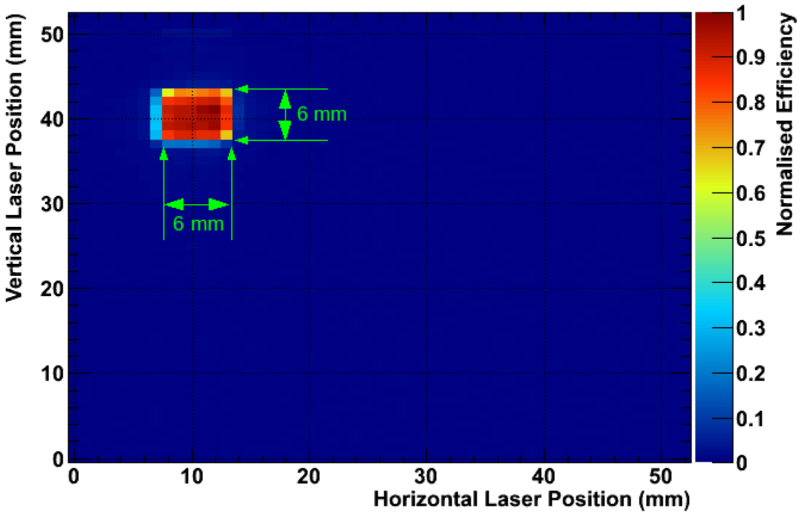

Figure 4.21: Normalised single channel efficiency map obtained in response to a 1 mm step single photoelectron scan across the entire area of an H8500 MAPMT, where the signal from one channel only is plotted by colour fill. The labels indicate an area of 6 mm × 6 mm.

signals caused by the large diameter of the laser beam in comparison to the quoted deadspace dimensions. These signals appear to be strongest between side sharing neighbours, than in the diagonal directions, and in particular within the same horizontal row. The effect however is small and beyond this crosstalk the signal drop off is extremely sharp.

The 1 mm step single PE scan was also successfully used to assess the spatial resolution of the H8500 MAPMT. For instance Fig. 4.22 (a) shows the super-imposed individual horizontal projections taken for each of the 8 pixels lying along one central row of the H8500 MAPMT and extracted from the un-normalised version of Fig. 4.19. The absolute magnitude of the projections is not inspected here and it is not relevant that the un-normalised version of the map is used, since only the widths and behaviours of the tails of the distributions are important. The FWHM values of each projection are extracted as that pixel's corresponding pixel size. The measurement however has an overall precision of 1 mm, due to the binning of the original scan, and so the actual value of the FWHM is rounded to the nearest integer value in each case. For the horizontal result of Fig. 4.22 (a) FWHM pixel size values of 6 mm were extracted in all cases, in extremely close agreement with the 5.8 mm pixel sizes quoted by Hamamatsu. In the vertical projections however, shown in Fig. 4.22 (b), there was slightly more variation, with values of 5 mm, 6 mm and 7 mm obtained across the 8 pixels. The average pixel size obtained in the vertical direction is therefore (5.88 ± 0.25) mm, which again agrees very well with expected value of 5.8 mm. A comparison between the results in Figs. 4.22 (a) and (b) also

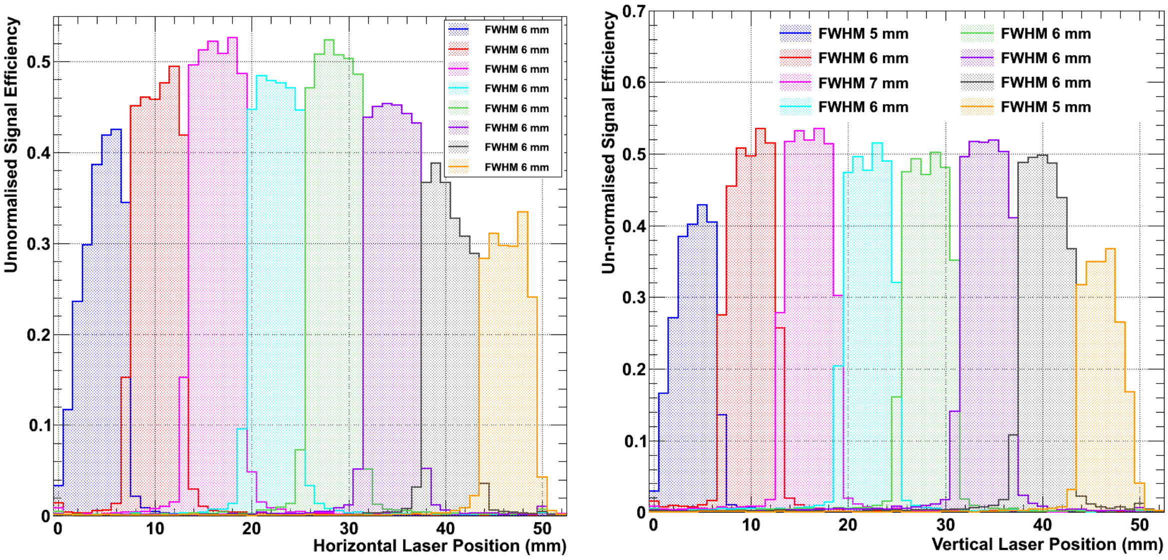

(a) (b)

Figure 4.22: (a) Horizontal and (b) vertical projections for each of the constituent pixels lying across central orthogonal rows of the H8500 MAPMT in response to a 1 mm step single photoelectron scan.

confirms the results shown in Figs. 4.20 (a) and (b), with stronger drops in signal efficiencies obtained between channels in the vertical direction. Nonetheless, the pixel boundaries are very sharp in both directions, despite the presence of crosstalk tails in all cases. The crosstalk tails, which are observed as remnants of a certain channel's signal efficiency as the laser is moved onto its neighbouring channel, also appear to be slightly stronger in the horizontal direction. However, in all cases the crosstalk magnitudes are easily distinguishable from the true pixel signal strengths. It should be noted again that the diameter of the laser beam used here was larger than the quoted deadspace dimensions, and so signals extracted whilst the laser was centered upon deadspace locations will also partly include pixel responses.

For completeness Fig. 4.23 shows the corresponding 1 mm step scan repeated at the 20 PE light level. A similar pattern to the single PE result (see Fig. 4.19) is obtained, whereby the central group of pixels show high gain signals and relatively homogeneous inner-pixel responses. The outer-most pixels and furthest right two columns of pixels show significantly lower gain and less uniform responses within the pixel areas themselves. Crosstalk and false signals are again visible at inter-pixel boundaries and the effect appears to be strongest between pixels in the horizontal direction, confirming the behaviour observed at the single PE level.

As indicated by the 1 mm step results (see Figs. 4.19 and Fig. 4.23), the inner-pixel uniformity also varies and may therefore compromise the homogeneity of the resulting CLAS12 RICH imaging plane. To study this further, finer scans of individual H8500 MAPMT pixels,

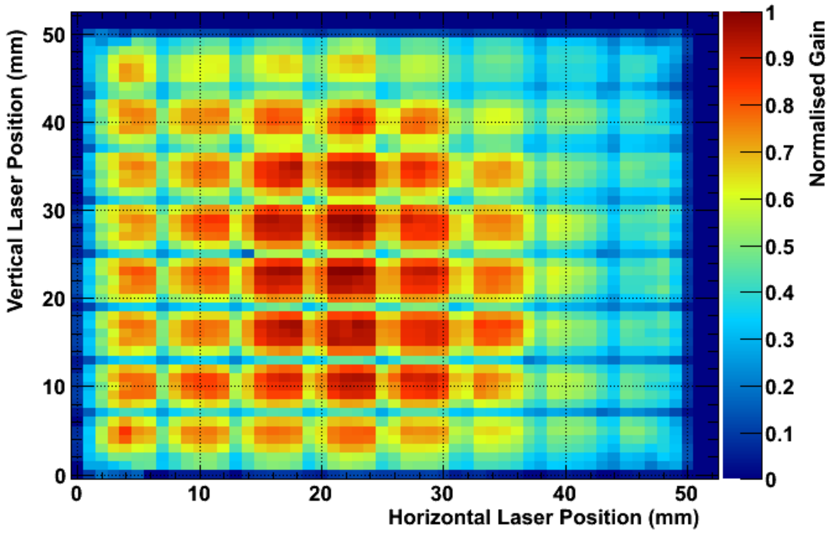

Figure 4.23: Normalised global signal gain map obtained in response to a 1 mm step, 20 photoelectron level, scan across the entire area of an H8500 MAPMT.

with step sizes of 0.5 mm, were performed at the single PE light level. The selected pixels corresponded to those with the highest and lowest single PE efficiency values, as extracted from Fig. 4.16 (a). Figs. 4.24 (a) and (b) give their single channel signal efficiency maps respectively. The result for the higher efficiency pixel (Fig. 4.24 (a)) displays a very uniform response across

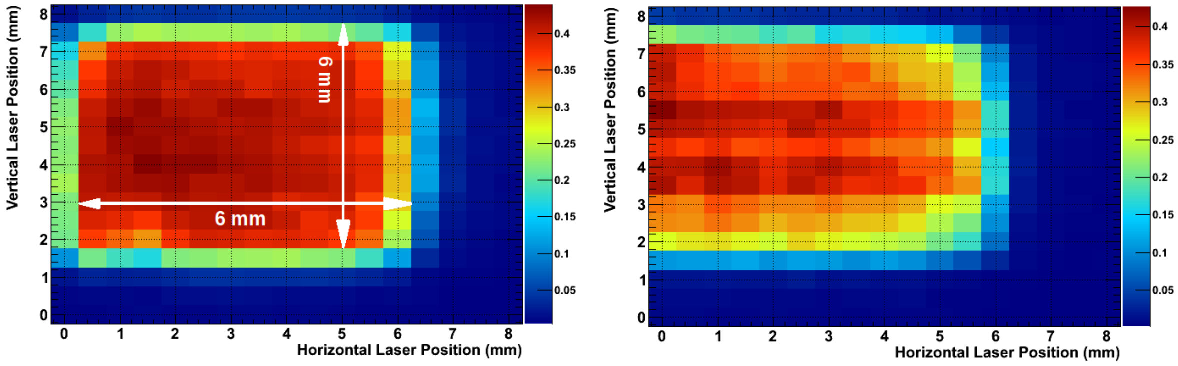

(a) (b)

Figure 4.24: Un-normalised single photoelectron signal efficiency maps, from 0.5 mm step scans, for the (a) highest and (b) lowest efficiency pixels of a tested H8500 MAPMT. The colour fill indicates the absolute single photoelectron signal efficiencies.

the pixel area and relatively low values of crosstalk are observed when the laser strikes outside the pixel edges. Additionally, the signal drop-off at the edge of the pixel is very sharp. The area subtended by the pixel which shows significantly >10 % absolute signal efficiency agrees well with the expected pixel size, considering the resolution of the scan, and is in agreement with the previously obtained 6 mm × 6 mm spatial resolution results (see Figs. 4.22 (a) and (b)). The signals observed beyond the region indicated by the arrows in Fig. 4.24 (a) represent the crosstalk seen by the pixel as the laser strikes its surrounding area. The single channel efficiency map shown in Fig. 4.24 (b) is comparatively less uniform across its area. The single PE signal efficiency increases across the centre of the pixel and decreases towards the edge by ~ 20 %. Unlike pixel - to - pixel average gain differences, which may be equalised by amplifiers in each channel of the readout electronics, there is no way to overcome such inner-pixel inhomogeneities. However, the magnitude of the non-uniformity in the worst case, as shown here, is not completely limiting for the overall single photon performance of the pixel. Low crosstalk values outside the edges of the pixel and a sharp drop-off in the signal response are again observed with the less efficient pixel, and the pixel dimensions extracted are also as expected.

Angular Uniformity

As previously described (see Section 2.3), the CLAS12 RICH detector will be positioned after the magnetic torus of the spectrometer. This will yield particle tracks which will strike the RICH detector surface with incident angles ranging from ~ 5 ° - 35 °, in the upper limit. An important parameter which must be studied is, therefore, the single photon response and corresponding uniformity as a function of incident photon angle.

The response of the pixel whose single PE signal efficiency map is shown in Fig. 4.24 (a) was further scanned, again with a 0.5 mm step size and at the single PE light level, but for several angles of MAPMT rotation with respect to the axis of the laser beam propagation. Figs. 4.25 (a), (b), (c) and (d) display the resulting un-normalised single channel signal efficiency maps obtained for rotation angles of 0 °, 10 °, 20 ° and 30 ° respectively. The results indicate that the uniformity of the single PE signal efficiency across the pixel area does not depend on the angle of incidence of the incoming light, up to angles of 30°, and as a result fulfills the CLAS12 RICH angular response requirements. In addition to the homogeneity of the pixel response, the crosstalk observed when the incident light strikes the surrounding area is also observed from the rotational tests. Increased cross talk is observed, as expected, at larger rotation values when the laser strikes the neighbouring pixel. The level remains sufficiently low and the effect, although observed up to 3 mm from the pixel edge in the case of 30 ° rotation, appears to drop off in severity with distance from the illuminated pixel area. The source of the crosstalk is optical and is likely caused by the divergence of the incident photons in the entrance window of the MAPMT at large angles of incidence.

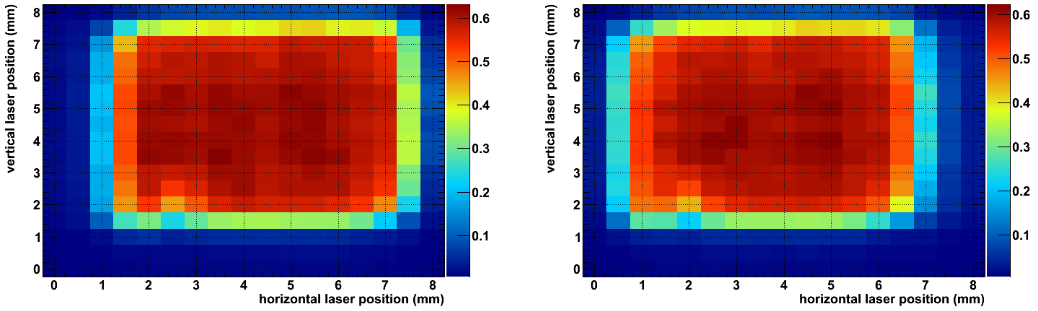

(a) 0° rotation (b) 10° rotation

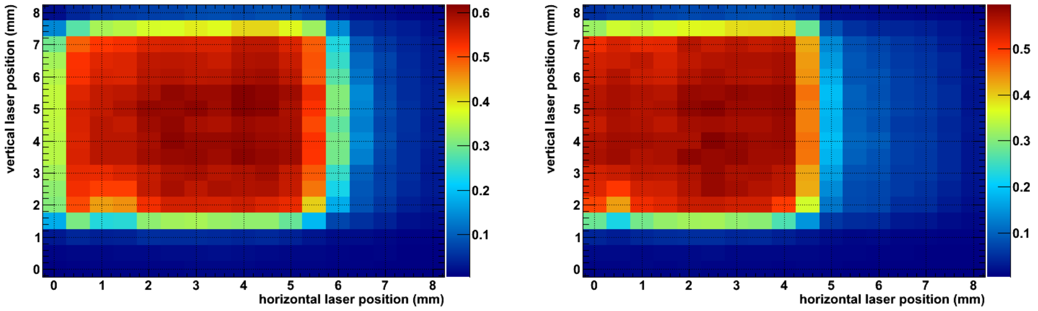

(c) 20° rotation (d) 30° rotation

Figure 4.25: Un-normalised single photoelectron signal efficiency (shown by colour fill) maps obtained for a 0.5 mm step scan of an individual pixel of an H8500, at different rotations of the MAPMT with respect to the laser beam direction.

Crosstalk Observations

Some of the observed crosstalk behaviours have already been briefly introduced, for instance with the 1 mm step scans of the H8500 MAPMT, and further observations are commented on here to give an overview of the observed effects.

The results from both the single and 20 PE level 1 mm step scans (see Fig. 4.19 and Fig. 4.23) indicated that crosstalk was stronger in the horizontal direction, as the laser strikes the deadspace lying between pixels residing on the same row, as opposed to in the vertical direction. This effect is further confirmed by the examples shown in Figs. 4.26 (a) and (b), which give individual pixel responses when the laser strikes the deadspace in-between neighbours, at single and 20 PE levels respectively. The different laser positions are mapped by colour in Fig. 4.26 (c). At the single PE level the charge spectrum when the laser strikes the horizontally neighbouring deadspace almost matches the response when the laser strikes the pixel itself, with a slightly smaller tail to large QDC bins and a lower peak-to-valley ratio. This is not the case however when the laser strikes the deadspace in the vertical direction, where the in-

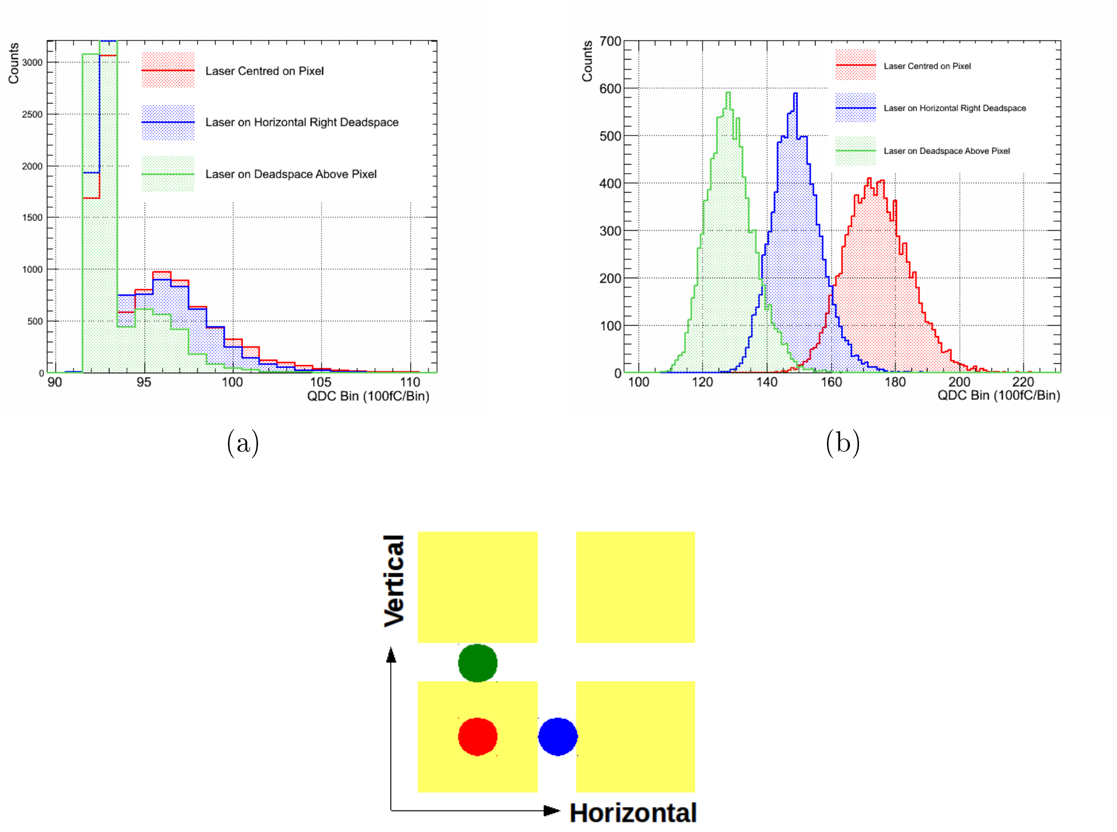

(a) (b)

(c)

Figure 4.26: Typical signals obtained with the Hamamatsu H8500 when the laser is either centered upon a pixel or striking surrounding deadspace at (a) single and (b) 20 photoelectron light levels. (c) Diagram illustrating the laser positioning for the compared charge spectra.

tegrated charge is significantly lower than the true pixel response. A similar observation is obtained from the 20 PE level results, however in this case the relative difference between the spectra is stronger. The changing resolution of the different peaks also agrees with the lower signal strengths when the laser strikes the surrounding deadspace.

From pixel-to-pixel pitched scans of the H8500 MAPMT at both the single and multi-PE levels it is concluded that crosstalk in the MAPMT is strongest in side-sharing neighbours to the illuminated pixel. Examples of this are given in Figs. 4.27 (a) and (b), which show individual channel response maps extracted at single and 20 PE levels respectively. The maps show the normalised signal efficiency values obtained at each of the 64 positions of the laser scan, for the same single channel only. The locations marked by the red colour fill, and therefore having the strongest signal efficiency, identify the pixel position on the MAPMT face. In the single PE case the crosstalk level is very low (note the restricted colour fill scale, for visualisation) and relative signal efficiencies of $< 3\,\%$ with respect to the true signal strength are extracted when

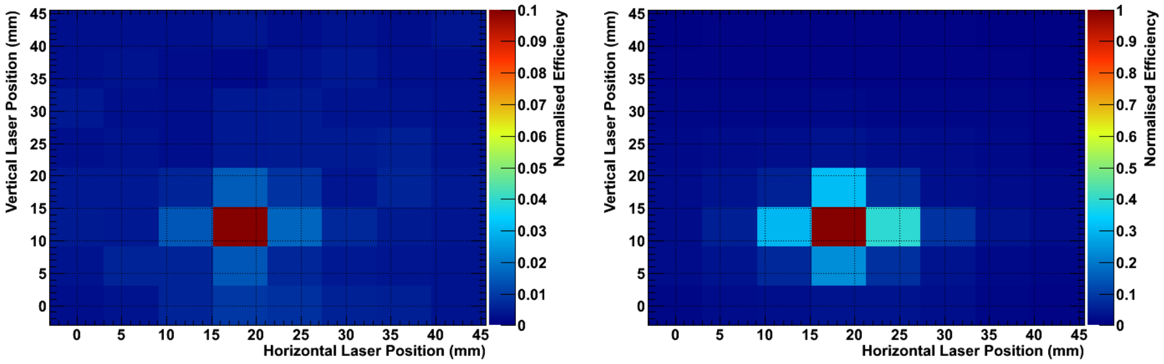

(a) (b)

Figure 4.27: Normalised single channel signal efficiency maps obtained from pixel - to - pixel pitched scans performed with the H8500 MAPMT at both the (a) single and (b) 20 photoelectron light levels.

the laser strikes the side-sharing neighbours - with values ranging from 1.4 % - 1.7 % obtained. Crosstalk is also observed in the corner sharing pixels and beyond, although the magnitude of the signals is much smaller (< 1 %) and falls off with distance from the pixel location. At the 20 PE level similar crosstalk directional behaviour is observed. The magnitudes of the crosstalk signals are larger in this case, as a result of the higher probabilities for crosstalk mechanisms to occur and the higher fraction of crosstalk signals produced above the pedestal threshold, caused by the larger original signal strengths involved. The crosstalk in side-sharing pixels ranges from 23 % to 39 %, and from 5.7 % to 8.0 % in diagonally neighbouring pixels. Similar behaviour was observed with all channels of the device.

Fig. 4.28 shows the crosstalk magnitudes obtained in side-sharing neighbours to the illuminated pixel during a pixel - to - pixel pitched scan of an H8500 MAPMT [15] at the single PE light level. The values plotted are the ratio of each pixel's crosstalk signal efficiency when the laser is incident upon one of its side-sharing neighbours compared to its own true signal efficiency when the laser strikes the pixel itself. The crosstalk magnitudes in side-sharing neighbours to the illuminated one are <3 %, which is in agreement with the expected values from Hamamatsu (see Table 4.1). The result also implies that, contrary to the false signals arising immediately in the deadspace surrounding pixels, at this level of precision and when the centres of individual pixels are illuminated, there is no directional dependence of the side-sharing neighbour crosstalk values. From the result, it appears that the horizontal-right and -left neighbours demonstrate the largest and smallest magnitudes of crosstalk respectively, however this is most likely caused by a slight horizontal shift in the alignment of the laser beam upon pixel centres,

---

[15] S/N DA0269.

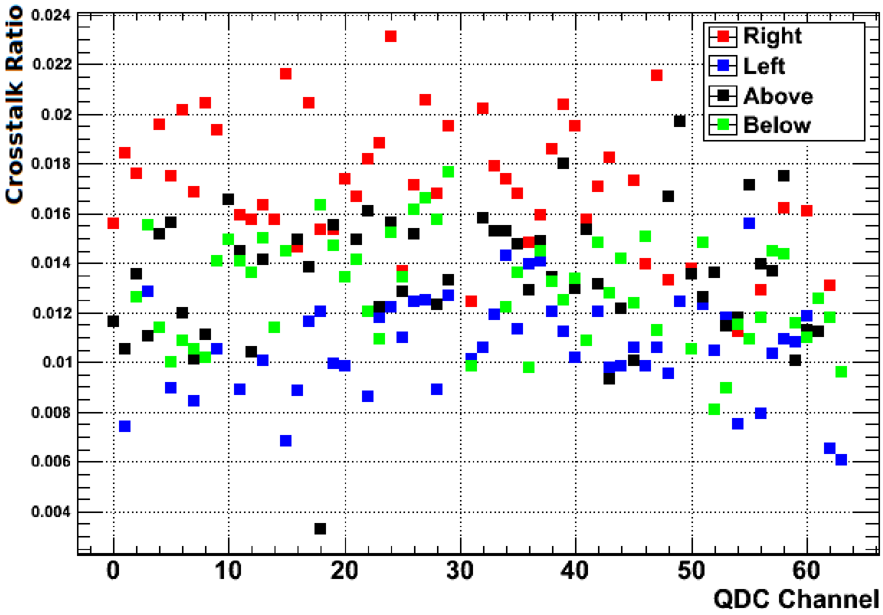

Figure 4.28: Magnitude of crosstalk signals in side-sharing neighbours, obtained from a pixel - to - pixel pitched scan of an H8500 MAPMT at the single photoelectron light level.

which is done by eye and therefore subject to ∼ ±1 mm uncertainty. This systematic error could be minimised through the use of dedicated laser scans to align the laser beam with the centres and edges of the MAPMT pixels within the reference frame of its coordinates.

4.5.2 Hamamatsu H9500 and H7546 Results

The uniformities of the H9500 and H7546 MAPMTs were briefly studied with low resolution laser scans, but to a lesser extent than with the H8500 MAPMT. In general, some of the results obtained with the H8500 MAPMT were also observed with pixel - to - pixel-pitched and 1 mm scans of the H9500 and H7546 MAPMTs. An example is shown in Fig. 4.29 (a), which gives a normalised H9500 single channel signal efficiency map obtained at a single PE light level. The result was obtained with an HV setting of -1 000 V for the MAPMT [16], corresponding to a gain of $\sim 1.86 \times 10^6$ [167]. Analogous to the H8500 centre-pitched scan results (see Figs. 4.27 (a) and (b)), the crosstalk in the H9500 MAPMT is strongest amongst side-sharing pixels. At the single PE level the relative strengths of the crosstalk, compared to when the channels themselves are illuminated, are also comparable with the H8500 MAPMT. Crosstalk is present in the diagonal directions, at a negligible level, and the effect again reduces with distance.

Fig. 4.29 (b) gives an un-normalised global signal efficiency map obtained from a 0.4 mm

---

[16] S/N BA0146.

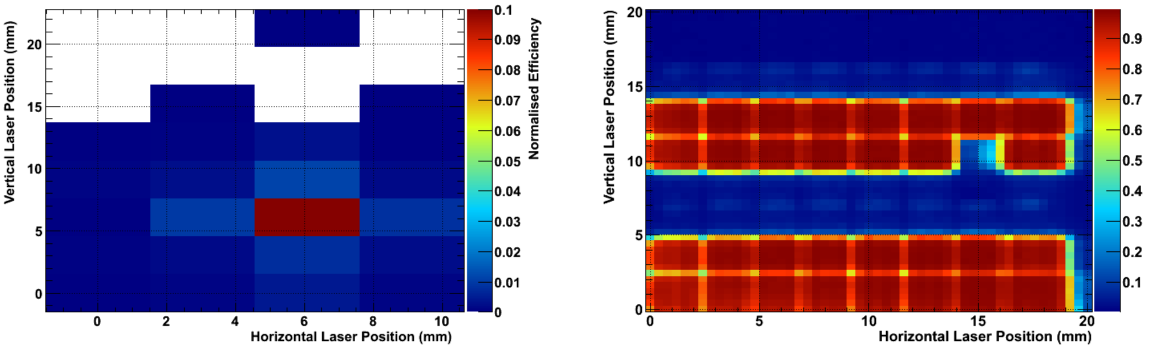

(a) (b)

Figure 4.29: (a) Normalised single channel signal efficiency map obtained from a single photoelectron level pixel-to-pixel pitched scan across an area of the H9500 MAPMT. (b) Un-normalised global signal efficiency (shown by colour fill) map obtained for a subset of 32 channels readout from the H7546 MAPMT, in response to a 1 mm step laser scan performed at a light level corresponding to a few photoelectrons.

laser step scan across the H7546 [17] MAPMT surface. The light level corresponded to roughly a few PE and not the single PE level, which is why the signal efficiencies are so high and the pixel-to-pixel response is so uniform. The map is of interest with regard to the MAPMT response in the deadspace areas separating pixels, where crosstalk is stronger amongst side-sharing pixels than between diagonally-neighbouring ones, again confirming the results obtained from the H8500 scans. For the scan only a subset of 32 channels were readout, with one of these readout channels being faulty, and crosstalk signals with rather large relative signal efficiencies are extracted when the laser strikes the areas of the 4 rows of pixels which were not readout. Since these pixels were not connected to any readout cables at all, it is concluded that this crosstalk originates either within the MAPMT itself or is caused by charge build up at the unconnected anodes.

4.6 High Resolution Laser Scan Studies

The low resolution scan results indicated that higher resolution scans may reveal interesting response features of the devices, in terms of: inner-pixel uniformities, false signals arising in the deadspaces of the active areas; directional crosstalk dependencies; true pixel sizes in terms of their responsive areas and pixel boundaries, and would consequently yield explanations for behaviour observed at the 1 mm beam precision level, in particular for the H8500 MAPMT results, and a greater understanding of MAPMT response and noise mechanisms.

---

[17] S/N ZB4089.

Upon visual inspection of the MAPMTs, the opening face of the metal dynode mesh structures are very clearly visible. In both the H8500 and H9500 MAPMTs this structure is extremely similar and Fig. 4.30 shows a close-up photograph of the H9500 MAPMT surface, where the metal mesh arrangement can be seen in detail. The area subtended by one pixel is highlighted in red, illustrating that each pixel comprises 6 entrance slits to a 12-stage dynode chain which is segmented horizontally along the pixel length. A similar sub-structure is observed for the H8500 MAPMT, although in this case each pixel combines 11 entrance slits due to the larger pixel areas involved. Also highlighted in Fig. 4.30 is what is postulated to be a dynode mesh support structure, which is visible as a pixel-cornering square on the MAPMT face. These structures may also act as focussing electrodes in the device. Structurally the H7546 MAPMT makes for an interesting comparison with the H8500 and H9500 MAPMTs since it possesses a slightly different dynode mesh arrangement, as shown in Fig. 4.31. The entrances to the dynode chains along with the area of material between them are relatively larger, furthermore each pixel only comprises two dynode chain entrance slits. High resolution laser scans with a sub-millimeter precision aimed to study and compare these dynode arrangements and any resulting impact upon the uniformities of the MAPMT responses, and were carried out to evaluate the homogeneity of the candidate imaging planes for the CLAS12 RICH detector.

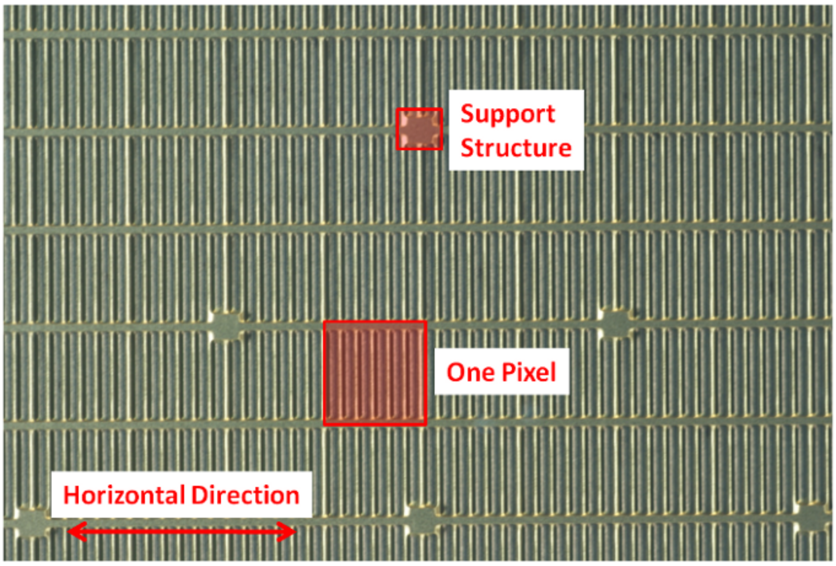

Figure 4.30: Close-up view of the H9500 MAPMT surface showing the opening face of its metal dynode mesh structure. As marked, each pixel comprises six dynode chain openings which are segmented in the horizontal direction across the pixel area. The location of a dynode support structure is also given.

For these high resolution studies, the laser beam was focussed to a diameter of 0.1 mm using the CCD method previously described in Section 4.1.1 and finely stepped laser scans

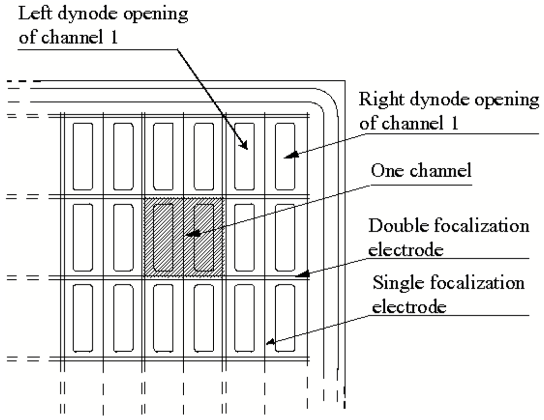

Figure 4.31: Diagram of the H7546 MAPMT metal dynode mesh design, where each pixel comprises two dynode chains. Image taken from [168].

were performed across individual pixels, deadspace areas and dedicated regions of interest of the H8500, H9500 and H7546 MAPMTs and at several light levels. The responses and noise mechanisms at single PE levels were studied since they are crucial for the CLAS12 RICH application, however again multi-PE level scans were also performed. Results from the H8500, H9500 and H7546 MAPMT high resolution scans are presented and discussed in the following sections, where MAPMT responses and crosstalk noise strengths were found to be extremely dependent upon the dynode mesh design of the devices. To investigate these effects further a dedicated study was performed which confirmed the origins of these signal patterns as arising from optical sources, whereby unconverted photons are scattered from the dynode mesh structure before conversion and detection, and the corresponding results are also described below.

4.6.1 Hamamatsu H8500 Results

The Hamamatsu H8500 MAPMT [18] results, including pixel response and observed crosstalk behaviour at single and multi-PE light levels, are given below and followed by an investigation of the crosstalk origins.

Single Photoelectron Light Level

Fig. 4.32 shows the normalised global signal efficiency map obtained from a 0.04 mm step laser scan of a 7.5 mm × 7.5 mm subsection of the H8500 MAPMT including one complete pixel, its surrounding neighbours and deadspace regions. Two dynode mesh support squares are

---

[18] S/N DA0269.

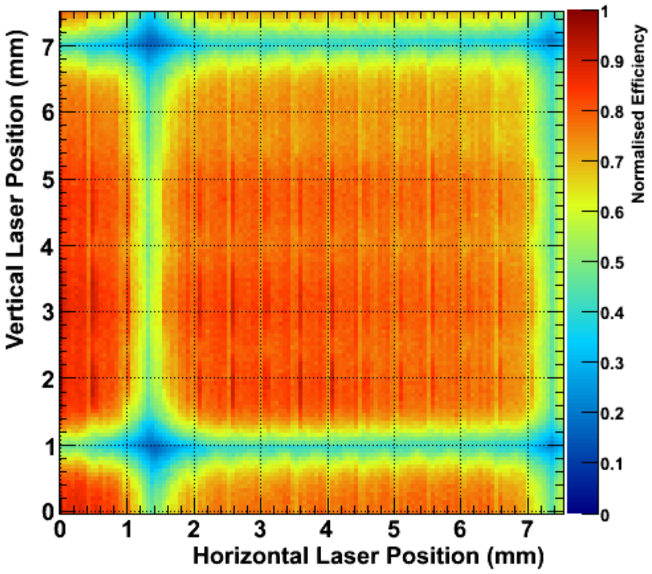

Figure 4.32: H8500 MAPMT normalised global efficiency map obtained from a laser scan of step size 0.04 mm and at a single photoelectron light level.

also present in the scan area, the locations of which are centred at laser positions of roughly $(1.25\,\text{mm}, 0.95\,\text{mm})$ and $(1.25\,\text{mm}, 7.00\,\text{mm})$. Immediately visible in the response map is the fine mesh dynode structure and corresponding horizontal separation of dynode chain entrances in the MAPMT. Such a sub-structure was not visible at the 1 mm beam precision level. The number of dynode chain openings is 11, which agrees with visual inspection of the H8500 MAPMT face. The signal efficiencies are strongest when the laser strikes the dynode chain entrances themselves, and drops in efficiency are observed when the laser strikes constructional walls separating dynode chain openings. Similar surface sensitivities have previously been reported for different MAPMT types, for example the Hamamatsu R5900 MAPMTs, which have a slightly different mesh structure [169]. Additionally, there appears to be some higher efficiency bands separated vertically across the pixel response, the origins of which are currently unknown. It is also interesting to note that the pixel corners are not orthogonal edges as expected, but more rounded in shape. This is likely to arise from charge sharing effects occurring between neighbouring pixels, which arise either during the electron multiplication stage or amongst the readout anodes as the laser strikes the pixel boundaries, and could be studied further by summing the signals extracted from 4 cornering channels. Nonetheless, the boundaries between individual channels and the efficiency drop-offs at their edges are very sharp.

Figs. 4.33 (a) and (b) show horizontal and vertical projections which are taken from central slices of the global signal efficiency map, confirming the presence of the metal mesh dynode structure in the MAPMT response. In the horizontal direction periodic drops in signal effi-

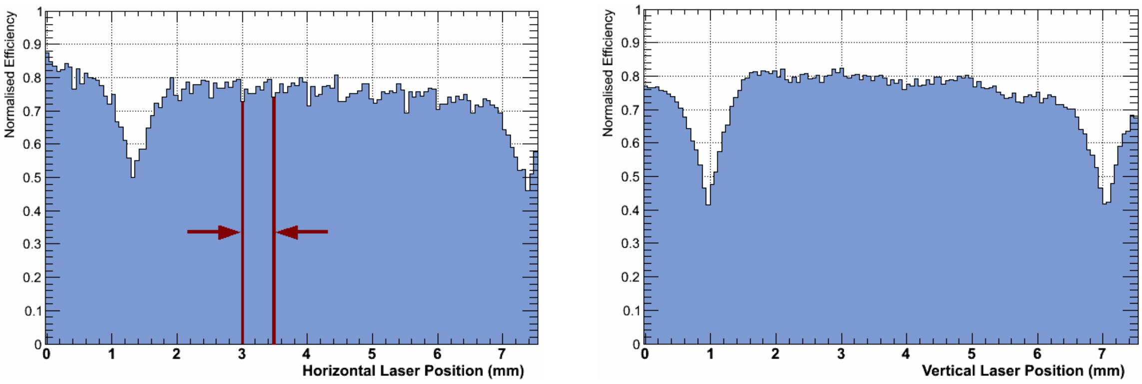

(a) (b)

Figure 4.33: (a) Horizontal and (b) vertical projections extracted from a normalised global signal efficiency map obtained from a single photoelectron level, 0.04 mm step laser scan of the H8500 MAPMT.

ciency are observed, aligning with positions of the inter-dynode chain walls. The labels shown in Fig. 4.33 (a) indicate the distance between two such drops in efficiency, which corresponds to 0.49 - 0.50 mm. The relative signal efficiency drops are on average lower by ∼5 - 10 % when compared with the responses when the laser strikes the entrances to the dynode chains themselves. Such periodic drops are not visible in the vertical projection, although the striped vertical efficiency variation is observed and across the height of the pixel the relative signal efficiency drops by ∼ 10 %. Overall the magnitude of these efficiency drops in the scanned pixel area response are not a significant concern for the CLAS12 RICH application.

The scan also allowed the true active areas of the pixels and the MAPMT response in inactive areas, to be assessed. For instance, in Fig. 4.32 the area of the deadspace in the horizontal direction, defined as the region returning the lowest relative signal efficiency values between two neighbouring pixels, appears smaller than the value of 0.28 mm extracted from the datasheet [162]. The normalised signal efficiency in this region is always greater than zero, with typical relative signal efficiency values of ∼ 50 % obtained. In the vertical direction the dimension of the deadspace area separating pixel rows is closer to the 0.28 mm quoted by Hamamatsu, however again the extracted relative signal efficiency values are always non-zero and are close to ∼ 40 %. In the pixel cornering deadspace regions the signal efficiencies are reduced further, as expected from the previous observations with the low resolution laser scans (see Fig. 4.19, for example), and the relative efficiency values extracted at these locations are on the order of ∼20 % with respect to the highest signal obtained throughout the scan.

To assess individual pixel sizes further, along with pixel edge effects, the normalised single channel signal efficiency map, showing only the response from the pixel which was completely scanned, is shown in Fig. 4.34. In the horizontal direction the dimension of the pixel yielding

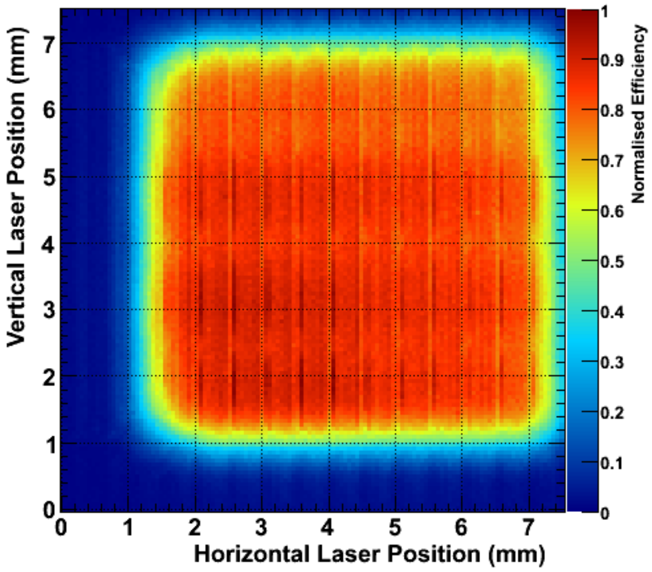

Figure 4.34: Normalised single channel signal efficiency map from an H8500 MAPMT pixel scanned entirely at the single photoelectron light level with a step size of 0.04 mm.

relative signal efficiencies of 60 % or more is (5.94 ± 0.02) mm, whereas in the vertical direction the equivalent dimension is closer to (5.82 ± 0.02) mm. Such results therefore confirm the previously described findings obtained from the low-resolution scans (see Fig. 4.21, for example), whereby false signals obtained in deadspace regions extend further between pixels lying upon the same row, compared to in the orthogonal direction.

The crosstalk observed throughout the laser scans displayed similar sensitivities and for illustration purposes related to subsequent crosstalk patterns which will be shown immediately below, Fig. 4.35 gives the spatial relation of non-illuminated channels from the scanned pixel. The scanned region is shown in red, the non-illuminated pixels are highlighted in green, the

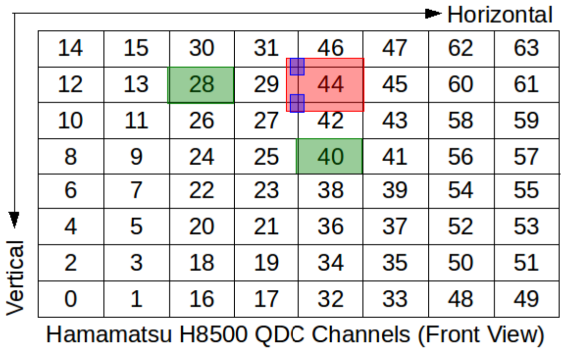

14	15	30	31	46	47	62	63
12	13	28	29	44	45	60	61
10	11	26	27	42	43	58	59
8	9	24	25	40	41	56	57
6	7	22	23	38	39	54	55
4	5	20	21	36	37	52	53
2	3	18	19	34	35	50	51
0	1	16	17	32	33	48	49

Figure 4.35: QDC channel mapping and layout scheme used throughout the H8500 MAPMT high resolution scans (front view, i.e. laser into page).

location of two pixel cornering dynode support structure squares (see Fig. 4.30) are highlighted in blue and the text numbers arbitrarily indicate QDC channel nomenclature used.

Example crosstalk patterns obtained in QDC channels 28 and 40 respectively during the single PE scan of QDC channel 44 are shown in Figs. 4.36 (a) and (b). The horizontal and vertical axes remain the relative laser position throughout the scan, and the colour fill here indicates the normalised signal efficiency in individual MAPMT channels which were not illuminated during the scan. At the locations returning an absence of colour fill, the extracted efficiency was zero. A pattern corresponding to the fine structure of the MAPMT itself is clearly observed in Fig. 4.36 (a), where higher values of crosstalk are obtained when the laser strikes the walls separating dynode chains. Furthermore, the strength of the pattern increases as the laser is scanned in the direction towards the non-illuminated pixel. As observed in Fig. 4.36 (b), the constructional features which separate different rows of pixels, in addition to the pixel-cornering support squares, arise as crosstalk hot-spots. The result also confirms the increase in crosstalk magnitude as the laser is scanned towards the non-illuminated channel, since the edges of the constructional features closest to the non-illuminated channel are the points which display the largest crosstalk signals.

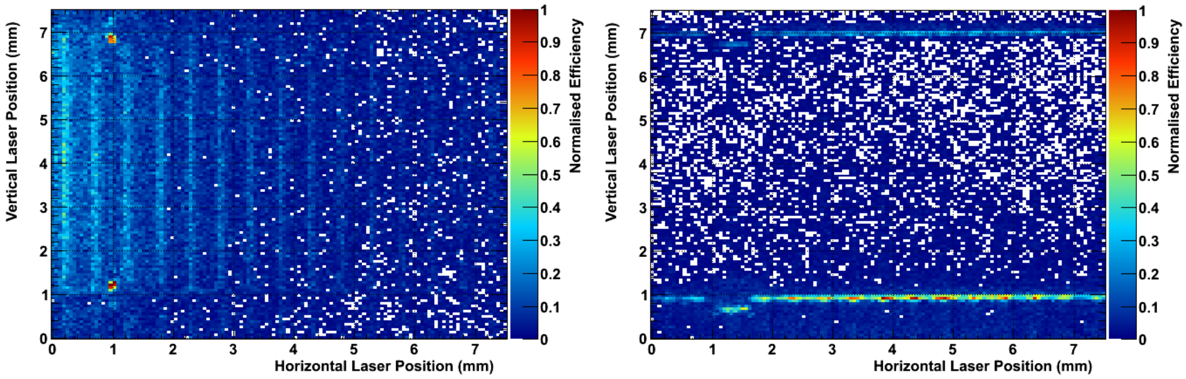

(a) (b)

Figure 4.36: Crosstalk patterns obtained in non-illuminated channels of the H8500 MAPMT during a single photoelectron level scan with a step size of 0.04 mm. The results correspond to QDC mapping channels (a) 28 and (b) 40.

The magnitudes of these crosstalk effects are negligible, and are not problematic for the CLAS12 RICH detector. For instance, in both Figs. 4.36 (a) and (b) the highest absolute signal efficiency values extracted were ∼1 %. This also confirms the extremely low-noise environment of the laser test-bench setup, whereby it is possible to observe these tiny crosstalk effects with clear separation from the baseline noise. It is also important to note that such patterns are not present in all non-illuminated channels at the single PE level, and the magnitude/frequency of such patterns appears to fall off with distance from the scanned area.

To study the dynode 12 signal dependency upon the MAPMT sub-structure and any resulting impact upon its performance, its charge and signal timing were also mapped through high resolution laser scans, and the corresponding normalised dynode 12 single PE signal efficiency map for the scan shown above is given in in Fig. 4.37 (a). The locations of the two dynode mesh support squares, which corner the scanned pixel, are also immediately visible in the dynode 12 response and highlighted by ∼50 % relative drops in efficiency. These squares are not immediately visible in the equivalent MAPMT pixel responses themselves (see Fig. 4.32), due to the significantly lower signal efficiencies in these regions when compared with the pixel responses. In the dynode 12 response, higher relative signal efficiencies are obtained at these locations due to the summing of both nearby pixel responses/false signals and distant crosstalk signals such as that shown in Fig. 4.36 (b). The structural features dividing pixel rows are also visible in Fig. 4.37 (a), again contrary to the scanned pixel response and due to the same inclusion of crosstalk components in the dynode 12 signal. Across the pixel centre the pattern does however mirror the scanned pixel response of Fig. 4.32, with the extraction of lower relative efficiency signals when the laser strikes constructional walls separating dynode chains and higher efficiency signals when the laser strikes the entrances to the dynode chains themselves. A vertical variation pattern matching the one observed in the true pixel response is also obtained. Typical un-normalised absolute values for the calculated signal efficiency of the dynode 12 signals range from ∼40 % to 50 % of the charge signal lying above 95 % of the pedestal distribution, as the laser is scanned across the centre of the pixel. This indicates that the dynode 12 signals, when used with at least a × 200 pre-amplifier, are a feasible option for triggering purposes in the CLAS12 RICH detector to provide background hit rejection. However, one should also

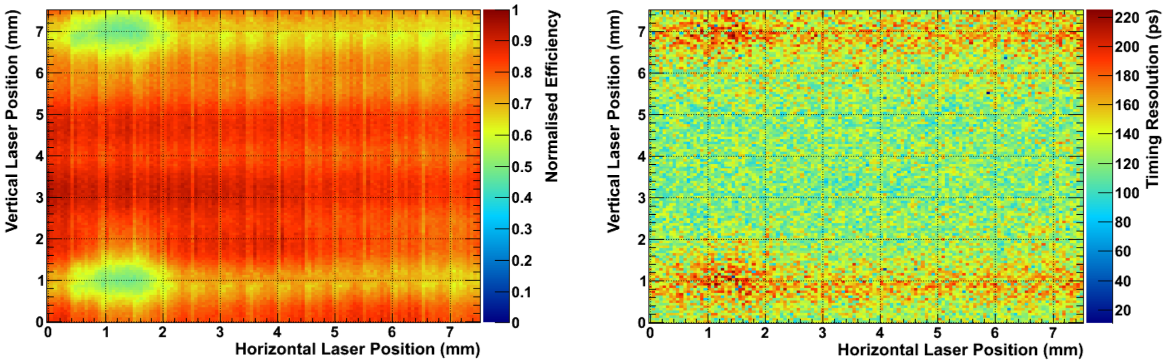

(a) (b)

Figure 4.37: (a) Normalised signal efficiency and (b) un-normalised timing resolution maps obtained from dynode 12 signals during a 0.04 mm step laser scan of an individual H8500 pixel and its surrounding deadspace at a single photoelectron light level.

consider the fact that, at a low level, crosstalk hits will also be included amongst the dynode 12 signals. The matching σ_1 time resolution map is shown in Fig. 4.37 (b), where an average σ_1 value of (106.5 ± 41.9) ps is obtained across a 3 mm × 3 mm central area of the scanned pixel. The row dividing structures and support squares remain visible as areas of degraded timing resolution, which again is attributed to the inclusion of crosstalk. The inter-dynode chain walls and vertical variation pattern are not visible in the timing map at the single PE light level.

Multi-Photoelectron Light Levels

Similar high resolution scans were performed at multi-PE light levels, and the resulting response and crosstalk patterns also appear to be convoluted with the design and construction of the MAPMT. As the light level is increased the magnitude of the crosstalk patterns also increases, however, eventually the segmented response of the scanned area appears to slightly wash out. This is possibly a result of either the MAPMT response becoming non-linear and beginning to saturate, or the increased effectiveness and smaller fluctuations of the focussing electrodes' behaviours in response to the larger incident charges.

For example, the normalised global signal gain map obtained at an ∼8 PE light level, in response to a 0.04 mm step scan of the same area previously scanned at the single PE level, is shown in Fig. 4.38 (a). The response of the pixel maintains its dependence on the dynode mesh structure of the MAPMT and in comparison to the single PE response (see Fig. 4.32) the highest gain area of the pixel appears to concentrate towards its central region. Fig. 4.38 (b) displays the equivalent global signal gain pixel ID map, showing the QDC mapping channel number of the pixel which returned the largest signal gain at each position of the laser scan. The pixel boundaries are extremely sharp, even in the cornering deadspace where lower relative

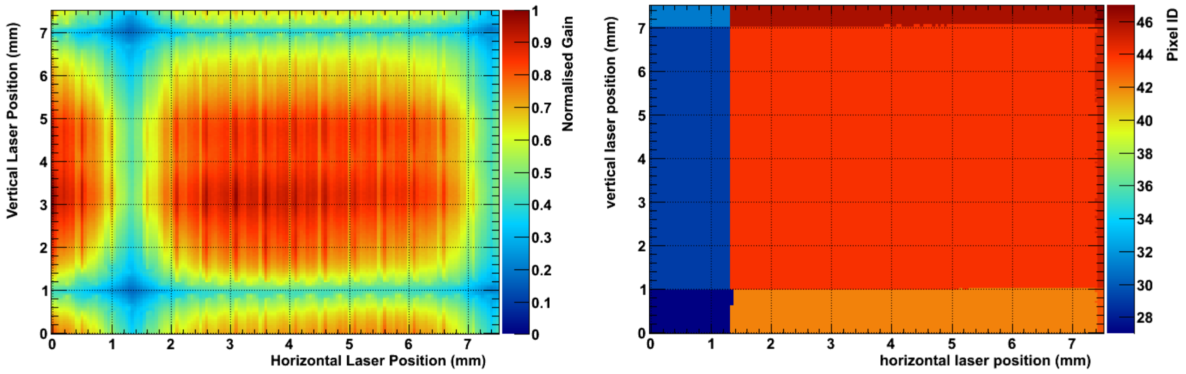

(a) (b)

Figure 4.38: (a) Normalised global signal gain and (b) global signal gain pixel ID maps obtained from an ∼8 photoelectron light level and 0.04 mm step scan of the H8500 MAPMT.

signal gains are obtained and all cornering pixels exhibit false signals. The area is also extremely rectangular, as opposed to the rounded-corner pixel shapes observed for the pixel responses.

Similar dynode-mesh dependent crosstalk patterns were obtained at the ∼8 PE level and two examples are given in Figs. 4.39 (a) and (b). Fig. 4.39 (a) shows the response from QDC channel 29, which is a side-sharing neighbour to the scanned pixel and so a section of its own response is also observed in the scan region. As the laser is moved across QDC channel 44, crosstalk patterns emerge corresponding to the dynode mesh structure and, again, the relative strength of the crosstalk signals increase towards the position of channel 29. Fig. 4.39 (b) shows an example of the crosstalk pattern obtained in QDC channel 40. As observed at the single PE level, the location of the two dynode support squares and the row-separating structures remain clearly visible. The absolute signal efficiencies of the hottest spots in this crosstalk map are now 30 %, which is significantly increased in comparison to the 1 % value obtained at the single PE level. Already such a pattern at the ∼ 8 PE level is present in all non-illuminated channels of the MAPMT, apart from those which lie close enough to the scanned region to yield a pattern similar to that shown in Fig. 4.39 (a). This implies that these constructional points are the most probable areas to result in crosstalk signals at large distances from the scanned area.

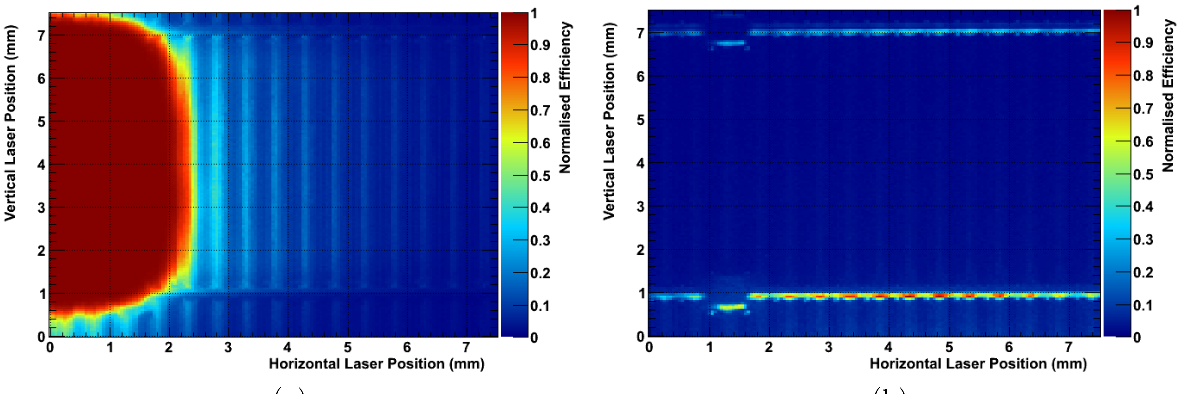

(a) (b)

Figure 4.39: Example crosstalk patterns obtained in non-illuminated H8500 channels from an ∼ 8 photoelectron level scan with a step size of 0.04 mm. The results are from QDC mapping channels (a) 29 and (b) 40.

The matching normalised dynode 12 signal gain and un-normalised σ_1 timing resolution maps obtained for the 8 PE light level setting are shown in Figs. 4.40 (a) and (b). The normalised gain result is extremely similar to the equivalent single PE level result (see Fig. 4.37 (a)), but with an enhanced pattern. The timing resolution map indicates that as the incident photon level is increased, the constructional walls separating dynode chain entrances do influence the

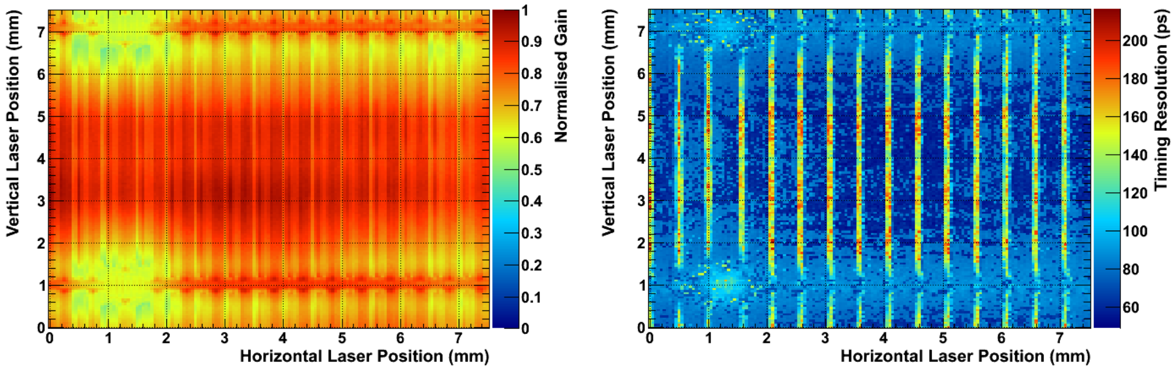

(a)

(b)

Figure 4.40: (a) Normalised gain and (b) un-normalised timing resolution maps obtained from dynode 12 signals during the 0.04 mm step scan of an individual H8500 pixel at a light level corresponding to ∼ 8 detected photoelectrons.

dynode 12 signal timings, contrary to the equivalent single PE result (see Fig. 4.37 (b)), and become visible in the map as strips of degraded timing resolution. It is postulated that this arises as a result of unconverted incident photons reflecting from the dynode mesh structure of the MAPMT and travelling to different positions within the MAPMT before detection, as will be described later. In most cases the timing resolution at these positions is at least twice as worse as when the laser strikes the highest gain regions of the pixel. Since the majority of signals in the CLAS12 RICH detector are expected to be single photons, this is not of great concern for the application.

The light level was increased even further, arbitrarily to a level of ∼260 PE, for a final cross-check of the behaviour, and a different pixel of the H8500 MAPMT was scanned with the same step size. The scanned pixel corresponds to QDC channel 40 of Fig. 4.35 and the resulting normalised signal gain map for the scanned pixel only is shown in Fig. 4.41 (a). It

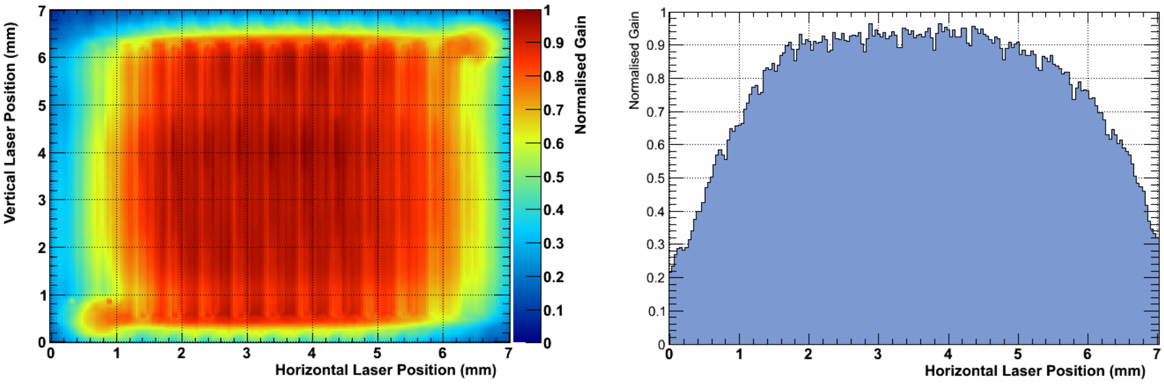

(a)

(b)

Figure 4.41: (a) Normalised scanned pixel signal gain map and (b) corresponding central-horizontal projection obtained with a 0.04 mm step laser scan at a light level corresponding to ∼260 photoelectrons.

appears that at such high PE levels the response segmentation begins to slightly wash out and become marginally more uniform. However upon inspection of Fig. 4.41 (b), which shows a horizontal projection taken across the centre of the pixel response map, the relative signal gain drops at inter-dynode chain walls remain present. This pixel was cornered by two support structure squares, which are also visible in the scanned pixel response, in contradiction with the single and ∼8 PE results. Corresponding crosstalk maps, such as that shown in Fig. 4.42 (a), maintain pattern dependencies on the dynode mesh design. Additional crosstalk components arise when the laser strikes the dynode chain entrances themselves at this light level, which is confirmed on inspection of the crosstalk patterns obtained in side-sharing neighbours, such as that shown in fig. 4.39 (b). Here, when the laser is relatively close to the non-illuminated channel the constructional features of the H8500 MAPMT dynode mesh result in crosstalk hotspots, however as the laser is scanned further away the dynode chain entrances in the scanned pixel yield the largest crosstalk signals. This is likely caused by a position-dependent shift in the most dominant crosstalk mechanism, from optical sources, as is described in the following study, to charge sharing processes.

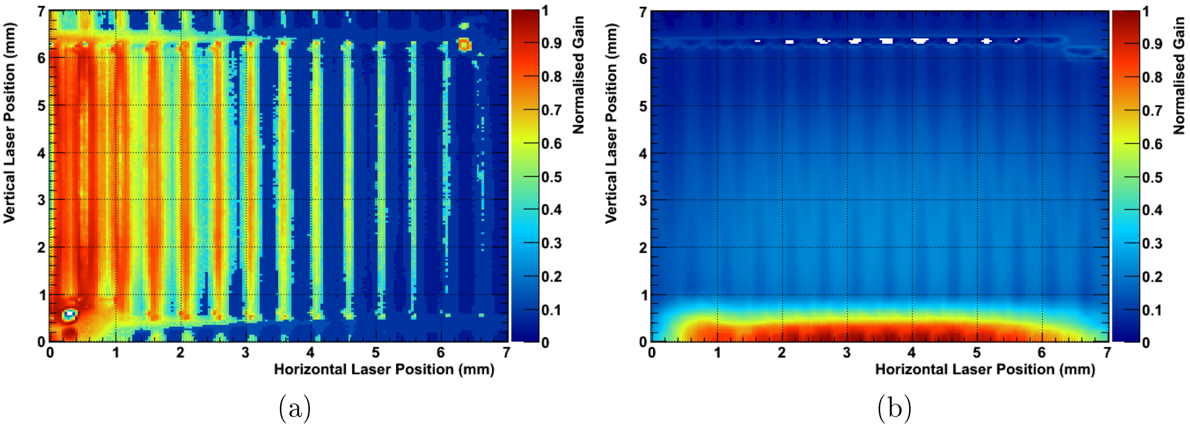

(a) (b)

Figure 4.42: Example crosstalk patterns obtained in non-illuminated channels of the H8500 MAPMT from a ∼260 photoelectron level scan with a step size of 0.04 mm. The results are from QDC mapping channels (a) 24 and (b) 38.

4.6.2 Origins of Crosstalk Patterns

It is postulated that the observed H8500 MAPMT crosstalk patterns and their dependence on the opening face of the dynode mesh arrangement of the MAPMT arise from several steps. First, an incident photon passes through both the entrance window and the photocathode without conversion into a PE. The unconverted photon then reflects, at some angle, from the dynode mesh structure of the MAPMT back towards the photocathode, and upon striking the photocathode the photon is converted to a PE. The possibility of several reflections of the unconverted photon back and forth from the photocathode and dynode mesh may also exist before a final conversion occurs. After conversion the PE is then focussed and accelerated to the first dynode of nearest relevant dynode chain in the normal manner, but at a different location from the incident photon position upon the MAPMT entrance window.

To confirm the validity of this hypothesis a dedicated study was carried out, which involved comparing the crosstalk patterns obtained from high resolution scans performed at two different wavelengths of 407.2 nm and 634.7 nm (a subset of the 634.7 nm results are shown above in Section 4.6.1). Since the QE of the H8500 MAPMT is higher at 407.2 nm than at 634.7 nm (see Fig. 3.5), a larger fraction of incident photons should be converted upon striking the photocathode with a wavelength of 407.2 nm. The proposed result of this is that the crosstalk patterns, which arise when the laser strikes constructional features of the MAPMT, should appear with smaller frequency/magnitude.

Experimental Setup and Method

The laser scan setup scheme, the Hamamatsu H8500 MAPMT used [19], the readout electronics models and the analysis methods remained consistent between the 634.7 nm and 407.2 nm wavelength comparison studies. Despite the same configurations however, the tests performed with the 407.2 nm laser diode used a different test-stand, located at a different laboratory [20], and so due to the different noise environments the pedestal noise distributions were slightly broader. This is shown in the example of Fig. 4.43 (a), where the pedestal RMS - width obtained with the blue laser is a factor of 1.7 larger than with the 634.7 nm laser. Nonetheless, the pedestal widths were consistently narrow enough to resolve single PE spectra and, since the majority of scans were performed at a multi-PE level to benefit from increased levels of crosstalk, this slightly increased noise factor was negligible.

Fig. 4.43 (b) shows an example of one constructional feature of the MAPMT which was subjected to dedicated crosstalk scans with both the 634.7 nm and 407.2 nm wavelength lasers. This area was specifically studied since such constructional features frequently existed as prominent sources of crosstalk patterns throughout the series of high resolution laser scans. In particular, at the multi-PE light levels these structures yielded crosstalk patterns in non-illuminated

---

[19] S/N DA0269.

[20] The 407.2 nm laser facility was provided by the JLab12 group of the Laboratori Nazionali di Frascati (LNF) section of the Instituto Nazionale di Fisica Nucleare (INFN).

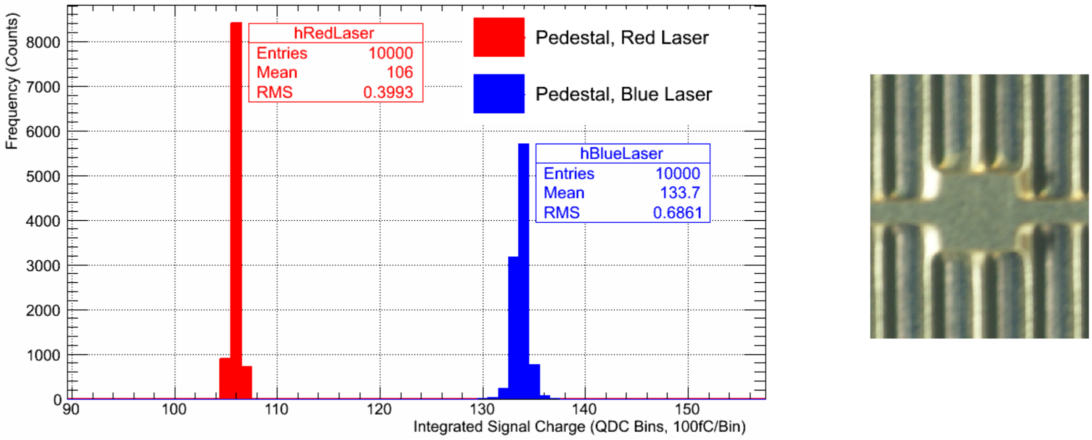

(a) (b)

Figure 4.43: (a) Typical pedestal distributions obtained with the 407.2 nm and 634.7 nm laser setups, for the same example pixel of the same H8500 MAPMT. (b) Close-up of a constructional support structure, and surrounding area of the H8500 MAPMT, which was scanned to study crosstalk patterns arising from the scattering of un-converted photons.

channels across the entire H8500 MAPMT face. A 4 mm × 4 mm area of the H8500 MAPMT, centred around such a support structure, was therefore scanned at both wavelengths and the results compared. The laser beams were focussed to a diameter of 0.09 mm for the scans and the scan step sizes were 0.08 mm. To ensure observation of the crosstalk patterns in as many channels of the H8500 MAPMT as possible and to provide a proof of concept measurement, rather than a single PE measurement tailored specifically for direct projection to the CLAS12 RICH application, the scans were carried out at a multi-photon level corresponding to 25 PE.

Laser Scan Results

Figs. 4.44 (a) and (b) show unnormalised global signal gain maps obtained from the different wavelength laser scans respectively. The response of the area when scanned at 634.7 nm appears significantly more non-uniform, segmented and dependent upon the dynode mesh construction of the MAPMT than the equivalent 407.2 nm laser result. In particular, the locations of the square support structure and the inter-dynode chain walls are clearly visible at 634.7 nm, but not visible at 407.2 nm where the constructional features are smeared out. It is likely that such a constructional support square of the MAPMT also acts as a focussing electrode for the PEs and therefore at 407.2 nm the greater fraction of converted PEs are focussed into the relevant dynode chain, creating a more uniform response. Whereas, at 634.7 nm an increased fraction of unconverted photons scatter from the constructional feature.

Crosstalk patterns obtained from identical pixels during 407.2 nm and 634.7 nm laser scans

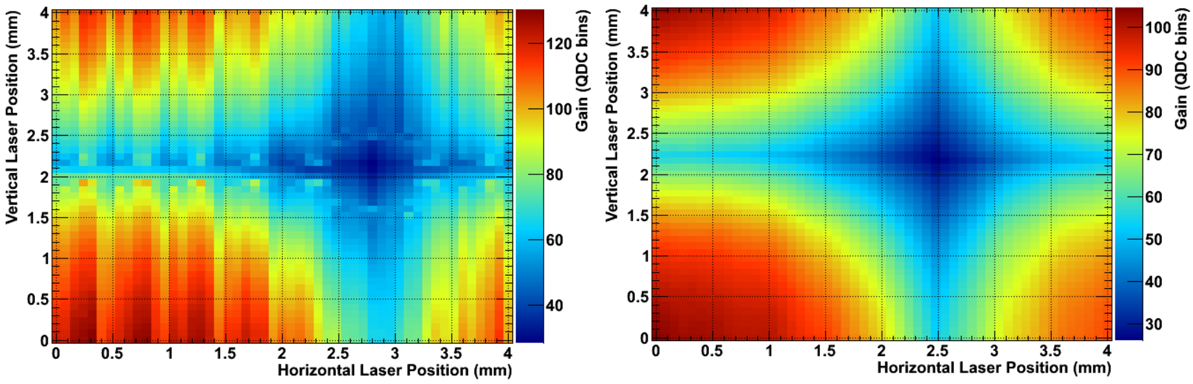

(a) (b)

Figure 4.44: Un-normalised global signal gain maps obtained from an 0.08 mm step scan of a 4 mm × 4 mm area of the H8500 MAPMT, at a light level corresponding to 25 photoelectrons and with wavelengths of (a) 634.7 nm and (b) 407.2 nm.

were directly compared and examples of the results are shown in Figs. 4.45 (a), (b) (c) and (d). The patterns give the un-normalised (i.e. absolute) signal efficiencies obtained in distant non-illuminated channels. The examples confirm that the presence of dynode mesh constructional structures in crosstalk patterns obtained throughout the 634.7 nm laser scans are more pronounced than the equivalent 407.2 nm laser scan results. Additionally, upon comparing the signal efficiency values, the crosstalk strengths are also higher in magnitude at 634.7 nm. Such findings successfully confirm the postulation that the origins of such crosstalk patterns lie in the optical reflection of unconverted photons from the fine dynode mesh face.

The signals and crosstalk arising in deadspace regions, such as that described above for the wavelength comparison study, were also mapped as a function of the dynode 12 signal properties. For the dynode 12 investigations, this was performed at 634.7 nm only. Fig. 4.46 (a) shows the un-normalised dynode 12 single PE signal efficiency map extracted as the laser was scanned in 0.05 mm steps across one of the pixel-cornering dynode support squares and its surrounding region (see Fig. 4.43 (b)). The comparison in Fig. 4.46 (b) gives the un-normalised global signal efficiency obtained from the MAPMT pixels throughout this scan. In general, the response observed from the two maps agree with each other. However, the area of lower signal efficiencies corresponding to the dynode support square location is slightly larger for the dynode 12 signal map than for the global pixel response map. Additionally, the areas of deadspace lying between pixels of the same row show considerably smaller drops in dynode 12 signal efficiency values when compared with the pixel response map, where the boundaries between neighbouring pixels are clearly visible. This again confirms the higher magnitudes of crosstalk present in the MAPMT between neighbouring pixels lying on the same row than between neighbouring pixels

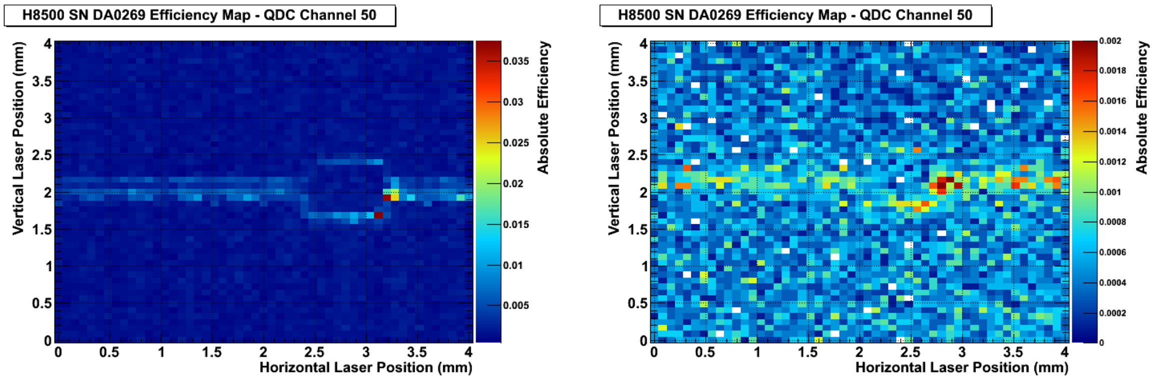

(a) 634.7 nm, QDC Channel 50 (b) 407.2 nm, QDC Channel 50

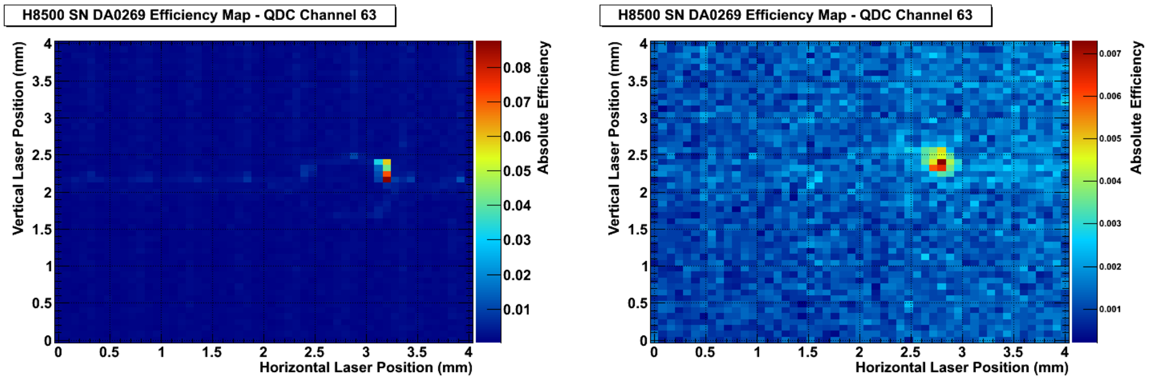

(c) 634.7 nm, QDC Channel 63 (d) 407.2 nm, QDC Channel 63

Figure 4.45: Crosstalk patterns obtained from distant non-illuminated H8500 MAPMT channels during 0.08 mm step laser scans across one square dynode mesh support structure, performed at 634.7 nm and 407.2 nm wavelengths. The light level corresponded to 25 photoelectrons.

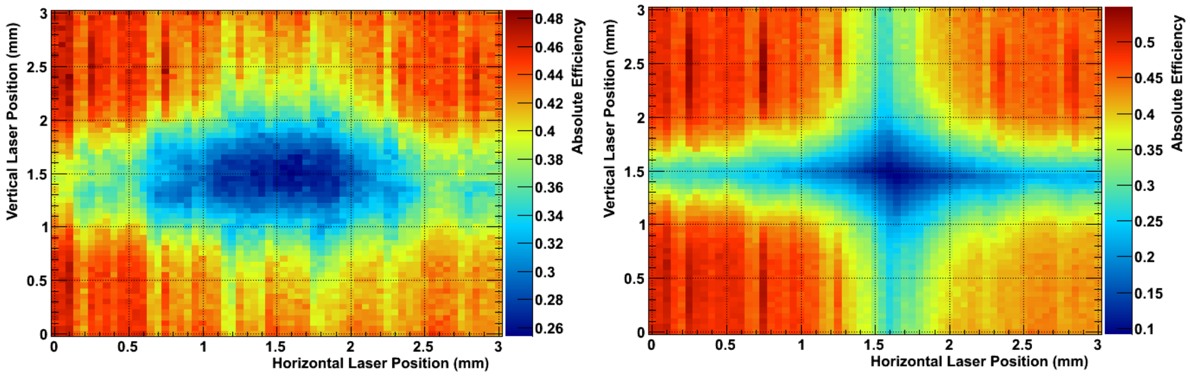

(a) (b)

Figure 4.46: Un-normalised single photoelectron (a) dynode 12 signal efficiencies and (b) global signal efficiency map obtained from the pixels of the H8500 MAPMT during a 0.05 mm step scan of a deadspace region containing one of the square constructional features visible upon the MAPMT face.

which are vertically separated. The corresponding σ_1 timing resolution of the dynode 12 signals obtained throughout the deadspace dedicated scan is shown in Fig. 4.47 (a). The resolution is significantly degraded when the laser strikes the constructional support square structure and the horizontal row separating feature which is adjoined to the constructional square on either side, compared to the areas corresponding to the pixels themselves. Fig. 4.47 (b) shows the matching TDC time stamp map for the measured dynode 12 signals at each position of the laser scan. The result implies that the signals obtained when the laser strikes the square support feature arrive later than signals extracted when the laser strikes the pixels themselves. The time differences between signals arriving from the constructional feature in the centre of the map and active pixel areas themselves roughly correspond to distances on the order of 0.06 m. This result confirms the optical origins of crosstalk signals present in the H8500 MAPMT as arising when unconverted photons reflect from the metal dynode mesh structure, yielding longer path lengths of the photon before conversion and detection. A further confirmation of this measurement could be achieved through recording the timestamp of each crosstalk hit as a function of the hit position from the illuminated point on the MAPMT surface, and furthermore to perform this study for several angles of incidence of the laser light. These measurements would likely require the simultaneous readout of each MAPMT pixel to both a QDC and TDC.

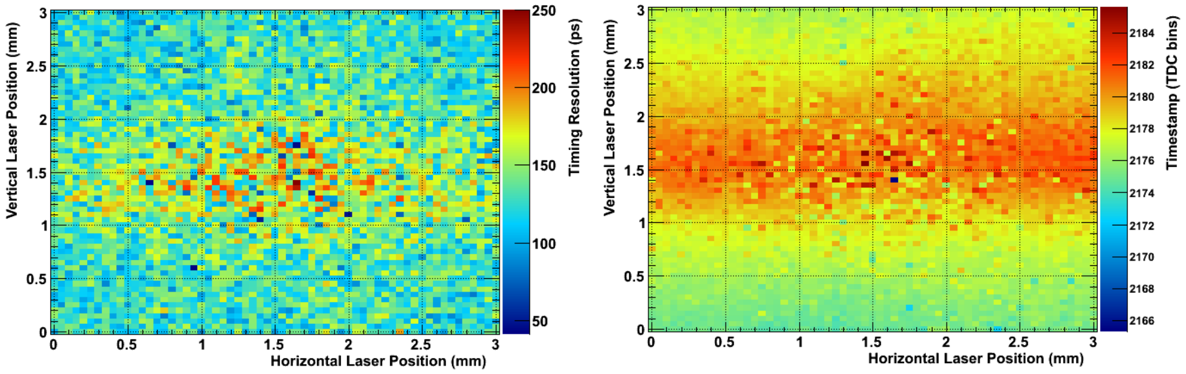

(a) (b)

Figure 4.47: Single photoelectron dynode 12 signal (a) timing resolutions and (b) corresponding TDC signal timestamps obtained during a 0.05 mm step scan across one of the constructional features of the H8500 MAPMT.

4.6.3 Hamamatsu H9500 Results

For confirmation of the H8500 MAPMT response and crosstalk results it was extremely useful to crosscheck the findings with similar scans from an H9500 MAPMT, since it is comprised of a very similar dynode mesh structure. For the H9500 MAPMT measurements the laser beam was once again focussed to a diameter of 0.1 mm, and a subset of example response and crosstalk results obtained at several light levels are described below.

Scanned Pixel Responses

Figs. 4.48 (a) and (b) show the normalised global and scanned single channel signal efficiency maps obtained from a 0.04 mm step laser scan of a 4 mm × 4 mm area of the H9500 MAPMT, at the single PE level. The segmentation of the scanned pixel response at the single PE level is again extremely sensitive to the construction of the MAPMT. There are very sharp peaks in signal efficiency when the laser strikes the entrances to the dynode chains and rather broad drops in efficiency as the laser scans constructional walls of the device. The number of dynode chain openings agrees with the value of six which was extracted from visual inspection of the device (see Fig. 4.30). From Fig. 4.48 (a) the false signals/crosstalk arising in the deadspace between pixels of the same row is relatively high, and significantly larger than the equivalent values obtained in the vertical direction. In the vertical deadspace separating pixels, false signals with relative efficiencies of $\sim$35 % - 45 % are extracted, which is slightly higher than the efficiencies of $\sim$20 % - 30 % extracted in the pixel cornering deadspace regions. In the horizontal deadspace, on the other hand, the signal efficiencies depend on vertical position and relative strengths vary from $\sim$55 % - 70 %. Fig. 4.48 (b) illustrates that in the horizontal direction, the active area for the individual pixel which returns relative efficiencies > 60 % is larger than the expected pixel size of 2.8 mm (see Table 4.1), with a value of $\sim (3.2 \pm 0.02)$ extracted. In the vertical direction, the equivalent value matches well the expected dimension of 2.8 mm.

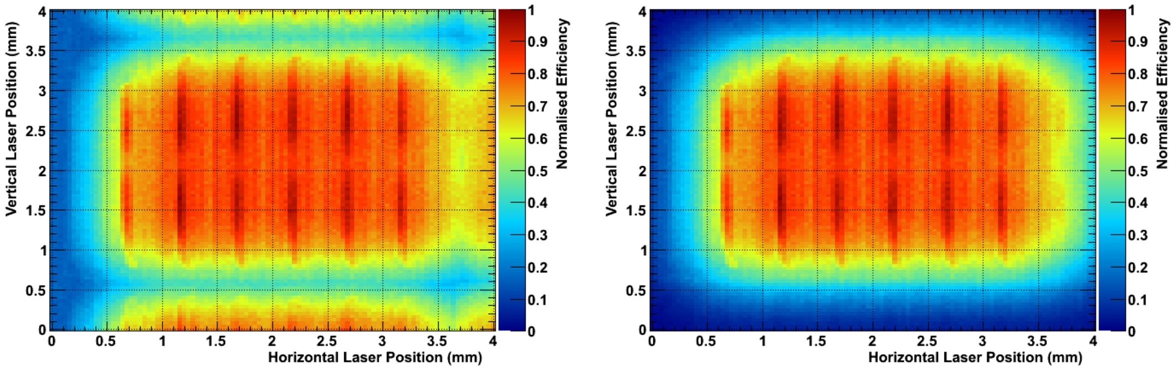

(a) (b)

Figure 4.48: Normalised (a) global and (b) scanned pixel signal efficiency maps obtained from a 0.04 mm step laser scan of the H9500 performed at the single photoelectron level.

Figs. 4.49 (a) and (b) display the horizontal and vertical projections of the normalised global signal efficiency map respectively. The horizontal projection emphasises the peaks in relative signal efficiency when the laser strikes the dynode chain opening slits. In some cases the relative drops in signal efficiency when the laser strikes the constructional features reach values as high

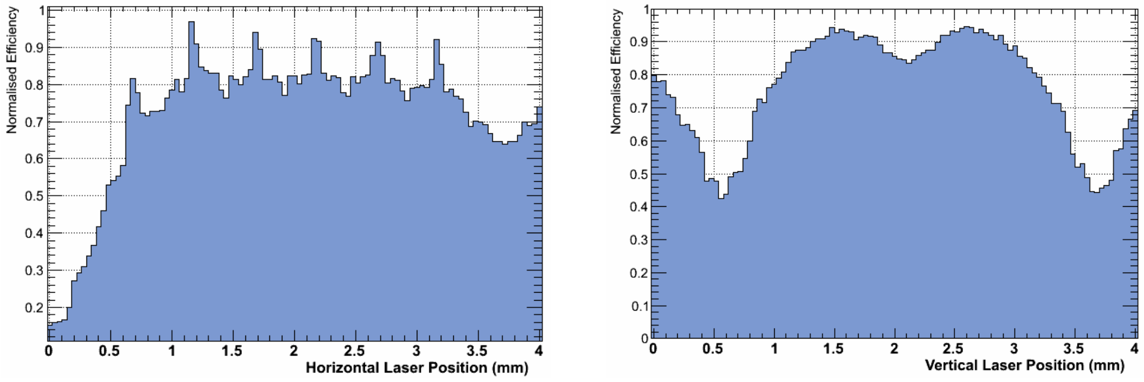

(a) (b)

Figure 4.49: (a) Horizontal and (b) vertical projections of the normalised global signal efficiency map obtained from a 0.04 mm stepped laser scan of the H9500 at the single photoelectron level.

as 15 %, which is a stronger effect than observed with the H8500 MAPMT (see Fig. 4.33 (a)). Furthermore, the vertical projection highlights the existence of a band of ∼10 % lower relative strength signal efficiencies, obtained across the centre of the pixel, and the origins of this are currently unknown. This effect is similar to the H8500 MAPMT vertical pixel uniformity variation observed in Fig. 4.33 (b).

The same pixel was scanned at a higher level of 20 PE, and for further confirmation of the consistency of the observed effects the pixel was additionally scanned with a light level corresponding arbitrarily to 530 PE. The resulting normalised single channel gain plots are shown in Figs. 4.50 (a) and (b) respectively. Immediately visible in the responses is the fact

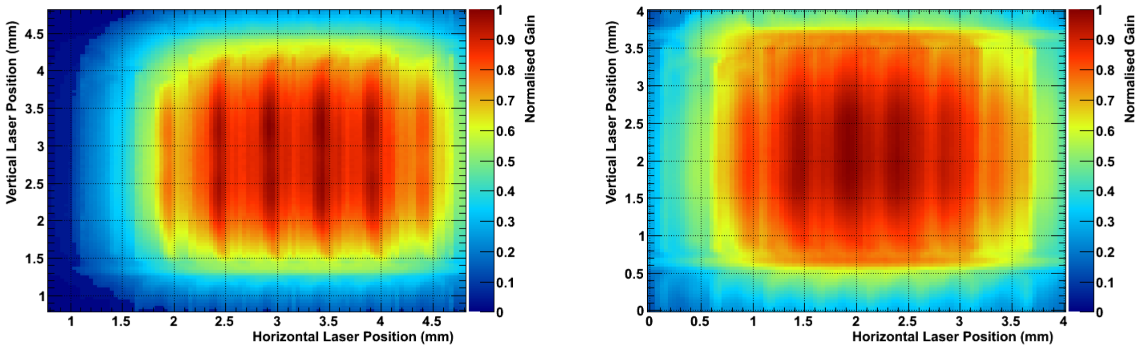

(a) (b)

Figure 4.50: Normalised H9500 MAPMT signal gain maps obtained from 0.04 mm step scans at (a) 20 and (b) 530 photoelectron light levels.

that the vertical variation in the pixel uniformity becomes more homogeneous with increasing PE levels, however the CLAS12 RICH will require the detection of single photons and so may not benefit from this effect at higher light levels. Furthermore, the horizontal segmentation of the responses also starts to wash out, but remains present at all tested light levels.

Crosstalk Patterns in Non-Illuminated Channels

As with the H8500 MAPMT results, the dependence on construction of the H9500 MAPMT was also present in the crosstalk patterns obtained. An example of a typical crosstalk pattern obtained at a single PE level is given in Fig. 4.51 (a), where crosstalk hot-spots, which were common throughout a large sample of the non-illuminated channel crosstalk maps, are visible. Higher relative signal efficiencies are obtained when the laser strikes the pixel-cornering dynode support square included in the scan, in addition to the joints between inter-dynode chain walls and the structures separating pixel rows. Fig. 4.51 (b) gives a crosstalk example obtained throughout the 20 PE level scan. In the example part of pixel's own response may also be observed by the highest efficiency region. Sources of crosstalk which are present in the pattern include the pixel-cornering dynode support square, the dynode chains themselves and the walls separating dynode chain openings. In agreement with the H8500 MAPMT crosstalk behaviour, the strength of these crosstalk signals increases as the laser is scanned towards the non-illuminated channels. The observations from the single and 20 PE levels were further confirmed through the patterns obtained at the 530 PE level, where the effects were much more defined. Examples are given in Figs. 4.52 (a) and (b), which show the crosstalk extracted in side-sharing and distant neighbours respectively.

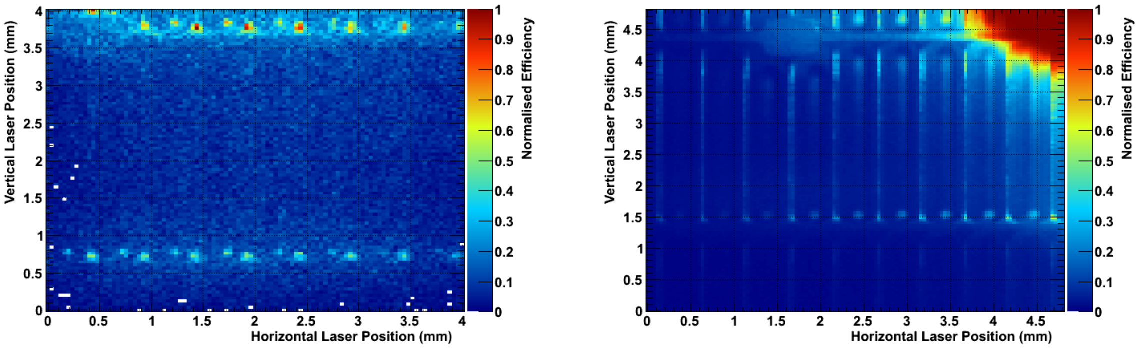

(a) (b)

Figure 4.51: Crosstalk patterns obtained in non-illuminated channels of the H9500 throughout 0.04 mm step scans performed at the (a) single and (b) 20 photoelectron light levels.

At the single PE level, as with the H8500 MAPMT results, the magnitude of the crosstalk patterns are sufficiently negligible for application to the CLAS12 RICH detector. However, the uniformity of the H9500 pixel responses obtained was significantly less homogeneous than for the H8500 MAPMT results, with periodic relative drops in signal efficiencies typically as high

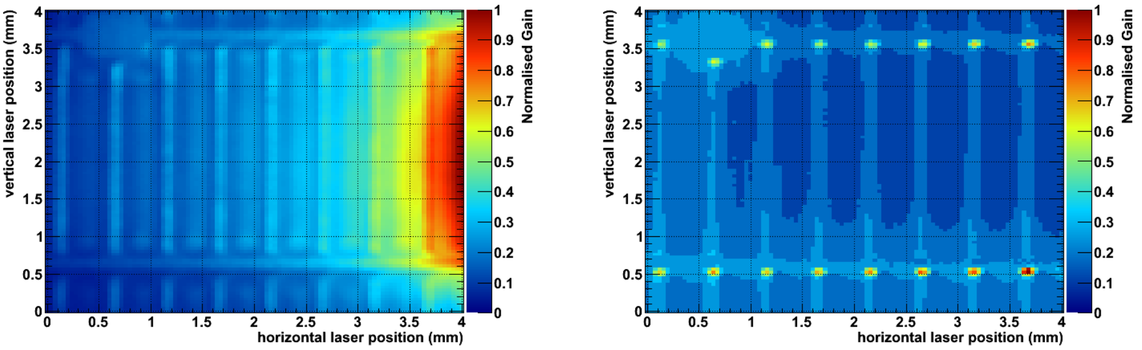

(a) (b)

Figure 4.52: Crosstalk patterns obtained in non-illuminated (a) side-sharing and (b) distant channels of the H9500 at the 530 photoelectron light level.

as ∼15 % caused by the construction of the device. These results indicate that the Hamamatsu H8500 MAPMT is the more attractive candidate for the CLAS12 RICH application. Although the H9500 MAPMT is less favorable in comparison to the H8500 MAPMT, such high resolution scans with the H9500 were extremely useful in confirming the H8500 results and observed behaviours, due to their almost identical dynode mesh designs.

4.6.4 Hamamatsu H7546 Results

Since the fine structure of the H7546 MAPMT is different from the H8500 and H9500 devices (see Fig. 4.31), it was therefore similarly studied through equivalent high resolution laser scans to provide a final cross-check for the uniformity studies of the MAPMTs. The results also revealed and confirmed a signal response and crosstalk dependence on the MAPMT construction, which for the H7546 differs from the H8500 and H9500 MAPMTs.

Fig. 4.53 (a) shows the normalised global signal efficiency map for a 4 mm × 4 mm area of the H7546 MAPMT which was scanned with a single PE light level in steps of 0.04 mm. The corresponding single channel normalised efficiency map for the pixel which was scanned entirely is shown in Fig. 4.53 (b). The immediate pertinent observation from the scan results is the different dynode mesh structure of the H7546 MAPMT compared to the H8500 and H9500 MAPMTs. In a similar fashion, however, the most efficient regions of the response arises when the laser strikes the dynode chain entrances and there exists a slight drop in signal efficiency in the region between these two entrances, where there lies a mechanical support and focussing structure. Similar to the previous results, the deadspace regions in the horizontal and vertical spaces between pixels again appear smaller than the 0.3 mm value quoted on datasheets, and this is caused by signal efficiencies from false signals extracted in these regions which are non-

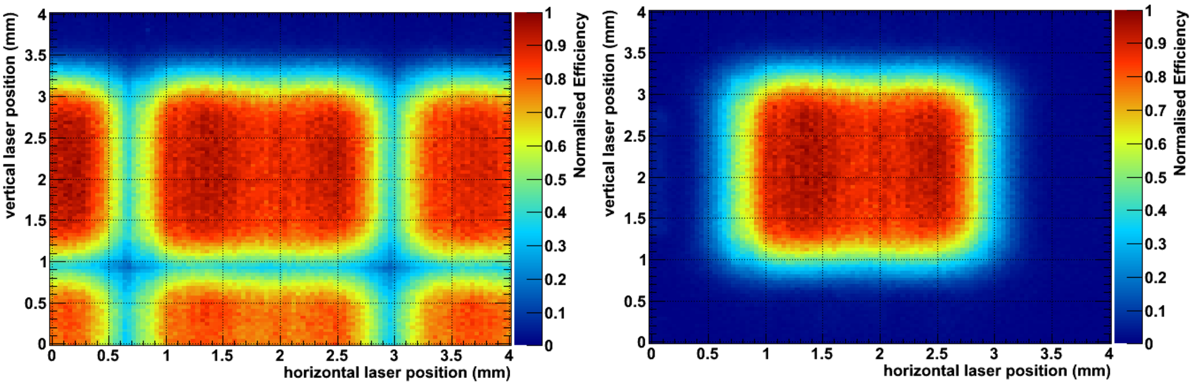

(a) (b)

Figure 4.53: Normalised (a) global and (b) individual scanned pixel signal efficiency maps obtained from a 0.04 mm step laser scan of the H7546 MAPMT performed at a single photoelectron light level.

zero. For example, typical relative signal efficiency values obtained in these regions are between 30 % and 40 % of the highest pixel response, and for the pixel cornering deadspace these values are smaller in magnitude with ~20 % relative efficiency values extracted. From inspection of Fig. 4.53 (b) the pixel area yielding signals with relative signal efficiencies >60 % agrees well with the quoted 2 mm × 2 mm pixel sizes (see Table 4.1, and if the entire responsive area is calculated it corresponds well with the pixel pitch dimensions of 2.3 mm × 2.3 mm. Horizontal and vertical projections taken from central slices of the single PE normalised global efficiency map are shown in Figs. 4.54 (a) and (b). The horizontal projection emphasises the relative drop

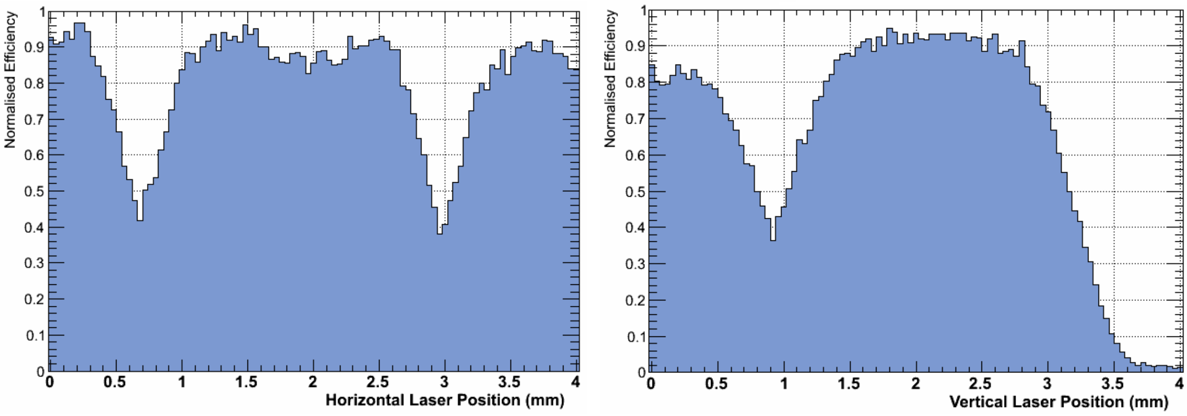

(a) (b)

Figure 4.54: (a) Horizontal and (b) vertical central projections from the normalised global signal efficiency map obtained from a 0.04 mm step laser scan of the H7546 MAPMT at a single photoelectron light level.

in signal efficiency obtained when the laser strikes the structure separating the two dynode chain entrances, an effect which is not present in the very uniform vertical projection. The vertical efficiency variations observed with the H8500 and H9500 MAPMTs, across individual pixel responses, appear to be missing in the H7546 MAPMT vertical projection and overall the homogeneity of the pixel response in both directions would be appropriate for the CLAS12 RICH application.

Fig. 4.55 gives a typical crosstalk pattern obtained at the single PE level. As expected the observed crosstalk patterns highlight constructional features of the MAPMT. This includes the dynode chain slits themselves, visible as the structure arising at a horizontal laser position of 3.6 mm, in addition to the constructional walls and focussing electrodes of the dynode mesh structure. The result slightly varies from the H8500 and H9500 results, where the dynode chains themselves did not induce crosstalk signals until the light level was increased to extremely high PE levels and at the single PE level the dynode mesh construction represented the origins of crosstalk hot-spots. This agrees with visual inspection of the MAPMT surfaces, since the dynode metal mesh structure of the H7546 MAPMT does not appear, to the eye, to be as optically reflective as for the H8500 and H9500 MAPMTs. Similar to the H8500 and H9500 results, and common to all light levels tested, is the fact that the crosstalk strength increases and the pattern becomes more defined as the laser is scanned in the direction of the non-illuminated channel. Furthermore, at the single PE level the crosstalk magnitudes are again extremely low, with the maximum absolute signal efficiency obtained in Fig. 4.55, which represents one of the stronger crosstalk patterns obtained at the single PE level, being ~ 0.7 %.

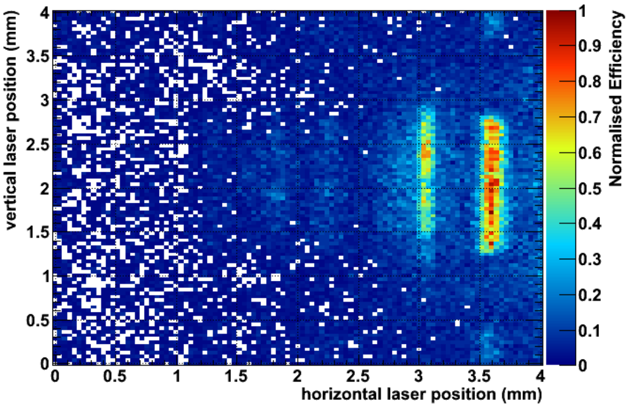

Figure 4.55: Crosstalk pattern observed in a non-illuminated channel of the H7546 MAPMT at the single photoelectron level and in response to a 0.04 mm step laser scan.

The MAPMT signal responses and crosstalk patterns were also mapped at increased light levels, and an example is given below in Figs. 4.56 (a) and (b). Fig. 4.56 (a) gives the normalised single channel signal gain map obtained at a light level corresponding to 20 PE. At 20 PE the active area of the pixel remains consistent with the single PE result, however, the strongest

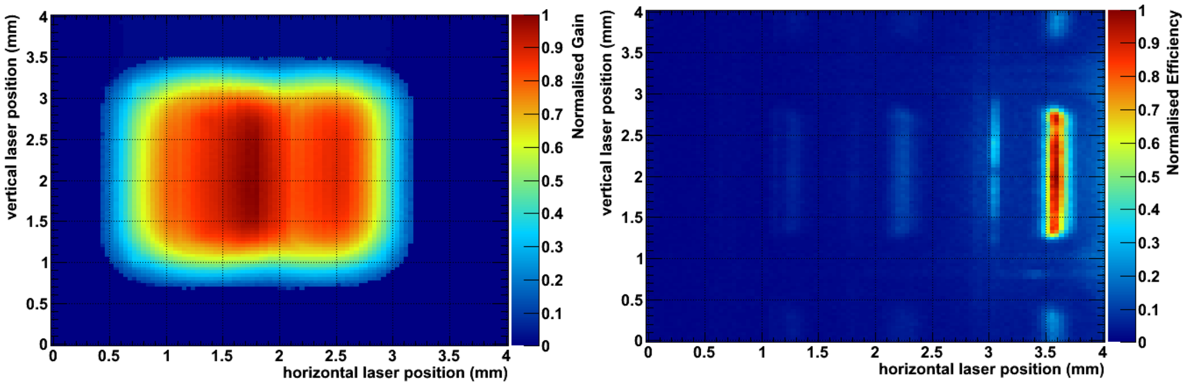

(a) (b)

Figure 4.56: Normalised (a) scanned pixel signal gain map and (b) example crosstalk pattern observed in a non-illuminated channel obtained from 0.04 mm step laser scan of the H7546 MAPMT and performed at a light level corresponding to 20 photoelectrons.

gain region of the pixel begins to move towards its centre, and this effect was further confirmed through an even higher PE level scan. Since the region in the middle of the pixels acts as a focussing electrode, this behaviour at higher PE levels in the H7546 MAPMT is possibly caused by space charge effects, whereby at high currents space charge can influence electron trajectories [92]. This behaviour is not a concern for the CLAS12 RICH detector, as it was not observed at the single PE level, however it would require further study for applications involving multi-photon level signals and high count rates. Features observed in the single PE crosstalk patterns were emphasised at the 20 PE and higher light levels. For instance, Fig. 4.56 (b) gives the equivalent crosstalk pattern to that shown in Fig. 4.55, obtained with the 20 PE light level. The result confirms the observations at the single PE level, with regard to the relative contributions to crosstalk hot-spots in the H7546 MAPMT, and the fact that the largest crosstalk signals are obtained when the laser strikes the positions of the dynode chain entrances.

Overall, the response and crosstalk patterns extracted from the high resolution scans with the H7546 MAPMT were useful for confirming its different dynode mesh construction compared to the H8500 and H9500 MAPMTs and the influence of this upon the detector's behaviour, which at the single PE level was generally more uniform than the H8500 and H9500 devices. In terms of the homogeneity of its imaging plane, this MAPMT would be satisfactory for application to the CLAS12 RICH detector. Crosstalk patterns obtained at the single PE level were also dependent upon the MAPMT design, however the magnitudes are again extremely low-level and the effect drops off significantly with distance from the scanned area.

The increased QE and CE of the selected H7546 MAPMT would be ideal for the low yield application of the CLAS12 RICH detector, but unfortunately the MAPMT suffers from high proportions of deadspace and it does not have a high enough packing fraction for immediate tiling of the devices in the CLAS12 RICH application. It would therefore have to be used in conjunction with either a complicated lens system, such as those used for the COMPASS RICH-1 [54, 85, 86, 87] or HERA-B RICH detectors [88, 140, 141], or be attached to a light catcher. A light catcher could provide a cost-effective solution by providing an imaging plane with larger pixel sizes and minimal dead space to funnel the light and positional information to the H7546 surface. The performance of the H7546 was tested in conjunction with light catcher devices. The prototype light catchers were designed and developed by Contalbrigo *et al* at the Ferrara section of the INFN, and supplied for testing. An individual light catcher consists of 16 channels, where the opening dimensions of each channel are 8 mm×8 mm on the front face and on their lower side correspond to a 2×2 array of H7546 pixels. Photographs of the tested light catchers are shown in Figs. 4.57. Laser scans of the MAPMT when coupled to a light catcher resulted in crosstalk signals arising across the entire MAPMT face and so, to further understand their design, CCD imaging of the light catcher optics were performed. For this: a light catcher was mounted on top of a CCD [21] and flood field irradiated with a mercury lamp. Images were taken for varying angles of incidence between the light source and light catcher. Two example images, corresponding to 0 ° and 30 ° angles, are shown in Figs. 4.58 (a) and (b) respectively. In Fig. 4.58 (a) an example width corresponding to the expected 4 mm of the light catcher channels on the CCD surface is marked by the white arrow above the channel numbered *5*. Visible in the image is the fact that the light catcher channels

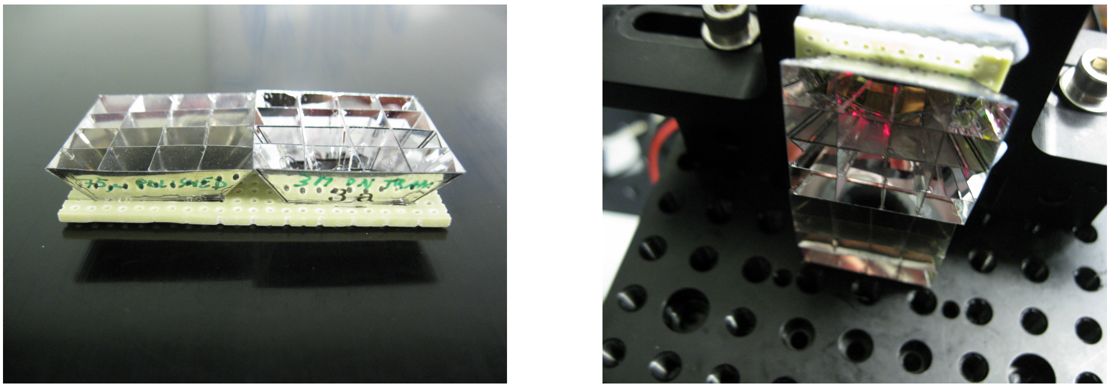

(a) (b)

Figure 4.57: (a) Side views of light catchers tested with the H7546 MAPMT and (b) one of their attachments to the H7546 MAPMT face.

---

[21] Hamamatsu C9260-901 board camera.

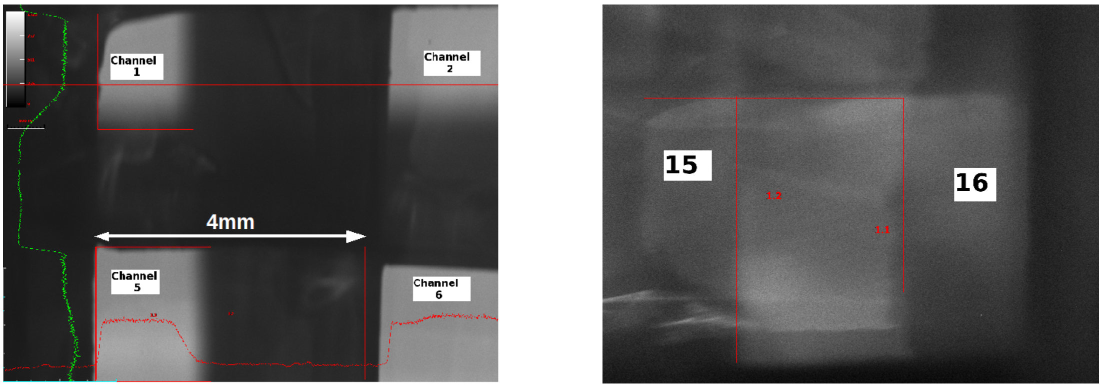

(a) (b)

Figure 4.58: CCD images obtained from different channels of a light catcher which was flood field irradiated with light at incident angles of (a) 0 ° and (b) 30 °.

exhibit shadowing effects caused by the inclinations of its structural walls. With increasing angles of incidence between the light source and the light catcher, as shown in the example of Fig. 4.58 (b), various stray reflection and crosstalk effects come in to play, and it becomes difficult to identify the different channels. The optical separation of 4 individual channels should be visible in Fig. 4.58 (b), however due to stray reflection effects the channel boundaries are smeared. The light catcher results, obtained through both laser-scan and CCD imaging techniques, indicate that significant further investigation would be required to understand and optimise the optics of such devices.

4.7 Discussion and Selected Candidate Photon Detector

An extremely stable laser test-stand has been developed and commissioned, allowing for the in-depth study of candidate MAPMTs for the CLAS12 RICH application. The Hamamatsu H8500, H9500 and H7546 MAPMTs were studied through a variety of low and high resolution laser scans, with an emphasis placed upon the H8500 MAPMT due to its early proposal as the most appropriate technology for the CLAS12 RICH. All MAPMTs were found to be sensitive to single photons, exhibited low levels of crosstalk at the single PE level and provided spatial resolutions conforming with the $< 1\,\text{cm} \times 1\,\text{cm}$ required for the CLAS12 RICH, however, each MAPMT also has its own advantages and disadvantages as discussed below.

The low resolution laser scan results obtained with the H8500 MAPMT demonstrate sufficient performance for the CLAS12 RICH application. In the worst case a uniformity ratio of $1.00 : 3.49$ was obtained between the lowest and highest efficiency pixels of an H8500 device. The spatial resolution of the device was measured to be in accordance with the values quoted by Hamamatsu, and the level of crosstalk present in the device at the single PE level is sufficiently low for single photon counting applications, at $<3\,\%$. The angular response of the H8500 MAPMT was also investigated and the single PE response uniformity within a pixel does not depend on incident photon angles up to the tested value of $30\,^{\circ}$. High resolution laser scans demonstrated that the H8500 pixel responses display a non-uniformity dependent on the construction of the MAPMT metal dynode mesh structure, however this variation does not approach levels high enough to cause concerns for the RICH application. This behaviour was also found to vary with wavelength and at 407.2 nm, towards the region where the highest intensity of Čerenkov radiation is produced, this effect is diminished. The high-precision laser scans also yielded crosstalk patterns which arise from the design of the metal dynode mesh structure of the MAPMT, however, the magnitude of these signals at the single PE level are negligible and not problematic for the CLAS12 RICH. A comparison of crosstalk patterns obtained at 407.2 nm and 634.7 nm confirmed that they are caused by reflections of unconverted photons from the dynode mesh structure back to the photocathode, before conversion and subsequent detection. The response uniformity and crosstalk patterns were further confirmed through high resolution scans of the H9500 and H7546 MAPMTs.

The MAPMTs also offer a common last dynode signal, the signal efficiency and timing of which were studied for the H8500. Through the low resolution scans, the results revealed that the uniformity of the dynode 12 signal strength is directly derived from the gain of each MAPMT channel and the results indicated that if at least a $\times\,200$ amplifier is used, then its single PE signal efficiencies are comparable to those extracted from the pixel responses themselves. An average dynode 12 single PE timing resolution of $\sigma_1 \sim (128.99 \pm 1.76)$ ps was obtained amongst the channels of an H8500 MAPMT. Dynode 12 response maps extracted throughout high resolution scans confirmed the dependence of the H8500 MAPMT single PE response and crosstalk mechanisms upon the MAPMT construction. Furthermore, since the dynode 12 signal also includes crosstalk signals this allowed optical origins of the crosstalk patterns to be further confirmed. Overall, from the results obtained, the dynode 12 signal of the H8500 MAPMT is a promising option to improve the reduction of background hits in the CLAS12 RICH offline through self-triggering mechanisms, however it is important to consider that dark counts will also be included in this signal.

The signal response and crosstalk behaviour observed with the H9500 MAPMT were very similar to those obtained from the H8500 MAPMT, due to their almost identical construction. The H9500 MAPMT displayed a significantly less homogeneous inner-pixel response during high resolution scans performed at the single PE level, compared to both the H8500 and H7546 MAPMTs. Moreover, since the position resolution of the photon detector for the CLAS12 RICH application requires pixel sizes with dimensions $<1\,\mathrm{cm}\times 1\,\mathrm{cm}$, any possible increase in performance resulting from the H9500 pixel sizes is not required and, due to the drastically increased number of electronic channels which would require instrumentation, it no longer exists as a candidate for the CLAS12 RICH detector.

Similar laser scans performed with the H7546 MAPMT confirmed a crosstalk pattern and surface sensitivity dependent on its dynode mesh design. Just as for the H8500 and H9500 MAPMTs the level of these patterns is not a significant concern for the CLAS12 RICH application. The improved CE and increased QE in the visible wavelengths offered by the selected H7546 MAPMT, in comparison to the H8500 and H9500 MAPMTs, is appealing for the single photon counting aspect of the CLAS12 RICH. For its successful use in the CLAS12 RICH the H7546 MAPMT would have to be coupled to a lens or light-catcher device, to minimise both dead-space in the resulting imaging plane, caused by its bulky outer package, and a redundancy in the required number of electronic readout channels, caused by its small pixel sizes. Preliminary light catcher studies indicated that significant further investigation would be required to optimise such an optical system for use across the required wide angular acceptance range of $\sim 5^{\circ}$ - 35°. For this reason, combined with the short time-scale of the project, the H7546 MAPMT also no longer exists as an option for the CLAS12 RICH detector.

In summary, from the collection of MAPMT characterisation tests performed, the Hamamatsu H8500 MAPMT was selected as the candidate for the CLAS12 RICH detector. The laser tests proved to be extremely valuable for understanding the intrinsic performance of the device. However, they were not enough alone to confirm the H8500 MAPMT as the optimal detector on the market today for application to the CLAS12 RICH, and consequently further testing of the device response to true Čerenkov photons was required. One important aspect which required further testing was the single photon detection efficiency of the device and whether it can provide the detection of a sufficient yield per Čerenkov event to obtain the required Čerenkov angle resolution for the CLAS12 RICH detector. This was especially important because MAPMTs are not the superior single photon detectors on the market, and correspondingly an average single PE signal loss fraction of $\sim 20\,\%$ [22] was obtained for the H8500 MAPMT throughout the laser tests. It was also important to determine whether the low-noise performance of the MAPMT is maintained in more realistic environments, which are

---

[22] The 20 % value was obtained at an HV setting of - 1 000 V for the H8500 MAPMT.

closer to the final configuration of the CLAS12 RICH detector. The H8500 MAPMT was therefore subject to further tests in response to Čerenkov light and in different prototype setups, to confirm its selection for installation into the first sector of the CLAS12 RICH, and these studies will be described in the following Chapter.

Chapter 5

MAPMT Studies within Prototype Čerenkov Detectors

The laser characterisation tests described in the previous Chapter were successful in selecting the Hamamatsu H8500 MAPMT as the strongest candidate MAPMT for the CLAS12 RICH application. These characterisation studies were performed in a noise-controlled laboratory, with a very stable experimental setup, allowing the intrinsic detection and noise behaviour of the device to be well understood. Further to these investigations, it was crucial to evaluate the performance of the MAPMT in response to Čerenkov light, under conditions closer to those which will exist in the final CLAS12 detector.

Two prototype detectors were constructed to further evaluate the potential of the H8500 MAPMT to detect Čerenkov light produced by aerogel radiators in the CLAS12 RICH application. Described first is a small-scale prototype constructed with one H8500 MAPMT, which was tested using cosmic rays in a controlled laboratory environment. Secondly, results obtained with a large-scale prototype, which incorporated several H8500 MAPMTs arranged together into a larger photodetection plane, and was subject to experimental studies in a test-beam environment using mixed hadrons, are given. Both prototypes demonstrated that the H8500 MAPMT can be used to successfully detect the required 7 photons per Čerenkov event to achieve π/K separation in the CLAS12 RICH, and in fact a π/K separation of $> 3\sigma$ at 6 GeV was observed through a preliminary analysis of data extracted with the large-scale prototype. As a result of the prototype tests, the choice of the H8500 as the current photon detector for the CLAS12 RICH was confirmed.

5.1 Small-Scale Prototype Studies with Cosmic Muons

The small-scale prototype comprised one H8500 MAPMT as an imaging plane to detect Čerenkov light produced by cosmic muons passing through aerogel radiator material. The setup was arranged as a proximity imaging Čerenkov counter, with no focussing optics. The main aim of these tests was to determine the Number of detected PEs (NPE) by the H8500 MAPMT per Čerenkov event, as a function of aerogel thickness. The results allowed assessment of the capability of the H8500 MAPMT to detect Čerenkov light and whether it meets the demand of 7 detected photons per event in the direct light case of the CLAS12 RICH, in order to achieve a $>3\,\sigma$ π/K separation at 8 GeV/c. The prototype fulfilled this demand, with Čerenkov yields of (10.58 ± 1.06) PE and (15.40 ± 1.54) PE extracted from data, with aerogel radiator thicknesses of 1 cm and 2 cm respectively. Due to increased absorption and scattering effects, the yield from the 2 cm radiator thickness is not exactly double the value obtained with the 1 cm radiator thickness. Further to this, a detailed simulation of the prototype was developed, and comparison of the simulation results with data allowed for successful confirmation of the H8500 MAPMT model descriptions to be made, which may be transferred to and used in the full-scale CLAS12 RICH simulations.

The experimental setup, recorded data-sets, simulation study, analysis and results are described in the sections below. The results obtained from two reconstruction analysis algorithms, named the *template* and the *clustering* algorithms, are compared for validation purposes. The clustering analysis algorithm and corresponding results were developed [170] and obtained by M. Hoek [171], whereas the composition of the template reconstruction algorithm and its matching analysis was performed by the author. The development of the prototype experimental design, setup and the detailed simulation was also carried out by the author.

5.1.1 Experimental Setup

It is assumed that the cosmic rays [20, 30, 41] detected by the RICH prototype were mainly comprised of muons since they are the most numerous charged cosmic particles remaining at sea level. Here, for instance, the background flux from other charged particles such as protons, $\pi^{\pm}$, and electrons, is at most 2% compared to that of muons [41]. The cosmic muons provided a free source of charged particles, with velocities above the required Čerenkov threshold of $\beta_{thr} = 0.952$ for the aerogel refractive index used ($\mathrm{n} = 1.05$).

The cosmic muon prototype was operated in an air-conditioned basement room to minimize temperature-related response variations and to benefit from the five-storey concrete building structure to harden the cosmic muon energy spectrum. The experimental setup, as shown in Fig. 5.1, consisted of two components: the *muon counter* and the *RICH prototype*. The RICH prototype was mounted in the centre of the setup, between two scintillator bars which comprise the muon counter and were used for tracking and triggering purposes. The detector components were mounted using aluminium profile, as visible in Fig. 5.1. Both the muon counter and RICH prototype components are described below.

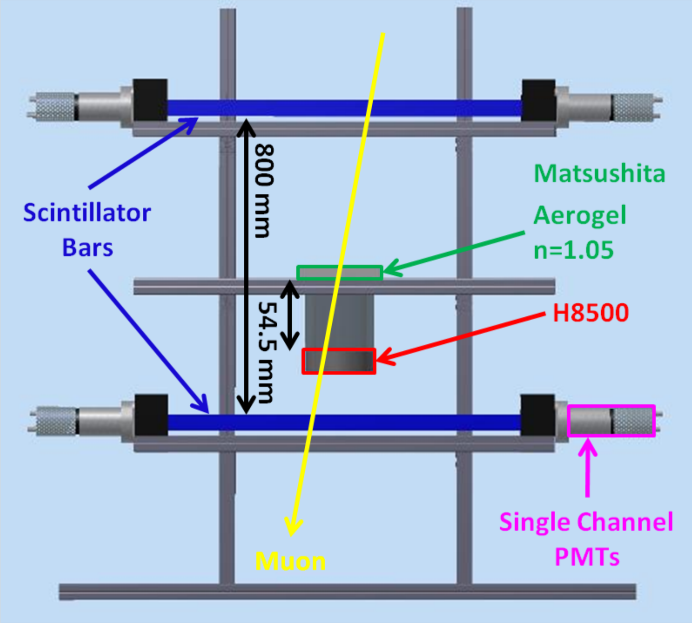

Figure 5.1: Annotated CAD model of the cosmic muon RICH prototype (side view). The RICH prototype is mounted in the centre between two scintillator bars which were used as a muon counter. The CAD model was produced by A. Clarkson.

The Muon Counter

The muon counter comprised two plastic scintillator bars [1], named *top* and *bottom*, with dimensions of 600 mm × 30 mm × 25 mm (length × width × height). Each bar was first wrapped in a white Teflon sheet [2], to improve light yield, and then light-proofed with black Tedlar. Both ends of each bar were readout by single-channel PMTs [3], whose signals were extracted to a QDC [4] and a TDC [5] for both charge and timing analyses. The PMTs were mounted in custom-made POM [6] holders and optically coupled to the scintillator bars using 1 mm thick

---

[1] Eljen EJ-200 plastic scintillator material.
[2] Tetratex®crystal wrap, Donaldson Company Inc, Newton-le-Willows, UK.
[3] Photonis XP2262B PMTs.
[4] CAEN V792 QDCs, with a resolution of 100 fC per bin.
[5] The CAEN V775 TDC, with a resolution of 35 ps per bin.
[6] POM denotes PolyOxyMethylene plastic.

silicone pads. The two bars were separated vertically by a distance of approximately 800 mm. For particles with velocities equivalent to the Čerenkov threshold, this corresponds to a 2.8 ns flight-time.

The muon counter was primarily used for event triggering and to determine the muon track angles. DAQ events were triggered if and only if the muon passed through both the top and bottom scintillator bars. The point of impact of a muon along a scintillator bar was determined by the time difference (Δ_T) between the signals of its two readout PMTs. Combination of impact points on both the top and bottom bars then allowed for the muon track angle to be calculated. The muon counter was initially designed, set-up and studied as a tracking detector by M. Hoek, A. Gordon and G. Smith. Their subsequent investigation of its performance [172] estimated that the spatial resolution along the bar is $\sigma_x \sim 3$ cm, which translates into a muon track angle resolution of $\sigma_\theta \sim 1.8^\circ - 4.0^\circ$ depending on the track angle.

Throughout the runtime of the cosmic muon prototype, the correlation parameters between Δ_T and particle hit position along the scintillator bars were calibrated weekly using a β^- emitting ^{90}Sr source. This process is illustrated in Fig. 5.2. The Δ_T spectrum was recorded,

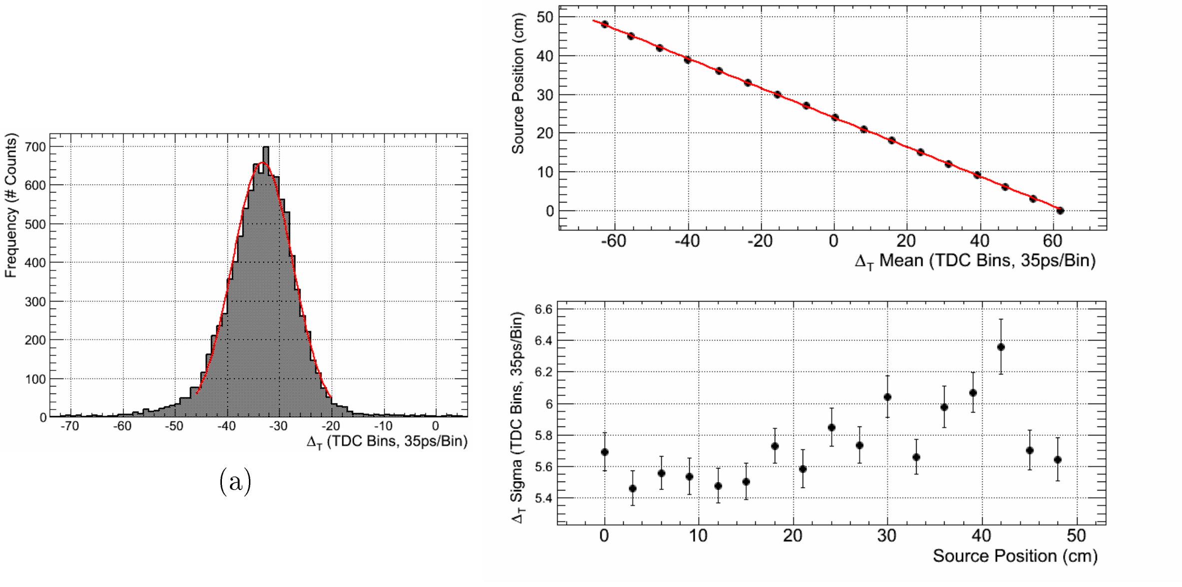

(a)

(b)

Figure 5.2: Examples illustrating the procedure used to calibrate the muon counter are given. (a) A typical time signal difference (Δ_T) spectrum from the dual-ended readout of one scintillator bar, for an arbitrary source position along the bar, with a Gaussian fit applied. (b) Top-panel shows the source position along a scintillator bar against the mean position of the appropriate Δ_T distribution, a linear fit has been applied. Bottom panel shows the sigma width of the corresponding Δ_T distribution for each source position along a bar.

and a Gaussian fit applied, for 17 equidistant positions of the source along a scintillator bar, an example of which is shown in Fig. 5.2 (a). The correlation between source position and mean value from the Gaussian fits was then plotted, and a first order polynomial fit applied. The resulting slope and intercept parameters allowed an offset parameter to be calculated, such that a Δ_T mean value of zero aligned with the centre of the scintillator bar. The corresponding source position and shifted Δ_T mean values were then again re-plotted, as shown in Fig. 5.2 (b) and a linear fit retrieved the correlation parameters which, in addition to the offset value, allowed the conversion of Δ_T to muon impact position in the cosmic-data. Excellent stabilities were obtained for the correlation parameters of both scintillator bars throughout the runtimes, examples of which are shown in Appendix B. The muon counter stability, in terms of PMT signal charges and count rates, was also monitored throughout runtimes of the cosmic muon prototype and found to be extremely consistent. These monitoring measurements were analysed by M. Hoek [173] and examples of the results are shown in Appendix C.

The RICH Prototype

The RICH prototype consisted of one or more aerogel radiator tiles positioned above one Hamamatsu H8500C-03 MAPMT [7], which is a UV-extended glass window type MAPMT. For the aerogel material square Matsushita Electronic Works SP-50 aerogel tiles, with refractive index $n = 1.05$, cross-sectional dimensions of 100 mm × 100 mm and thicknesses of 10 mm were used.

Both the aerogel tiles and the MAPMT were held in-place by custom-designed POM mounts and enclosed in a mu-metal cylinder, as shown in Fig. 5.3. The entire RICH prototype was then light-proofed. The vertical position of the MAPMT could be set and fine-tuned using

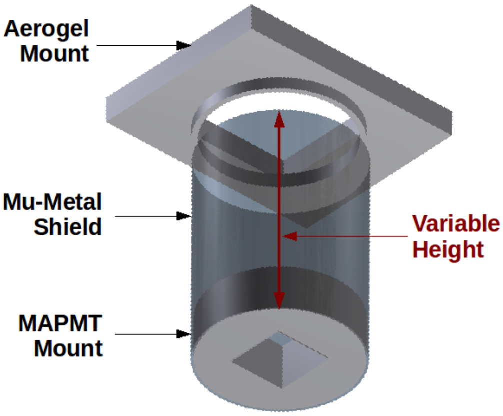

Figure 5.3: Annotated CAD model of the cosmic muon RICH prototype, illustrating the POM mounts for both the aerogel and H8500 MAPMT. The CAD model was produced by A. Clarkson.

---

[7] S/N DA0269.

an attached vernier scale. Between the bottom of the aerogel and the surface of the MAPMT window there was a gap of 54.5 mm, used as an expansion volume for the Čerenkov ring. This gap-length was selected to both contain as much of the Čerenkov rings as possible on the MAPMT face and provide enough separation of the aerogel ring image from the signal caused by the muon passing through the MAPMT window.

MAPMT Calibration

Prior to its installation and use in the RICH prototype, the H8500 MAPMT was fully calibrated in accordance with the methods described in Section 4.5. The HV supplied to the H8500 was maintained at -1 000 V throughout the duration of the calibrations and RICH prototype runs.

Both relative and absolute gain characterisations, performed at laser wavelengths of 634.7 nm and 407.2 nm, were used for calibration of the MAPMT. The relative gain calibration results, performed at a multi - PE light level, were used to equalise the pixel responses, arising from their different gains, in the analysis of cosmic muon data. The pixel - to - pixel pitched laser scan result used for this was shown previously in Fig. 4.15 (a) and was performed with the 634.7 nm laser set to a light level corresponding to 20 PE. Since extraction of the NPE per Čerenkov ring event was the main aim of the cosmic muon prototype study, an absolute gain calibration was essential to correlate measured signal charges with NPE. For this, single PE-level pixel - to - pixel pitched scans of the H8500 were used and the resulting charge spectra were fitted using Equation 4.2 (see Section 4.4). To estimate the systematic effects of the calibration method, the absolute gain calibration was performed using both the 634.7 nm (see Fig. 4.12) and 407.2 nm lasers. The absolute gain values for the highest gain pixel only were extracted from the fit results, since the fitting function is slightly less reliable for lower gain pixels. This then allowed the absolute gains of all remaining 63 pixels to be calculated relative to the highest gain pixel result, using the relative gains obtained from the 20 PE measurement.

The single PE charge spectra obtained from the highest gain pixel with the 634.7 nm and 407.2 nm laser wavelengths are shown in Figs. 5.4 (a) and (b) respectively, where significant differences were observed between absolute gain values extracted. The fit results indicate that the corresponding light level of the 407.2 nm laser scan was slightly higher than for the 634.7 nm scan, with mean values of 1.30 PE and 0.74 PE extracted respectively. This is most likely a result of the technique used to find the single PE spectra, combined with the higher QE of the MAPMT at the wavelength of 407.2 nm. Furthermore, this effect should have no influence upon the fitting of the single PE peak position, since the fit incorporates contributions from

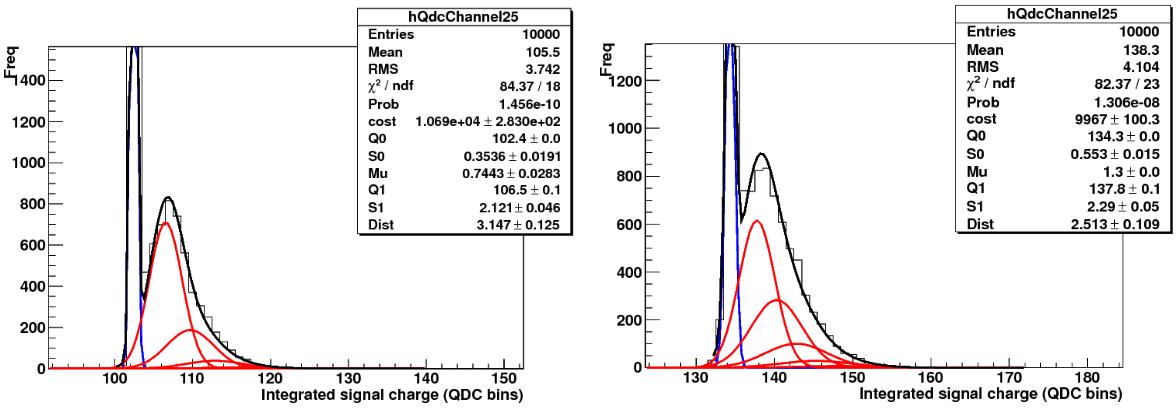

(a) (b)

Figure 5.4: Single photoelectron charge spectra for the highest gain pixel of the H8500 MAPMT which was installed in the cosmic muon RICH prototype. The spectra were obtained with (a) 634.7 nm and (b) 407.2 nm laser wavelengths.

higher level signals. The main difference observed was a mismatch between the single PE gain parameter extracted from the different scans, with the 634.7 nm laser tests returning a larger distance between the pedestal and single PE peak. The pedestal mean positions obtained with both wavelengths are different because the calibrations were performed in completely different laboratories, using different readout boards, cables, DAQ electronics and noise environments. The pedestal is a measurement of the integrated baseline noise present on the signal line, within a pre-defined time which may also have been slightly different in both cases, leading to different mean values. One origin of the difference in the signal gains could be the broader pedestal noise distribution observed with the 407.2 nm laser setup, which is visible as a diminished peak - to - valley ratio in Fig. 5.4 (b). From Figs. 5.4 (a) and (b), pedestal widths of (0.354 ± 0.019) QDC Bins and (0.553 ± 0.015) QDC Bins were obtained at 634.7 nm and 407.2 nm respectively. A broad pedestal distribution may influence the fit to the single PE peak by pulling the mean position towards the noisy peak - to - valley region. The un-avoidable systematic uncertainties arising from the use of two different test-stands is also likely a contributing source to the measured gain difference. The gain results would therefore require further testing and study to attain a full understanding of the systematic uncertainty of this approach in obtaining the absolute gain of the MAPMT. It is therefore also not possible to draw any firm conclusions about the gain dependence of the detector upon the incident photon wavelength. To overcome the gain mismatch, an average gain of 3.78 QDC Bins [100 fC/Bin] was calculated from the two results. This corresponds to a gain factor of 2.36×10^6 for the highest gain pixel of the MAPMT. In the cosmic muon data analysis hit-pixel signal charges were extracted as a QDC Bin separation from the pedestal position. This charge was then converted into NPE through division by each pixels own absolute gain, as calculated relative to the average value of 3.78 QDC Bins. This average absolute gain extraction method results in a systematic error of 10 % for all such PE number conversions within the cosmic muon RICH prototype data analysis.

Trigger and Readout Electronics

A schematic showing the electronics setup for trigger generation from the muon counter hits and readout of the muon counter and RICH prototype is shown in Fig. 5.5. The trigger logic was based on standard NIM modules and the readout used VME units. The specific modules used are given in Appendix. D for the interested reader.

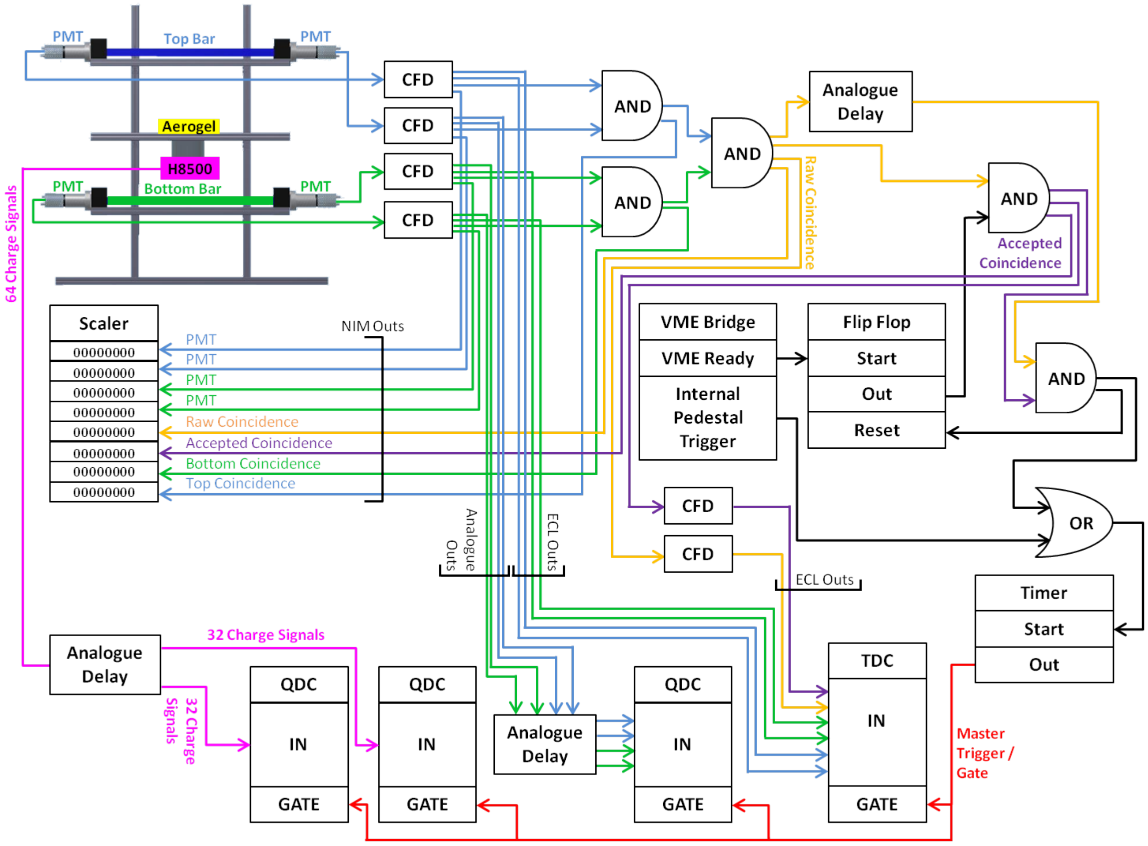

Figure 5.5: Schematic of the electronics setup for trigger generation and the readout of detectors in the cosmic muon RICH prototype.

The concept for the trigger generation was derived as follows. First coincident hits between the two readout PMTs of one scintillator bar were required to determine that an event occurred in that bar. On the next level a coincidence between the two scintillator bars was required, which is termed the *raw coincidence*. The DAQ system provided an inhibit signal, to ensure that data was only readout if the DAQ is in a ready-state, and the final accepted trigger signal was therefore synchronised with the raw coincidence to avoid jitter due to the inhibit logic. The analogue charge signals from the H8500 MAPMT and the muon counter PMTs were delayed passively by ∼140 ns, before being readout by QDCs. The discriminated muon counter PMT signals were readout by TDCs, without delay, for timing analysis. A gate, of length 150 ns, for readout of the QDCs was produced by a timer unit and was also used as a common-stop signal for the TDCs.

The timings of all signals used for generation of the DAQ trigger, along with the alignment of the trigger with the signals extracted to QDCs and TDCs, were first calibrated through the use of an oscilloscope and either a ^{90}Sr source or cosmic events to generate triggers. Throughout all measurements, a scaler was used to monitor the count rates from all four muon counter PMTs, the top and bottom scintillator bar coincidences and the raw and accepted triggers. This was particularly useful in, for example, setting discriminator thresholds and high voltages of the muon counter PMTs to equalise count rates and check for light leaks.

5.1.2 Cosmic Muon Characteristics, Accumulation of Data and Data-Sets

It is known from literature [41] that the overall angular distribution of muons at the ground level is roughly $\propto cos^2\theta$, where θ is the angle of the muon track from the vertical. The track angles of cosmic muons used for triggering events which were accepted for data analysis with the RICH prototype are shown in Fig. 5.6, which gives an overlay of the distributions obtained from three different data-sets. For comparison, and due to the different number of events in each data-set, the distributions have been normalised to unity by their independent areas. All

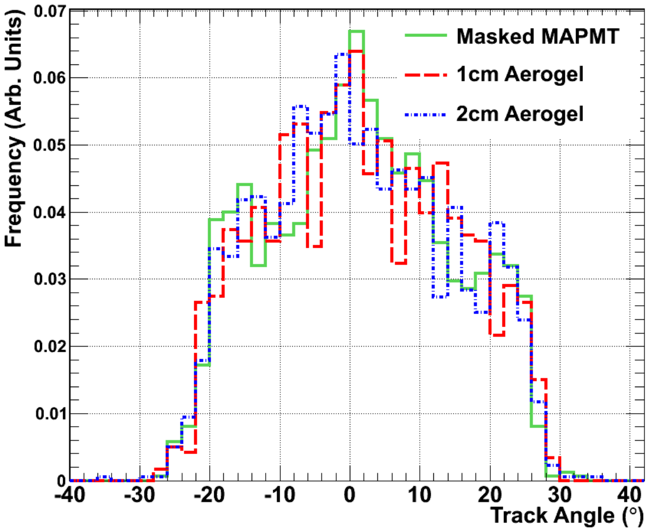

Figure 5.6: Cosmic muon track angles obtained from three experimental configurations of the RICH prototype. All distributions peak at 0° incident angle, implying that the majority of measured tracks are vertical.

distributions peak at 0° incident angle, implying that the majority of measured tracks were almost vertical. This is most likely caused by the fact that the scintillator bars were placed 0.8 m apart and in the analysis stage it was required that the muon must also pass through the MAPMT, resulting in a strict acceptance for the incident track angles.

An example of a relatively clean Čerenkov event obtained from data taken with the RICH prototype is shown in Fig. 5.7. In addition to the Čerenkov light created from the aerogel material, as the cosmic muons traverse the MAPMT glass window Čerenkov light is also produced and detected by the MAPMT. This muon hit in the MAPMT window is visible as the strongest hits in the centre of the event shown in Fig. 5.7, surrounded by the larger image created by the muon traversing the aerogel. The signal generated by the muon passing through the MAPMT is more localised than that produced by the muon passing through the aerogel and in fact in the saturated case of $\beta_{muon} \sim 1$ the radius of the Čerenkov cone produced in the MAPMT glass window is 1.78 mm, leading to Čerenkov rings which are smaller than the size of one H8500 pixel (see Table 4.1). In this way, the strongest signal recorded by the MAPMT may be attributed to the position at which the muon struck the MAPMT. Fig. 5.8 shows the maximum hit positions recorded for each event by the MAPMT, after an accumulation of 135 832 triggers. The distribution clearly shows an image corresponding to the profile of the scintillator bars, with a high efficiency central strip in agreement with the width of the bars and a sharp drop off in frequency beyond this region. To better locate true muon hit positions a fiducial cut has been applied, whereby all edge rows and columns are removed. The reason for this lies in the

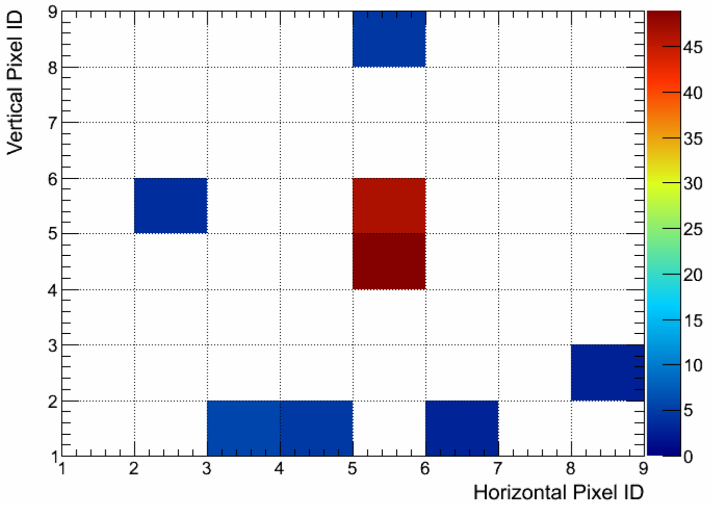

Figure 5.7: A ring image obtained from data with the cosmic muon RICH prototype. The colour-fill gives the signal strength in terms of QDC bins [100 fC/bin]. The Čerenkov light created by the muon passing through the MAPMT window is visible as the strongest hits, in the centre of the ring image obtained from the muon traversing the aerogel radiator.

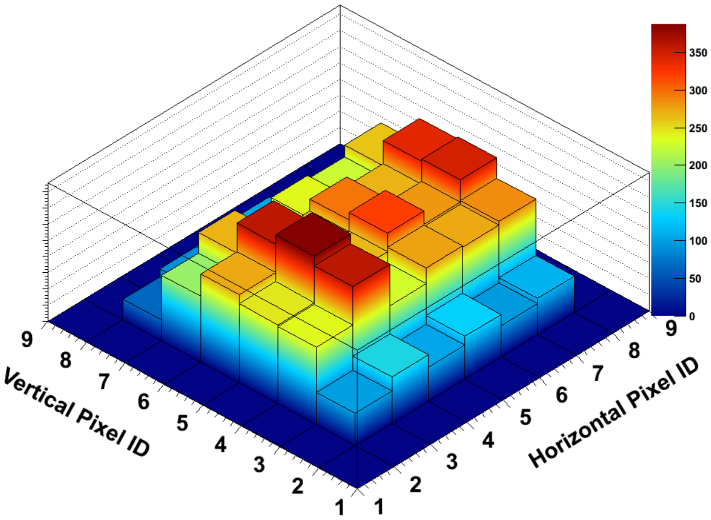

Figure 5.8: Maximum hit distribution upon the MAPMT face of the cosmic muon RICH prototype, revealing an image corresponding to the profile of the scintillator bars of the muon counter. The colour-fill indicates frequency, in arbitrary units.

dimensions of the muon hit in the MAPMT window, which will be further described below. If the maximum hit position corresponds to an edge pixel, it is unclear whether this represents the true muon hit position or the fringe of the muon signal. Such a distribution as that shown in Fig. 5.8 verifies the efficiency of the trigger scintillator bars.

Throughout runtimes with the cosmic muon prototype, data and pedestal runs were taken in alternating order with 3 000 events per data run and 10 000 events per pedestal run. This allowed for monitoring of the stability of the electronics in between data runs and in general over the long data-set runtimes, which spanned several weeks. The average trigger rate for pedestal runs was 2 kHz, whereas during data runs the observed count rates were much lower. This is due to a combination of the $\sim$1 $\mathrm{cm}^{-2}\mathrm{min}^{-1}$ integral intensity of muons with energies $> 1\,\mathrm{GeV/c}$ at sea level [41], the geometry of prototype and the strict trigger requirements whereby the cosmic muon must pass through both the top and bottom scintillator bars. The average cosmic-data trigger rate recorded by the DAQ software was 0.05 Hz. An example cross-check of this is shown in Fig. 5.9, which shows the time between successive triggers for an accumulation of 9 cosmic data runs. An exponential function has been fitted to the distribution, yielding a slope value of (-0.04913 ± 0.00031) Hz, the magnitude of which agrees well with the average DAQ trigger rate.

Three different experimental configurations were studied with the prototype: a basic configuration which used one aerogel tile, an enhanced radiator thickness configuration, and a masked MAPMT configuration where the MAPMT window was covered to block Čerenkov

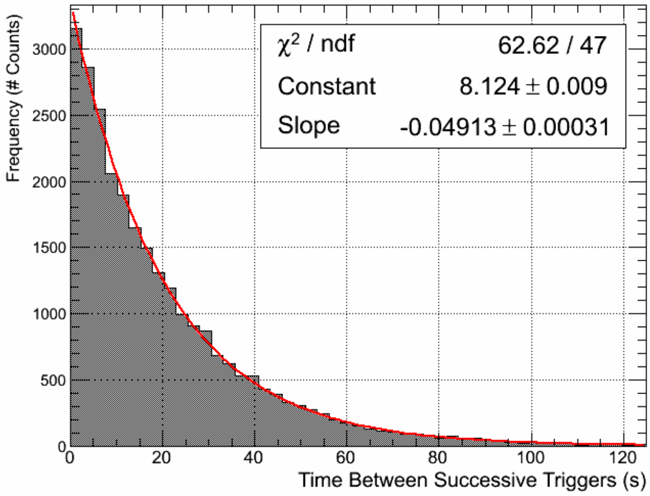

Figure 5.9: Recorded time between successive triggers of the cosmic muon RICH prototype.

light emitted by the aerogel tiles. In the enhanced radiator thickness configuration two aerogel tiles of the same type were stacked on top of each other, with the distance between the bottom aerogel tile and the MAPMT window the same as that used for the single 1 cm aerogel tile configuration. The masked data-set aimed to study background effects caused by the Čerenkov light created by the muon passing through the MAPMT window. A table summarising the details of the lengths of runs and number of raw events extracted for each of the configurations is given in Tab. 5.1. To image as much of the Čerenkov ring events as possible and to minimise the requirement of any scaling parameters, which may introduce additional uncertainties in the yield measurements, only events in which muon hits were recorded in the central 2×2 area of pixels on the MAPMT face were used in the data analysis stages. From the geometry of the prototype setup, this acceptance cut for the position of the muon hit results in the majority of the aerogel Čerenkov rings being imaged. There was therefore no spatial acceptance cut for the aerogel Čerenkov ring hits. Furthermore, if both the cosmic muon hit in the MAPMT window and as many of the aerogel Čerenkov hits as possible are imaged, this aids and was used in the pattern recognition stage. There was no analysis cut on the minimal number of aerogel Čerenkov hits required to perform an event analysis, however one central muon hit was always required. The resulting number of events for this extremely strict analysis cut is also given in

Table 5.1: Data-sets, runtimes and number of events extracted with the cosmic muon RICH prototype.

Data-set	**Runtime**	**Raw Events**	**Central Hits**
1 cm aerogel	5 weeks	135 832	1 205
2 cm aerogel	7 weeks	198 000	1 797
Masked	7 weeks	189 000	1 749

Tab. 5.1. Compared to the number of raw events, the number of accepted events is very low due to the reduced acceptance area of 12.16 mm × 12.16 mm, for central muon hits, compared with the dimensions of the scintillator bars.

A calculation performed by M. Hoek [174] to study the acceptance losses beyond the active area of the MAPMT in the experimental setup yielded values of $\sim 3\,\%$ and $\sim 10\,\%$ with the 1 cm and 2 cm thicknesses of aerogel respectively. This is caused by the increased uncertainty in emission point with the thicker radiator, broadening the Čerenkov ring width. A data-set with 3 cm thickness of aerogel was not taken since the acceptance loss would increase even further, and possibly the Čerenkov signal produced by the muon passing though the MAPMT window would begin to merge with the aerogel Čerenkov ring. The setup is adjustable however for future studies of aerogel tiles with varying optical properties. For example, to obtain data with different refractive indices the distance between the MAPMT and the aerogel would need to be adjusted, but this is easily achievable with the prototype design.

5.1.3 Simulation of the RICH Prototype

A detailed Geant4 (GEometry ANd Tracking) [8] Monte Carlo simulation of the RICH prototype detector was developed to validate the modelling of the H8500 MAPMT and aerogel tiles, through the cross-checking with data results. Geant4 is an object-orientated software toolkit for simulating the passage of particles through matter as described in [175,176,177]. Some of the Geant4 functionalities which were important and incorporated in the cosmic muon prototype simulation include: the generation of the primary particles; the setup of user-defined geometries and materials; the physics modelling of the interactions of particles traversing matter, including electromagnetic and optical interactions; modelling of the Čerenkov effect and the generation of Čerenkov photons; transport and tracking of event particles and photons; the response of sensitive detector elements and corresponding hit collections, and visualisation.

Primary Particles

The Geant4 General Particle Source (GPS) module was used in the prototype simulation to provide the primary particles. The GPS allows the user to define the energy spectrum, the angular distribution and the spatial sampling of the incident particles [177]. Several incident particle source variations and their influence on the Čerenkov ring radii and yield distributions

---

[8] http://geant4.cern.ch/

were cross-checked, to validate the selection of incident particles. Results obtained from incident muons with either normal angles of incidence or angles following a $cos^2\theta$ distribution were modelled and cross-checked. No significant difference was observed, and the normal angle of incidence was chosen due to an increased efficiency and as suggested by the track angle distributions obtained from data, in which the majority of incident cosmic muons were observed to have normal angles of incidence (see Fig. 5.6). The composition of the primary particles was also studied. For example, results obtained with only muon incident particles and an initial mixture of both muons and electrons were crosschecked. This comparison did not yield any significant differences in the results, and in fact multiple scattering of the electrons in the aerogel created rather severe acceptance issues for these contributions.

For the results which will be presented the incident particles were negative muons only, with a Gaussian smeared momentum spectrum. The mean value of the momentum spectrum was set to 2 GeV/c, and the sigma width of the distribution was 1 GeV/c. To increase the efficiency of accepted events for analysis, the muons were generated from a planar surface and distributed with a normal angle of incidence upon the area corresponding to the central four central pixels of the MAPMT.

Prototype Geometry

The Geant4 geometry module was used to describe the prototype simulation detector geometry, matching the design of the experimental setup as close as possible. Only the RICH counter was modelled in the prototype simulation and this is shown in Fig. 5.10 (a), where a primary muon passes through an aerogel tile, producing a cone of Čerenkov light which is detected by the H8500 MAPMT. The mu-metal shield (yellow) and mechanical mounts (grey-shades) are also visible in the visualisation [9].

The geometry of the H8500 MAPMT [162], including window thickness (1.5 mm), pixel sizes (5.8 mm), deadspacing between the pixels (0.28 mm) and surrounding the active area (3 mm), was described precisely in the simulation. The MAPMT was modelled as a glass window, photocathode material and corresponding array of 64 pixels. A close up of the simulated MAPMT geometry is shown in Fig. 5.10 (b), where Čerenkov photons produced in the aerogel and in the window of the MAPMT may be observed in green and the muon track is shown in red. The H8500 pixels were set as *sensitive detector* volumes, meaning any particles tracked

---

[9] The Geant4 visualisation software FreeWRL was used for visualisation purposes.

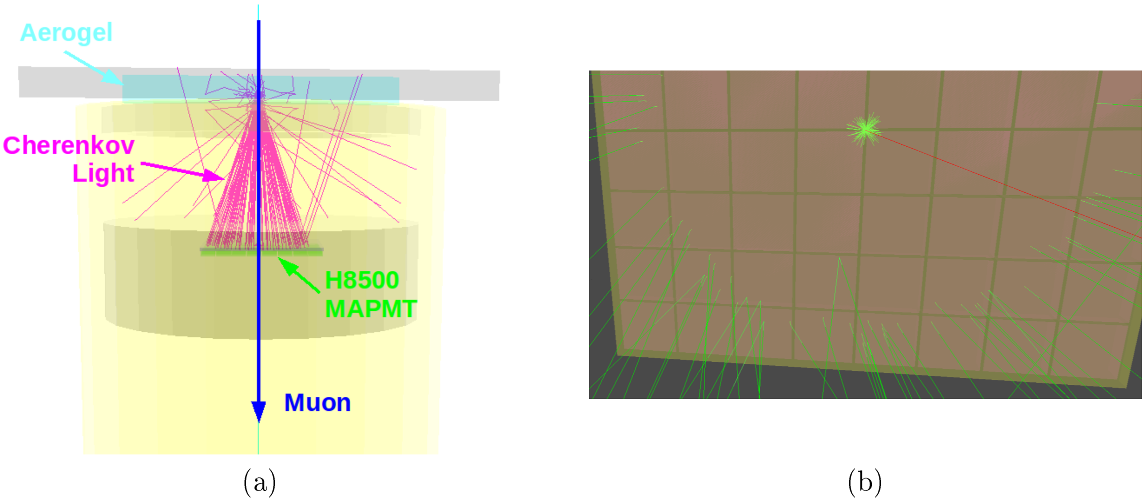

Figure 5.10: GEANT4 simulation geometry of (a) the RICH prototype and (b) the H8500 MAPMT.

within them were registered as hits and information such as event ID, particle type, position, momentum and energy was recorded. This hit information was provided in an output file for analysis and event reconstruction.

In Geant4 materials may be defined by the user through the combination of isotopes into elements and of several elements into compounds. Some of the most crucial materials used in the cosmic muon prototype for the generation, transport and detection of the Čerenkov light included: the aerogel, which was described as a combination of silica (SiO_2) and water (H_2O); the glass of the MAPMT which was described by SiO_2 and the bialkali photocathode which was described as a mixture of antimony, rubidium and caesium.

All three experimental configurations were simulated for comparison with the data. Fig. 5.11, for example, shows the simulated prototype setup for the masked MAPMT datarun, where black card was placed over the MAPMT to absorb Čerenkov photons produced in the aerogel. Čerenkov photons and the incident muon track are shown in green and red respectively. For the 2 cm thickness of aerogel radiator, two tiles of thickness 1 cm were simulated, where the second aerogel tile was placed on top of the first and an air-gap of 1 mm was placed between the tiles.

Optical Photon Processes and Material Properties

The flux, spectrum, polarisation and emission of Čerenkov radiation in Geant4 are well-modelled from the appropriate Čerenkov theory [177]. The treatment of the resulting optical photons is also performed by Geant4, and was crucial for the success of the cosmic muon prototype simulation. A photon is considered optical by Geant4 when its wavelength is much

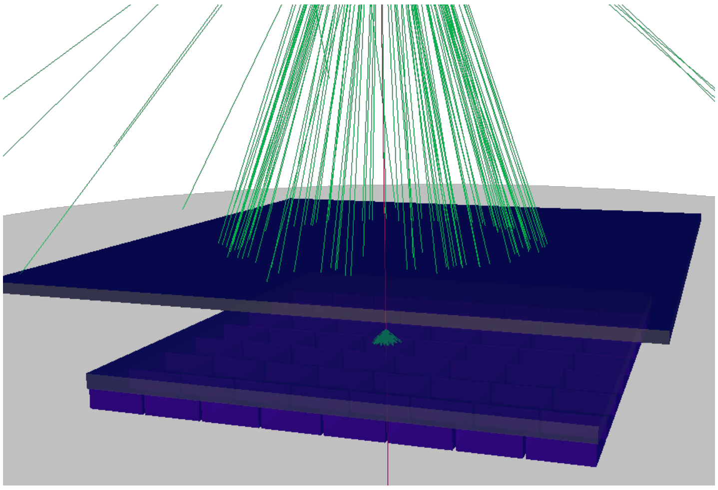

Figure 5.11: The simulated RICH prototype geometry for the masked MAPMT datarun, where a piece of absorbing material blocked Čerenkov photons produced in the aerogel from reaching the MAPMT.

greater than the typical atomic spacing, and it is consequently treated as a wave [177]. The definition of a photon as optical in Geant4 allows for the modelling of such processes as dispersion, bulk absorption, refraction and reflection at medium boundaries, or Rayleigh scattering. Such optical physics packages, amongst others, were included in the prototype simulation and comprehensive descriptions of how Geant4 models them may be found in [177]. In order to track optical photons in materials within Geant4, the material must have pre-defined optical properties - such as refractive index, absorption and scattering lengths. In the prototype simulation, these properties were input as a function of photon energy, along with the material definitions. Emphasis in the prototype simulation development was placed upon the optical models for the aerogel radiator, the MAPMT entrance window, and the bialkali photocathode.

The optical models for the aerogel radiator material were consistent with those used at the same time in the CLAS12 GEant4 Monte Carlo (GEMC) RICH simulation and were provided by N. Baltzell [178]. These models were based on and modified from several measurements and parameterisations described in literature [179,180,181]. Aerogel tiles with a nominal refractive index of $n = 1.05$ were used in the simulation, but with their refractive index depending upon photon energy as described by dispersion. To define the optical characteristics of the aerogel, the absorption and scattering lengths of the aerogel are also important and were modelled in the prototype simulation as a function of energy. The absorption length is used by Geant4 in the implementation of optical photon bulk absorption, and is the average distance travelled by a photon before being absorbed by the medium. This parameter will therefore directly affect the Čerenkov yield. Whereas the scattering length describes the average distance travelled by a photon before it is scattered in the medium and for the Čerenkov light inside the aerogel this will be important for the modelling of Rayleigh scattering, or in other words the coherent scattering of the photons from the aerogel atoms [29]. It should be noted that the aerogel optical models were originally developed to describe material from a different manufacturer than the Matsushita-produced aerogel which was used in the prototype, and the models were tailored for aerogel material produced by the Budker Institute for Nuclear Physics in Novosibirsk (Russia). Although the nominal refractive indices are the same there are slight differences amongst the optical properties of the aerogel tiles from the two manufacturers, for instance Novosibirsk tiles have a slightly higher transparency than the Matsushita type and are strongly hygroscopic, whereas the Matsushita tiles are less hygroscopic. This may arise as one source of discrepancy between simulation and data results, and for a completely accurate description of the aerogel in the simulation the tile used in the prototype setup should be characterised.

In addition to the aerogel material, the MAPMT optical models used in the prototype simulation were also important for realistic detection of the Čerenkov photons and description of the muon hit in the MAPMT window. The MAPMT used in the prototype had a UV-glass entrance window, which extended the sensitivity down to ∼180 nm from ∼280 nm, in comparison with the transmission of a standard Borosilicate glass window. The transmission curve for a UV extended window type, of thickness 2.25 mm, was extracted from documentation provided by ET Enterprises [182] and used to describe the MAPMT window absorption length in the simulation setup. The refractive index of the glass was approximated to a value of 1.54 across the entire energy range used for the optical models. The quantum efficiency spectrum for MAPMT type H8500C-03 was obtained from the Hamamatsu H8500 data sheet [162] and input to the simulation as the bialkali photocathode efficiency.

Dark Current, Crosstalk Noise and Resolution Smearing Effects

Noise and detector resolution effects were not included within the Geant4 simulation code itself, but were instead added in analysis of the simulation output on an event by event basis. This allowed for fast checking of the effects of different noise and smearing models without requiring to re-run the Geant4 simulation, which was more time consuming. The mechanisms for this are described below, where the added effects include: dark noise, optical and electrical crosstalks, and the single PE resolution of the MAPMT.

The process of adding noise and resolution effects to the output of the simulation is shown further in Fig. 5.12. For each event dark counts were first added to the array of raw hits

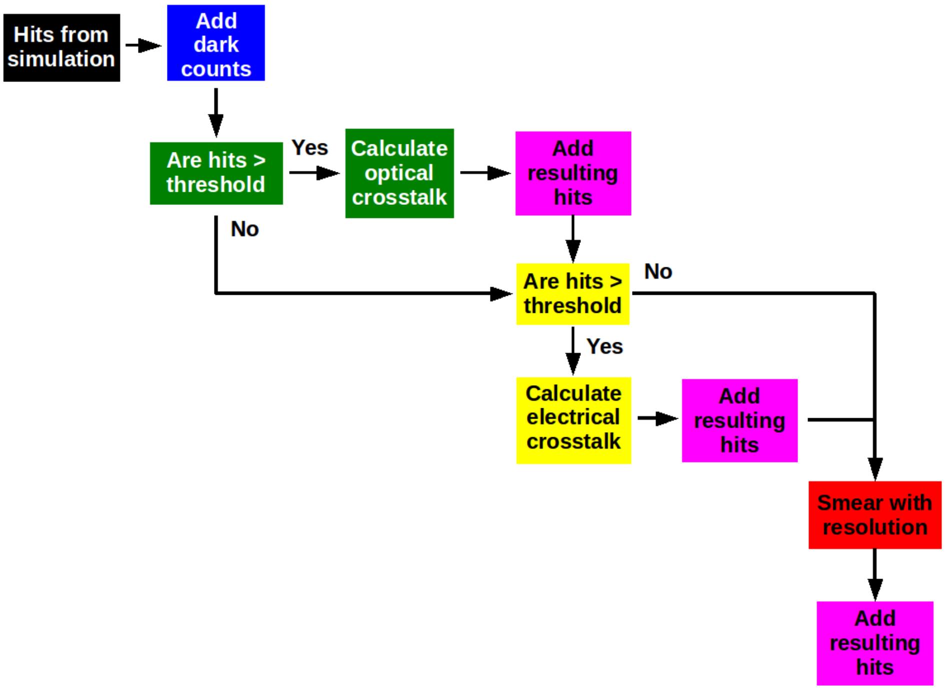

Figure 5.12: A flow-chart illustrating the process of incorporating resolution and noise effects into the cosmic muon RICH prototype simulation. This includes the addition of: dark counts; optical crosstalk; electrical cross and smearing by the single photon resolution of the H8500 MAPMT.

output from the simulation. Next, for every MAPMT pixel, if the hits were greater than a pre-set threshold value then optical crosstalk was calculated, distributed and added to the hit array. Following this, again for every pixel and if the hits in a pixel surpass a threshold value, electrical crosstalk was calculated, distributed and added to the hits. The next step for every pixel involved the smearing of its updated hits, where the hits were smeared by a factor scaling as $\sqrt{N_{Hits}} \times \sigma_{single\,PE}$, where $\sqrt{N_{Hits}}$ and $\sigma_{single\,PE}$ are the number of hits contained within the pixel and the single PE resolution of the MAPMT respectively. Finally, and not shown in Fig. 5.12, a signal gain correction factor was applied to tune the simulation signal gains with those extracted from data. A summary of the parameters used in each step to tune the simulation in this way, and the optimal values selected for comparison with the data results which will be shown further below, are given in Table 5.2.

The addition of dark counts was performed once per event, where a Poisson distribution, with a pre-specified mean number of dark counts (see Table 5.2), was randomly sampled to obtain the number of dark counts to be distributed within that event. For each of these resulting counts, one of the 64 MAPMT pixels was selected at random and one dark count hit only was added to the hit array for that pixel and for that event. The mean number of dark counts did not strongly affect the results, in comparison with the crosstalk magnitudes

Table 5.2: Noise and smearing effects added to tune the cosmic prototype simulation.

Parameter	**Description**	**Value Used**
Mean dark counts	Mean of a Poisson distribution randomly sampled to determine the number of dark counts for that event	4 hits
Optical crosstalk threshold	Minimum number of hits required in a pixel for generation of optical crosstalk	4 hits
Optical crosstalk magnitude	Fraction of hits in a pixel which equals the mean of the Poisson sampled to determine the number of muon optical crosstalk hits created from that pixel	25 %
Electrical crosstalk threshold	Minimum number of hits required in a pixel for generation of electrical crosstalk	1 hit
Electrical crosstalk magnitude	Fraction of hits in a pixel which equals the mean of the Poisson sampled to determine the number of intrinsic crosstalk hits created from that pixel	5 %
Single PE resolution smearing	Fraction of hits in a pixel which equals the mean of the Gaussian sampled and used to smear the final number of PE extracted from that pixel	70 %
Signal gain correction	Scale factor applied to simulation hits to correct for a gain mismatch with data	0.89

used, and a value of 4 was selected since the noise effects were added in the simulation analysis before the application of pedestal threshold cuts, which subsequently reduces the number of dark counts present in the final extracted yield values.

Following the allocation of dark counts, the optical crosstalk was modelled and for each event this was calculated for every pixel of the H8500 MAPMT. If the number of hits extracted from a pixel, after inclusion of dark counts, passed a minimal optical crosstalk threshold (see Table 5.2) then that pixel was allocated to produce optical crosstalk effects for that event. In this case, the optical crosstalk was used to describe crosstalk arising from scattered Čerenkov light created by the muon hit in the MAPMT window. The threshold requirement aimed to connect the source of this crosstalk mechanism with the location of the muon hit in the MAPMT window. The mean value for the Poisson distribution governing the optical crosstalk was calculated as: the number of hits extracted from the pixel multiplied by an optical crosstalk magnitude value (see Table 5.2). The Poisson distribution was then sampled randomly to yield the number of crosstalk hits generated by the pixel. For each of these generated crosstalk hits, one hit was added to one of the pixel's four side-sharing neighbours, selected at random, and after all crosstalk was distributed the hit arrays were again updated. The exact same method was then employed for every MAPMT pixel to allocate electrical crosstalk hits per event. In this case *electrical* crosstalk was used to describe all crosstalk mechanisms which are intrinsic to the MAPMT, such as improper PE focussing, charge spillover during PE multiplication and charge sharing amongst the readout anodes. The term *electrical* is only used to distinguish it from the optical crosstalk created by the muon hit in the window and therefore these crosstalk mechanisms are not only electrical. As demonstrated for example in Section 4.6.2, optical components to the intrinsic crosstalk of an MAPMT also exist. For the electrical crosstalk the minimal hit threshold for its generation was lower than in the optical case (see Table 5.2), and electrical crosstalk was calculated and distributed for every hit recorded. The electrical crosstalk magnitude factor was also smaller than for the optical crosstalk (see Table 5.2). Comparisons between the simulation and data results were very sensitive to the values selected to tune the optical crosstalk of the simulation and less sensitive to the magnitudes used for the electrical crosstalk, indicating that the muon hit in the MAPMT window plays a major role in the data extracted from the cosmic muon prototype.

The H8500 MAPMT has an intrinsically smeared single photon resolution, visible in the widths of its single PE spectra, which must be accounted for in the simulation before comparison with data. The magnitude of this effect was estimated broadly from inspection of H8500 pixel responses obtained throughout the laser scan tests and calibrations performed, where the resolution is defined as the σ width of a Gaussian fit to the single PE charge distribution divided by its mean position. Typically this resolution was calculated to be $\sim$70 % amongst the various pixels studied, and therefore for the results which will be shown this value was used as the single PE resolution smearing value (see Table 5.2). After the distribution of dark counts and crosstalk for each event a smearing factor was calculated for every pixel of the MAPMT which contained any hits, and was equal to the single PE resolution smearing value multiplied by the square root of all hits within a pixel ($\sigma_{single\,PE} \times \sqrt{N_{Hits}}$). A Gaussian distribution, which was centered on zero and had a width equal to the resulting smearing factor, was then randomly sampled and the result was added to to the number of hits in that pixel. The value sampled from the smeared Gaussian may be positive or negative. A different method of accounting for the H8500 MAPMT single photon resolution would be to use the calibration fit function described in Equation 4.2 to generate realistic spectra for each of the hit pixels, and then randomly sample from this distribution to obtain the smeared number of hits.

Finally, after the addition of noise and smearing effects, a 0.89 scale factor was applied to the simulation hits to correct for a gain mis-match between simulation and data (see Table 5.2).

The reason for this is subsequently described along with the results of the muon hit in the MAPMT window given in Section 5.1.5. Once the simulation output was treated in this way, analysis of both simulation and data was performed, including the application of the pedestal threshold cuts, the methods of which are described in the following section.

5.1.4 Analysis Techniques

For the analysis of Čerenkov events two completely independent pattern recognition algorithms, the *template* and the *clustering* algorithms, were used for cross-checking of results. In both algorithms the maximum recorded hit found in each event, or the *leading pixel*, was used as the seed for pattern recognition and assigned to the muon hit in the MAPMT window. The cut used for finding this maximum hit was that the signal extracted had to correspond to at least 6 PEs. This cut was determined and concluded to be satisfactory from inspection of typical muon hit characteristics in both simulation and data. Additionally, in both algorithms, only events in which the leading pixel position lay in one of the central 2×2 array of MAPMT pixels were kept for analysis.

The Template Algorithm

In the template algorithm, a mask of 9 pixels is assigned to the region of the MAPMT face which is assumed to contain hits resulting from the muon traversing the MAPMT window. First, for each event, relative gain corrections are applied to all pixels and then pedestal threshold cuts are applied to all channels. The pixel with the highest charge above threshold is recorded and assumed to be the location of the muon hit in the MAPMT window. A search is then performed in the immediate eight neighbouring pixels, defining the muon template region. This is illustrated in Fig. 5.13, and the template is highlighted by a green square. If hits in this region with signals above the pedestal cuts exist then the muon hit position centroid is calculated. The centroiding uses the charge extracted from each pixel as weights to locate a more accurate position for the muon hit, as calculated by Equation 5.1, where: X and Y indicate the horizontal and vertical centroided muon hit positions respectively; i is the number of pixels with signals above threshold; q is the charge in each pixel; x and y are the horizontal and vertical hit pixel IDs respectively.

$$(X,Y) = \left(\frac{\sum_i (q_i \times x_i)}{\sum_i (q_i)}, \frac{\sum_i (q_i \times y_i)}{\sum_i (q_i)} \right) \tag{5.1}$$

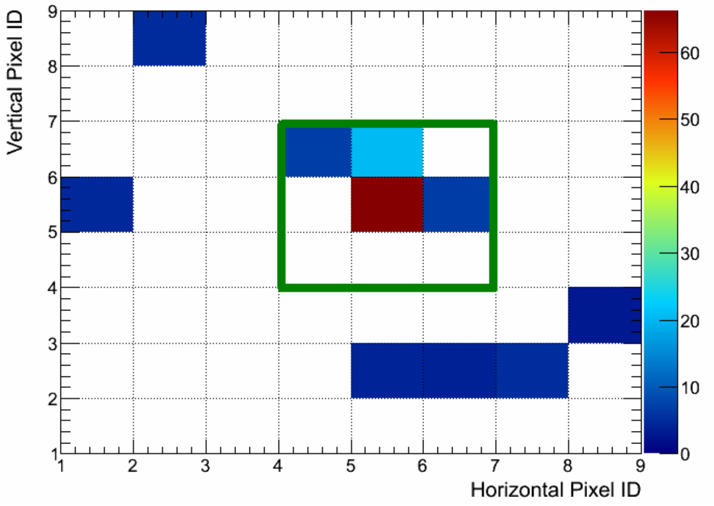

Figure 5.13: A ring image obtained from data with the cosmic muon RICH prototype. For the template algorithm analysis, the area designated to the muon hit in the MAPMT entrance window is outlined by green. All hits lying outwith this region are assumed to originate from Čerenkov light produced as the muon passes through the aerogel radiator. Colour fill indicates signal charge expressed in QDC bins [100 fC/bin].

The total signal in these template pixels with hits above threshold is summed and assigned as the muon hit sum charge. The absolute MAPMT calibration and relative pixel gains are used to convert this number to a corresponding NPE. Additionally, the number of contributing pixels within the muon template is recorded as the muon signal size. For example in Fig. 5.13 the recorded muon signal size is 4 pixels.

For the remainder of the analysis, the 9 pixels comprising the muon template region are completely excluded. Any remaining pixels on the MAPMT surface which show hits above threshold are assumed to originate from Čerenkov light produced in the aerogel. The charge recorded in each pixel is also converted into NPE, in the usual way, and the sum of these values, per event, yields a value for the NPE detected by the H8500 MAPMT per Čerenkov ring event. The number of pixels contributing to the Čerenkov ring is also extracted, for example in Fig. 5.13 the ring comprises 6 pixels.

The Clustering Algorithm

Contrary to the template algorithm, the clustering algorithm does not make any prior assumption about the shape or size of the muon hit in the MAPMT window and in this case clusters are found on the MAPMT face. The principle of the clustering algorithm is illustrated and described in Fig. 5.14. Once the leading pixel of an event is found, the algorithm searches for hit neighbours using either a *direct neighbour* or *all neighbour* approach. In the direct neigh-

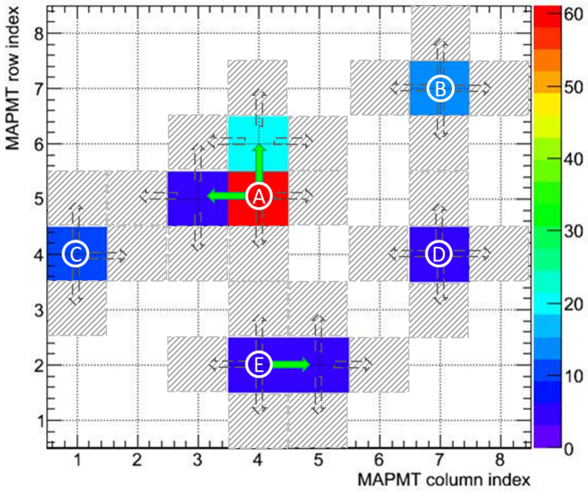

Figure 5.14: Principle of Cluster Algorithm acting on a typical event. Seed pixels are marked by letters A–E (ordered by signal amplitude). The green (grey) arrows indicate successful (failed) neighbour searches. The hatched grey areas denote pixels without signals defining the cluster boundary. Cluster A corresponds to a muon hit in the MAPMT window while clusters B–E are Čerenkov photons from the aerogel radiator. Colour fill indicates signal charge expressed in QDC bins [100 fC/bin]. Image provided by M. Hoek [171].

bour case only the four side-sharing pixels of the leading pixel are considered, whilst in the all neighbour case all 8 neighbouring pixels are incorporated. For the results which will be shown, the direct neighbour algorithm was used. Any pixel found to have a signal above threshold is included in the cluster. An identical search of the added pixel's neighbours is then performed, and subsequently adding more hit pixels to the cluster. The search finishes when no more pixels can be added to the cluster. This cluster, which contains the leading pixel, is designated as the muon cluster. If the cluster size is greater than one pixel, then the centroided position for the muon hit is calculated as described in Equation 5.1. If any separated hit pixels remain then a new seed is determined and a new cluster search starts. This process is repeated until all hit pixels are assigned to clusters constituting the aerogel Čerenkov ring. For each cluster the pixel signals are summed and, just as for the template algorithm, the extracted charge is converted into NPE using the absolute gain calibration of the MAPMT and the relative gain values.

Both analysis algorithms have advantages and disadvantages. For example, in the ring image shown in Fig. 5.15 (a) it is unclear where the muon hit in the MAPMT window ends and the aerogel Čerenkov photons begin. The template algorithm would possibly include a slight amount of crosstalk with the aerogel Čerenkov signal, however the clustering algorithm would combine a significant proportion of the aerogel hits into the muon hit in the MAPMT window. Fig. 5.15 (b) provides another example, where in this case the clustering algorithm would completely enclose the entire muon MAPMT window hit, however, the template algorithm would include a small fraction of crosstalk from the muon hit into the aerogel Čerenkov signal.

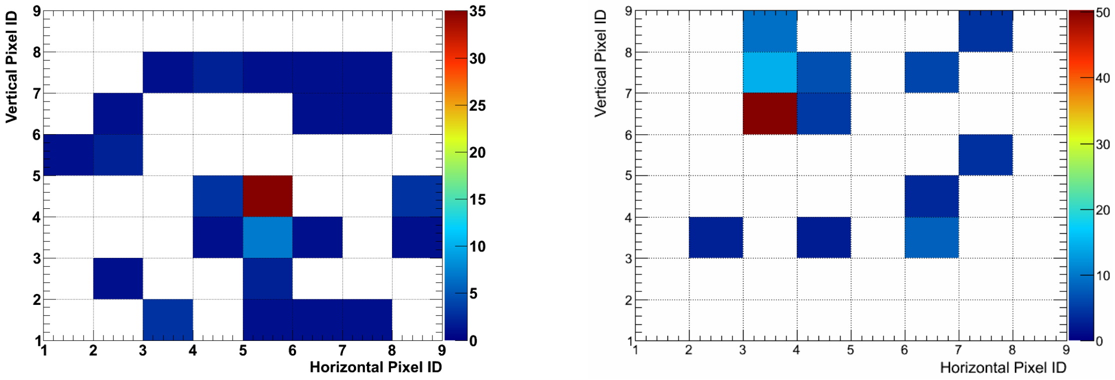

(a) (b)

Figure 5.15: Example ring images obtained with the cosmic muon RICH prototype from both (a) simulation and (b) data, where the colour fills indicate (a) number of recorded photoelectrons and (b) signal charge expressed in QDC bins [100 fC/bin].

5.1.5 Results

Results obtained with the cosmic muon RICH prototype are described below. This includes data and simulation comparisons which revealed that the main quantities obtained from experimental data were reproduced by simulations. The results, however, also indicated that there was a resolution mis-match between the measured and simulated aerogel Čerenkov yields, with the distributions obtained from data being broader than those extracted from simulation. This issue currently remains under investigation. A focus is placed on results from the template algorithm, however cross-checks with the clustering algorithm are made throughout. The cross-checks indicated a general agreement in the extracted quantities, with differences accounted for by the algorithm designs and systematic uncertainties of the absolute gain calibration. For comparison, due to the different sized data-sets, result distributions which will be shown are all normalised to unity by their areas.

Unless stated otherwise, a $4\,\sigma$ pedestal threshold cut was applied to H8500 charge spectra in the experimental and simulated data analysis. It was concluded from the laser studies that this provides an adequate compromise between noise rejection and signal retention. This is illustrated in Fig. 5.16, which shows an example single PE spectrum obtained from an H8500 pixel in response to laser light, with the locations of $3\,\sigma$, $4\,\sigma$ and $5\,\sigma$ pedestal thresholds marked. In some cases threshold cut scans were also studied, to investigate the impact on the results.

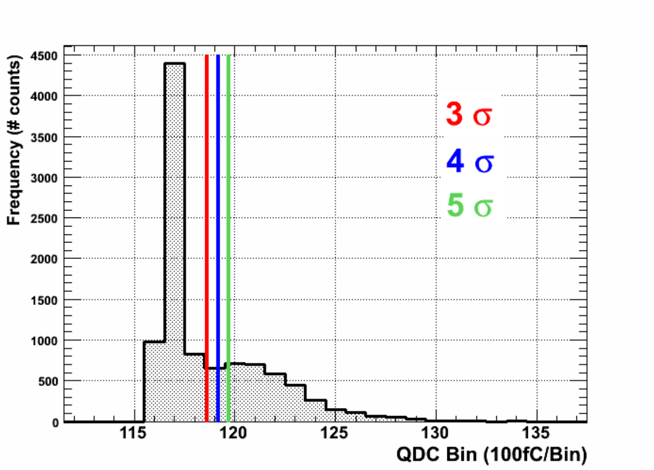

Figure 5.16: Example of the locations of $3\,\sigma$, $4\,\sigma$ and $5\,\sigma$ pedestal threshold cuts with a typical pixel of the H8500 MAPMT.

Čerenkov Ring Images

Overlays of accumulated Čerenkov events obtained with the 1 cm and 2 cm thicknesses of aerogel and the template algorithm are shown in Figs. 5.17 (a) and (b) respectively. In each of the plots the muon template has been removed and beyond this region crosstalk remnants resulting from the muon hit in the MAPMT window may be observed before the aerogel rings begin. Events in which the muon hit was not central have been included, with the rings shifted to a central position for visualisation purposes. The result for an aerogel thickness of 2 cm (Fig. 5.17 (b)) shows on average similar mean ring radii to the 1 cm case (Fig. 5.17 (a)), however there exits an addition of entries at higher radii caused by the increased radiator thickness.

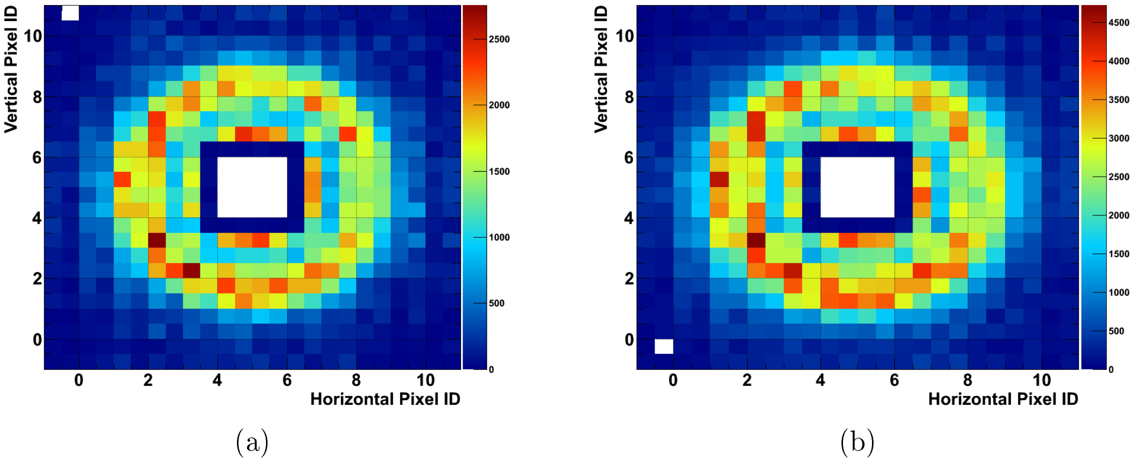

(a) (b)

Figure 5.17: Overlay of ring images obtained with the cosmic muon RICH prototype. The muon hit in the MAPMT window has been removed and the results are shown for the (a) 1 cm and (b) 2 cm aerogel thickness data-sets. The colour-fill indicates frequency of hits.

Fig. 5.18 displays the result obtained with the masked MAPMT setup and shows hits which are mis-identified as originating from the aerogel radiator. The result illustrates that there exists a significant background level across the MAPMT face caused by the muon hit in the glass window, which must be corrected for before the calculation of any aerogel yields.

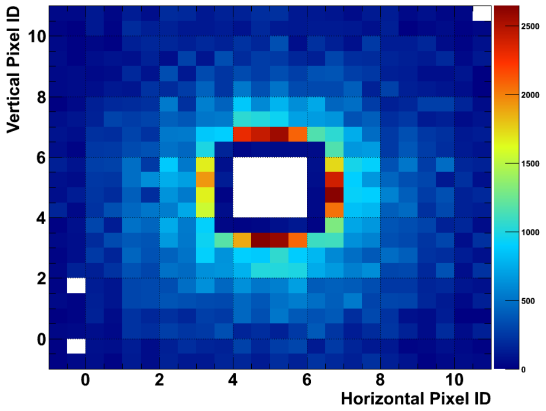

Figure 5.18: Overlay of ring images obtained with the masked MAPMT configuration of the cosmic muon RICH prototype. The colour-fill indicates hit frequency of hits, and implies that crosstalk and remnants from Čerenkov light produced by the muon hit in the MAPMT window contribute to background of the aerogel runs.

Čerenkov Ring Radii

Although extraction of Čerenkov ring radii values were not a main goal of the cosmic muon prototype, radius distributions were a useful method to cross-check the geometry of the setup and the event topologies. Radius distributions extracted from data, for all three experimental setups, are given in Fig. 5.19. The distributions show the calculated distance of the centre of each pixel corresponding to every aerogel Čerenkov ring hit from the centroided muon hit position, for all events. Although this parameter is technically not the Čerenkov ring radius, since the shape of the Čerenkov events were not fitted, it is termed radius for the remainder of this section. The pixelisation effect of the MAPMT is immediately visible as separated peaks in the distributions. The masked data-set distribution arises from muon window hits which are mis-identified as aerogel Čerenkov ring hits. The distribution peaks at a radius value of 2 pixels, in agreement with the overlay ring image shown in Fig. 5.18. Beyond this the contributions from larger radius values decrease, however the shape mimics that of the 1 cm and 2 cm aerogel data-sets. The distributions for both the 1 cm and 2 cm thicknesses of aerogel are both peaked at a value of 3.2 pixels and small peak at a radius value of 2.0 - 2.2 pixels, caused by crosstalk from the muon hit in the MAPMT window, is observed in both distributions. Furthermore,

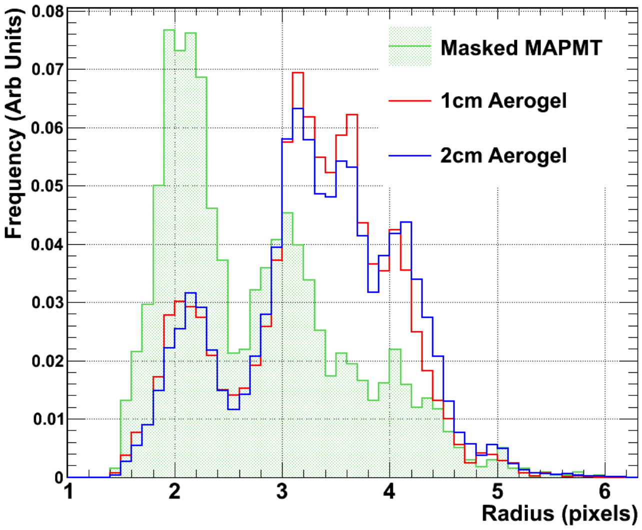

Figure 5.19: Radius plots extracted with the cosmic muon prototype data, compared between all data-sets and extracted using the template analysis algorithm. The radius parameter describes the geometrical distance of each aerogel hit from the centroided muon hit position, and is plotted for all hits of all events. The structures arise from the pixelisation of the MAPMT.

contributions from radii larger than the 3.2 pixels peak also exist, with the 2 cm data-set in particular having a slightly larger tail to higher radii values.

The averaged radii distributions are shown in Fig. 5.20, where here the average value of each of the distances of all individual hits from the centroided muon hit position is calculated per event and plotted on the event by event basis. Again, the masked MAPMT distribution peaks close to a value of ∼ 2 pixels, with a tail extending to higher values. The 1 cm and 2 cm aerogel thickness distributions, yield mean average distance values of (3.289 ± 0.010) pixels and (3.348 ± 0.008) pixels respectively. The observed resolutions, quantified here as the σ widths of the peaks when fitted by Gaussian function, are roughly the same for both the 1 cm and 2 cm aerogel thickness settings, with values of (0.316 ± 0.009) pixels and (0.314 ± 0.008) pixels extracted respectively. The 2 cm distribution is shifted slightly to higher radius values, in comparison with the 1 cm distribution, since in this case the muon passes through an extra 1 cm of radiator material in which it may produce Čerenkov light. Since the second aerogel tile was placed on top of the first tile, and hence further from the MAPMT face, this results in a larger ring expansion volume and hence larger Čerenkov ring radii.

Comparisons with simulations in general showed close agreement between the main features and radius values extracted, however the distributions obtained from simulations yielded much higher resolutions than those extracted from data. Some examples are given below for

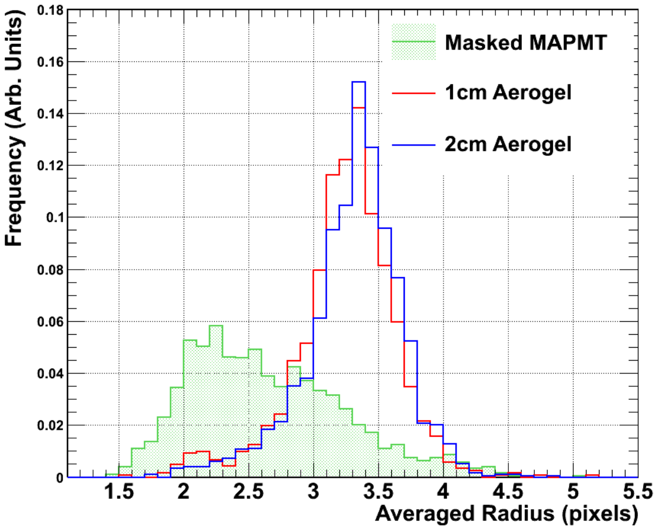

Figure 5.20: Averaged Čerenkov ring radii plots extracted with the cosmic muon prototype data, compared between all data-sets and using the template analysis algorithm. The averaged radius is defined as the average distance calculated from each of the individual hit distances from the centroided muon position for each event and is therefore histogrammed on the event by event basis.

illustration purposes. Fig. 5.21 (a) provides a comparison between data and simulation hit radius distributions with a radiator thickness of 1 cm, where again the distance of all hits from the centroided muon position are plotted for all events. The pixelisation of the MAPMT is visible in both simulation and data curves, with the radius peaks occurring at the same mean positions. However, in the data distribution there is much more background present between

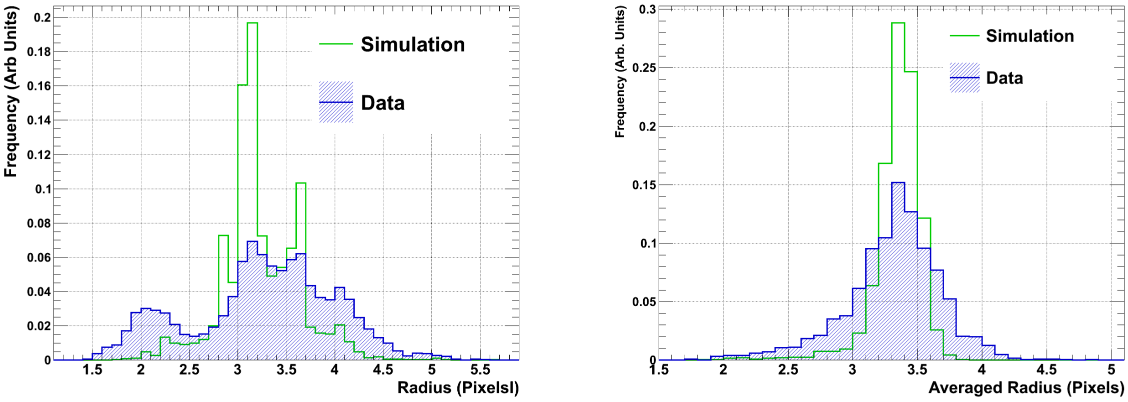

(a) (b)

Figure 5.21: Data and simulation radius distribution comparisons for runs with the MAPMT unmasked. Examples of two different distributions, from two different configurations are given. (a) The calculated distance of all hits from the centroided muon position is plotted for all events, for the 1 cm thickness radiator. (b) The averaged event radius distribution for 2 cm thickness of aerogel radiator, where the average distance of all hits from the muon centroided position are plotted per event.

the peaks, and the resolution is smeared to a greater extent than in simulation. An increased level of crosstalk also exists in the data distribution, at a radius of ∼2.2 pixels, which is postulated to originate from remnants of the muon hit in the MAPMT window. The same effect is observed with the equivalent comparison for the 2 cm thickness aerogel data-set. Fig. 5.21 (b) shows the averaged radii distributions for both simulated and experimental data corresponding to the setup with an aerogel radiator thickness of 2 cm, where the average distance of all hits from the muon hit per Čerenkov event are plotted. Again, the mean values agree very well, however the data curve exhibits a much broader width, with tails towards extreme values of radius.

The close agreement between the mean radius values extracted from simulations and data acts a validation of the simulated experimental setup, since this relies upon the geometry and the pixelisation of the MAPMT. The comparisons, however, indicate that there exists a resolution effect which is not properly accounted for in the simulation. It is postulated that the main origin of this lies in the optical models for the aerogel, for example within such user-defined properties as the scattering or absorption lengths. The reason for this is because the comparison between simulation and data agree very well for the masked MAPMT configuration, which is independent of the aerogel models. An example of this is given in Fig. 5.22, which shows the distances of each individual hit from the muon hit position for all events, obtained from both simulation and data for the masked MAPMT configuration. In this case, both the mean values and the resolution of the contributing peaks are well matched between simulation and data, and the distributions are in accordance with the theory that the hits are from crosstalk produced by the muon passing through the MAPMT window. The corresponding characteristics of the muon hit in the MAPMT window and the resulting background levels were subject to further characterisation, as described below.

The Muon Hit in the MAPMT Window

Analysis of the muon hit in the MAPMT window was extremely valuable for validation of the MAPMT simulation and for the tuning of the free parameters used in analysis of the simulation data (see Table 5.2). Since it is assumed that Geant4 accurately modelled the Čerenkov effect, the resulting comparison with data therefore depended upon the geometry, optical physics and noise models used to describe the MAPMT. To confirm the MAPMT models used, then, an in-depth comparison study was performed between properties of the muon hit in the MAPMT window extracted from simulation and experimental data.

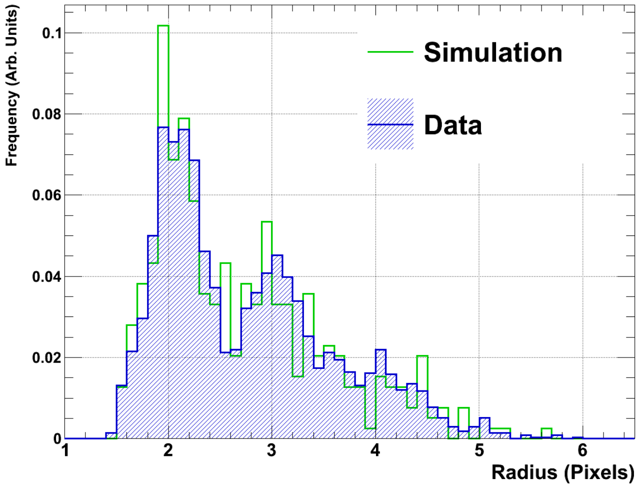

Figure 5.22: Comparison between data and simulation hit-radius distributions for the masked MAPMT configuration of the cosmic muon RICH prototype, where the distance of all hits from the muon hit position are plotted for all events.

The leading pixel of the muon hit in the MAPMT window was attributed to the incident point of interaction of the cosmic muon with the MAPMT window. The leading pixel signal charges extracted from experimental data, for all setup configurations, are shown in Fig. 5.23. The experimental configuration does not influence the strength of the signal, as expected,

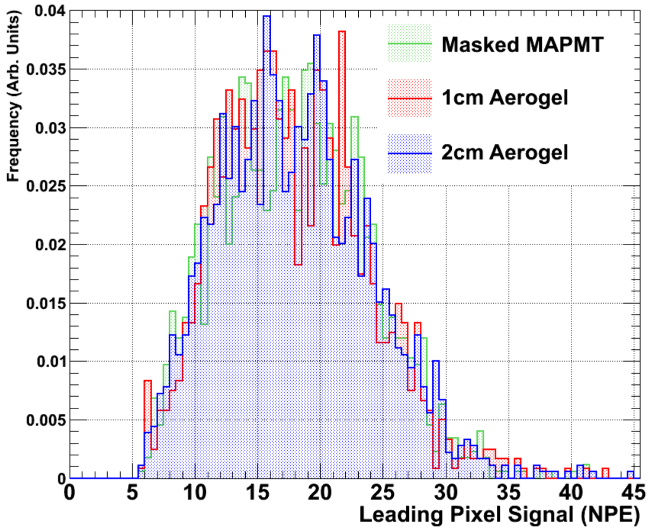

Figure 5.23: The charge extracted, in terms of NPE, from the leading pixel of the muon hit in the MAPMT window. A mean value of (17.76 ± 0.20) NPE is obtained.

and the curves are in extremely close agreement with each other. A summary of the values extracted for the means and widths of the leading pixel signal charge distributions is given in

Table. 5.3, including a comparison between the results obtained from both analysis algorithms. For the template analysis the mean and σ - widths from Gaussian fits to the distributions have been quoted, whereas for the clustering analysis mean and RMS - widths obtained from the histogram statistics provided by ROOT, without fitting, are given. Separately, each of the algorithms yield similar mean and width values extracted across all data-sets. Average leading pixel signal strengths of (17.76 ± 0.20) PE and (18.94 ± 0.02) PE are obtained respectively for the template and clustering algorithms. There is a slight mismatch between the algorithm results, which is of the order of 1 PE. The origins are not obvious, since only the response from the leading pixel alone is evaluated and the MAPMT calibration used in both algorithm analyses is the same. It is possible that the mismatch arises from slight discrepancies in conversions of QDC channels into NPE and the corresponding threshold definitions, which are extracted from data, or the use/absence of fitting the distributions in the analysis.

Table 5.3: Comparison between different data-sets and analysis algorithms for the strength of the signal obtained from the leading pixel of the cosmic muon hit in the MAPMT window.

Data Set	**Analysis Algorithm**	**Mean Position [NPE]**	σ/**RMS Width [NPE]**
1 cm aerogel	Template	17.45 ± 0.17	5.493 ± 0.129
	Cluster	18.92	6.2
2 cm aerogel	Template	17.77 ± 0.15	5.993 ± 0.123
	Cluster	18.97	6.17
Masked MAPMT	Template	18.06 ± 0.15	5.719 ± 0.108
	Cluster	18.93	6.34

Since the leading pixel signal was independent of any crosstalk effects, comparison of its strength between simulation and data allowed for a global gain correction factor to be determined. This parameter should depend only upon the MAPMT simulation models used and the MAPMT calibration used throughout the analysis. Originally, the mean of the simulated leading pixel charge was higher than observed in data. Comparison of extracted values yielded a scaling factor of 0.89 (see Table 5.2), which was then applied to the hits extracted from all simulated data. The scaling factor is thought to originate from an over-estimation of either the MAPMT window refractive index or the bialkali QE modelled in the simulation. An example of one of the resulting data and simulation comparisons, obtained using the template algorithm and the masked MAPMT setup, is given in Fig. 5.24 (a). Although the simulation has a slightly larger tail to higher values, the means and widths of the curves are very well-matched. Similarly close comparisons between simulation and data were obtained for the remaining two experimental configurations and, in addition, the agreement amongst the simulation results for

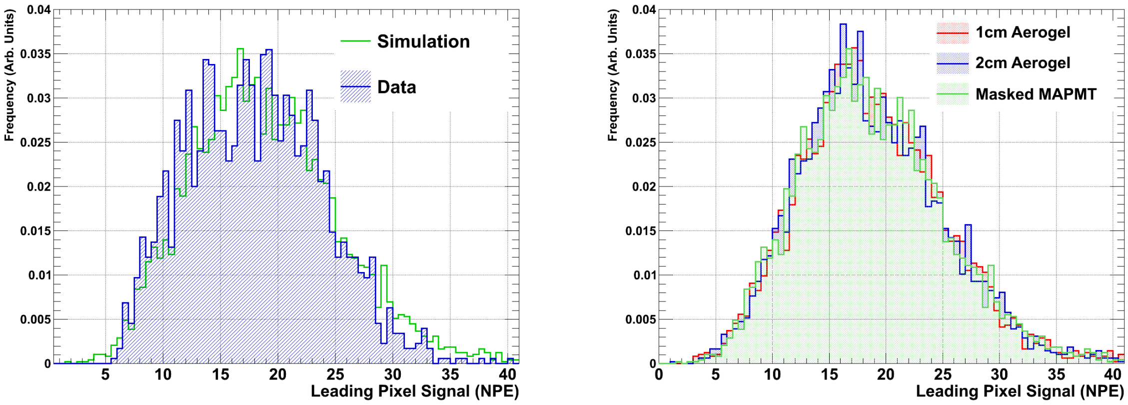

(a) (b)

Figure 5.24: (a) Comparison between simulation and data for the signal from the leading pixel of the muon hit in the MAPMT window. The comparison is made for the masked MAPMT experimental setup. (b) Comparison between the simulated distributions, for all three experimental setups, of the leading pixel signal charge of the muon hit in the MAPMT window.

the different experimental setups was also confirmed, as shown in Fig. 5.24 (b). The results from Gaussian fits to the simulation distributions are given in Table. 5.4. An average signal strength of (18.65 ± 0.03) PE is obtained from the simulated experimental setups and the mean and width values extracted between the different setups are in extremely close agreement. The widths additionally agree well with results extracted from data (see Tab. 5.3). The simulated mean values are slightly larger, though this effect is on a scale less than 1 PE and is likely caused by the larger tails in simulation curves.

Table 5.4: Comparison between simulations of different experimental setups for the strength of the signal obtained from the leading pixel of the muon hit in the MAPMT window. The analysis was performed using the template algorithm.

Data Set	**Mean [NPE]**	**σ Width [NPE]**
1 cm aerogel	18.69 ± 0.09	5.958 ± 0.067
2 cm aerogel	18.64 ± 0.10	5.941 ± 0.066
Masked MAPMT	18.61 ± 0.10	5.927 ± 0.069

The geometry and material of the MAPMT window result in Čerenkov rings with maximum radii of 1.78 mm as the muons pass through it, and so these signals may be contained entirely within one H8500 pixel. If the incident muon strikes deadspace between pixels, or close to the edge of a pixel, then signals will be observed in all neighbouring pixels (see Section 4.5.1). Additionally, the strength of the muon hit is rather large and so charge-sharing and crosstalk effects will contribute to the characteristics of the muon hit. The critical angle of total internal reflection in glass is ~42°, and since a maximum value of $\theta_C \sim 49.82^\circ$ is produced by the muons in the MAPMT window, some of the Čerenkov light will also reflect inside the window before detection. The combination of such effects results in a group of pixels being assigned to the muon hit in the MAPMT window, as opposed to an individually hit pixel. The analysis of the muon hit size and corresponding sum charge therefore allowed for a useful method of tuning of the local optical and electrical crosstalk magnitude parameters of the simulation analysis (see Table 5.2). Fig. 5.25 provides an example of this, where the muon hit size in pixels as determined by the template analysis algorithm and after tuning of the crosstalk parameters is shown, for all data-sets. The width of the distribution is limited between values of 1 and 9 pixels due to the definition of the muon template. The shape of the distributions are again in extremely close agreement for all data-sets as expected and this is further confirmed in Tab. 5.5, which shows the mean values and widths of the muon hit size distributions, obtained with both analysis algorithms and for all data-sets. The values are extracted from the histogram statistics

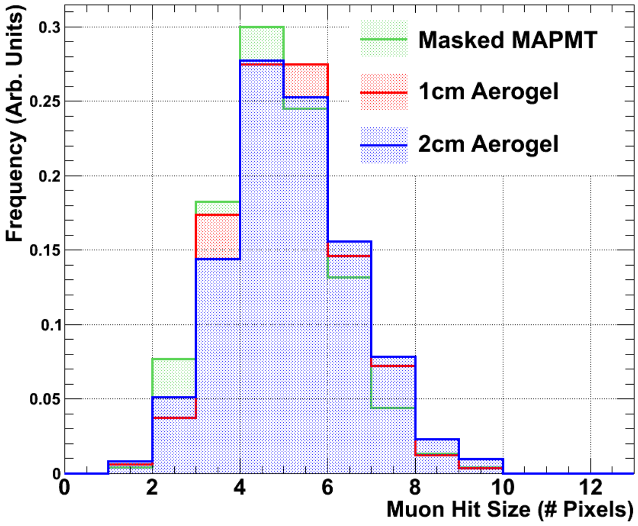

Figure 5.25: Typical size of the region attributed to a cosmic muon hit in the H8500 MAPMT window.

Table 5.5: Comparison between different data-sets and analysis algorithms for the size of the signal produced by the cosmic muon hit in the MAPMT window.

Data Set	Analysis Algorithm	Mean [Pixels]	RMS Width [Pixels]
1 cm aerogel	Template	5.084	1.351
	Cluster	5.130	2.580
2 cm aerogel	Template	5.167	1.471
	Cluster	5.270	2.680
Masked MAPMT	Template	4.865	1.367
	Cluster	4.840	2.220

provided by ROOT, and therefore no fitting errors have been provided. The results obtained from the template and clustering algorithms are in extremely close agreement, with muon hit sizes of (5.04 ± 0.10) pixels and (5.08 ± 0.14) pixels extracted respectively, averaged over all three data-sets. The widths of the clustering algorithm are larger than for the template algorithm, since in this case the algorithm may search for as many pixels as required until it finds the end of the allocated muon hit. For both algorithms a very slight decrease in hit size is recorded for the masked MAPMT data-set. Although the effect is very small and almost negligible, it implies that a small fraction of hits on the MAPMT face which result from photons created in the aerogel material are also mis-identified as belonging to the muon hit in the window.

The simulation results for the size of the muon hit in the MAPMT window are also consistent amongst setup configurations as shown in Fig. 5.26 (a) where the resulting distributions overlay very closely, as expected. Upon comparison with data results, the simulation curves

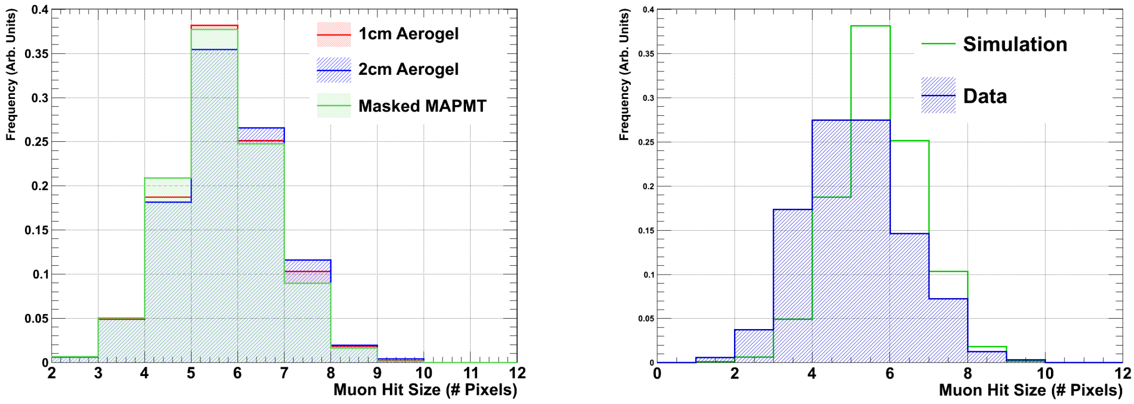

(a) (b)

Figure 5.26: (a) Simulated signal size of the muon hit in the MAPMT window, in pixels, for the three different experimental configurations. (b) Example of a simulation and data comparison for the muon hit size, for the configuration of 1 cm aerogel thickness.

show slightly higher peaked and narrower distributions. An example is shown in Fig. 5.26 (b), which provides a comparison between the simulation and data curves for the 1 cm thickness aerogel configuration. The comparisons between the two remaining experimental setups exhibited the same behaviour. The size of the muon hit was strongly linked to the value of optical crosstalk set in the simulation analysis and, although this represents the optimal comparison obtained, perhaps further tuning of the crosstalk parameters could improve the match between the shape of the distributions. For instance, it is possible that the geometrical distribution of the optical crosstalk into the side-sharing neighbours of the leading pixel only is too naive. A summary of the muon hit sizes obtained from the simulation distributions with the template algorithm, and the previously stated crosstalk values (see Table 5.2), is given in Table. 5.6. The results may be compared with those given in Table. 5.5, confirming the increase in mean values of the distributions. This increase, however, is relatively small and in-fact lies below a difference of 1 pixel in each case. A value of (5.70 ± 0.04) pixels is extracted for the simulated muon hit size, from the average calculated over all setups.

Table 5.6: Comparison between different data-sets for the size of the signal produced by the cosmic muon hit in the MAPMT window, in pixels, obtained from simulations and analysis with the template algorithm.

Data Set	**Mean [Pixels]**	**RMS Width [Pixels]**
1 cm aerogel	5.710	1.126
2 cm aerogel	5.758	1.173
Masked MAPMT	5.646	1.117

Combining the charge from the cluster of pixels which form the region assigned to the muon hit in the MAPMT window yields the muon sum charge parameter. This again will include crosstalk noises, signals arising from total internal reflection of the Čerenkov light within the window, and effects where the Čerenkov light is spread out over several pixels. The result is a signal which is significantly stronger than that obtained from the leading pixel hit charge and the corresponding distributions were again useful for tuning the crosstalk parameters of the simulation study. Fig. 5.27 shows the muon sum charge, expressed in NPE, obtained from data and using the template algorithm, for all experimental configurations. Agreement is once more strong amongst the different experimental setups and the corresponding results from Gaussian fits to the distributions, along with a comparison of analogous results obtained with the clustering algorithm, are shown in Table. 5.7. Mean values of (27.84 ± 0.12) PE and (30.68 ± 0.06) PE are obtained with the template and clustering algorithms respectively. This

Table 5.7: Comparison between different data-sets and analysis algorithms for the sum charge of the cosmic muon hit in the MAPMT window.

Data Set	**Analysis Algorithm**	**Muon Sum Charge [NPE]**	**σ/RMS Width [NPE]**
1 cm aerogel	Template	27.63 ± 0.18	5.506 ± 0.144
	Cluster	30.74 ± 0.10	6.71
2 cm aerogel	Template	27.90 ± 0.14	5.738 ± 0.118
	Cluster	30.73 ± 0.01	6.89
Masked MAPMT	Template	27.98 ± 0.18	5.883 ± 0.153
	Cluster	30.57 ± 0.12	6.7

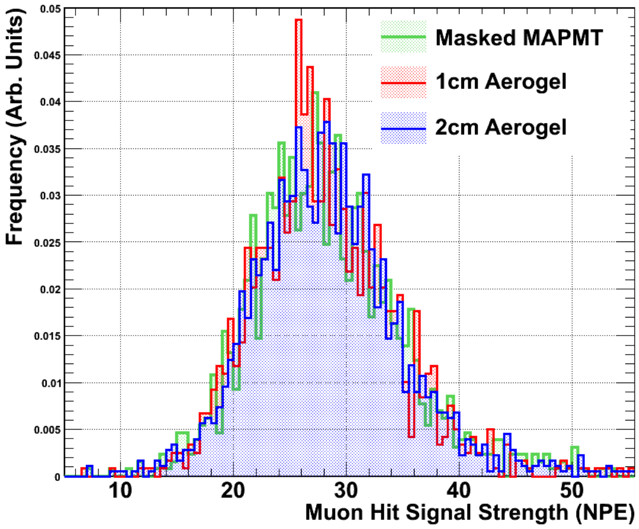

Figure 5.27: The sum charge extracted, in terms of NPE, as a result of the muon hit in the MAPMT window. A mean value of (27.84 ± 0.12) NPE is obtained.

most likely originates from the fact that the cluster algorithm may sum as many pixels as required into the muon sum signal, whereas the template algorithm is limited to only include 9 pixels. When the 10 % systematic uncertainty on all yield results caused the absolute gain calibration is included, the results do agree well with each other.

The curves obtained for the simulated muon hit sum charge are shown in Fig. 5.28 (a) and the corresponding Gaussian fit results are given in Table. 5.8. The widths of the distributions

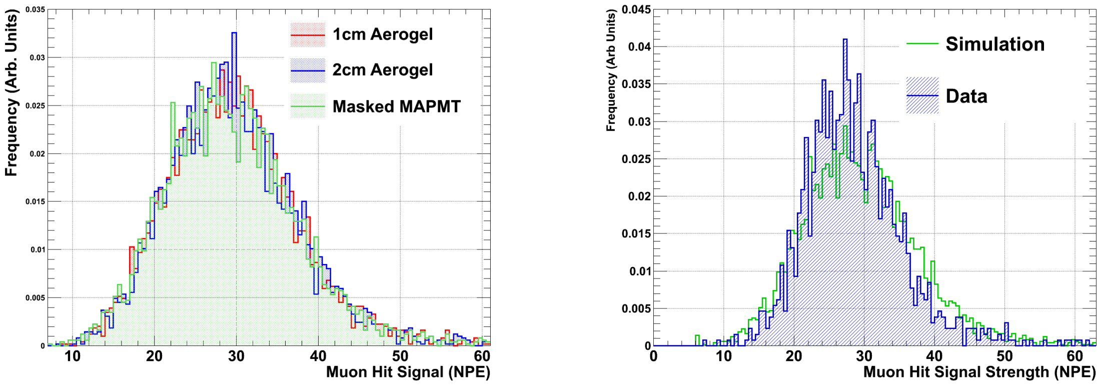

(a) (b)

Figure 5.28: The simulated distributions for the sum charge, in terms of NPE, as a result of the cosmic muon hit in the MAPMT window. A mean value of (29.14 ± 0.12) NPE is obtained.

obtained from simulations are very slightly higher than observed in data, and an example of the reason is shown in Fig. 5.28 (b). In general the curves match each other relatively well,

Table 5.8: Comparison between different data-sets for the simulated sum charge of the cosmic muon hit in the MAPMT window. Analysis was performed using the template algorithm.

Data Set	**Mean [NPE]**	**σ Width [NPE]**
1 cm aerogel	29.27 ± 0.11	7.180 ± 0.080
2 cm aerogel	29.25 ± 0.11	7.131 ± 0.082
Masked MAPMT	28.91 ± 0.12	7.356 ± 0.086

however the simulation shows a larger tail towards high PE values. The mean values are extremely consistent, irrespective of the data-set, and an average value of (29.14 ± 0.12) PE is obtained, which is slightly higher than the equivalent value obtained with experimental data, but again is in rather close agreement when the 10 % scale gain calibration uncertainty is considered. Fig. 5.29 shows a comparison, for all data-sets, between simulation and data muon sum results obtained with both the template and clustering algorithms. The simulation and data points for the clustering algorithm results obtained with the masked and 2 cm thickness aerogel data-sets lie on top of each other. The error bars indicate the 10 % scale uncertainty

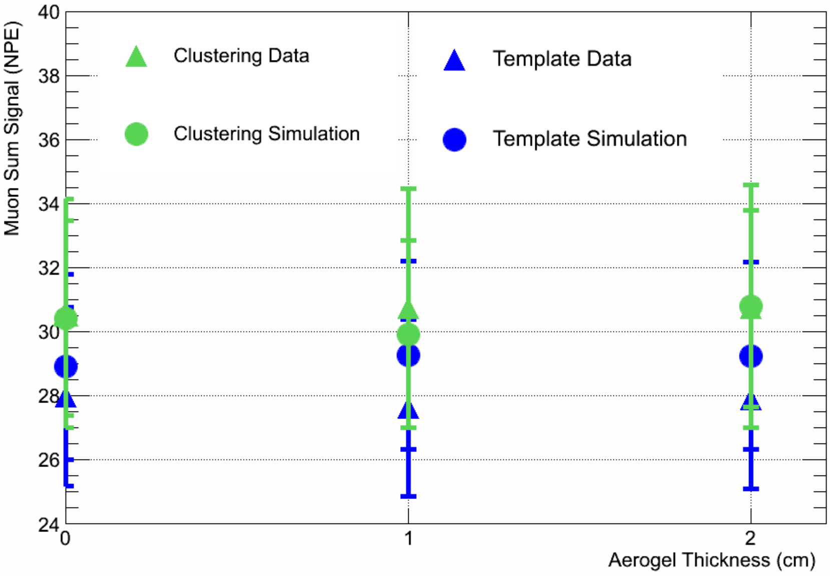

Figure 5.29: Data and simulation comparisons between the values obtained for the sum charge extracted, in terms of NPE, as a result of the muon hit in the MAPMT window and for all experimental setups. 0 cm aerogel denotes the masked MAPMT setup, where no Čerenkov light which is produced in the aerogel should reach the MAPMT.

from the MAPMT calibration, and when considered indicate that the complete set of results from both analysis algorithms, and obtained from data and simulation, are in agreement with each other.

Such results from the muon hit in the MAPMT window were used successfully to validate the simulation of the MAPMT and its corresponding optical models, since the simulation adequately reproduced the results from data when the systematic uncertainties are considered. These models may therefore be used in the full-scale simulation of the CLAS12 RICH detector. The muon hit in the MAPMT window however, although useful for validating the simulation, produced a background component which had to be accounted for before extracting the yield from the aerogel radiator, as described below.

Background Estimation from the Muon Hit in MAPMT Window

To estimate the background level produced by the muon hit in the MAPMT window the masked MAPMT data-set was used. The standard template analysis was performed, and the NPE which were mis-identified as originating from Čerenkov photons produced in the aerogel was evaluated. This was performed for $3\,\sigma$, $4\,\sigma$ and $5\,\sigma$ pedestal threshold cuts, to study how this influenced the mis-identified yield, as shown in Figs. 5.30 (a), (b) and (c). The yield plots show a strong dependence upon the pedestal threshold cut, with the $3\,\sigma$ cut displaying a significantly higher tail towards large values for the mis-identified yield in comparison with the $4\,\sigma$ and $5\,\sigma$ results.

The estimation of the amount of background signal was performed through analysis of the mis-identification yield plots. The distributions were fitted with an exponential decay, defined generically by ROOT as $f(x) = exp(constant + slope \times\ x)$. The slope parameter λ then allowed calculation of the expectation value of the exponential function, defined as $\frac{1}{\lambda}$. A weighting factor was also calculated as the fraction of hits above zero compared to the total number of entries. Subsequently the expectation value was multiplied by this weighting factor, to obtain the expected background level caused by the mis-identification of hits produced by the muon passing through the MAPMT glass window.

Table 5.9 gives the resulting weighting factors and background levels extracted with the template algorithm, for the three different pedestal threshold cuts examined. As the threshold

Table 5.9: Background yield values extracted with the template algorithm, to estimate for correction of the mis-identification of Čerenkov light created by the muon hit in the MAPMT window as originating from the aerogel radiator.

Pedestal Cut [σ]	**Weighting Factor**	**Mis-identification [NPE]**
3	0.93 ± 0.03	4.56 ± 0.20
4	0.74 ± 0.03	1.78 ± 0.18
5	0.54 ± 0.02	0.99 ± 0.06

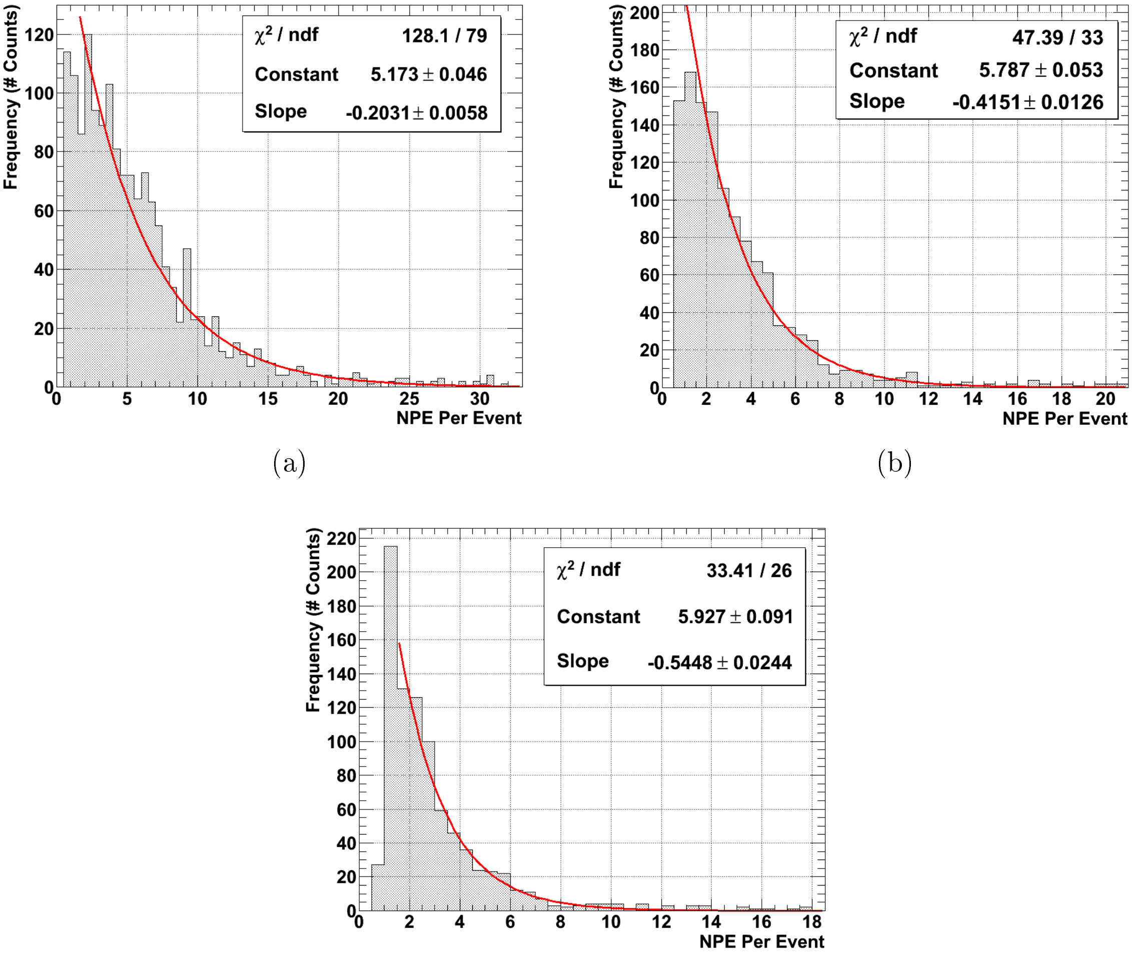

(a)

(b)

(c)

Figure 5.30: Hit yields from Čerenkov light produced by the cosmic muon passing through the MAPMT window which are mis-identified as originating from the aerogel tile. The analysis is performed using the masked MAPMT data-set, and pedestal threshold cuts of (a) $3\,\sigma$, (b) $4\,\sigma$ and (c) $5\,\sigma$.

cut increases, the weighting factors and level of mis-identification decrease rather significantly, from an expected value of (4.56 ± 0.20) PE at a $3\,\sigma$ cut to (0.99 ± 0.06) PE at $5\,\sigma$.

The background levels obtained using the masked data-set and the template analysis algorithm, with a $4\,\sigma$ pedestal threshold, were compared to the equivalent quantity extracted from simulation. Fig. 5.31 (a) shows the corresponding comparison between the mis-identified Čerenkov yield distributions. At low mis-identification values there is a slight mis-match between the shape of the curves, however the general trend and the tail to larger background yield values are matched very well. Fig. 5.31 (b) shows the result of an exponential fit to the simulated distribution. The corresponding analysis yielded a weighting factor of (0.77 ± 0.02), and a slope parameter of (-0.4998 ± 0.0073). Therefore, an expected background value of (1.54 ± 0.02) PE per simulated Čerenkov event in the MAPMT window is expected, at the $4\,\sigma$

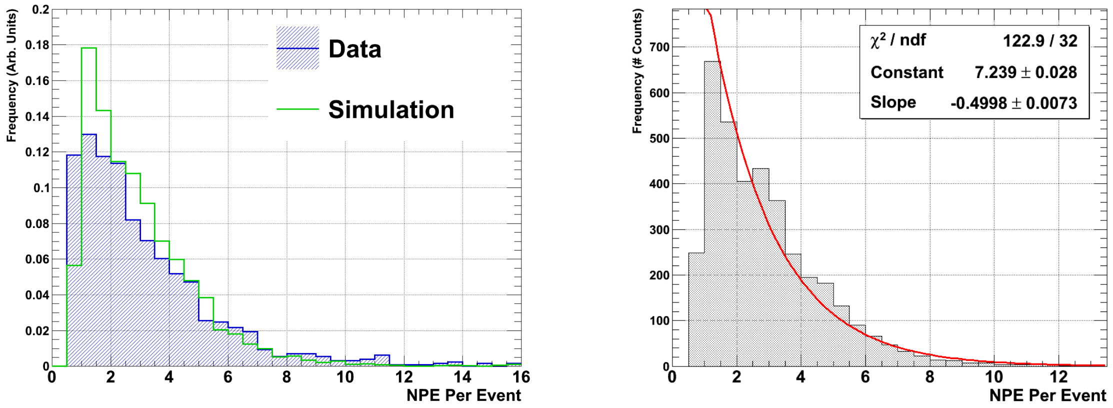

(a) (b)

Figure 5.31: (a) Comparison between simulation and data curves for mis-identified hit levels resulting from Čerenkov light produced by the cosmic muon passing through the MAPMT window. The masked MAPMT experimental configuration and a pedestal threshold cut of $4\,\sigma$ are used. (b) An exponential decay function is fit to the simulated distribution, to quantify the resulting expected background in simulated measurements.

cut level. This is close to the value of (1.78 ± 0.18) PE extracted from data.

The weighting factors and background levels obtained from data with the clustering algorithm are given in Table 5.10 for comparison purposes with the template algorithm. In general the backgrounds obtained with the clustering algorithm were lower than those extracted with the template technique. This is expected, since the template technique is limited in the topology of events in which it will completely eliminate crosstalk from the muon hit in the MAPMT window. The clustering algorithm has more chance to identify hits resulting from the muon event in the glass window, beyond the 9 pixel mask area of the template algorithm. However, the independent evaluation of the background in both analysis techniques allows for the appropriate mis-identification correction to be applied in each analysis case, resulting in the extraction of the yields of Čerenkov light produced from the aerogel as described below.

Table 5.10: Background yield values extracted with the clustering algorithm, to allow correction for the mis-identification of Čerenkov light created by the muon hit in the MAPMT window as originating from the aerogel radiator.

Pedestal Cut [σ]	**Weighting Factor**	**Mis-identification [NPE]**
3	0.87	2.75 ± 0.13
4	0.67	1.31 ± 0.06
5	0.44	0.62 ± 0.05

Čerenkov Yields from Aerogel

The raw aerogel Čerenkov ring yield distributions obtained from data for 1 cm and 2 cm thicknesses of radiators, using a 4 σ pedestal threshold cut with the template analysis algorithm, are shown in Fig. 5.32. The yields have not been corrected for background or geometrical effects, and Gaussian fits to the curves are also visible. As expected, the yield obtained with the 2 cm radiator thickness is larger than that with 1 cm. The equivalent comparisons with simulation results are shown, for 1 cm and 2 cm aerogel thicknesses, in Figs. 5.33 (a) and (b) respectively. Both comparisons indicate that in general the mean positions of the distributions are well-recovered from simulation, but there exists a resolution mis-match between the simulation and data, where the simulation curves are slightly narrower and have smaller tails than the data distributions.

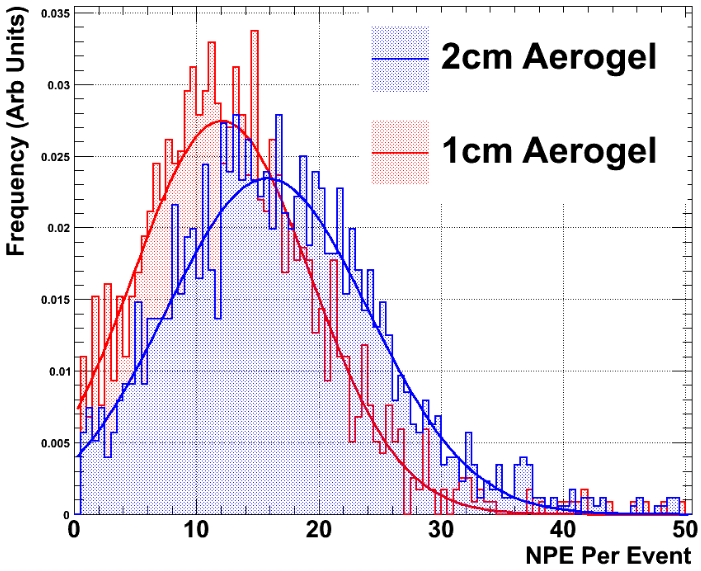

Figure 5.32: Uncorrected aerogel Čerenkov yield distributions for 1 cm and 2 cm thicknesses of aerogel, using the template algorithm and a 4 σ pedestal threshold. In other words the NPE detected per aerogel Čerenkov ring event by the H8500 MAPMT.

Further analysis of these aerogel Čerenkov yields and their characteristics confirm the requirement of an absolute calibration of the MAPMT before performing yield measurements in this specific experimental setup. It is not sufficient to simply count the pixels with hits above threshold, but rather the extracted charge in each hit pixel must be converted to a corresponding NPE. To convert the charge from one pixel into NPE, the extracted charge is divided by that pixel's gain value. As described in Section 5.1.1, the gain is determined from a combination of absolute and relative calibrations of the MAPMT. This conversion is neces-

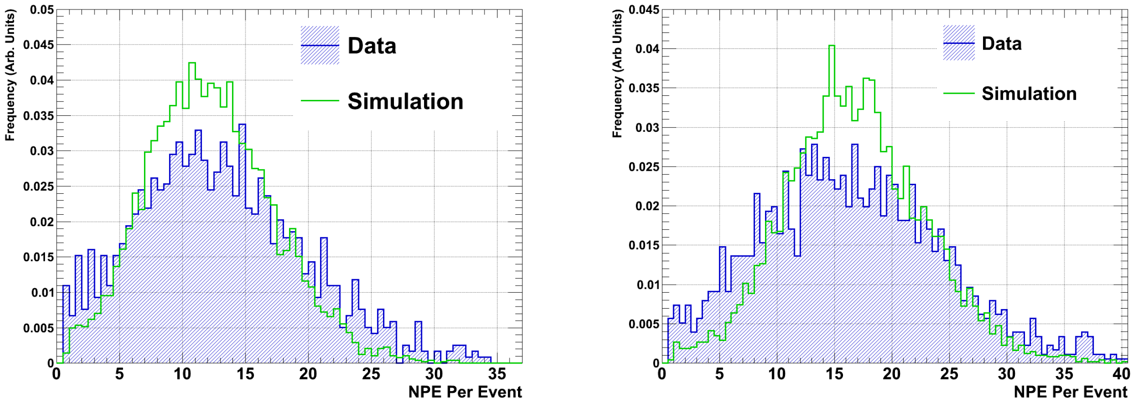

(a) (b)

Figure 5.33: Comparison between simulation and data curves obtained for the aerogel Čerenkov ring yields with (a) 1 cm and (b) 2 cm thicknesses of aerogel.

sary due to the relatively short expansion volume of the setup, required to catch the entire Čerenkov ring on one MAPMT face and resulting in the density of Čerenkov photons striking individual pixel areas being greater than one. For example, Fig. 5.34 (a) shows the number of pixels per Čerenkov event with hits above threshold, and reveals mean values which are lower than those extracted for the Čerenkov yield distributions shown in Fig. 5.32. The origins of this are shown in Fig. 5.34 (b), which gives the signal strength in terms of the NPE extracted from each hit pixel. The distributions are clearly peaked above a value of 1 PE per

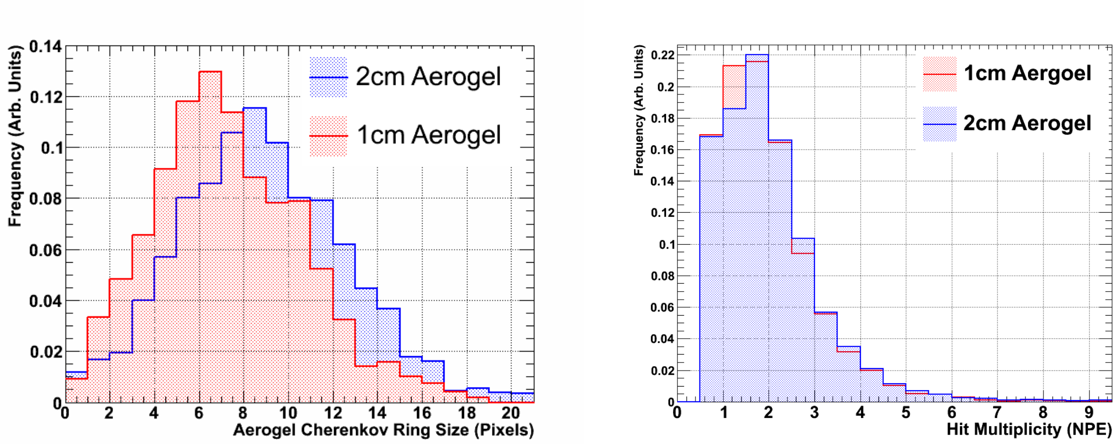

(a) (b)

Figure 5.34: Multiplicity and occupancy characteristics of the aerogel Čerenkov rings, for data analysed with the template algorithm and a $4\,\sigma$ pedestal threshold. (a) The number of pixels per event showing hits above the pedestal threshold and (b) the corresponding extracted signal charge, in terms of NPE, from each of the hit pixels.

hit pixel and both data-sets demonstrate significant tails to even higher values. This effect is also observed in the simulation studies, examples of which are shown in Figs. 5.35 (a) and (b) for the 1 cm thickness aerogel radiator setup. From Fig. 5.35 (a), mean values of 7.046 pixels

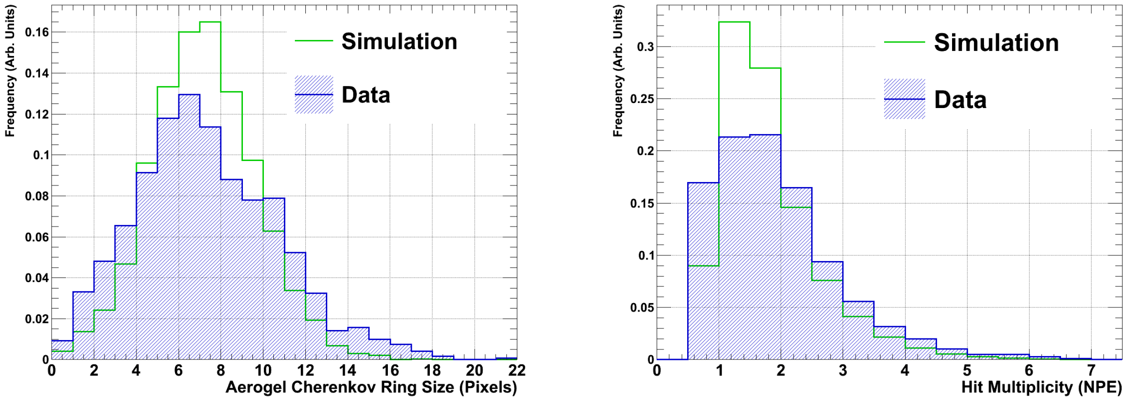

(a) (b)

Figure 5.35: Comparison between data and simulated multiplicity and occupancy characteristics of the aerogel Čerenkov rings for the 1 cm aerogel thickness configuration, analysed with the template algorithm and a 4 σ pedestal threshold. (a) The number of pixels per event showing hits above the pedestal threshold and (b) the corresponding extracted signal charge, in terms of NPE, from each of the hit pixels.

and 7.193 pixels are extracted from data and simulation respectively for the number of pixels with hits above threshold in one aerogel Čerenkov ring event, indicating a strong agreement. Furthermore, from Fig. 5.35 (b), the mean occupancy of each pixel is returned as 1.973 PE and 1.817 PE from data and simulation respectively, validating the observation in data. Very similar agreements between data and simulation are obtained with the 2 cm radiator setup.

A pedestal threshold cut scan was performed in order to assess the resulting influence upon the aerogel yield measurements. The resulting Čerenkov yield distribution curves obtained with the template analysis algorithm, for the different thresholds and both radiator thicknesses, are shown in Figs. 5.36 (a) and (b). The results obtained from Gaussian fits to the distributions are summarised in Table 5.11. As expected, since at higher thresholds the cut begins to

Table 5.11: Template algorithm raw aerogel Čerenkov yield distribution mean and width values, prior to application of background or geometrical corrections.

Pedestal Cut [σ]	**Aerogel Thickness [cm]**	**Yield Mean [NPE]**	**Yield Width [NPE]**
3	1	15.65 ± 0.27	8.010 ± 0.270
	2	19.62 ± 0.24	9.184 ± 0.220
4	1	12.05 ± 0.26	7.269 ± 0.272
	2	15.78 ± 0.23	8.273 ± 0.207
5	1	10.73 ± 0.19	5.492 ± 0.166
	2	13.73 ± 0.19	6.766 ± 0.151

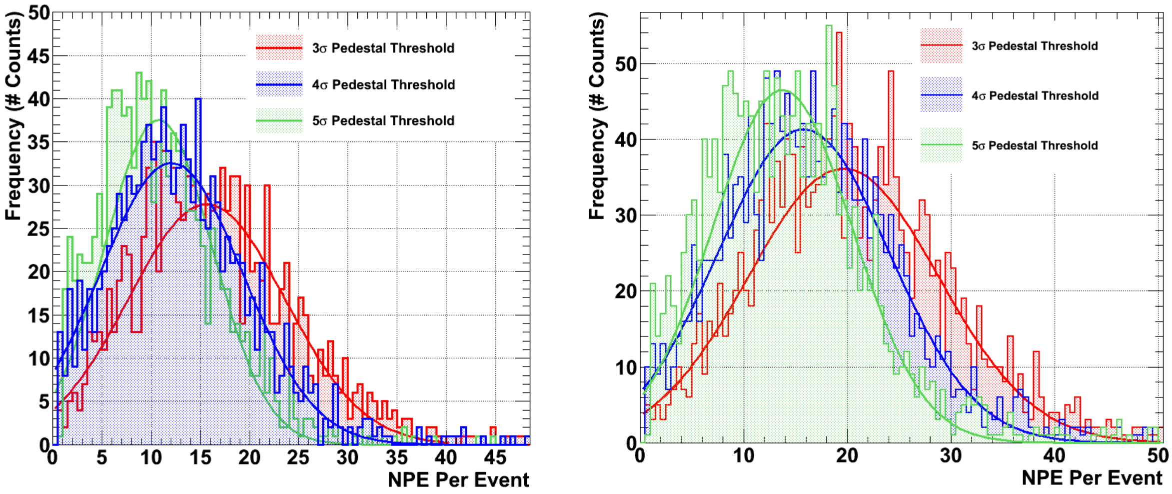

(a) (b)

Figure 5.36: Aerogel Čerenkov yield distributions obtained for $3\,\sigma$, $4\,\sigma$ and $5\,\sigma$ pedestal threshold cuts with (a) 1 cm and (b) 2 cm thicknesses of radiator material.

remove signal events, the Čerenkov yield decreases. At the $3\,\sigma$ level it may include some noise additions, resulting in the significantly higher yields at this cut level in both of the 1 cm and 2 cm thickness cases. The widths of the distributions decrease with increasing pedestal threshold cut, and in general the widths of the 2 cm case are slightly larger than those for 1 cm thickness of aerogel, as expected. Equivalent sigma width values obtained from simulations, for 1 cm and 2 cm aerogel thicknesses and for a $4\,\sigma$ pedestal cut threshold, yield (5.012 ± 0.063) PE and (5.893 ± 0.071) PE respectively. This confirms the observation from Figs. 5.33 (a) and (b), that the data curves are broader than those extracted from simulation. The data mean and width results are further illustrated in Fig. 5.37, where the error bars indicate the minimisation fitting errors of the Gaussian fits applied to the data. It should be emphasised here, that both the results in Table 5.11 and Fig. 5.37 are uncorrected for the background from the muon hit in the MAPMT window, and they are subject to 10 % scale uncertainty from the absolute calibration of the device.

The results from the threshold scan, of the mean yields per Čerenkov ring for different radiator thicknesses, are compared to the equivalent results from an analysis performed with the clustering algorithm in Table 5.13. The appropriate background corrections to subtract scattered light resulting from the muon hit in the MAPMT window, specific to both analysis algorithm and pedestal threshold, have been applied. The error bars represent the convolution of fitting errors from the Gaussian fits applied to the Čerenkov and mis-identified yield distributions. The yields obtained from the template algorithm are systematically higher than those extracted using the clustering algorithm. In the extreme cases the difference is greater

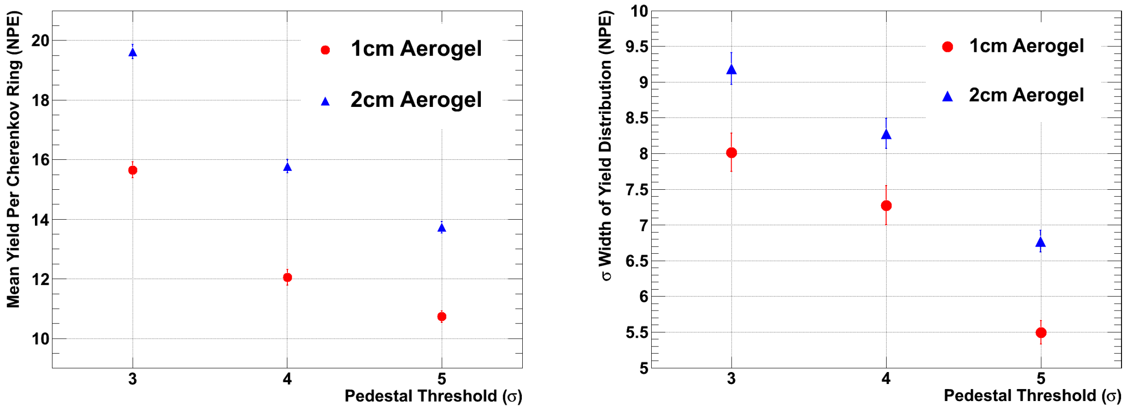

(a) (b)

Figure 5.37: Template algorithm results for raw aerogel Čerenkov yield distribution mean and width values, prior to application of background or geometrical corrections.

Table 5.12: Template and clustering algorithm results, as a function of pedestal threshold cut, for the aerogel Čerenkov yield values after background correction to subtract light scattered by the muon hit in the MAPMT window.

Pedestal Cut [σ]	**Aerogel Thickness [cm]**	**Analysis Algorithm**	**Background Corrected Yield Mean [NPE]**
3	1	Template Clustering	11.09 ± 0.34 9.20 ± 0.33
3	2	Template Clustering	15.06 ± 0.31 12.02 ± 0.32
4	1	Template Clustering	10.27 ± 0.32 9.22 ± 0.29
4	2	Template Clustering	14.00 ± 0.29 12.87 ± 0.24
5	1	Template Clustering	9.74 ± 0.20 7.49 ± 0.40
5	2	Template Clustering	12.74 ± 0.20 12.56 ± 0.20

than 2 PE, however on average the results are relatively close to each other when considered with the 10 % calibration uncertainty. The values extracted for the 2 cm data-set, with the 5 σ cut are almost identical. Although the results from the template algorithm consistently decrease with increasing pedestal cut, in both the 1 cm and 2 cm radiator thickness cases, this is not observed with the clustering algorithm. For the 2 cm data-set with the clustering algorithm, the yield appears to be almost independent of the pedestal cut. However with the 1 cm data-set, there is a significant decrease in the yield when a 5 σ cut is used. These results are summarised further in Fig. 5.39. The difference between the trends is most likely caused by the different ways with which each analysis algorithm handles crosstalk signals. For instance,

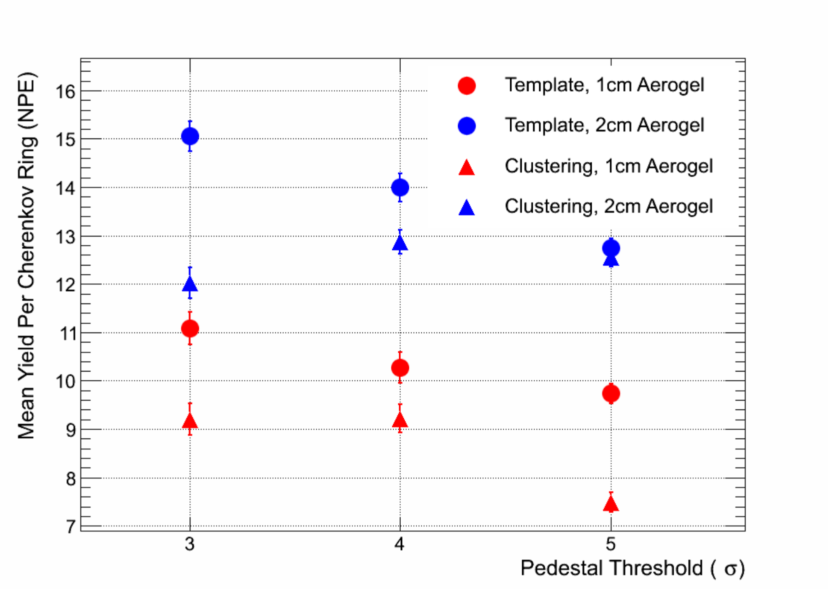

Figure 5.38: Čerenkov yields obtained with both the template and clustering algorithms as a function of pedestal threshold cut, and for both thicknesses of radiator which were tested, after background correction to subtract light scattered by the muon hit in the MAPMT window.

at the $3\,\sigma$ threshold cut an increased level of random noise and crosstalk originating from light scattered from the muon hit in the MAPMT window is included in the measured signals. In the case of the clustering algorithm this results in the muon cluster merging with the aerogel Čerenkov ring. The overall effect, therefore, is to increase the muon cluster size and decrease the measured yield from the aerogel ring. This is not observed with the template algorithm, since the muon hit size is always limited, and in this case the excess noise will be included in the aerogel Čerenkov yield measurement. This results in an increased yield for the template algorithm at the $3\,\sigma$ cut value, as shown in Fig. 5.39. As the threshold cut is increased these noise effects are diminished, however eventually the threshold begins to exclude true aerogel Čerenkov signals and the yield values therefore decrease in all cases.

The simulation studies were used to validate the uncorrected Čerenkov yields. Therefore, the un-corrected results obtained with the standard $4\,\sigma$ pedestal threshold cut and both analysis algorithms are compared to the equivalent values which are extracted from simulations and are shown in Table 5.13. The comparisons obtained between simulation and data are extremely close, with the simulation results only slightly higher than those extracted from data, in most cases. The detection of Čerenkov light is extremely sensitive to the single photon resolution of the photon detector, and so it is possible that this quantity is not simulated accurately enough for the H8500 MAPMT. In the prototype simulation one resolution value is used for all pixels of the MAPMT, whereas results from laser scans illustrate the individual pixels display different

Table 5.13: Raw aerogel Čerenkov yields compared between both analysis algorithms and simulation results. A 4 σ pedestal threshold cut has been applied and the errors are the corresponding fitting errors.

Aerogel Thickness [cm]	**Data or Simulation**	**Analysis Algorithm**	**Un-Corrected Yield Mean [NPE]**
1	Data Simulation	Template	12.05 ± 0.26 12.00 ± 0.10
1	Data Simulation	Clustering	10.53 ± 0.33 10.81 ± 0.08
2	Data Simulation	Template	15.78 ± 0.23 16.64 ± 0.09
2	Data Simulation	Clustering	14.18 ± 0.20 14.35 ± 0.02

resolutions depending upon their absolute gains. In the raw hits obtained from the analyses, even before the tailored background corrections, the template yields are consistently slightly higher than the cluster algorithm results. Upon consideration of the MAPMT calibration 10 % uncertainty however, the results between the different algorithms and also between data and simulation all agree within systematic errors, as shown graphically in Fig. 5.39. The points for the template algorithm simulation and data results obtained with the 1 cm thickness aerogel setting appear extremely close to each other in Fig. 5.39.

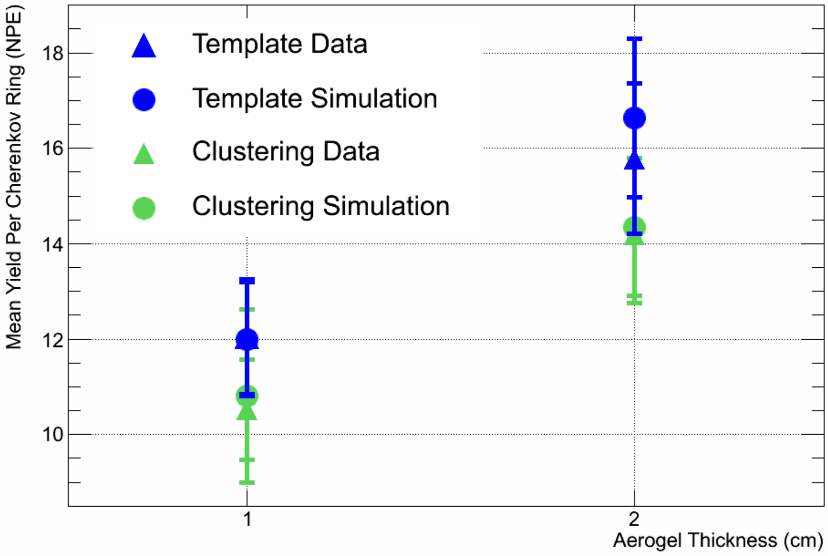

Figure 5.39: Raw aerogel Čerenkov yields compared between both analysis algorithms and simulation results. A 4 σ pedestal threshold cut has been applied. All results are in agreement, on considering the error bars which are derived from a 10 % scale gain uncertainty in the absolute calibration method of the MAPMT.

Since the raw results obtained are confirmed through the simulations, within error bars, the final values are then extracted from data. The standard 4 σ pedestal cut threshold is used, and the yields are corrected for both the background from the muon hit in the MAPMT window and the previously described 3 % and 10 % geometrical acceptance factors. The resulting finalised aerogel yields obtained per Čerenkov ring from data, for both analysis algorithms and thicknesses of aerogel radiator, are given in Table 5.14 and agree with each other within systematic errors.

Table 5.14: Final aerogel Čerenkov yields compared between radiator thicknesses and analysis algorithms, obtained with the cosmic muon RICH prototype. The values have been corrected for the background levels caused by the muon hit passing through the MAPMT window and geometrical acceptance losses. The errors indicate the uncertainty in the absolute gain calibration of the MAPMT.

Aerogel Thickness [cm]	**Analysis Algorithm**	**Yield [NPE]**
1	Template	10.58 ± 1.06
	Clustering	9.50 ± 0.95
2	Template	15.40 ± 1.54
	Clustering	14.16 ± 1.42

5.1.6 Summary: Small-Scale Prototype Studies

The finalised Čerenkov yield results illustrate that the H8500 MAPMT is capable of detecting the low yield Čerenkov light produced from aerogel radiators. The H8500 may therefore be successfully used, in a similar experimental configuration, to detect a sufficient number of photons from Čerenkov rings events corresponding to the direct light case requirements of the CLAS12 RICH detector. However, further confirmation of this H8500 MAPMT success was required in a setup closer to that which is expected in the final CLAS12 RICH detector and this confirmation will be demonstrated through results obtained with a study of a large-scale RICH prototype.

5.2 Large-Scale Prototype Studies with Mixed Hadrons

In addition to studies with the small-scale cosmic muon RICH prototype, investigations were performed using a large-scale prototype RICH detector at a test-beam facility, in a more realistic noise environment and with a configuration more comparable to that of a final CLAS12 RICH detector. The experiments were performed collaboratively within a group of researchers constituting the *CLAS12 RICH Collaboration*, from several institutes world-wide. The majority of the RICH prototype was designed and assembled by members of the CLAS12 RICH Collaboration from the LNF and Ferrara sections of the INFN. The setup of the equipment at the test-beam experiment and the acquisition of data was all performed collaboratively by the author with other members of the CLAS12 RICH Collaboration. The results which are shown were obtained by the author only, and where input from others has been made it is stated and/or referenced explicitly.

The main aim of the prototype RICH test-beam study within the scope of this thesis was to further confirm the choice of the Hamamatsu H8500 MAPMTs as the photon detector for the CLAS12 RICH. To achieve this, the prototype Čerenkov light yield and ring resolution parameters as measured by the MAPMTs were studied, both of which are crucial observables for any RICH detector and contribute significantly towards its separation power. The resulting π/K separation power of the test-beam prototype was also studied as a function of momentum. Techniques developed throughout the small-scale cosmic muon RICH prototype study were incorporated into the analysis of data from the large-scale prototype, such as the use of hit clustering to minimise the influence of crosstalk effects. The test-beam facility, experimental setup of the large-scale RICH prototype, analysis methods and results are described below.

5.2.1 Test-Beam Facility

The test-beam studies were carried out at the the T9 dedicated test-beam area, situated in the East Area [183] of the CERN Proton Synchrotron (PS) [184]. Two separate test-beam allocations were used, in both July - August and November - December of 2012, and the results shown are mostly from the second test-beam period. The T9 beam line [183, 185, 186] offers a secondary beam of mixed hadrons, mostly pions and kaons, with tunable momenta from 0 - 15 GeV/c and selectable polarity. It is therefore ideal for studying situations which are likely to exist in the final CLAS12 RICH detector, in terms of particle species and kinematics. For the duration of the test-beams the particles were set to have a negative polarity, and reference beam momenta of 6 GeV/c, 7 GeV/c and 8 GeV/c were used.

A schematic of the beam lines present in the PS East Area is shown in Fig. 5.40 (a), and the derivation of the T9 beam is further described by the diagram in Fig. 5.40 (b). The primary beam consists of protons with energies of 24 GeV, which are initially extracted slowly from the CERN PS. The protons then strike a fixed target, termed the North Target. Several target materials are available, however for the test-beam studies aluminium (Al) was used since it provided the maximum yield. The structure of the beam delivered to the T9 test-area is pulsed, with 1 - 3 spills of particles delivered every 40 s. The maximum theoretical flux of the beam is $\sim 10^6$particles/spill [186]. Individual particle species fluxes will depend upon the beam

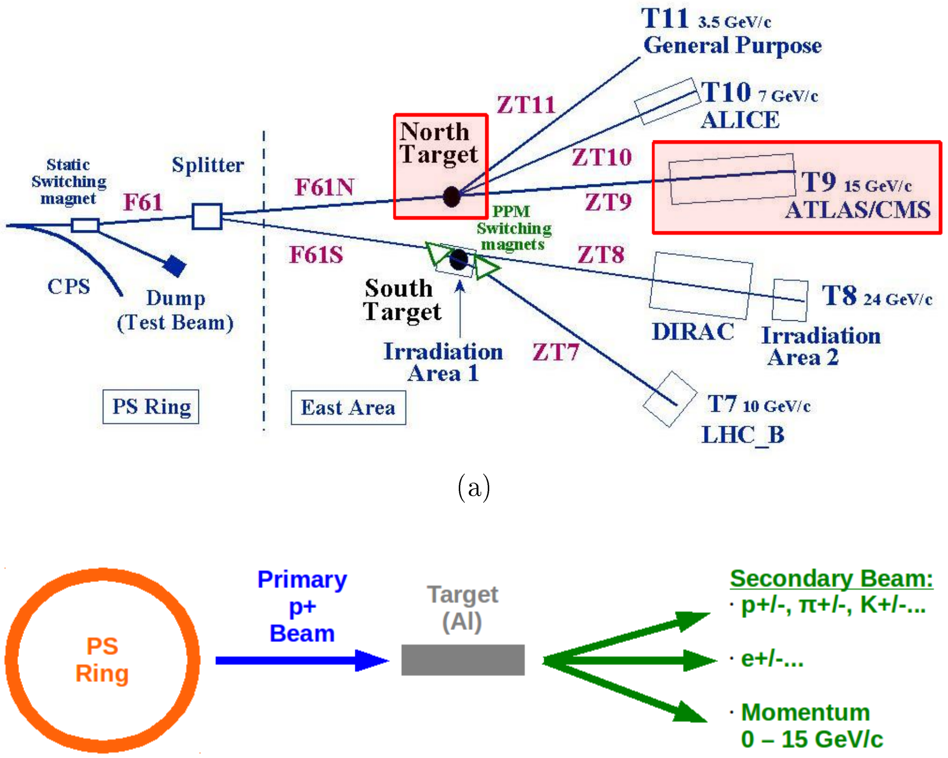

(a)

(b)

Figure 5.40: (a) Aerial view of the CERN Proton Synchrotron (PS) East Area. The T9 beam-test area, which was used for RICH prototype tests, is highlighted, along with the North Target which is used to produce the beam. Image taken from [183]. (b) Derivation of the T9 beam. Protons are extracted from the CERN PS and then strike the North Target, producing a secondary beam of mixed hadrons.

momentum, as shown in the example given in Fig. 5.41. The example is not an experimental measurement and is a typical calculation to give an idea of the magnitudes of the relative intensity differences between particle species only, which in reality may vary from the values shown. With the negative particle polarity and over the reference momenta which were studied with the prototype, pions were expected to be the most abundant component of the beam, followed by kaons and then antiprotons. The beam momentum uncertainty in the test-beams relied upon the opening widths of the slits used to collimate the beam. Throughout the test-beams the horizontal and vertical collimator settings yielded beam momentum uncertainties of 1 % and 2.2 % respectively, and the dimensions of the beam were larger in the horizontal than in the vertical directions. For the test-beam studies the focus of the beam was placed behind the photon detection plane of the RICH prototype, with respect to the beam direction, and the beam profile at the focal point was slightly less than $\sim$(15 mm $\times$ 10 mm). The test-beam experimental and RICH prototype setups are described in further detail below.

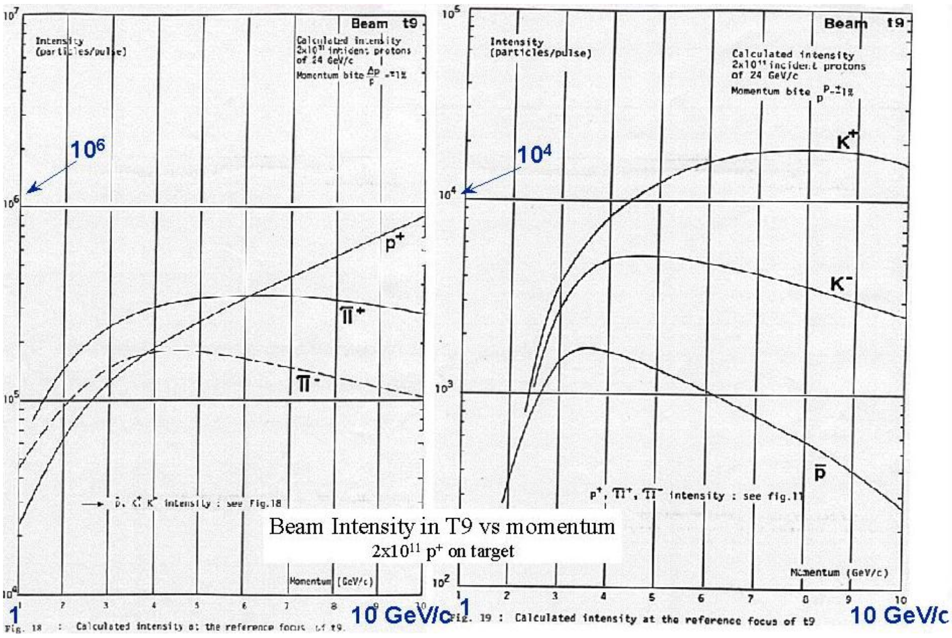

Figure 5.41: Example intensity of the T9 secondary beam as a function of momentum for several particle species and different polarities, calculated for 2×10^{11} protons with momenta of 24 GeV/c incident upon the target. Image taken from [183].

5.2.2 Prototype Experimental Setup

Several detectors were used in conjunction with the large-scale RICH prototype throughout the test-beam studies, these included: a beam line threshold Čerenkov counter, Gaseous Electron Multiplier (GEM) chambers and scintillation counters. The arrangement of the detectors in the experimental setup is given in Fig. 5.42. A second, smaller-scale RICH prototype was also included in the setup, which used SiPMs as the photon detectors in a proximity-imaging arrangement to measure Čerenkov rings produced from aerogel tiles directly. This RICH was used to study the feasibility of SiPM technology for future upgrade plans of the CLAS12 RICH detector, beyond the first sector of the CLAS12 RICH, and will not be described further in this thesis.

Figure 5.42: Setup of the large-scale RICH prototype test-beam. A combination of a threshold Čerenkov counter, trigger scintillators, and GEM chambers were used alongside the RICH prototype under study, and a second smaller-scale RICH incorporating SiPMs as the photon detectors.

The first detector to be seen by the beam was the beam line threshold Čerenkov counter, which was provided by CERN in the T9 test-beam area. The Čerenkov counter was filled with CO_2 gas and read out by a single channel PMT. The pressure of the gas was set at 2 ATM for pions to be above the Čerenkov threshold, producing signals in the detector, and for kaons and any other heavier particles to be below threshold. The signal from the Čerenkov counter was extracted to a QDC and used as an offline trigger for pion/kaon separation analyses. An example of a QDC spectrum obtained with the Čerenkov counter is shown in Fig. 5.43. The events which create signals above the pedestal peak, corresponding to the range marked by the blue arrow, were flagged as originating from pions. Below the vertical line no signal is extracted from the Čerenkov counter, indicated by the green arrow, and these events were assumed to mostly consist of kaons. Although, there will exist some contamination from heavier particles present in the beam and also pions with velocities below β_{thr} may also contribute to these events. Readout of the beam line Čerenkov counter was only included in the November-December test-beam.

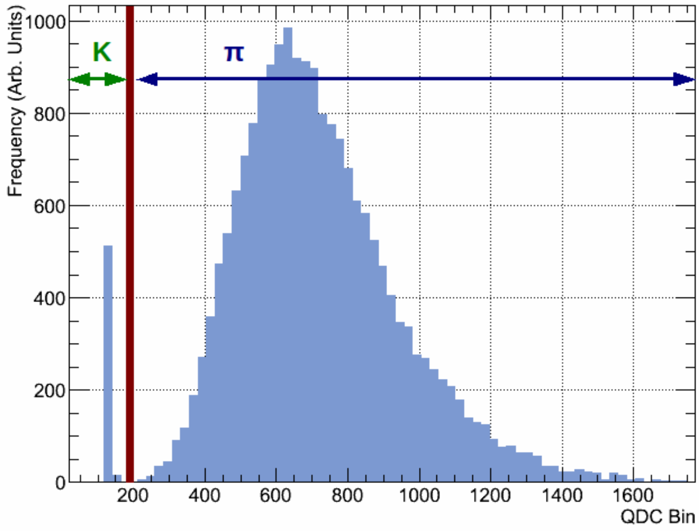

Figure 5.43: Example of a charge spectrum extracted from a beam line threshold Čerenkov counter, using a beam momentum of 8 GeV/c. The Čerenkov counter was used with tests of the large-scale prototype to select pion and kaon events in offline analyses.

Two GEM chambers were used for charged particle tracking in the setup. Descriptions of GEM technology and electron multiplication principles in gaseous detectors may be found in [20, 29, 30]. The upstream GEM was placed in front of the RICH prototype, and the downstream GEM was placed at a distance of 4 227 mm away, located behind the large-scale RICH prototype. An image of one of the GEM chambers is shown in Fig. 5.44. The GEM chambers were assembled in-house at JLab, and the charge signals were amplified and integrated using

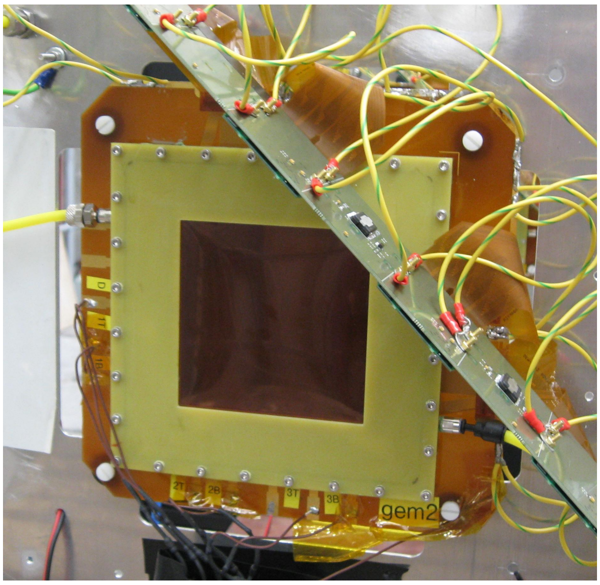

Figure 5.44: One of the two gaseous electron multiplier chambers used for charged particle tracking in the test-beam of the large-scale RICH prototype.

a combination of the APV readout chip [187] and custom made readout boards which were designed by members of the CLAS12 RICH Collaboration. The GEM chambers were filled with a $30:70$ $\mathrm{CO_2}:\mathrm{Ar}$ gas mixture, they had dimensions of $10\,\mathrm{cm} \times 10\,\mathrm{cm}$ and contained 256 horizontal and 256 vertical wire strips for the configuration of electric fields and signal collection. The horizontal and vertical strips offered a combined spatial resolution of $\sim 400\,\mu\mathrm{m}$. The use of charged particle track information from the GEMs aimed to improve Čerenkov ring resolutions and fitting procedures, by fixing the ring centre positions. This is analogous to the situation envisaged in the final CLAS12 RICH apparatus, where precise tracking of the particles will be performed by the DCs.

Two scintillation counters were used to provide a common trigger signal for the readout of all detectors of the setup. Each scintillation counter comprised of $3\,\mathrm{cm} \times 2\,\mathrm{cm}$ rectangles of plastic scintillator material coupled to a single channel PMT. The trigger counters were arranged orthogonal to each other and provided an overlapping area of $\sim 1\,\mathrm{cm}^2$ for the beam to pass through. The counters were mounted on a motorised table which was moveable in both the horizontal and vertical directions. Before data-taking their position in the beam was optimised, using a scaler to map their count rates as a function of the position of the table and find the location corresponding to the maximum coincidence count rates. The trigger electronics scheme was setup using standard NIM electronics. In order for the DAQ to be readout, a coincidence was required between both trigger counters and then the resulting trigger signal was distributed amongst all detectors, which each had individual readout electronics.

The RICH prototype consisted of two setups, dedicated to study the direct and reflected Čerenkov light imaging cases individually. The direct light imaging case, looked at in detail in this thesis, provides ample data to validate the choice of the H8500 MAPMTs as the photon detector for the CLAS12 RICH. A full study of the reflected light case would require an in-depth analysis taking mirror mis-alignment effects and the optical qualities of the aerogel materials and mirrors used into account. Furthermore the main aim of the reflected light setup was to assess the validity of the CLAS12 RICH design feature whereby Čerenkov light produced must be reflected and pass through aerogel material a further two times after production. The geometry of the reflected light test-beam setup is not directly transferrable to projections for the CLAS12 RICH performance, although analysis studies performed by other members of the CLAS12 RICH Collaboration will be crucial to gain understanding of the reflected light case and confirm model inputs for the Monte Carlo simulations of the CLAS12 RICH system. Due to the similarity of the geometries, the direct light test-beam results may be extrapolated for CLAS12 RICH performance projections and model inputs to the CLAS12 RICH simulations. The direct light case of the prototype is described below.

RICH Prototype: Direct Light Configuration

For the direct light imaging case the prototype geometry was matched as closely as possible to the proposed final CLAS12 RICH geometry - a schematic of the setup is shown in Fig. 5.45. Aerogel tiles, with cross-sectional dimensions of 6 cm × 6 cm, from the Budker Institute of Nuclear Physics in Novosibirsk (Russia) were used as the Čerenkov radiators, as shown in Fig. 5.46 (a). Several properties of the aerogel radiators were studied throughout the test-beams, including thickness ($t = 2$ cm - 4 cm), optical quality and refractive index (n = 1.04 -

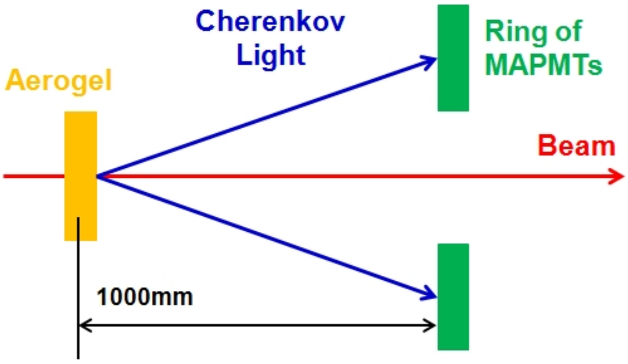

Figure 5.45: Cross-sectional schematic of the direct light configuration of the RICH test-beam prototype, as viewed from the side.

1.06), to evaluate the corresponding impact on the RICH prototype performance. By design, the radiator was placed at 1 000 mm upstream from the photon-detection plane, matching the envisaged expansion gap of the final CLAS12 RICH detector. A geometrical survey of the experimental setup, performed by members of the CLAS12 RICH Collaboration found the actual distance between the aerogel mount and plane of MAPMTs used throughout the test-beams to be 1 004 mm, with an accuracy of 1 or 2 mm [188].

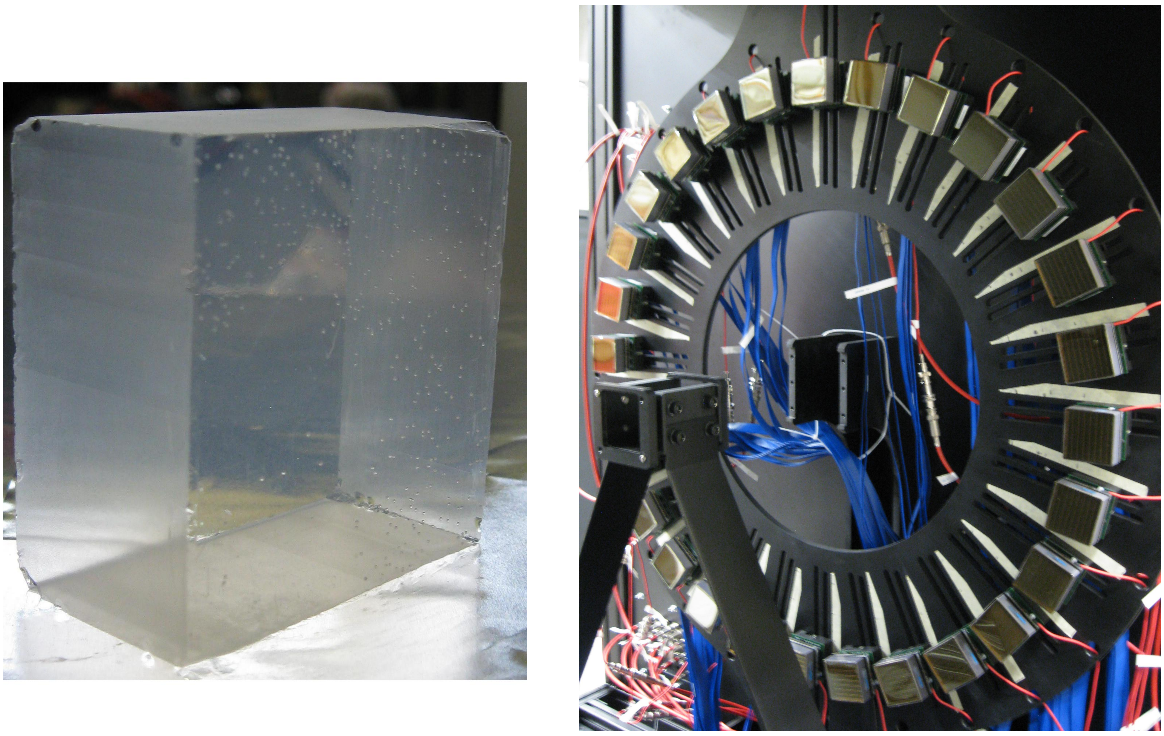
(a) (b)

Figure 5.46: (a) Example aerogel tile used as a Čerenkov radiator in the test-beam prototype. The tile has a nominal refractive index of n = 1.05 and dimensions of 6 cm × 6 cm × 2 cm. (b) Setup of the H8500 MAPMTs in the direct light imaging configuration of the test-beam study. 28 H8500 MAPMTs were arranged in a ring, and could be moved radially to image Čerenkov rings of different radii.

Immediately before and after the test-beam studies, the optical properties of the aerogel tiles were fully characterised by members of the CLAS12 RICH Collaboration from the INFN section of Ferrara. The refractive indices of the tiles were measured using the standard prism method [189], and the transmittance curves of the tiles were mapped through measurements with a spectrophotometer. The transmittance measurements allowed the extraction of absorption and scattering length spectra from the Hunt formula as described in Section 2.3.1. Throughout the test-beam studies relative shifts in the transmittance of the aerogel tiles were monitored offline, by measuring the current extracted from a photodiode in response to a laser beam as it was shone through the aerogel tiles.

For the photon detectors, a ring of 28 H8500 MAPMTs was used as shown in Fig. 5.46 (b). The MAPMTs could be moved radially to allow for imaging of Čerenkov rings with different radii, resulting from tests performed with various aerogel refractive indices. Both standard borosilicate and UV-extended window type MAPMTs were tested, to study both yield differences caused by the higher intensities of Čerenkov photons produced in the UV-wavelengths and Čerenkov ring resolution smearing effects caused by the Rayleigh scattering of photons at the UV-wavelengths. The MAPMT types were arranged in alternating order around the circumference of the ring. Prior to the test-beam studies, the gain uniformities of the 28 MAPMTs used were fully characterised by CLAS12 RICH Collaboration members of the LNF section of the INFN, using a laser-scanning technique similar to that previously described in Section 4.5 and performed at a wavelength of 407.2 nm. The HVs of the H8500 MAPMTs were set to -1 075 V throughout the entire test-beam studies. This HV value reduced the fraction of single PE events lost below the pedestal distributions to ~12 - 15 %, in comparison with the value of 20.8 % extracted with the H8500 MAPMT tested at 1 000 V and as described in Section 4.5.1. The readout of the signals from the MAPMTs was based upon the MultiAnode ReadOut Chip (MAROC).

RICH Prototype: MAROC3 Readout Electronics

The MAROC ASIC [190, 191, 192, 193] was originally developed by the IN2P3 Omega micro group [10] for the charge readout of the 64-channel Hamamatsu H7546 MAPMTs used in the ATLAS luminometer, and it is readily applicable to similar photon detectors. The most recent version of the ASIC, named MAROC3, was used in the large-scale prototype setup. The ASIC was designed to provide 100 % trigger efficiency for charge signals covering the dynamic range of $\frac{1}{3}$ PE to ~30 PE, which translates to charge values of ~50 fC and 5 pC respectively for an MAPMT operated with a gain of $\sim 1 \times 10^6$. The linearity over this dynamic range is $< 2\,\%$ and the noise should be less than 2 fC. In principle, the chip is therefore suitable for the CLAS12 RICH detector, which requires the detection of single photon level signals.

The MAROC3 ASIC is also very appealing for use with photon detectors such as the H8500 MAPMT, since it offers pre-amplification for each of the 64 individual channels of the MAPMT through an 8-bit variable gain pre-amplifier. The amplification allows for relative gain uniformity corrections up to a maximum factor of 4, in 255 steps, with an accuracy of

---

[10] http://omega.in2p3.fr/

1.5 % Additionally, noisy channels may be switched off by setting the amplification to zero. A 1 : 4 uniformity correction would be sufficient to equalise all pixel gains in the two H8500 MAPMTs which were tested so far with the laser scanning setup, as shown for example in the relative gain map results given in Fig. 4.15 (a) and Fig. 4.16 (b).

A simplified schematic of the chip design is shown in Fig. 5.47, and fuller descriptions of the electronic design of the chip may be found in [190, 191, 192, 193]. The simultaneous extraction of both an analogue charge measurement and a digital trigger output for each of the 64 MAPMT channels is available with the MAROC3 ASIC, as illustrated in Fig. 5.47. For the analogue chain, termed the *slow channel* (on the order of tens of μs), the pre-amplified signal is fed through a variable slow-shaper, programmable to optimise signal to noise ratios for different pulse-shapes, and Sample and Hold (S&H) buffers. Analogue to Digital charge Conversion (ADC) is provided through a Wilkinson ADC, which is not shown in Fig. 5.47, and the multiplexed output signals are available from all 64 channels of the MAPMT. In parallel, 64 discriminated trigger outputs are produced via the *fast channel* (~30 ns). In this channel, the pre-amplified MAPMT signals pass through a fast shaper and are then discriminated by comparators with 10-bit programmable Digital to Analogue Converters (DACs) used to provide the threshold voltage. The threshold voltage is common amongst all 64 input channels, and any required variation must be compensated for by correct setting of the 64 individual pre-amplifier values. If the MAPMT signal is above threshold, then a logic-1 state will be produced. Both

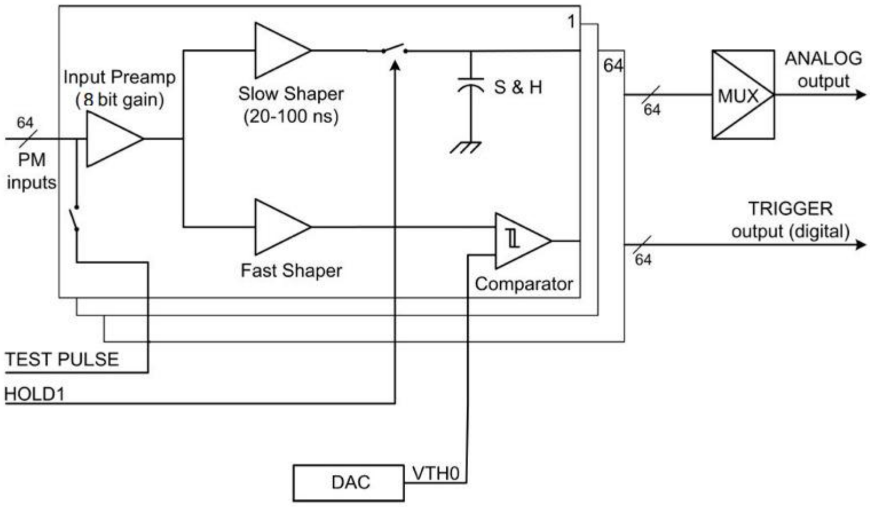

Figure 5.47: Schematic illustrating the principle of the MAROC3 ASIC used for readout of the MAPMTs of the large-scale prototype. Image created by P. Musico.

the slow and fast channels are extracted during readout of the MAROC3, however a sparsified mode may be enabled in which data from the fast channel only is recorded. The sparsified mode was not used in the test-beams, in order to accurately study the MAROC3 and H8500 charge responses. If these electronics were to be used in the final CLAS12 RICH, such a sparsified mode would be extremely useful in coping with the expected required readout rates of 20 kHz. This method would be suitable, once the detector system is fully understood after the commissioning period, as it would be sufficient to record only the hits above threshold in each event and their positions.

The architecture of the readout electronics used for the test-beam prototype setup was originally developed by P. Musico (Genova section of the INFN) and further description of its design may be found in [194]. Prior to their use in the test-beams, the readout electronics were fully calibrated and characterised by several members of the CLAS12 RICH Collaboration from the Federico Santa María Technical University, and the Istituto Superiore di Sanita and LNF sections of the INFN. A photograph of the electronics and a schematic of the readout architecture used are shown in Figs. 5.48 (a) and (b). In the prototype, each MAPMT connected to one Front-End (FE) card. The FE card contained one MAROC3 chip which was configured, triggered and controlled by a field programmable gate array. Several FE cards, up to a maximum of 16, were then attached to one Back Plane (BP). The main aim of the BP was to provide electrical connectivity and mechanical support for the FE cards. A Control Board (CB) was then used to distribute the trigger signal for DAQ, control the BP and FE cards,

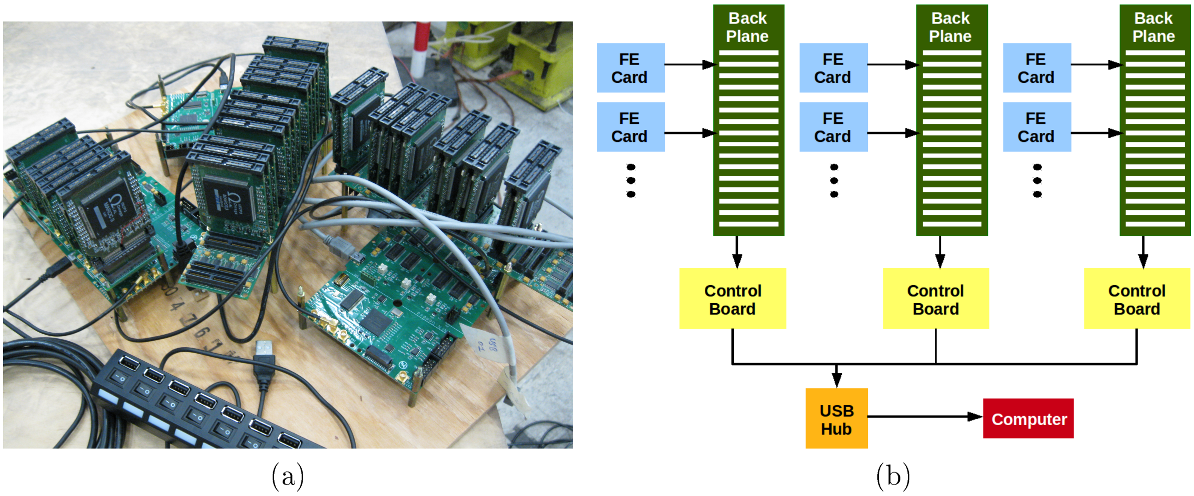

(a) (b)

Figure 5.48: (a) Photograph and (b) schematic of the readout electronics used with the large-scale prototype. One Front End (FE) card, containing one MAROC3 ASIC, is attached to each MAPMT. Several FE cards are then connected to a back plane module, which is in turn attached to a control board and interfaced with the data acquisition computer via USB connection.

accumulate the data and interface with a computer via a USB 2.0 connection. The FE cards were distributed across 3 BPs, which were controlled by 3 independent CBs. The coincidence signal from the trigger scintillators was split passively and sent simultaneously to the three CBs for DAQ triggering. A low voltage power supply was also used in the readout electronics setup, to provide the 3.5 V required for each MAROC3 ASIC.

Throughout the test-beam the maximum average readout rate obtained was ∼ 10 Hz and the maximum DAQ efficiency, defined as the ratio between the raw coincident trigger scintillator signals and the accepted DAQ triggers, was 13 %. These relatively low values resulted from a combination of the USB interface, the pulsed structure of the beam and the high intensity of particles delivered per spill. Furthermore, the electronics were extremely susceptible to pick-up noise in the test-beam environment, which had to be corrected for through the use of common mode noise subtraction techniques which will be described further below. Further studies of these electronics are being carried out by members of the CLAS12 RICH Collaboration to determine their suitability for the final CLAS12 RICH detector.

5.2.3 Analysis Methods

Several steps were performed in the analysis of data obtained with the test-beam prototype. The main aims of the analysis were to obtain the detected number of photons per Čerenkov ring event, to evaluate the Čerenkov ring radius resolutions and to obtain separation between pion and kaon particles species as a function of momentum.

To achieve these aims, the signals extracted from each of the 1 792 H8500 MAPMT pixels were evaluated as follows. For each data run, new pedestal thresholds were calculated for each readout channel. For this a single Gaussian distribution fit to the pedestal peak was obtained and the resulting threshold was calculated using a pre-defined multiple of the resulting σ - width, typically 4 σ thresholds were used throughout the data analysis. Per event, both the individual hits and the hit clusters above threshold were found and their corresponding MAPMT pixel locations were converted into spatial coordinates in the prototype setup geometry. To find the hit clusters, the clustering algorithm described previously in Section 5.1.4 was utilised. The number of hits or clusters above threshold obtained per event was then recorded as the Čerenkov event hit and cluster yield parameters respectively. Furthermore, if either the Čerenkov event hit or cluster yield was greater than 3, a circle was fitted to the distribution of either the hits or clusters across the MAPMT faces. The circle fit had 3-variable parameters, including the ring centre in both the horizontal and vertical directions (X_C and Y_C) and the ring radius (r). The circle fitting algorithm minimised the residuals between the variable radius parameter and the radius as calculated from the geometrical hit positions with respect to the variable ring centre parameters. This is shown in Equation 5.2, where: the χ^2 circle constraint is the parameter which is minimised, i denotes the number of hits above threshold per event, and x_i and y_i correspond horizontal and vertical positions of the hits respectively.

$$\chi^2 = \sum_i [(x_i - X_C)^2 + (y_i - Y_C)^2 - r^2] \tag{5.2}$$

The three results from the ring fit were plotted per event and evaluated, for example the width of the Čerenkov ring radius distribution was extracted as the radius resolution obtained with the prototype. A study performed by M. Mirazita has confirmed this event fitting method, by illustrating that the Čerenkov events obtained with the direct light imaging case of the test-beam prototype correspond to circles and not ellipses, which may arise from beam inclinations or misalignment effects [195].

This general analysis method is illustrated further in Fig. 5.49, which shows a typical Čerenkov ring event as imaged by the 28 H8500 MAPMTs (grey) and a ring fit (black dashed line) applied to the recorded hits above pedestal thresholds (red). For such an event several parameters are extracted and recorded, such as: hit and cluster multiplicities; cluster sizes; pixel occupancies; the geometric distance of either each hit pixel or hit cluster from the centre of the prototype setup; the ring radius extracted from the circle fit and the matching ring centre in both the horizontal and vertical positions.

The image shown in Fig. 5.49 was obtained with the event display software which was used throughout the test-beam and subsequent data analysis. The event display software package was both developed and written by M. Hoek [196] and is the basis of the analysis code which was then expanded upon by the author for further analysis of the test-beam data. The geometry of the experimental setup is replicated in the event display histogram using the *TH2Poly* histogramming class of the ROOT software toolkit, which allows the user to define histogram bins of arbitrary polygonal shapes, positions and rotations. For example, Fig. 5.50 gives a close-up view of one of the MAPMTs as described by the event display software. The histogram shows all hits above pedestal thresholds recorded by the pixels of the MAPMT, for an accumulation of ~20 000 events. Each of the 64 pixels are observed as separate bins in the event display histogram, with the frequency of hits above each pixel's individual pedestal threshold indicated by colour fill. As a result, the segment of the Čerenkov ring imaged by this

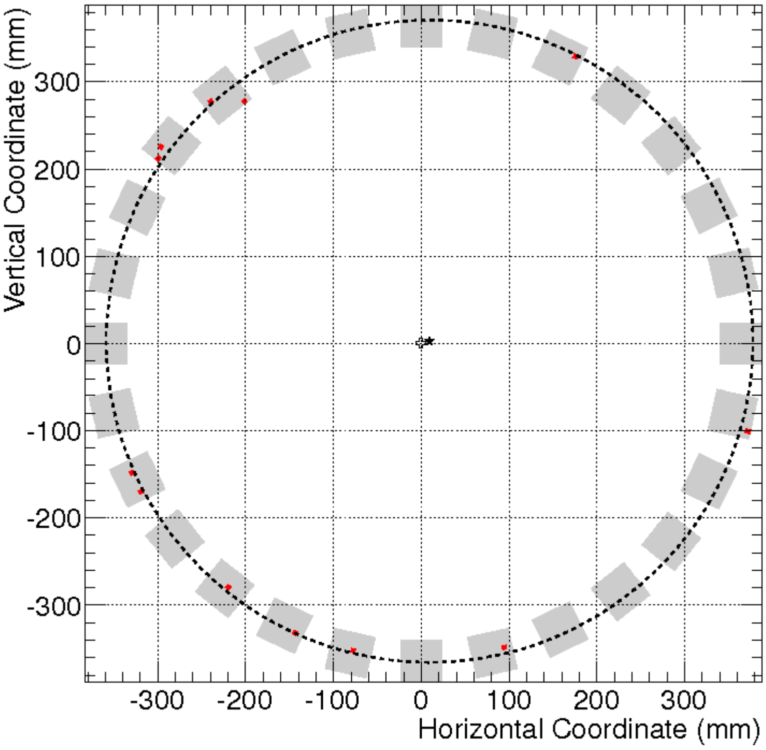

Figure 5.49: Typical Čerenkov ring event obtained with the test-beam prototype. The MAPMTs are shown in grey and pixels in which the extracted charge surpassed a $4\,\sigma$ pedestal threshold are indicated by red. A circle has been fit to the ring image, as shown by the dashed black line.

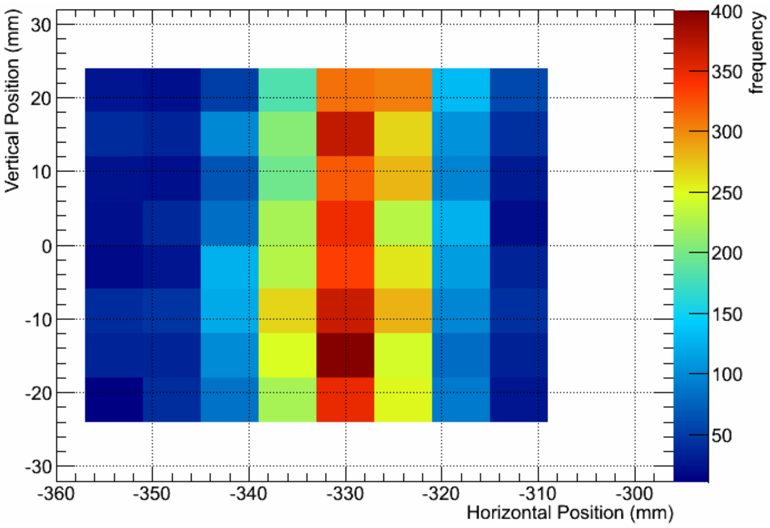

Figure 5.50: An example of the histogramming of an H8500 MAPMT in the event display of the test-beam RICH prototype. Each pixel of the H8500 MAPMT is represented by a separate histogram bin, with the colour fill representative of the number of hits recorded which surpass each pixel's $3\,\sigma$ pedestal threshold.

MAPMT is clearly visible. Each time the MAPMT positions were altered in the experimental setup, for example to image Čerenkov rings from different aerogel refractive indices, their locations were measured and recorded by hand. Using the event display software then, the position and orientation of each H8500 MAPMT and its constituent pixels was programmed as measured from the experimental setup and are subject to a ±1 mm measurement error, which will be propagated then to all ring radius measurements.

Čerenkov Event Yield and Hit Clustering Algorithm

In the case of the cosmic muon RICH prototype study described above (see Section 5.1), the density of Čerenkov photons per MAPMT pixel was >1 and therefore the conversion of extracted charge into NPE using the absolute calibration of the MAPMT was performed. In analysis of the test-beam RICH prototype data however, the number of hits above threshold per event was simply added and the ADC charge was not converted into PE. This is because the charge spectra recorded by each pixel were strongly representative of single photon signals only. This concept is analogous to that expected in the final CLAS12 RICH detector where a sparsified readout mode is envisaged, and trigger signals corresponding to hits above threshold only will be recorded per event. The validity of this method was confirmed on inspection of charge spectra extracted from hit H8500 MAPMT pixels which lie along the location of the Čerenkov ring, such as the example shown in Fig. 5.51. The charge spectrum has been fitted with Equation 4.2 which, as described in Section 4.4, may be used to perform absolute gain calibrations of MAPMTs. The fit result gives access to the mean NPE, which in this example was retrieved as (0.03054 ± 0.00259) PE and is significantly lower than a single PE level. If this mean value is used to calculate the total summed fraction of events expected at 0 PE and

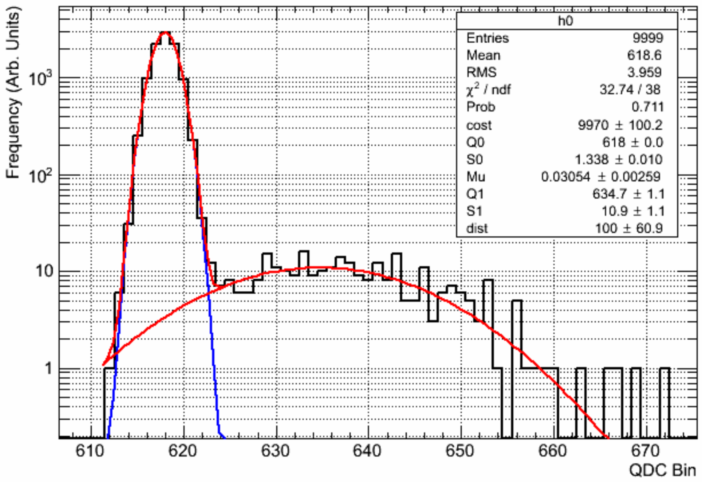

Figure 5.51: Example charge spectrum obtained from an H8500 MAPMT pixel which lies upon the Čerenkov ring, illustrating the pedestal and single photoelectron distributions. A fit has been applied which returns the mean NPE as (0.03054 ± 0.00259) PE.

1 PE levels from Poisson statistics then a value of 99.95 % is obtained, leaving 0.05 % events expected at higher PE-level contributions. Contributions from higher order photon-levels are therefore minimal, as expected, and it is assumed that the method of summing the number of pixels or clusters with hits above the pedestal threshold is satisfactory.

The principle for the extraction of event cluster multiplicities is further illustrated in Fig. 5.52, which shows the face of one H8500 MAPMT, where pixels returning hits above pedestal threshold highlighted in red. For the case shown, 4 hits and 3 clusters are extracted for this MAPMT. Equivalent numbers were extracted and summed from the 28 MAPMTs of the prototype setup, per event. The extraction of the cluster multiplicity aimed to reduce the influence of crosstalk signals upon the multiplicity measurements, since as observed through the laser scanning measurements described in Sections 4.5.1 and 4.6.1 cross-talk does exist at the single-PE charge level within the MAPMTs themselves. Based upon the laser scan results, it is assumed that the majority of crosstalk signals above threshold will occur in neighbouring pixels, as shown for example in the 2-pixel sized cluster of Fig. 5.52, and therefore the summing of clusters rather than individual hit pixels should eliminate the inclusion of noise hits to the Čerenkov yield results. Typical cluster sizes extracted from the data are shown in Fig. 5.53, which is taken from a 10 000 event data-set obtained with a beam momentum of 6 GeV/c, aerogel thickness of 2 cm and refractive index of n = 1.05. For the result shown in Fig. 5.53, the cluster search algorithm was set to include only the 4 side-sharing neighbours of each hit pixel. The majority of cluster sizes extracted had a size of 1 pixel, and comprise 95.33 % of the data-set shown in Fig. 5.53. This is almost in agreement with the measurements performed with

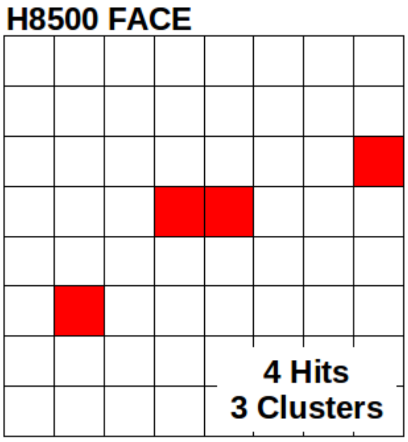

Figure 5.52: Schematic illustrating the difference between event hit and cluster multiplicities extracted from analysis of data from the test-beam RICH prototype. The face of one H8500 MAPMT is shown, with pixels recording hits above pedestal thresholds highlighted by red. For this MAPMT, 4 hits and 3 clusters are extracted.

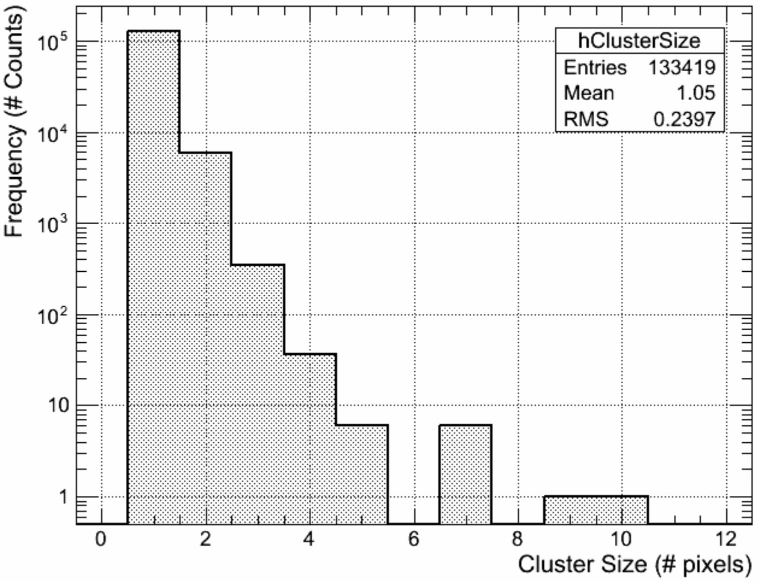

Figure 5.53: Hit cluster sizes, in pixels, extracted from RICH prototype test-beam data. At ∼95 %, the majority of the clusters have size corresponding to 1 pixel.

the laser test-stand, which studied crosstalk effects at an incident photon level corresponding to single - PE charge signals. For example, the previously attained result shown in Fig. 4.28 revealed that the crosstalk fractions exhibited in side-sharing neighbours to the illuminated channel is $< 3\,\%$, in the well-controlled environment of the laser laboratory. Considering the extremely different readout electronics used, the inclusion of extra noise effects present in the much less well-controlled test-beam environment and the detection of scattered Čerenkov light, the fraction of data with cluster sizes > 1 pixel and the crosstalk fraction extracted from the laser scan data agree quite well. The fraction of clusters having sizes > 1 pixel decreases with increasing cluster size in Fig. 5.53. For example, the fraction of clusters having sizes of 2, 3 and 4 pixels was 4.377 %, 0.259 % and 0.027 % respectively. In the further analysis steps, a cut was placed to exclude clusters with sizes of ≥ 5 pixels. Such events were assigned to originate from noise events in the readout electronics, which originated from the accelerator environment and were not true Čerenkov events. The frequency of such clusters was extremely low and the cut did not appear to impact the radius resolution or yield results. In order to reduce the inclusion of crosstalk noise, the event cluster multiplicity values were typically extracted and quoted as the Čerenkov yield values from test-beam data. Further systematic studies were performed to investigate the impact of clustering techniques on values extracted from the data.

The differences in yield obtained through use of the side-sharing (4 neighbours) or all-neighboring (8 neighbours) cluster search algorithms, previously described in Section 5.1.4, were examined. For instance, Fig. 5.54 gives the difference in event cluster multiplicity obtained with the different cluster search algorithms, for a $\sim 20\,000$ event sized data-set extracted with a beam momentum of 8 GeV/c, an aerogel thickness of 2 cm and refractive index of $n = 1.05$. Pedestal thresholds corresponding to $4\,\sigma$ cuts have been applied to the data. The statistics provided by the ROOT software to describe the two distributions are also visible in Fig. 5.54. The mean value of 12.31 clusters with the 8 neighbour search algorithm is very slightly less than the value of 12.56 clusters obtained with the 4-neighbour search technique, and a similar behaviour is observed with the RMS widths of the distributions. However the two results are extremely similar, as expected since the majority of clusters have sizes of 1 pixel, and any differences are concluded to be negligible. In analysis of the test-beam data the cluster search algorithm was set to perform side-sharing neighbour searches, since these are the most probable locations of crosstalk hits and with the 8-neighbour search algorithm the possibility exists for the algorithm to combine truly separated hits into large clusters.

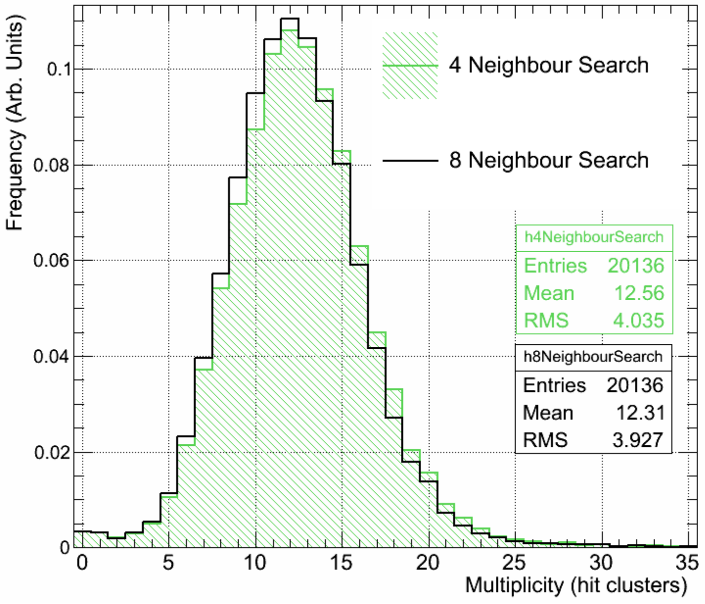

Figure 5.54: Example dependence of the event cluster multiplicity upon the cluster search algorithm and whether it is set to search either the 4 side-sharing (green) or entire 8 neighbouring (black) pixels of the hit channel.

In the analysis of Čerenkov ring events, the circle function may be set to fit to the positions of either the leading pixel of a cluster or the centroided position of a cluster, calculated by the relation given previously in Equation 5.1. Fig. 5.55 gives an example comparison of the resulting Čerenkov ring radius distributions obtained from the two methods, for the same data-set described immediately above. As expected, due to the small fraction of events with cluster sizes > 1 pixel and the crosstalk strength magnitudes, the extracted Čerenkov ring mean radius

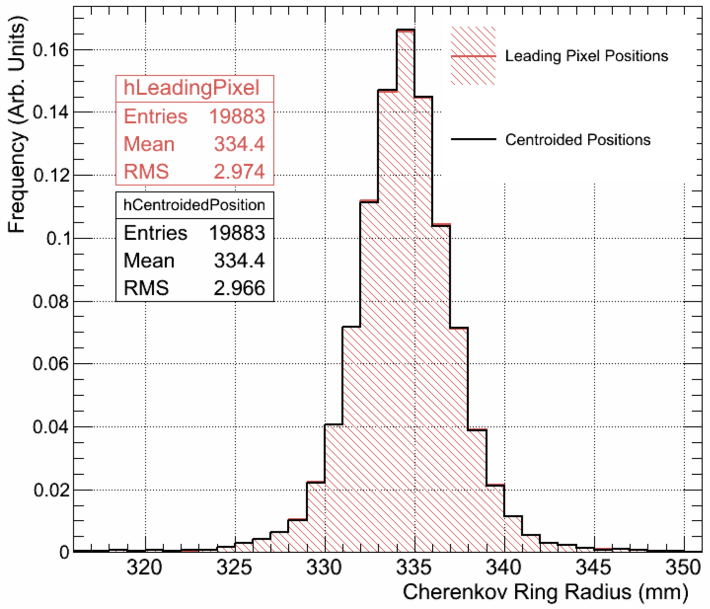

Figure 5.55: Example dependence of Čerenkov ring radius on whether the circle function is fitted to the cluster leading pixel or centroided positions.

values are the same and there is negligible difference between the widths of the two distributions. The same is true for the ring centre positions extracted from the circle fitting algorithm, as illustrated in Figs. 5.56 (a) and (b), where the Čerenkov ring fitting method does not appear to affect the mean or widths of the resulting ring centre distributions. For the results which

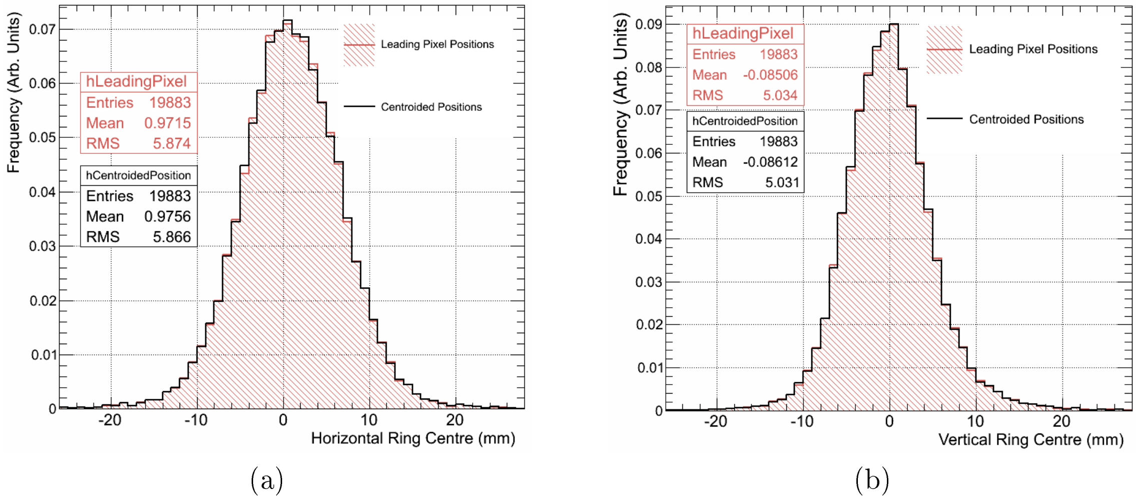

(a) (b)

Figure 5.56: Example dependence of Čerenkov ring fit centre in both the (a) horizontal and (b) vertical positions upon whether the circle function is fit to the cluster leading pixel or centroided positions.

will be shown subsequently, the Čerenkov ring fitting algorithm was set to fit to the leading pixel positions of each cluster.

Common Mode Noise Subtraction

Throughout the test-beam studies the pedestal noise distributions extracted from the MAPMTs with the MAROC3 readout electronics exhibited extremely broad widths and, in most cases, double peaked structures were obtained in the majority of readout channels. The noisy pedestal distributions were problematic for analysis of the RICH prototype data, since single PE charge spectra were expected. With the H8500 MAPMT a portion of the single PE charge spectrum is already intrinsically lost to the pedestal distribution, and so the broadened pedestal distributions may result in a significant loss of true Čerenkov events. Furthermore, one single Gaussian is not an applicable fit to a double peak structure, as is used in the typical analysis method to obtain the pedestal threshold cuts with the H8500 MAPMT charge spectra. A Common Mode Noise Subtraction (CMNS) filter was therefore developed and programmed by E. Cisbani and M. Turisini [197], and was applied to all data obtained throughout the test-beams.

There are several steps comprising the CMNS algorithm. Initially the 64 channels of an MAPMT are divided into two subsets of 32 channels and then, per event, the average ADC value amongst all channels of a subset is calculated and subtracted from the individual ADC values recorded in each of the 32 channels. The aim is that common mode noise present in the readout system will be averaged out and true signals, which are not common throughout the subset, will remain. An arbitrary offset is added to all resulting ADC values, to avoid any possible complications from resulting ADC values lying below the zero value. A typical example of the benefit of the CMNS filter application is shown in Fig. 5.57, where the vertical frequency axis is displayed on a logarithmic scale to emphasise the single PE signal distribution. The raw charge distribution obtained from the pixel is shown in blue, with the double peaked pedestal structure visible. The corresponding result obtained after application of the CMNS filter is shown in red, where the pedestal width is much narrower and the double peak structure is removed. The shape of the pedestal distribution after CMNS is in accordance with a Gaussian distribution, and therefore the typical analysis method for obtaining a pedestal threshold was successfully performed.

In rare cases the CMNS filter produced unwanted artifacts, such as the examples shown in Figs. 5.58 (a) and (b). In the case of Fig. 5.58 (a), for instance, the filtering has resulted in the presence of a second peak residing below the main pedestal distribution. Additionally, in Fig. 5.58 (b) the pedestal distribution has a large tail towards higher ADC values, which is almost separated as a second peak and results in increased noise counts lying above the threshold of the main pedestal distribution. Throughout the data analysis steps such features were

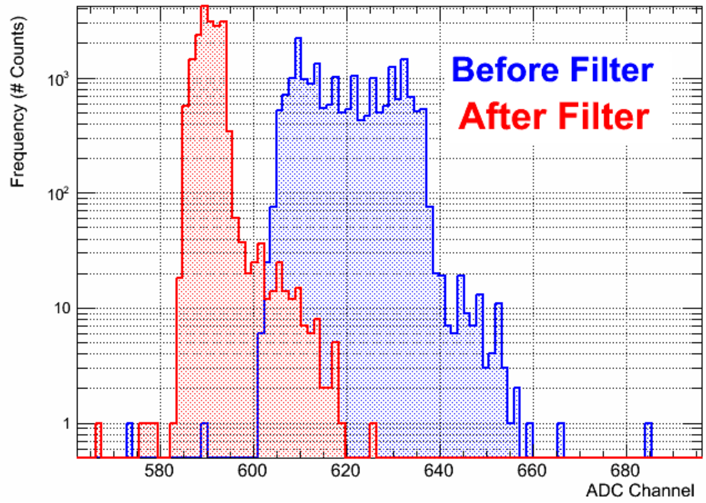

Figure 5.57: Typical charge spectrum extracted from one of the H8500 MAPMTs of the test-beam prototype before (blue) and after (red) application of a common mode noise subtraction filter to reduce pedestal widths and remove the double peaked pedestal structures.

monitored by eye, and for each analysed data-set the total number of channels displaying these noise or unwanted effects was typically ∼ 1 % of the 1 792 H8500 MAPMT readout channels.

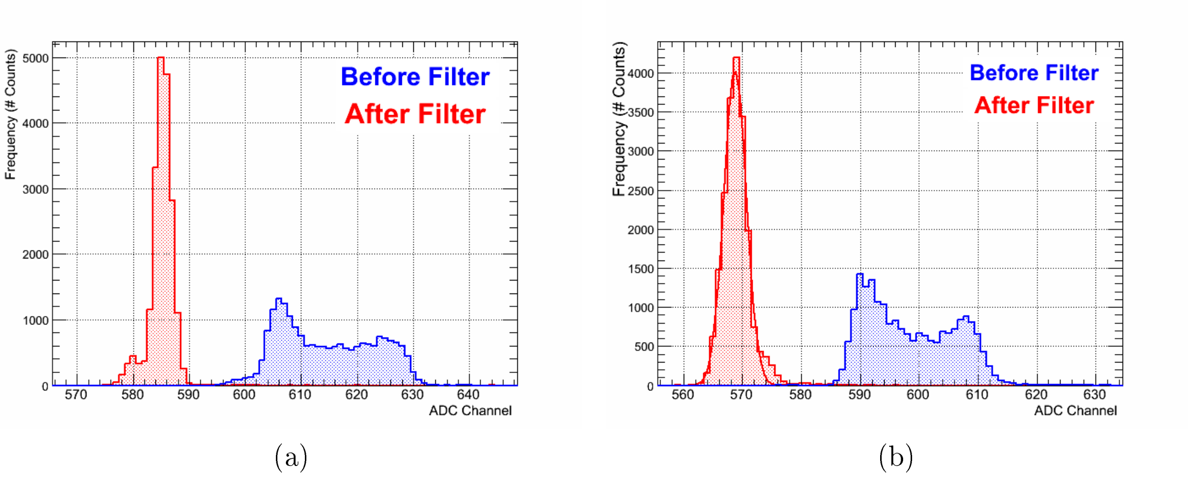

(a) (b)

Figure 5.58: Examples of detrimental effects resulting from application of the common mode noise subtraction algorithm to reduce pedestal noise observed in H8500 readout channels. Such effects, however, were rare and only occurred in <1 % of instances.

An example comparison between ring images obtained before and after application of the CMNS algorithm is given in Figs. 5.59 and 5.60 respectively. The rings are again produced from the same ∼ 20 000 event data-set obtained at the July - August test-beam, with an aerogel radiator thickness of 2 cm, a refractive index of n = 1.05 and beam momentum of 8 GeV/c. The colour fill indicates the frequency of hits above a 3 σ pedestal threshold, which was selected since it represents the cut level most susceptible to noise. The pedestal thresholds before common

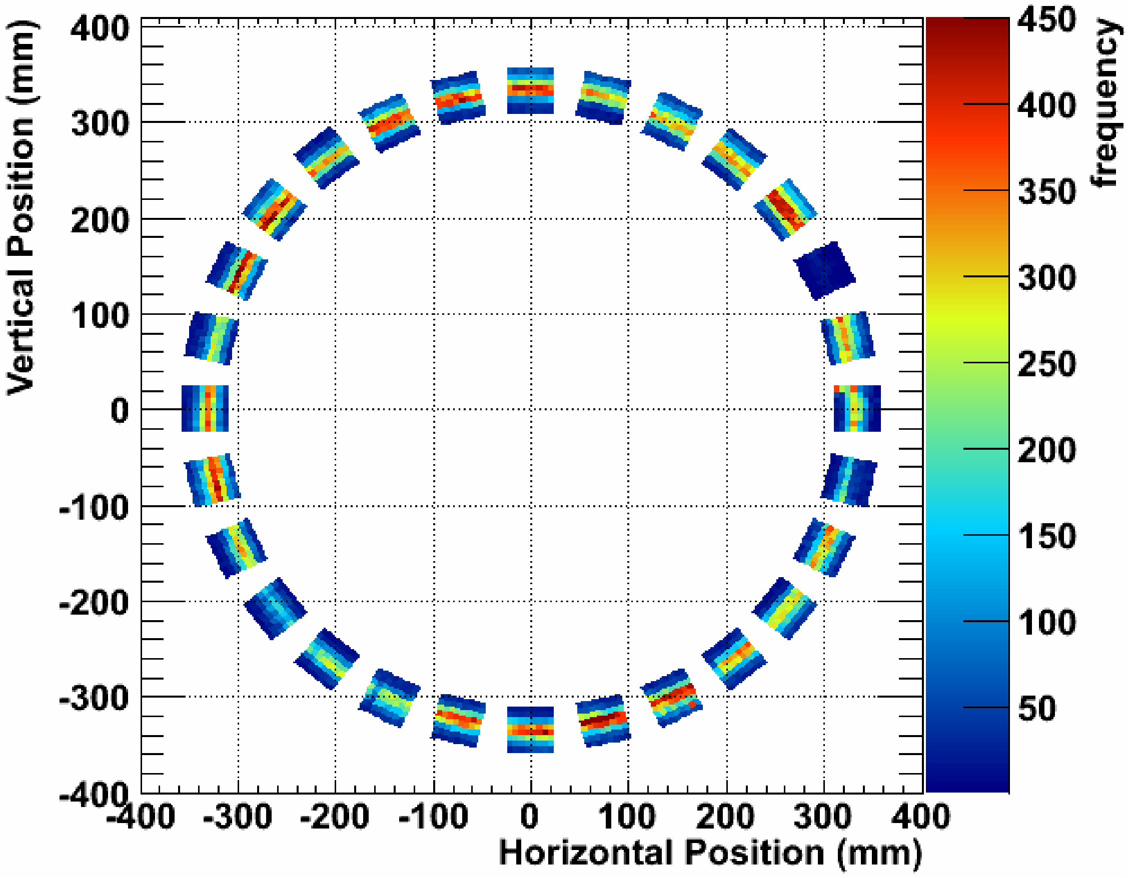

Figure 5.59: Example Čerenkov ring image obtained before the application of a common mode noise subtraction algorithm to improve MAPMT pedestal noise distributions. The colour fill indicates the frequency of hits above a $3\,\sigma$ pedestal threshold.

mode noise subtraction are however not reliable since a single Gaussian fit to the entire double peak structure does not describe the distributions well. Nonetheless the results indicate that as a result of the CMNS algorithm MAPMTs which previously showed relatively low yields and efficiencies, due to severely degraded pedestal distributions, are mostly recovered. This is confirmed on inspection of the corresponding average hit multiplicity per event obtained for each H8500 MAPMT, before and after CMNS, as shown in Fig. 5.61. The *PMT ID* value was used as a label for each MAPMT of the prototype setup, with $PMTID = 0$ corresponding to the MAPMT located at position (0.0 mm, -340.0 mm) in Figs. 5.59 and 5.60. The *PMT ID* value then increases, in the clock-wise direction, to a maximum value of 27. Due to the different absolute gains of the MAPMTs the average multiplicities are not expected to be exactly equal amongst the MAPMTs, however, the CMNS yields a stronger equalisation between the average multiplicities of the 28 MAPMTs. The average multiplicity is increased in MAPMTs which previously suffered severely from broad pedestal distributions lying on top of the single PE

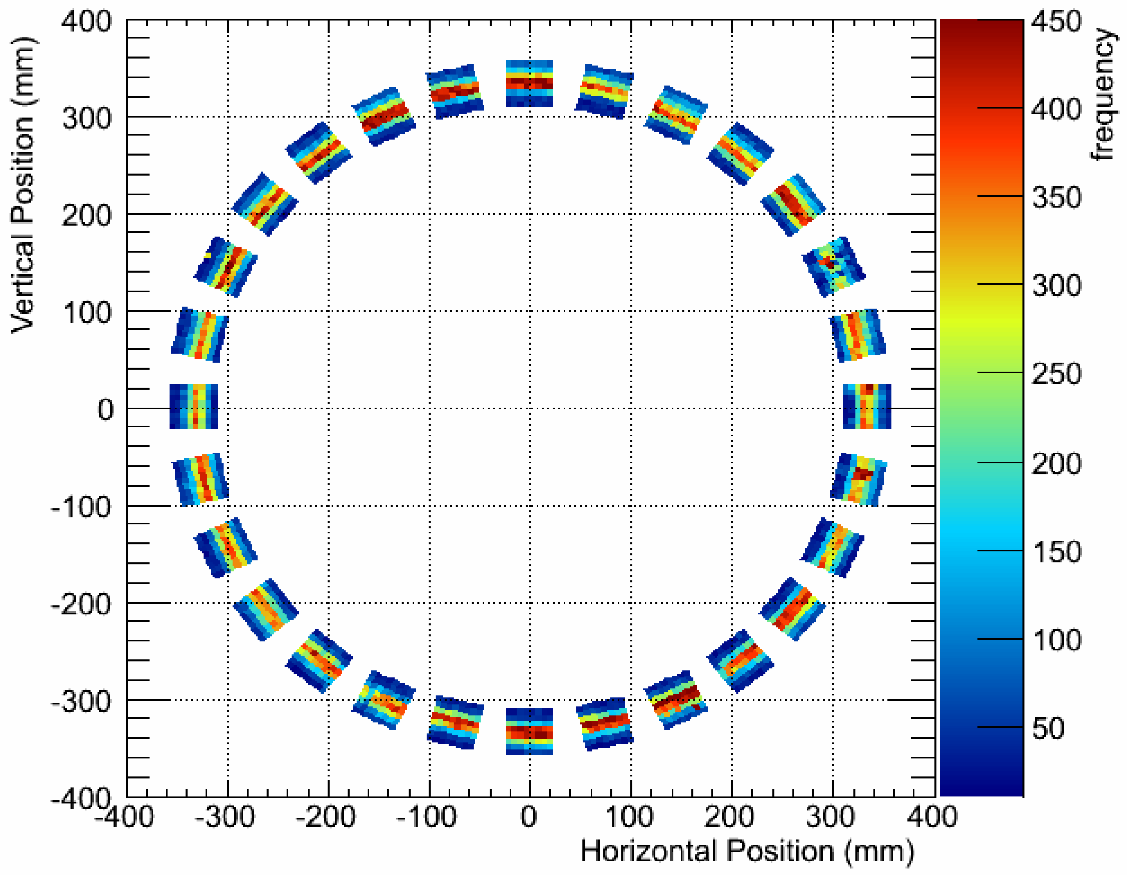

Figure 5.60: Example Čerenkov ring image obtained after the application of a common mode noise subtraction algorithm to improve MAPMT pedestal noise distributions. The colour fill indicates the frequency of hits above a $3\,\sigma$ pedestal threshold.

charge spectrum, and decreased in cases where a large fraction of mis-identified noise hits lying above the pedestal threshold existed.

Further examples of the impact of the CMNS on the Čerenkov event hit and cluster yields are given in Figs. 5.62 (a) and (b) respectively, for the same data-set described above and $3\,\sigma$ pedestal thresholds. The graphs show the results obtained from inclusion of all 28 MAPMTs, which provided 69.3 % coverage of the Čerenkov ring. The result of CMNS is to increase the yield of both the hit and cluster multiplicities, from 12.15 hits to 15.44 hits and 10.99 clusters to 14.03 clusters respectively. As expected, the hit multiplicity is generally slightly higher than the cluster yield. A study of the event hit and cluster multiplicities, obtained with a beam momentum of 8 GeV/c, an aerogel thickness of 2 cm and refractive indices of $n = 1.04, 1.05$ and 1.06, revealed that the hit and cluster yields were increased by 21 % and 23 % respectively through application the CMNS algorithm to the data.

The corresponding Čerenkov ring radius distributions obtained before (blue) and after (red) common mode noise subtraction are shown in Fig. 5.63. Gaussian fits retrieve the

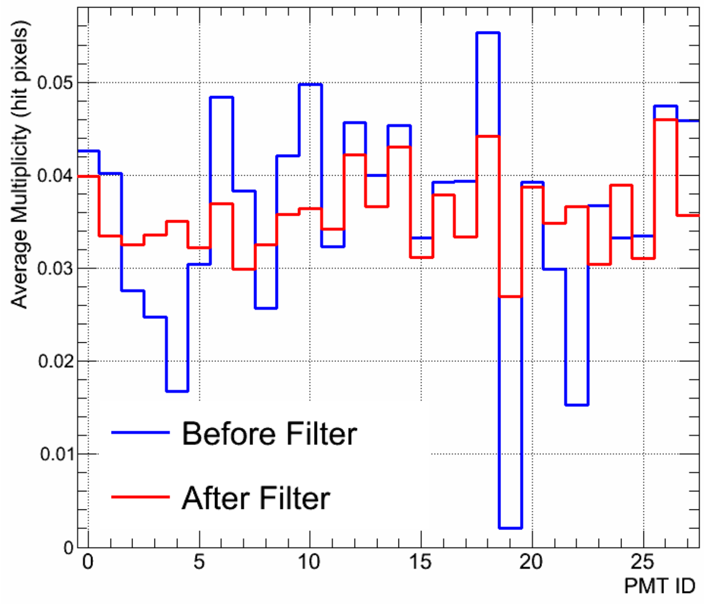

Figure 5.61: Example average hit multiplicities per Čerenkov ring event obtained for each of the 28 H8500 MAPMTs used in the test-beam RICH prototype before (blue) and after (red) common mode noise subtraction to improve pedestal distributions.

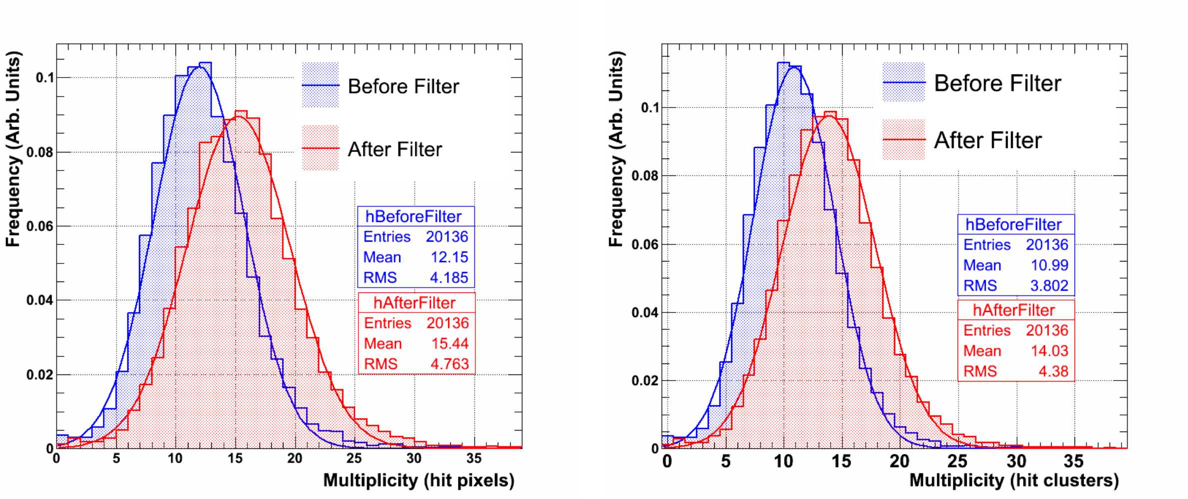

(a) (b)

Figure 5.62: Examples of Čerenkov event (a) hit and (b) cluster multiplicity distributions obtained before (blue) and after (red) common mode noise subtraction. The data was obtained with an aerogel radiator of thickness 2 cm, refractive index of n = 1.05 and beam momentum of 8 GeV/c.

mean positions of the distributions before and after noise subtraction to be (334.12 ± 0.02) mm and (334.44 ± 0.02) mm respectively, implying that the noise subtraction does not alter the mean Čerenkov ring radius distribution extracted significantly. The width, however, does slightly decrease after common mode noise subtraction from a value of (2.885 ± 0.019) mm to (2.595 ± 0.022) mm, indicating a slight improvement of the Čerenkov ring resolution which is in

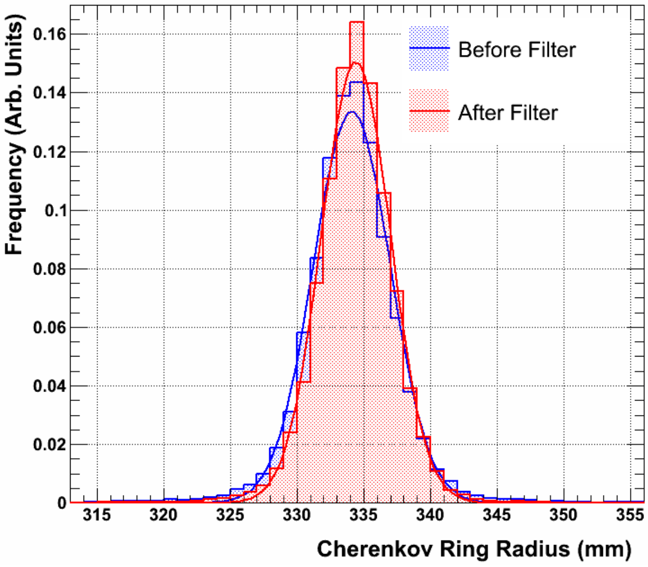

Figure 5.63: Example of the ring radius distributions extracted from circle fits to Čerenkov events before (blue) and after (red) common mode noise subtraction.

accordance with counting statistics. If one computes the ratio between $(1/\sqrt{Clusters_{After}})/(1/\sqrt{Clusters_{Before}})$, where $Clusters_{Before}$ and $Clusters_{After}$ are the mean cluster yield values obtained before and after CMNS from Fig. 5.62 (b), then a value of 0.90 is obtained. This matches well the value extracted if the equivalent ratio between the σ - widths of the ring radii distributions obtained before and after CMNS is calculated, confirming that the increase of Čerenkov yield obtained through the application of the CMNS algorithm is important as it improves the Čerenkov radius resolution. Equivalent observations were observed with the fitted Čerenkov ring centre in both the horizontal and vertical directions.

Such systematic studies of the influence of the CMNS on Čerenkov yield and geometrical ring properties confirmed the effectiveness of the technique in restoring the charge spectra of the H8500 MAPMTs. The Čerenkov yields were increased due to the improved pedestal noise distributions from the readout electronics, however the main Čerenkov ring geometrical features remained unaltered as required. For all results which are shown below the data was first treated with the CMNS filter. For readout of the H8500 MAPMTs with the MAROC3 electronics in the CLAS12 RICH detector, dedicated studies using the slow channels of the MAROC3 chips would be required during the commissioning and calibration period of the detector, to confirm the requirement of such a CMNS technique.

Pedestal Threshold Cuts

Since the readout electronics used differed from those incorporated in the cosmic muon RICH prototype, the influence of pedestal thresholds corresponding to 3, 4, and 5 σ values on the Čerenkov light yield extracted with the test-beam prototype was considered. A typical example of such threshold cut locations on an extracted H8500 hit pixel charge spectrum is shown in Fig. 5.64 (a), where the CMNS algorithm has previously been applied to the ADC data. The resulting dependency of the Čerenkov yield per event upon the pedestal threshold cut from the same data-set is shown in Fig. 5.64 (b), where the event corresponded to a Čerenkov ring with 66.8 % coverage provided by the 28 MAPMTs and the Čerenkov yield is defined as the cluster multiplicity recorded by the MAPMTs per event. Čerenkov yields of (13.90 ± 0.03) clusters, (12.49 ± 0.03) clusters and (11.89 ± 0.03) clusters per event are obtained with 3, 4 and 5 σ pedestal thresholds respectively. Similar behaviour was also observed with different data-sets. It was concluded again that a 4 σ pedestal threshold cut offers the optimal compromise between noise inclusion and signal rejection, and therefore was used for the analysis to obtain the following results.

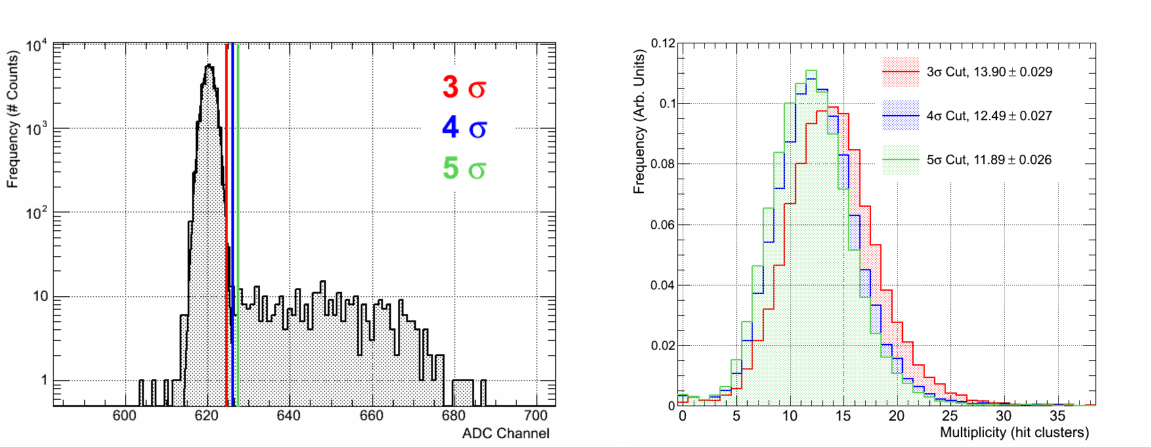

(a) (b)

Figure 5.64: (a) Typical charge spectrum obtained from one H8500 MAPMT pixel in response to Čerenkov light. The locations of three different pedestal threshold cuts, corresponding to 3, 4 and 5 σ pedestal widths, are marked upon the spectrum. (b) Example dependence of the cluster yield per Čerenkov event, obtained with 2 cm thickness of n=1.05 aerogel and a beam momentum of 8 GeV/c, upon the pedestal threshold cut.

5.2.4 Results

Within the scope of this project, the main aims of the data analysis studies were to obtain measurements of Čerenkov yields and ring resolutions attainable through the use of the H8500

MAPMTs as the photon detectors in the test-beam RICH prototype, and hence evaluate their corresponding intrinsic performance and potential for use in the CLAS12 RICH detector. Further to this, analysis was also performed to study particle species separation powers of the prototype detector over the tested momentum range of 6 - 8 GeV/c. These results are focussed upon the handling of the H8500 MAPMT data and the evaluation of the Čerenkov rings as imaged by these MAPMTs. There are therefore several steps beyond this analysis which may be taken to further refine the results and assess the overall performance of the entire RICH prototype imaging system and CLAS12 RICH design as a whole. Such refinements include: thorough optimisation of radiator materials, alignment studies, charged particle tracking with the GEM chambers to improve the Čerenkov ring fitting, or the inclusion of scattering background and dark noise rejection algorithms in the ring fitting method. Such investigations and comparisons with simulations are being undertaken by members of the CLAS12 RICH Collaboration. The finalised results may then be used to assess the overall performance of the RICH prototype and extrapolated, through simulation studies, to evaluate the final CLAS12 RICH detector design and performance projections.

Čerenkov Light Yields and Properties

The Čerenkov light yield per event, or the event multiplicity, is a crucial parameter for both the test-beam RICH prototype and the final proposed detector in CLAS12. It is expected from theory that the greater the Čerenkov yield, the greater the Čerenkov ring resolution and hence the higher the separation power of the RICH detector (see Section 2.2).

An example ring image obtained with the test-beam prototype is given in Fig. 5.65. The example displays the accumulated hits above $4\,\sigma$ pedestal thresholds as taken from a 20 000 event data-set [11] obtained using 8 GeV/c beam momentum, an aerogel refractive index of $n = 1.05$ and thickness of 2 cm. This configuration was tested thoroughly with the direct light imaging setup of the test-beam prototype and used as the standardised configuration, since it represents the most challenging direct light imaging case in the final CLAS12 RICH detector. Pixels which exhibited noisy pedestal distributions have been removed, and are visible as missing bins in Fig. 5.65. In addition, one of the H8500 MAPMTs was discovered to suffer from a significant proportion of *dead* pixels, which returned no signals above noise and extremely narrow pedestal noise distributions. For further analysis of this data-set, therefore, this MAPMT was removed

---

[11] November - December 2012 test-beam, run 1105.

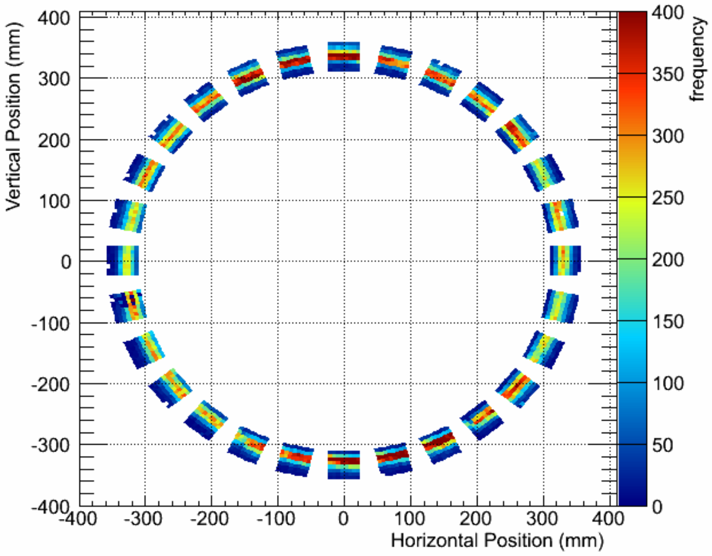

Figure 5.65: A Čerenkov ring image obtained with a beam momentum of 8 GeV/c, an aerogel thickness of 2 cm and refractive index of n = 1.05. The colour fill indicates the number of hits above 4 σ pedestal thresholds, accumulated with a 20 000 event sized data-set.

and the results were obtained from 27 H8500 MAPMTs only. The resulting comparison between the event hit (green) and cluster (blue) multiplicities is given in Fig. 5.66. Visible from

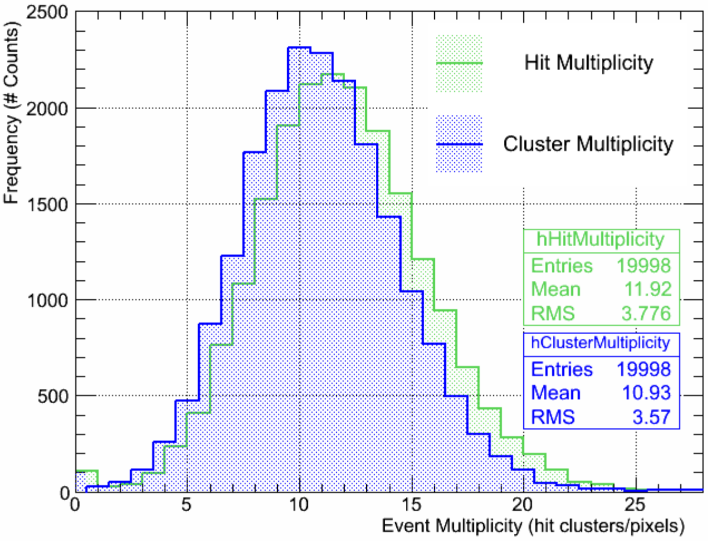

Figure 5.66: Event hit (green) and cluster (blue) multiplicity distributions obtained with the standard direct light imaging case configuration and 27 H8500 MAPMTs. The hit multiplicity distribution exhibits a slightly higher mean than the cluster distribution due to the inclusion of crosstalk noise events.

the statistics listed in Fig. 5.66, the hit multiplicity distribution exhibits slightly higher mean and width values than the cluster distribution, as expected, due to the inclusion and influence of neighbouring crosstalk noise events. The widths of the distributions are typical of those observed throughout the analysis of the test-beam data, and did not appear to depend strongly on the beam momenta or aerogel refractive indices studied. Gaussian fits to the distributions yield the number of hits and clusters per event as (11.96 ± 0.02) hits and (10.97 ± 0.02) clusters respectively. The hit multiplicity exceeds the cluster multiplicity mean by $\sim$1 hit, which was a typical observation among the data-sets analysed, and only the cluster multiplicity values are quoted in the following results.

To illustrate variations in event cluster properties and yields extracted throughout the test-beam with different experimental configurations of the prototype setup, further examples are given below. For example, Fig. 5.67 (a) gives the cluster multiplicity distributions extracted with radiators of different refractive indices. A full study of the effects of different radiator properties goes beyond the remit of this analysis, however the refractive index study below studied the ability of the H8500 MAPMT to detect a sufficient number of Čerenkov photons per event, for each of the three tested aerogel refractive indices which exist as options for the CLAS12 RICH detector. Firstly, it is important to assess the performance of the H8500 MAPMTs within the test-beam RICH prototype with an aerogel radiator refractive index of n = 1.05, since this currently exists as the chosen refractive index for use in the CLAS12 RICH detector. However, if it is shown that significant improvements in the RICH performance may be achieved with different refractive indices, then these values may be selected instead. The nominal refractive indices tested with the prototype and shown in Fig. 5.67 (a) are 1.04 [12], 1.05 [13] and 1.06 [14], with a tile thickness of 2 cm used in each case. The data-sets analysed and the results shown for each refractive index represent an accumulation of 50 000 events. For the n = 1.04 and n = 1.06 distributions the summed cluster multiplicities from all 28 MAPMTs are shown. For the n = 1.05 result the distribution obtained for 27 MAPMTs only is shown, due to the existence of dead pixels and as previously described for this configuration. The mean values and the shapes of the distributions are extremely similar, due to the differing number of MAPMTs and proportions of the Čerenkov rings detected by the MAPMTs. The corresponding cluster size distributions are shown in Fig. 5.67 (b). The result indicates that the refractive index does not influence the cluster sizes as measured by the H8500 MAPMTs, confirming that this is mostly caused by intrinsic crosstalk effects of the MAPMTs itself and, in the test-beam study case, also by the readout electronics. Furthermore, the fraction of

---

[12] November - December 2012 test-beam, runs 1137, 1138 and 1139.

[13] November - December 2012 test-beam, runs 1105, 1106 and 1107.

[14] November - December 2012 test-beam, runs 1128, 1129 and 1130.

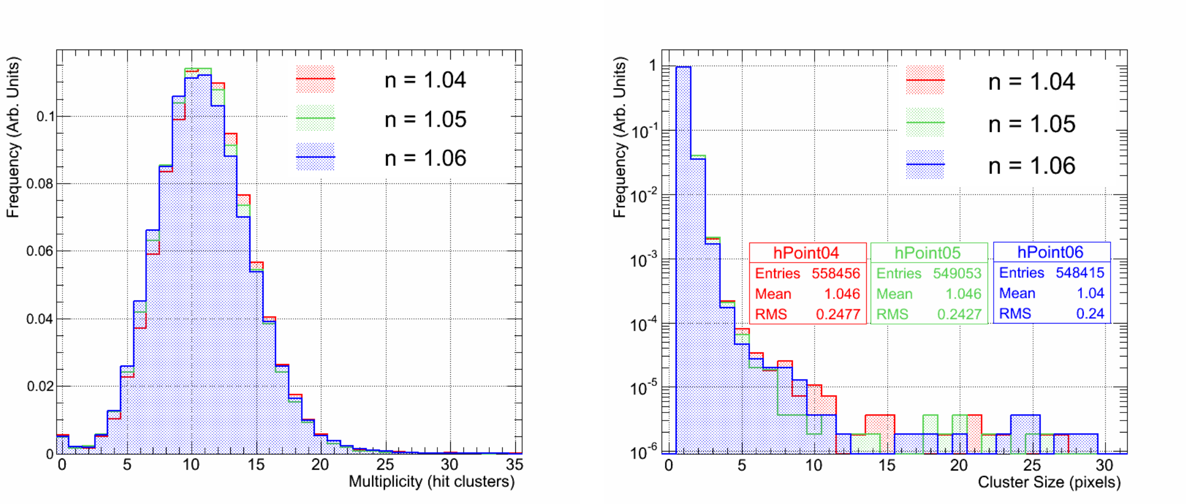

(a) (b)

Figure 5.67: The variation with refractive index of (a) the raw Čerenkov event cluster multiplicities and (b) cluster size distributions extracted with the test-beam RICH prototype.

cluster sizes corresponding to one pixel in all cases is ~95 %, which is again in accordance with the previously described low-noise behaviour of the H8500 throughout the single photon level crosstalk magnitude studies, if the different electronics and environmental conditions are considered.

The event cluster multiplicity distributions were each fitted with Gaussian functions and the mean values extracted. The result obtained from the n = 1.05 distribution was re-scaled to calculate the expected value for 28 fully functional MAPMTs. The resulting mean values are shown in Fig. 5.68 (a). The yield increases with refractive index, as expected, when moving

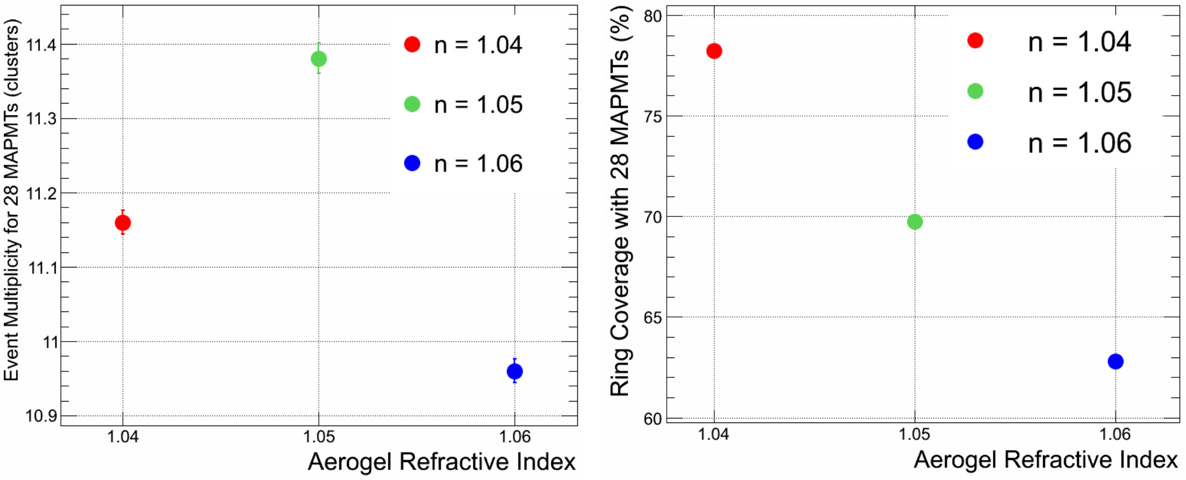

(a) (b)

Figure 5.68: Variation with refractive index of (a) the mean cluster multiplicities and (b) corresponding Čerenkov ring coverages, with the 28 H8500 MAPMTs of the prototype setup in the direct light imaging case.

from n = 1.04 to n = 1.05. However, at n = 1.06 the yield decreases due to the fact that the Čerenkov ring has a larger circumference and the ring coverage provided by the 28 MAPMTs is relatively low. This is confirmed in Fig. 5.68 (b), which gives the Čerenkov ring coverage provided by 28 MAPMTs for the three tested refractive indices. The ring coverages were calculated from the dimensions of the H8500 MAPMTs and the Čerenkov ring radius values extracted from ring fits to the data. The ring coverage decreases from 78.25 % at n = 1.04, to 69.74 % at n = 1.05, and finally 62.79 % at n = 1.06.

The mean multiplicity values extracted with 28 MAPMTs were re-scaled to the expected values for full coverage of the Čerenkov rings. The scaling factor is currently an estimate, and would need to be verified (by simulation studies, for example). The method used approximates the circumference of the Čerenkov ring as a straight line and so represents a lower-limit of the expected re-scaled yields, since the distance of a straight line segment is less than that of a curved one. The re-scaled results for full Čerenkov ring coverages are shown in Fig. 5.69. The re-scaled results confirm the expectation that the Čerenkov light yield increases with refractive index of the radiator, as expected (see Equation 2.4), validating the behaviour of the H8500 MAPMTs within the large-scale prototype in response to the Čerenkov rings of various properties.

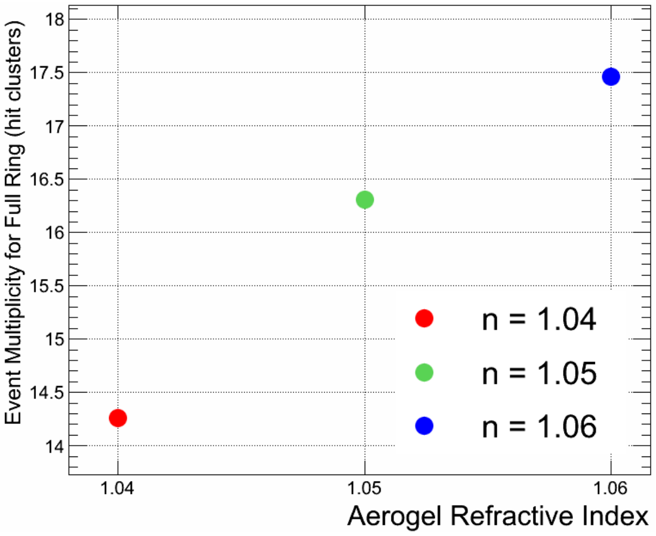

Figure 5.69: The mean event cluster multiplicities extracted with the direct light imaging case of the test-beam prototype, re-scaled to the expected values for full Čerenkov ring coverage and as a function of refractive index.

A summary of the raw and re-scaled cluster multiplicity results is given in Table. 5.15. The Čerenkov light yields obtained with the prototype are promising for extrapolation and projection to the envisaged CLAS12 RICH detector, considering that for the CLAS12 RICH

Table 5.15: Variation with refractive index of the event cluster multiplicity obtained for the 28 H8500 MAPMTs of the test-beam RICH prototype and also re-scaled for the expected values from full coverage of the Čerenkov rings.

Refractive Index	**Mean Multiplicity, 28 MAPMTs [clusters]**	**Ring Coverage, 28 MAPMTs [%]**	**Scaled Multiplicity, Full Ring [clusters]**
1.04	11.16 ± 0.02	78.25	14.26
1.05	11.38 ± 0.02	69.74	16.31
1.06	10.96 ± 0.02	62.79	17.46

the benchmark separation up to 8 GeV/c is $>3\,\sigma$ and that in all possible refractive index cases the Čerenkov yield measured with the test-beam prototype surpasses the minimal value of 7 detected photons to achieve this goal (see Section 2.3). The geometry of the test-beam prototype imaging plane is limited, due to the available ring coverage, and differs from the envisaged one for the CLAS12 RICH detector where a wall of MAPMTs will be closely packed. Nonetheless Čerenkov yield results such as those shown in Table 5.15, and their comparison with simulation studies of the large-scale prototype tests, will be extremely important for tuning of the CLAS12 RICH Monte Carlo simulation to allow for more accurate performance projections to be made. Overall, based upon the Čerenkov yield results obtained with the large-scale prototype, the H8500 MAPMT is a very suitable choice for use in the final detector.

Further Čerenkov yield improvements may be feasible in the CLAS12 RICH detector through optimisation of the aerogel radiators. The production techniques of aerogel radiator materials are constantly improving, resulting in the availability of aerogel with increased transparency and higher optical quality. A comparison is given in Fig. 5.70, which shows the event cluster multiplicity obtained with aerogel tiles from two different production techniques developed by the Budker Institute of Nuclear Physics, Novosibirsk (Russia). The older production tile, shown by the blue shaded curve, corresponds to the tile used for the $\mathrm{n} = 1.05$ results shown immediately above, whereas the red shaded curve gives the equivalent result from the newer production technique. The curves are generated from analysis of 20 000 event sized data-sets [15]. Mean values of (10.94 ± 0.03) clusters and (12.37 ± 0.03) clusters are extracted from the older and newer production tiles respectively. The transmittances of the aerogel tiles (see Equation 2.10) were subsequently measured with a spectrophotometer by members of the CLAS12 RICH Collaboration, as described in [198], and confirm the origins of the increased event multiplicity as arising from an increased transmittance of the newer production aerogel tile. Through such techniques, although the H8500 MAPMTs already offer sufficiently effi-

---

[15] November - December 2012 test-beam, runs 1051 and 1105.

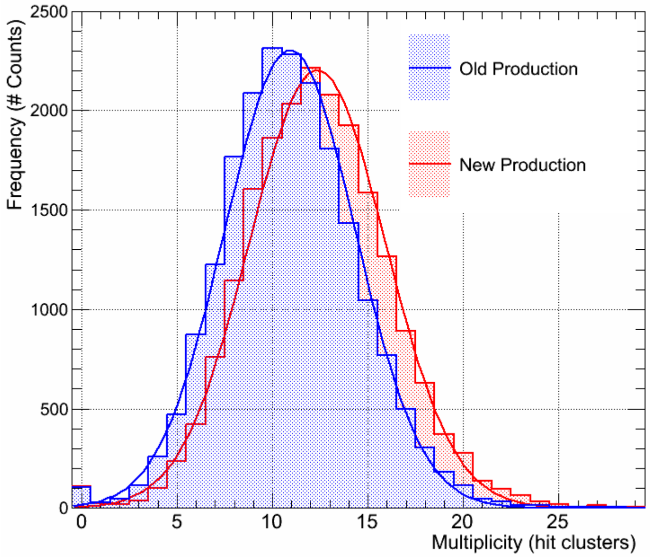

Figure 5.70: Cluster multiplicity distributions from aerogel tiles of older (blue) and newer (red) production techniques.

cient detection of Čerenkov photons to meet the CLAS12 RICH benchmark requirements, the availability of higher optical quality aerogel material may increase the detected Čerenkov yield even further, which in principle should improve the Čerenkov ring resolution available with the CLAS12 RICH detector (see Equation 2.6).

Čerenkov Ring Radii and Resolutions

The Čerenkov ring resolution is a crucial parameter of a RICH detector since it determines the precision with which the Čerenkov rings may be defined and plays an important role in the particle separation power of the detector. The Čerenkov ring resolution was studied through the ring radius distributions obtained with the test-beam RICH prototype, and some typical examples are given below.

Prior to performing a Čerenkov event ring fit, the raw Čerenkov ring resolution may be investigated by histogramming the individual geometrical radii of all hit clusters. The geometrical radius is defined as the distance of a cluster's leading pixel from the geometrical centre of the ring of H8500 MAPMTs, which is assumed to be the track position of the charged particle. An example of this, from a 20 000 event data-set [16], obtained with the standardised direct light imaging case configuration, is shown in Fig. 5.71. The quantisation of the distribution is caused by the spatial resolution of the H8500 MAPMT, with the distance between the main peak struc-

---

[16] November - December 2012 test-beam, run 1105.

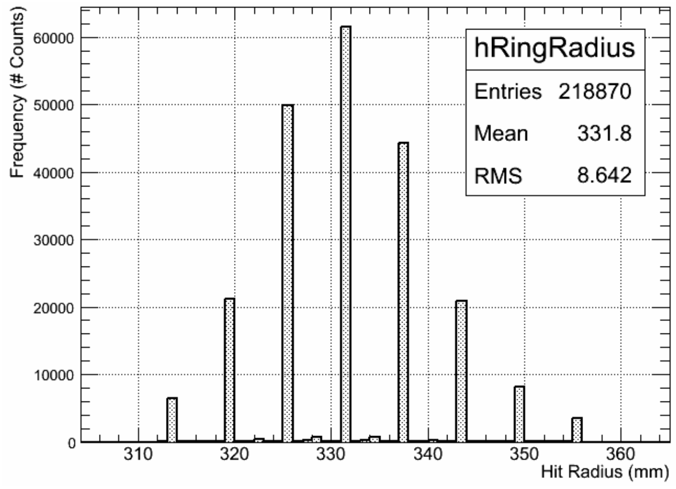

Figure 5.71: Typical hit cluster geometrical radius distribution, where for each event the distance of the leading pixel of each hit cluster from the geometrical origin of the plane of H8500 MAPMTs is calculated and plotted. The quantisation is caused by the spatial resolution of the H8500 MAPMT.

tures equal to the pixel - to - pixel pitch of the photon detector. The 8.642 mm RMS - width of the distribution, which is taken as the Čerenkov ring resolution, is rather broad and the event ring fitting method is therefore applied to smooth the results in an attempt to improve the radius resolution (see Section 5.2.3). The corresponding example is shown in Figs. 5.72 (a) and (b). In analysis of the radius distributions, both single and double Gaussian fits were evaluated, the outcomes of which are shown in both figures respectively. The single Gaussian fit method

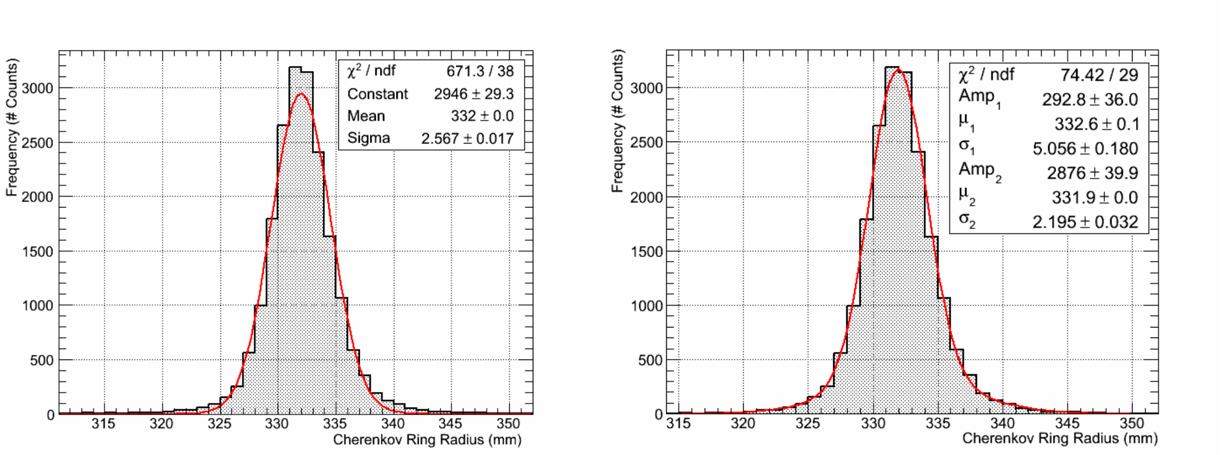

(a) (b)

Figure 5.72: Čerenkov ring radius distribution obtained from ring fits to hit clusters above pedestal thresholds, obtained with the standard direct light imaging configuration of the prototype RICH setup. (a) Single and (b) double Gaussian fits to the distribution have been evaluated.

involved fitting the function across the entire range of the radius distributions, to achieve fair comparisons between different data-sets by avoiding range selections and judgements by eye.

The double Gaussian fit function aims to account for the broad tails which are typically visible at both sides of the radius distributions, and may arise from contributions from scattered Čerenkov light, skewness introduced by different particle species and dispersion of the Čerenkov light. It has the functional form of $G = G_1(Amp_1, \mu_1, \sigma_1) + G_2(Amp_2, \mu_2, \sigma_2)$, where Amp, μ and σ denote the amplitude, mean and width values of each of the Gaussian components. The double Gaussian fit to the ring radius histogram returns two Gaussian distributions with roughly the same mean position. The first component has a smaller amplitude and broader width of (5.056 ± 0.180) mm to account for the tails, whereas the second corresponds to the main radius distribution and has a width of (2.195 ± 0.032) mm. This provides an improved resolution value to that of (2.567 ± 0.017) mm which is obtained with a single Gaussian fit. There is minimal difference in the mean values of (332.02 ± 0.02) mm and (331.95 ± 0.023) mm returned by the single and double Gaussian fits, and both values are also in extremely close agreement with the mean value of 331.8 taken from the hit distance distribution shown in Fig. 5.71. All radius mean values, however, do not agree with the expected mean of 320.91 mm, which is calculated for negative pions from: the beam momentum, the geometry of the setup and the Čerenkov equation.

There are several factors which may contribute to the discrepancy between the expected and measured mean radius values, including: the beam momentum uncertainty, the finite thickness of the aerogel and any geometrical offsets of the experimental setup. Combining the contributions from these systematical effects, in their most severe cases, there remains a mismatch between an upper calculated value of ~327.97 mm and the measured mean radius of ~332 mm. This however represents an upper extreme upper limit of these systematic effects and the main source of discrepancy is attributed to a shift in the aerogel refractive index from its nominal value of n = 1.05 quoted by the manufacturer. Confirmation of this effect has already been provided with a different aerogel tile used throughout the test-beam studies, and was validated through comparisons between Monte Carlo simulations and measurements performed by members of the CLAS12 RICH Collaboration [199]. In the final RICH detector a full characterisation of the aerogel tiles before installation will be able to monitor such effects.

The ring fit centre parameters obtained from the Čerenkov event ring fits are shown in Figs. 5.73 (a) and (b). As expected from the known dimensions of the beam, the horizontal ring centre distribution is broader than the vertical one, since the beam profile was wider in this direction. Again, Gaussian functions have been fitted to the distributions, yielding the width of the horizontal and vertical results as (7.120 ± 0.039) mm and (4.294 ± 0.025) mm. These

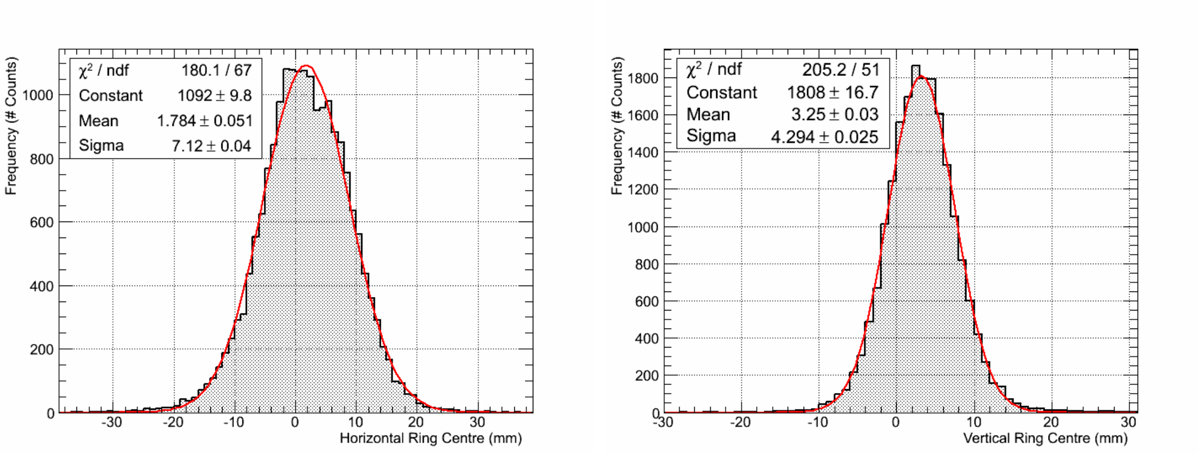

(a) (b)

Figure 5.73: Čerenkov ring centre distributions in the (a) horizontal and (b) vertical directions, obtained from ring fits to hit clusters above pedestal thresholds and the standard direct light prototype setup.

widths are typical amongst the data-sets analysed and the spread in the ring centre locations may be further visualised in Fig. 5.74. The mean ring centre positions are slightly offset from the origin of the MAPMT imaging plane, by (1.79 ± 0.05) mm and (3.25 ± 0.03) mm. This was typical of what was extracted with the test-beam data and indicates a slight mis-alignment between the setup and the beam. This effect was also observed using the tracks from the GEM chambers. The displacements were not greater than the magnitudes of these offsets, and this example represents one of the most extreme cases obtained with the direct light imaging setup.

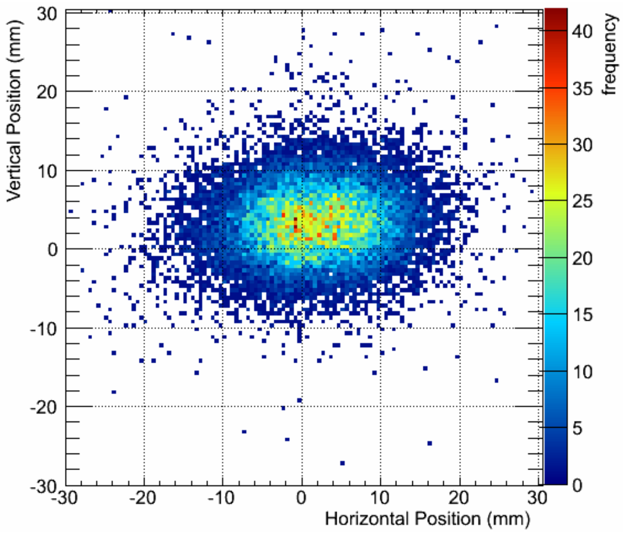

Figure 5.74: 2-Dimensional representation of the Čerenkov event ring fit centre values. The frequency is indicated by colour-fill.

Further to the refractive index study of the Čerenkov light yield, a similar study was performed with the Čerenkov ring radius distributions and resolutions. The three previously described aerogel refractive indices and data-sets were again used for the study [17], with tile thicknesses of t = 2 cm and a beam momentum of 8 GeV/c. Again, a full study into the effects of different aerogel radiator materials upon the Čerenkov ring resolution goes beyond the aim of this project. However, it is interesting to assess the general response of the MAPMT to the possible radiator refractive indices for the CLAS12 RICH, to check whether the imaged rings behave as expected and if any options are excluded due to the MAPMT's performance.

Fig. 5.75 (a) compares the hit distance distributions and Fig. 5.75 (b) compares the corresponding ring fit radius distributions obtained from analyses with data-sets extracted with the three different aerogel refractive indices. Immediately visible from both Figs. 5.75 (a) and (b) is that the mean Čerenkov ring radius values increase with aerogel refractive index as expected. This is illustrated further in Fig 5.76, which gives the mean values of the Čerenkov ring fit radius distributions shown in Fig. 5.75 (b), obtained from Gaussian fits, as a function of radiator refractive index. Mean values of (296.13 ± 0.01) mm, (332.27 ± 0.01) mm and (369.08 ± 0.01) mm for the increasing refractive indices are obtained. Similar to the previously described result of Fig. 5.72, the radius distribution means differ from the values of 286.22 mm, 320.91 mm and 352.49 mm expected from theory and geometry. This is again attributed to shifts in the refractive indices of the aerogel tiles from their nominal values.

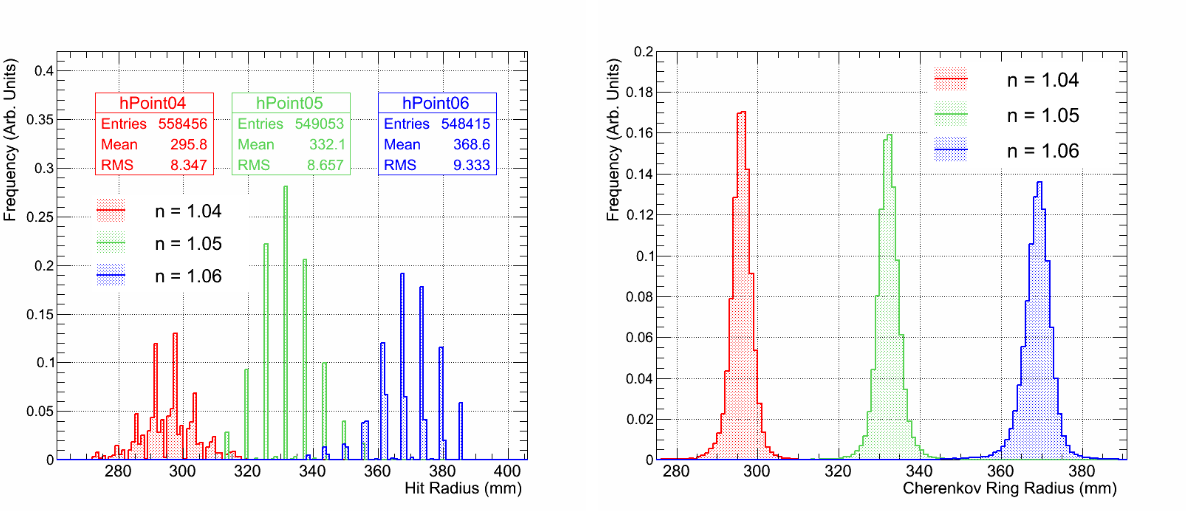

(a) (b)

Figure 5.75: Variation of (a) hit cluster distance and (b) Čerenkov ring fit radius distributions with aerogel refractive index, for tile thicknesses of 2 cm and a beam momentum of 8 GeV/c.

---

[17] The data-sets for each refractive index setting total 50 000 events. The tested refractive indices include n = 1.04 (November - December 2012 test-beam, runs 1137, 1138 and 1139), n = 1.05 (November - December 2012 test-beam, runs 1105, 1106 and 1107) and n = 1.06 (November - December 2012 test-beam, runs 1128, 1129 and 1130).

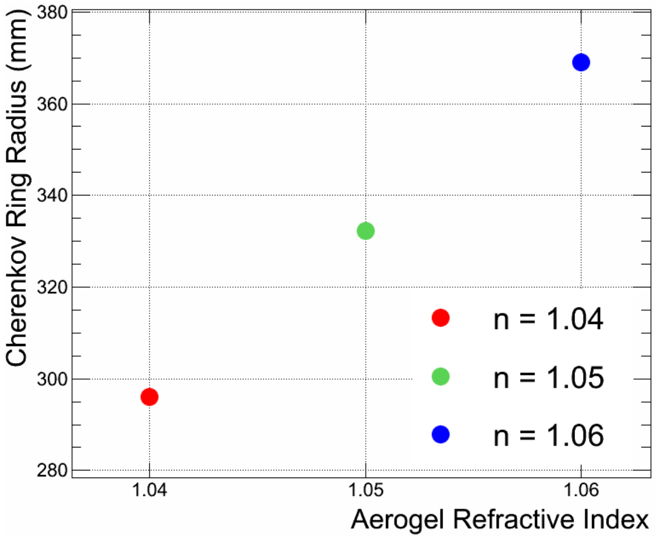

Figure 5.76: The mean Čerenkov ring radii extracted from Čerenkov ring fit radius distributions with a beam momentum of 8 GeV/c, aerogel thickness of 2 cm and refractive indices of n = 1.04, 1.05 and 1.06.

Another result visible in both Figs. 5.75 (a) and (b) is that the shape of the radius distributions and their resolutions also vary with aerogel refractive index, in particular for the shape of the hit distance distributions shown in Fig. 5.75 (a). The quantisation caused by the pixel size of the H8500 MAPMT is prominent in all cases, however the result for n = 1.04 has a greater proportion of counts lying between the peak structures and also the distribution for n = 1.06 is slightly more asymmetric than the others. For all refractive indices the resolution improves when the method of fitting the Čerenkov event rings is used, observed as a decrease in the widths of the distributions shown in Fig. 5.75 (b) in comparison to those shown in Fig. 5.75 (a). In Fig. 5.75 (b) the difference in resolutions between the refractive indices is visible, as the amplitudes and widths of the distributions decrease and increase respectively with increasing refractive index. The double Gaussian fits to these distributions account for any skews in the tails, for example in the n = 1.06 case where there exists a slightly extended tail to lower radius values the mean position of the broader Gaussian reflects this.

The σ - width resolution values extracted from both single and double Gaussian fits to the Čerenkov event ring fit radius distributions are shown in Fig. 5.77 (a). For all refractive index settings the extracted resolutions are significantly superior when the double Gaussian fit procedure is used. There also exists a dependence on the refractive index of the tiles, which will be discussed further below, where the resolution degrades as refractive index increases. The optimal σ-width of the ring radius distribution obtained is (2.070 ± 0.018) mm, with the n = 1.04 aerogel tile. Whereas the lowest resolution is (3.077 ± 0.013) mm, obtained with the

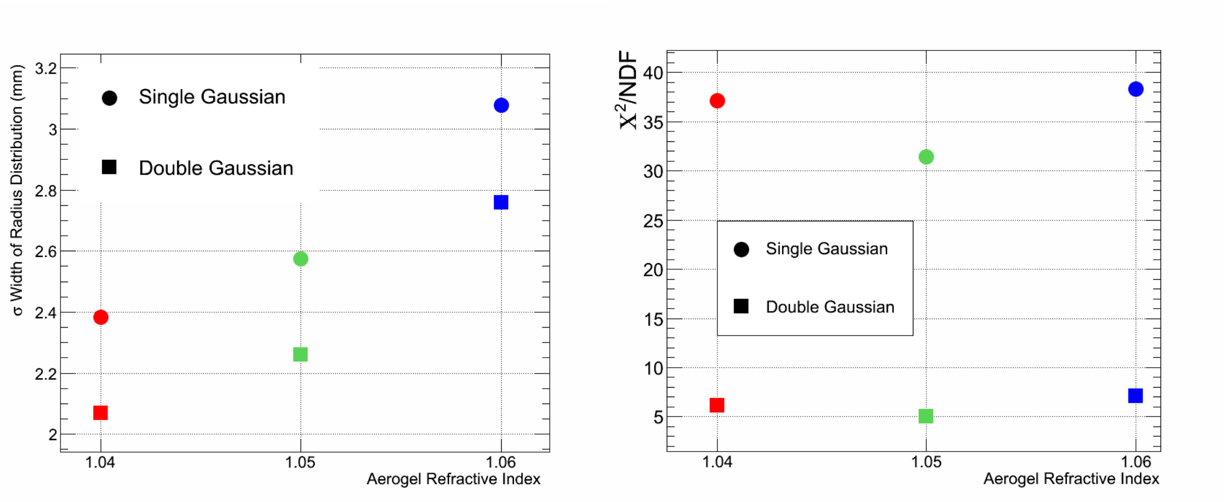

(a) (b)

Figure 5.77: (a) The variation with aerogel refractive index of the Čerenkov ring radius resolutions, defined as σ-widths of single and double Gaussian fits to the radius distributions and (b) the χ^2/NDF values returned from the fits to the radius distributions, used to gauge the successfulness of the fitting method.

n = 1.06 aerogel tile. The fitting procedure in the analysis software ROOT is based on a least squares minimisation technique, whereby the lowest χ^2 value between the fit function and data is found. The fit result returns a value for χ^2 divided by the Number of Degrees of Freedom (NDF) of the fit, which should be as close to one as possible. The result in Fig. 5.77 (b) gives the χ^2/NDF values for both the single and double Gaussian fits to all three refractive indices. In all cases the double Gaussian fit appears to be superior, compared to the χ^2/NDF values for the single Gaussian results.

A summary of the ring radius mean, coverage and resolution values is given in Table. 5.16. The results illustrate that the H8500 MAPMTs are sensitive to differences in Čerenkov ring properties and resolutions caused by varying aerogel properties as expected from the Čerenkov theory (see Section 2.1). The H8500 MAPMTs offer the same spatial resolution in all cases for

Table 5.16: Variation with refractive index of Čerenkov ring radius distribution means, resolutions and corresponding coverage provided by the test-beam prototype.

Refractive Index	**Mean Radius [mm]**	**Ring Coverage [%]**	**Fit Function**	**Resolution (σ-width) [mm]**
1.04	296.13 ± 0.01	78.25	Single Gaussian Double Gaussian	2.383 ± 0.010 2.070 ± 0.018
1.05	332.27 ± 0.01	69.74	Single Gaussian Double Gaussian	2.575 ± 0.011 2.256 ± 0.020
1.06	369.08 ± 0.01	62.79	Single Gaussian Double Gaussian	3.077 ± 0.013 2.758 ± 0.021

imaging of the Čerenkov rings. If one assumes the optimal configuration where the Čerenkov hits are uniformly distributed amongst the centres of the pixels then, as described in [20] for the example of tracking detectors, the spatial resolution available from the H8500 MAPMT is $6.08/\sqrt{12}$, and hence a lower value of 1.76 mm is achieved. In this case 6.08 corresponds to the magnitude of the pixel - to - pixel pitch of the H8500 MAPMT. The pixel sizes of the H8500 MAPMTs therefore are not the major limitation in the achievable Čerenkov ring resolution with the test-beam prototype setup.

The origins of the differing ring resolutions arise from the aerogel refractive indices, optical quality and artifacts of the experimental setup. Since the Čerenkov light yield increases with refractive index of the aerogel, this should in principle improve the Čerenkov ring resolution (see Equation 2.6). However, the density of the aerogel also increases with refractive index (see Equation 2.8), which may result in more scattering of the Čerenkov light after production and hence contribute a smearing effect to the Čerenkov ring resolution. Chromatic dispersion effects will also be more significant with the higher refractive index aerogel tiles. Furthermore the $n = 1.06$ result suffers from the 62.79 % ring coverage provided by the 28 H8500 MAPMTs in the test-beam prototype case, reducing its measured Čerenkov yield, and the optical quality of the aerogel tiles will also play a crucial role in the obtainable Čerenkov ring resolutions. The transmittance of the aerogel tiles (see Equation 2.10), as measured with a spectrophotometer by members of the CLAS12 RICH Collaboration, is similar for all the tiles [198], with transmittance values of 0.591, 0.574 and 0.578 measured for the $n = 1.04, 1.05$ and 1.06 tiles respectively [198]. The slightly higher transmittance of the $n = 1.04$ tile, in combination with its relatively high ring coverage in the prototype, may explain why the Čerenkov ring resolution is superior. A comparison of the $n = 1.05$ result with the higher transmittance aerogel tile manufactured using a newer production technique, as previously described and compared in the Čerenkov yield results, confirms the importance of the aerogel optical quality to the Čerenkov ring resolution. Ring resolutions of (2.220 ± 0.015) mm and (1.896 ± 0.024) mm are obtained with single and double Gaussian fits to the ring fit radius distributions with the higher transmittance aerogel tile respectively. A full study of such effects caused by choice of aerogel radiator material on the Čerenkov ring resolution will be extremely important for the final CLAS12 RICH application and the overall detector design.

The Čerenkov ring resolution obtained with a refractive index of $n = 1.05$ from the test-beam results has been compared with detailed Geant4 simulations by M. Contalbrigo [199,200], which have confirmed that the resolution is not only caused by the spatial resolution of the H8500

MAPMT but also several other factors such as: the uncertainty in the photon emission point; dispersion of the Čerenkov light in the aerogel material; misalignment effects in the setup, for example in MAPMT positions; dark counts arising in the H8500 MAPMTs and smearing caused by the detection of Čerenkov light which has undergone Rayleigh scattering within the aerogel material. Based upon information provided by Hamamatsu and experimental observations, the H8500 MAPMT dark counts in the large-scale prototype are quantified and confirmed by the simulation studies as corresponding to a probability of 3×10^{-4} dark count hits per pixel per event, yielding half a dark count per event for the entire RICH prototype [201]. The use of GEM tracks to fix the centre position of the ring fits, and fit events with the ring radius as the only free parameter, has been shown to improve the Čerenkov ring resolution by $\sim 10\,\%$ [202]. Even without these additional studies however, the results have shown that the H8500 MAPMTs offer Čerenkov ring resolutions approaching 2 mm through selection of the appropriate aerogel radiator material, which is significantly smaller than the pixel size of the MAPMT and, as will be shown, is sufficient to provide π/K separation at the most challenging momentum of 8 GeV/c for the RICH detector.

Comparison between UV-Extended and Standard Entrance Windows

The inclusion of both UV-extended and standard glass window type H8500 MAPMTs in the test-beam prototype setup allowed for a comparison between their performances in the detection of Čerenkov light and an assessment of which model would be most suited for the CLAS12 RICH application. The largest fraction of produced Čerenkov radiation is emitted in the UV wavelength ranges, and so one would initially expect that the UV-extended window option of the H8500 MAPMT offers the superior solution, since it should be sensitive to a greater proportion of the Čerenkov yield than the standard borosilicate glass option. An example of a comparison between the cluster multiplicities, sizes and Čerenkov ring radius resolutions available with both the UV-extended and standard glass windows is given below. The results shown were extracted from a 20 000 event data-set [18], in the standardised direct light imaging configuration at 8 GeV/c. For the analysis the 28 MAPMTs were divided into two subsets corresponding to the two window types, however one MAPMT was removed from each subset due to noise issues, leaving 13 MAPMTs in each subset.

The cluster multiplicity distributions obtained with the two different window type MAPMTs

---

[18] November - December 2012 test-beam, run 1105.

are shown in Fig. 5.78 (a). Gaussian fits retrieve the mean values of the distributions as (4.766 ± 0.011) clusters and (5.727 ± 0.011) clusters for the standard and UV-extended windows respectively. The results illustrate that the UV-extended window type provides about 1 cluster more per event, as expected. The overall yield magnitudes are lower than the previous results since only 13 MAPMTs are used in each case, as opposed to the full 28 MAPMTs of the test-beam setup. The resulting cluster size distributions for both window types are shown in Fig. 5.78 (b). Mean values of 1.047 pixels and 1.045 pixels and RMS-width values of 0.2493 pixels and 0.2381 pixels are extracted with the standard and UV-extended windows respectively. The cluster size results show minimal difference between the two MAPMT types. Hence, the shape of the distribution is further confirmed to be mostly due to intrinsic properties of the MAPMTs themselves, resulting from crosstalk occurring within the MAPMT and its substructure.

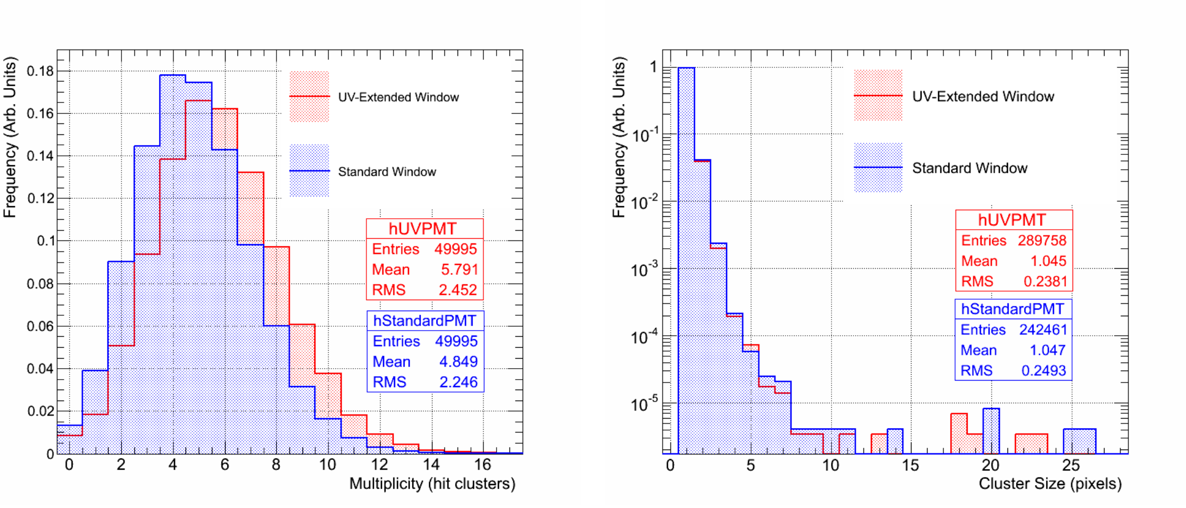

(a) (b)

Figure 5.78: (a) Cluster multiplicity and (b) cluster size distributions obtained using only either 13 standard (blue) or 13 UV-extended window type H8500 MAPMTs. The data was obtained with a beam momentum of 8 GeV/c, aerogel refractive index of n = 1.05 and thickness 2 cm.

Čerenkov ring fit radius distributions extracted with the two MAPMT window types are compared in Fig. 5.79. The two curves appear to differ in both mean position and width, which is confirmed on comparison of the fit results to the distributions, shown in Table 5.17. The

Table 5.17: Čerenkov event ring fit radius means and resolutions obtained using only either 13 standard (blue) or 13 UV-extended window type H8500 MAPMTs.

Window Type	**Mean Radius [mm]**	**Single Gaussian σ - width [mm]**	**Double Gaussian σ-width [mm]**
Standard	331.85 ± 0.02	3.509 ± 0.020	3.071 ± 0.025
UV-Extended	332.68 ± 0.02	3.880 ± 0.020	3.421 ± 0.026

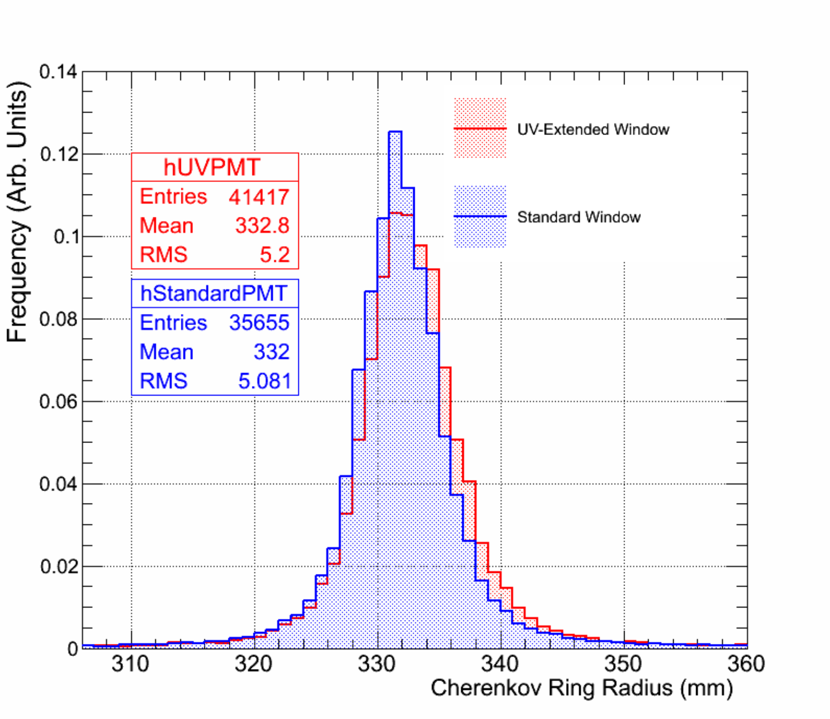

Figure 5.79: Čerenkov event ring fit radius distributions obtained using only either 13 standard (blue) or 13 UV-extended (red) window type H8500 MAPMTs. The data was obtained with a beam momentum of 8 GeV/c, aerogel refractive index of n = 1.05 and thickness 2 cm.

mean position of the radius distribution shifts by ∼1 mm towards higher values when the UV-extended window type MAPMTs only are used. This effect is due to dispersion of the Čerenkov light in the aerogel material, as will be shown later. The overall resolution is degraded in comparison with previously shown results due to the fact, again, that 13 MAPMTs are used here as opposed to 28 previously. The Čerenkov ring resolutions obtained with both MAPMT types are different, with the standard window MAPMT type offering a ∼10 % improved resolution compared with the UV extended window type MAPMT, irrespective of the type of fit used to describe the distributions. The result is contrary to what one may initially postulate, since with the UV-extended window type MAPMTs the Čerenkov yield is higher and hence this would imply a better defined Čerenkov ring. However, the Čerenkov light at the UV wavelengths are more likely to undergo Rayleigh scattering effects in the aerogel material than the visible wavelength light and the Rayleigh scattering effect smears the Čerenkov ring resolution. This effect is inhibited with the standard window type MAPMT through the exclusion of a greater proportion of these events caused by the transmission cut-off wavelength of the window.

These results imply that to attain a superior Čerenkov ring resolution in the CLAS12 RICH detector, the H8500 MAPMTs with the standard borosilicate glass window should be selected.

Wavelength Dependence of the Detected Čerenkov Light

Further to the MAPMT window type study, a series of measurements were performed to study chromatic effects and the overall influence of the Čerenkov light wavelength on the Čerenkov ring properties as measured by the H8500 MAPMTs.

For this study several optical bandpass filters were used and placed immediately downstream of the aerogel material, to select pre-defined wavelength (λ) ranges of the Čerenkov light produced by the incident particles. For the comparisons which will be shown the ranges studied comprised: $\lambda < 400$ nm; 400 nm $< \lambda <$ 450 nm; 450 nm $< \lambda <$ 500 nm; 500 nm $< \lambda <$ 550 nm; 550 nm $< \lambda <$ 600 nm and 600 nm $< \lambda$. For each wavelength setting an accumulation of 40 000 events were studied, and a list of the data-sets may be found in Table E.1. All 28 MAPMTs were used in the data analysis for all wavelength bands, in order to obtain sufficient statistics. The aerogel radiator used was previously described as the tile offering a relatively high transmittance value of 0.71. The tile has a thickness of $t = 2$ cm and a nominal refractive index of $n = 1.05$, however, again a shift in the refractive index of the tile has been observed, resulting in a mis-match between measured and expected mean Čerenkov ring radius values obtained with the tile.

The cluster multiplicity distributions obtained for each wavelength band are shown in Fig. 5.80 (a), where they are also compared with the result from no filter in place, and all wavelengths allowed to pass. As expected, the result from the $\lambda < 400$ mm setting provides the highest contribution to the Čerenkov yield measured by the H8500 MAPMTs, due to the high-

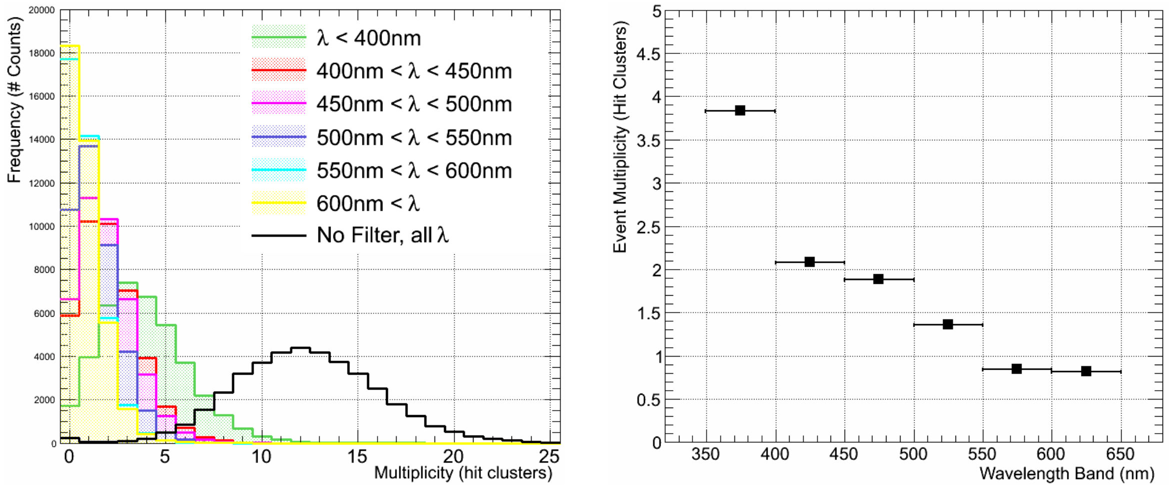

(a) (b)

Figure 5.80: Event cluster multiplicity (a) distributions and (b) mean values obtained with different wavelength bands of the Čerenkov light.

est intensity of the Čerenkov radiation at these wavelength ranges. The contributions from the wavelengths ranging up to 550 nm also provide relatively high yields, beyond which the relative contributions per event start to decrease. These results are also in accordance with the quantum efficiency response spectrum of the H8500 MAPMTs, which is peaked towards the blue wavelengths of the visible light spectrum. The mean values of the cluster multiplicity distributions are given in Fig. 5.80 (b), where the horizontal error bars represent the wavelength bands of the filters used for each measurement. If one adds the mean values from the individual filter configurations then the total is close to that obtained with no filter in place at all, confirming that all wavelength components contribute to the final measured quantity.

The cluster size distributions extracted from all filter configurations are compared with those obtained with no filter in place in Fig. 5.81. Any differences are caused by the yield levels for each wavelength band, since the histograms are unscaled, and in general there is negligible difference between the results from the various filter settings. The filter results are in accordance with those obtained with no filter in place, and with the crosstalk levels and noise behaviour as previously discussed. Furthermore the extremely stable cluster size of the MAPMT, resulting from the low levels of intrinsic crosstalk, confirms the H8500 MAPMT as an appealing choice for such a Čerenkov application, in which the photon detector is required to measure single photon level signals across a continuous range of wavelengths. This result cannot be directly compared with the previous crosstalk study which was performed at wavelengths

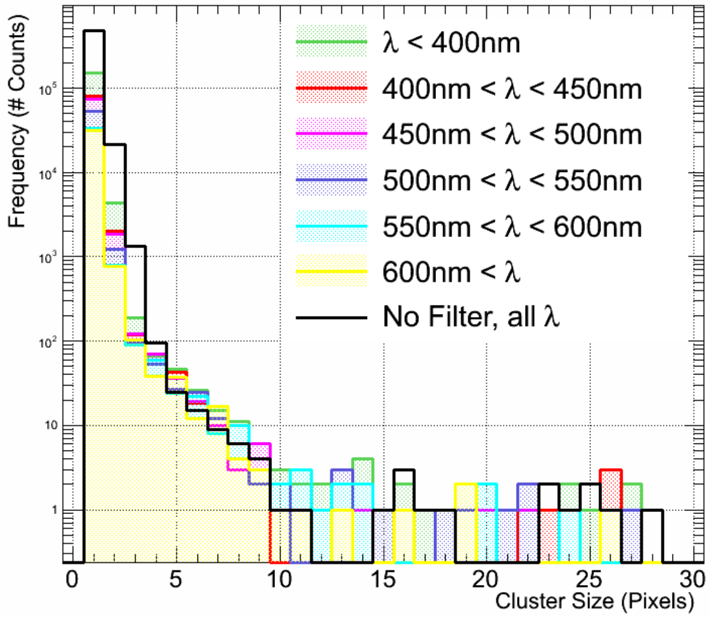

Figure 5.81: Wavelength dependence of the hit cluster sizes extracted from the H8500 MAPMTs.

of 407.2 nm and 634.7 nm and shown in Section 4.6.2. This is partly caused by a combination of the systematic uncertainties arising from the use of two different setups and the different readout electronics used with the laser tests. Moreover, the pedestal threshold cuts selected in each case are different, and the increased threshold of 4 σ used with the test-beam data is likely to remove the majority of the low-level optical crosstalk observed with the laser tests.

It has already been shown that the influence of the UV-wavelength Čerenkov light is detrimental to the Čerenkov ring resolution, if the UV-extended window type MAPMTs only are used. It is therefore important, since detection across part of the UV and the visible wavelength spectrum is required, to assess the Čerenkov ring properties obtained with different wavelengths of the Čerenkov light. The radius distributions obtained from Čerenkov ring fits to the data for each filter configuration are given in Fig. 5.82. The mean positions of the ring radius distributions decrease with increasing wavelengths, as expected. This is caused by dispersion of the Čerenkov light in the aerogel material itself. The result obtained with no filter in place will consist of an averaged value from all such contributions, weighted by the Čerenkov yields at each wavelength. This is why the result for all wavelengths is mostly in accordance with the distribution obtained for the $\lambda < 400$ nm filter configuration, where the Čerenkov yield is the highest. The mean values extracted from single Gaussian fits to the radius distributions are shown in Fig. 5.83 (a). The result for the wavelength band of $600\,\text{nm} < \lambda$ is anomalous,

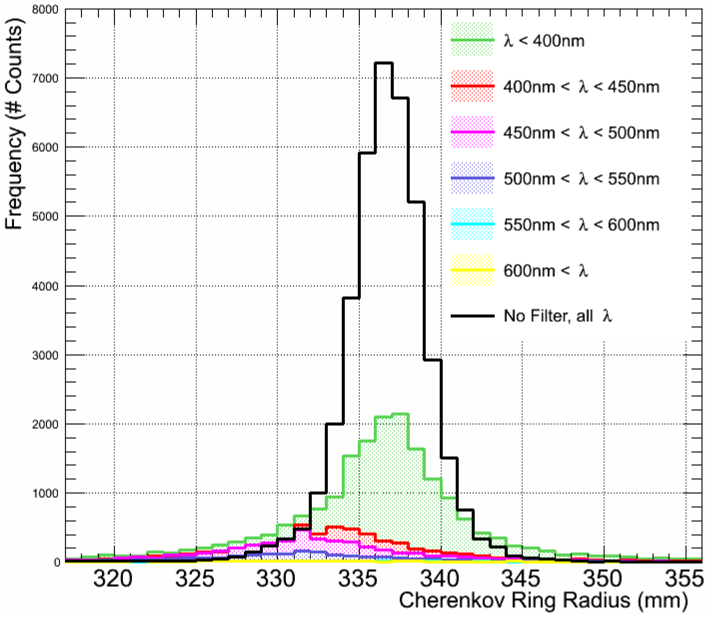

Figure 5.82: Wavelength dependency of the Čerenkov event ring fit radius distributions. Due to dispersion, the mean radius position varies with wavelength band. The resolution of the peaks is limited by statistics at higher wavelengths and affected more strongly by Rayleigh scattering at lower wavelengths.

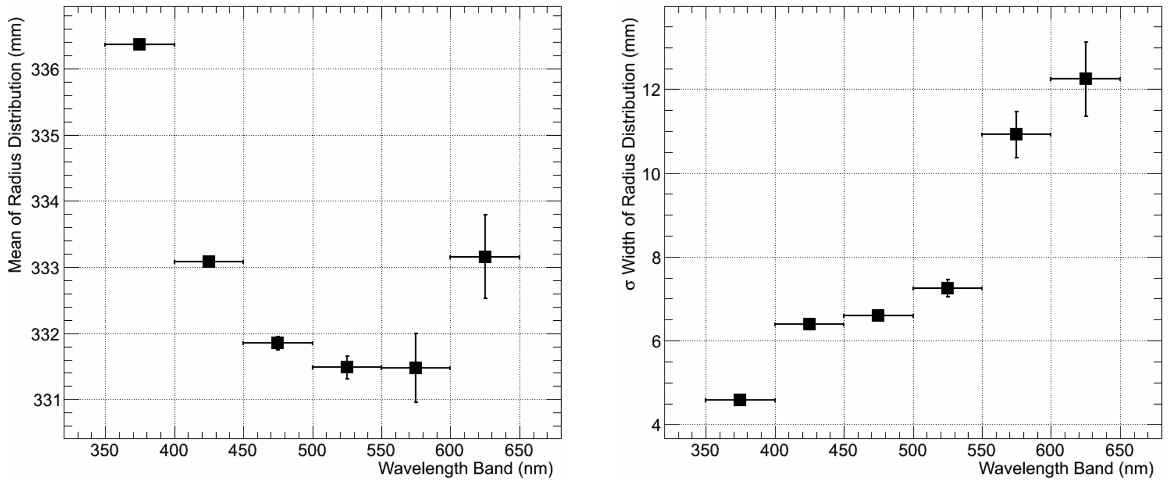

(a) (b)

Figure 5.83: Wavelength dependency of Čerenkov ring fit radius distribution (a) mean and (b) σ - width values obtained from Gaussian fits.

possibly due to a lack of statistics from this data-set. In the Čerenkov ring fit analysis at least 4 clusters are required to perform a ring fit to a Čerenkov event, in accordance with the data analysis technique used for the previous Čerenkov ring radius resolution results shown. For the higher wavelength bands the mean event cluster multiplicities are drastically lower than 4 (see Figs. 5.80 (a) and (b)), and low statistics become a detrimental issue in obtaining sufficiently defined radius distributions to allow for fair resolution comparisons to be made. This is confirmed in Fig. 5.83 (b), which gives the σ - widths of Gaussian fits to each of the radius distributions obtained. The general trend is that the width increases with the wavelength band of the filter, contrary to the expected behaviour. Again, this is an artifact of the significantly lower statistics available as the wavelength band was increased, and could be further studied by accumulating higher statistics for each filter setting.

The wavelength dependence measurements confirmed the expectations that the majority of the Čerenkov light yield is obtained from the blue and UV wavelength regions of the Čerenkov light produced, a region in which Rayleigh scattering of the light in the aerogel material will play an important role on the Čerenkov ring resolution. Dispersive effects within the aerogel material also yield a range of resulting Čerenkov angles and hence measured radii values, which will contribute significantly to the Čerenkov ring resolution by smearing the mean value, as shown in Fig. 5.82 and Fig. 5.83 (a). These dispersive effects, as measured by the wavelength dependence study, will be useful for tuning Monte Carlo simulation models of the aerogel radiator material in the CLAS12 RICH simulations. This is important for studying the chromatic error contributions to the achievable Čerenkov angle resolution with the RICH detector.

Particle Species Separation Power

The crucial factor of the final CLAS12 RICH detector in determining its success will be its ability to perform adequate π/K separation, in particular, across the entire momentum range of 3 GeV/c to 8 GeV/c. The benchmark goal is to attain a $> 3\,\sigma$ up to momenta of 8 GeV/c, which represents the most challenging configuration of the RICH. The determination of the separation power achievable with the test-beam RICH prototype was also one of the main goals of the experimental studies with the prototype. An understanding of the prototype's separation power, in terms of the measured Čerenkov yields and ring resolutions, will allow extrapolation of the results to performance projections for the final CLAS12 RICH detector.

Throughout literature there are several slightly different definitions of separation power for a particle identification detector. For analysis of data extracted with the test-beam RICH prototype, the definition of separation power used was equivalent to that adopted by the P̄ANDA collaboration's particle identification group, and is described fully in [203]. The definition is based on the assumption that the measured observables for the different particles, in this case the Čerenkov ring radius distributions, follow roughly that of a Gaussian shape. The separation power quantity then relates the mean values of the measured distributions for the different particles to their individual standard deviations, and is measured in terms of *number of Gaussian sigmas of the separation potential* [203]. The separation power N_σ, for two particle observable distributions numbered 1 and 2, is defined in Equation 5.3, where: μ_1 and μ_2 denotes the two mean values of the different particle distributions; $\sigma_{average}$ is their combined average standard deviation; σ_1 and σ_2 are the individual standard deviations of the two particle observable distributions.

$$N_\sigma = \frac{|\mu_1 - \mu_2|}{\sigma_{average}} = \frac{|\mu_1 - \mu_2|}{(\frac{\sigma_1}{2} + \frac{\sigma_2}{2})} \tag{5.3}$$

The separation power definition is symmetric for both particle species components, irrespective of their widths, which are accounted for.

For analysis of the separation powers obtained from test-beam data, the μ and σ values were extracted from Gaussian fits to the Čerenkov ring fit radius distributions for the different particle species. The radius distributions were obtained by using the beam threshold Čerenkov counter as an offline trigger for pions and veto for kaons in the analysis stage. This principle was illustrated previously in Fig. 5.43, where a pedestal peak corresponding to no signal extracted from the beam Čerenkov counter is obtained in the ADC spectrum and designated to arise from kaons, and any other heavier particles which may be present and below the Čerenkov threshold. For each analysed run a Gaussian distribution was fitted to the pedestal peak of the beam threshold Čerenkov counter charge spectrum, and a resulting $5\,\sigma$ threshold was set as the cut above and below which the particles were assigned as pions and kaons respectively. The separation power study was performed for varying beam momenta of 6, 7 and 8 GeV/c. The configuration was that adopted as the standardised setup for the direct light imaging case of the prototype RICH, with an aerogel refractive index of $\mathrm{n} = 1.05$ and thickness of $\mathrm{t} = 2\,\mathrm{cm}$, and the aerogel radiator used was the one produced by a novel aerogel production technique. A list of the experimental data-sets used for the analysis is given in Table F.1. Due to the available statistics, an accumulation of ~94 000, 40 000 and 50 000 events were used for the 8 GeV/c, 7 GeV/c and 6 GeV/c settings.

The Čerenkov ring fit radius distributions obtained at a momentum of 8 GeV/c with the beam threshold Čerenkov counter above (blue) and below (red) threshold are shown in Fig. 5.84 (a). The amplitude of the distribution obtained from particles with β-values below the threshold of the beam Čerenkov counter, assumed to be negative kaons, is significantly smaller than that obtained with particles above threshold, which are assumed to be negative pions, and were therefore scaled for visualisation purposes and to evaluate the relative intensities of the two particle species only. For this the amplitudes of both the pion and kaon peaks were found and used to calculate a relative amplitude scaling factor, which in this case was 62:1 for $\pi : K$. The kaon distribution was re-scaled by this factor to produce the result given in Fig. 5.84 (b), where the pion peak is visible in blue, and the kaon contribution is visible in red as the larger amplitude peak. There appears also to exist a third contribution in the scaled-result with a smaller Čerenkov ring radius, and hence a heavier mass than that of the

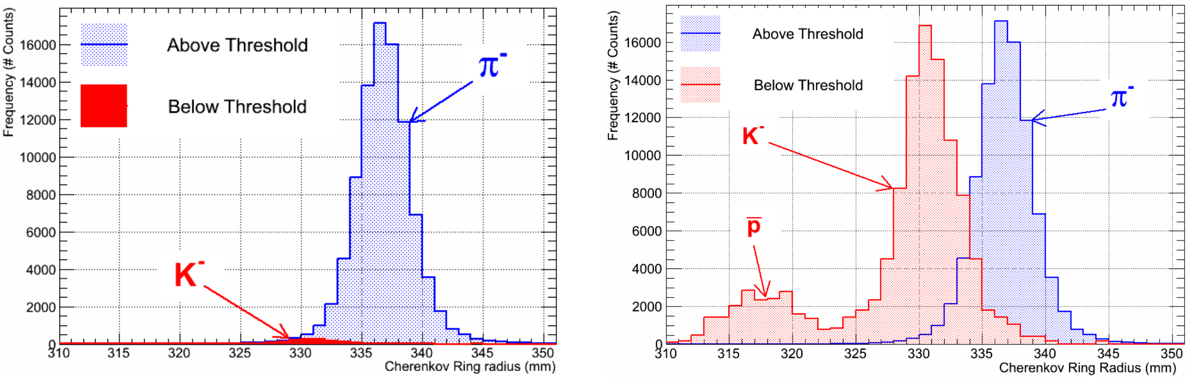

(a) (b)

Figure 5.84: (a) Un-scaled and (b) amplitude-scaled Čerenkov ring radius distributions for pions (beam Čerenkov counter above threshold) and kaons (beam Čerenkov counter below threshold) at 8 GeV/c.

kaons. This contribution is postulated to arise from antiprotons as will be discussed below. The amplitude scaling factor is of the correct order of magnitude and in a rough agreement with the expected relative intensities obtained from the example calculation found in [183] and shown in Fig. 5.41. An alternative scaling method was tested, in which Gaussian functions were fitted to both the pion and kaon peaks and the scaling factor calculated from the relative integrals of the resulting functions. The result was in agreement with the amplitude scaling factor obtained, but throughout all studies the amplitude scaling method was incorporated to exclude any possible influence of contamination from inclusion of events from other particle species in the distributions and Gaussian integrations.

The un-scaled Čerenkov ring fit radius distributions were fitted with Gaussian functions, the results of which are shown in Figs. 5.85 (a) and (b). The pion peak was again fitted with a double Gaussian function to compensate for the broad tail structures and any possible contaminations from the kaon distribution. The kaon and antiproton distribution was also fitted with a double Gaussian function. A triple Gaussian fit function was tested, to account for the extended tails of the kaon peak, and the resulting kaon Čerenkov ring resolution (and hence pion/kaon separation power) was significantly improved. However, this fit procedure was not used with the results obtained at different momentum settings and, for a consistent comparison, the double Gaussian function was therefore used to fit the distribution shown in Fig. 5.85 (a). The results are given in Table 5.18, where they are also compared with the mean radius values expected from Čerenkov theory and the setup geometry. Immediately obvious is the mis-match between the expected and measured radius values, which again is

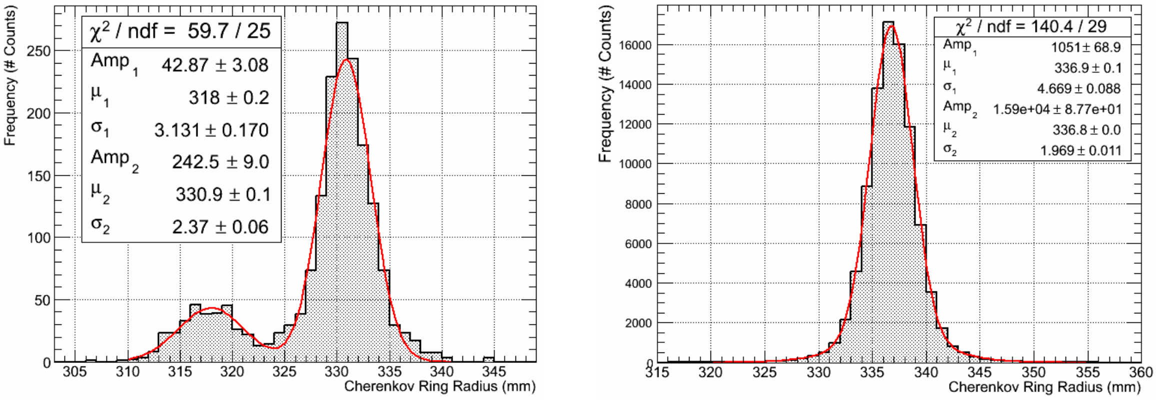

(a) (b)

Figure 5.85: (a) Kaon and antiproton and (b) pion Čerenkov ring fit radius distribution fitted with double Gaussian functions, the results of which are also shown on the plots. The results are obtained with a beam momentum of 8 GeV/c and the standard configuration for the direct light imaging case of the prototype.

Table 5.18: Expected ring radii and measured radius distribution means and widths obtained for pions, kaons and what is postulated to be antiprotons. The results were obtained with a beam momentum of 8 GeV/c and the standard direct light imaging case configuration.

Particle Type	**Expected Radius [mm]**	**Measured Radius [mm]**	**Measured σ-width [mm]**
Pions	320.91	336.81 ± 0.01	1.9690 ± 0.0112
Kaons	314.79	330.89 ± 0.06	2.3695 ± 0.0637
Antiprotons	296.71	318.00 ± 0.21	3.1306 ± 0.1704

postulated to be caused by shifts in the nominal refractive index of the aerogel tile. The ratios between the expected and measured ring radii for π and K particle species are consistent at values of $\sim$1.05, and so the source of discrepancy is considered to be common amongst them. However, the ratio between the expected and measured antiproton radii values is slightly different at $\sim$1.07, hinting that another effect also contributes to the mis-match in this case. The expected radius difference for pions and kaons is 6.12 mm, which agrees rather well with the radius difference of 5.92 mm as measured from the obtained pion and kaon distributions, confirming their identification. The expected radius difference for kaons and antiprotons is 18.08 mm, whereas the measured difference is 12.89 mm. There exists a discrepancy of 5.19 mm between the expected and measured radius differences, confirming an extra source of error within the antiproton measurement, nonetheless the contribution is still concluded to arise from antiprotons due to the prior knowledge of the beam composition. Using Equation 5.3 and the results from the Gaussian fits given in Table 5.18, a π/K separation power of $(2.73 \pm 0.02)\,\sigma$ is extracted. This does not exactly match, but is close to the benchmark π/K $3\,\sigma$ separation goal of the CLAS12 RICH detector at 8 GeV/c. The results also yield $\pi/\bar{\mathrm{p}}$ and $K/\bar{\mathrm{p}}$ separation powers of $(7.38 \pm 0.02)\,\sigma$ and $(4.69 \pm 0.02)\,\sigma$ with the test-beam RICH prototype respectively and, although $\bar{\mathrm{p}}$ separation powers do not represent the benchmark goal used for studies of the CLAS12 RICH projected performance, the $\bar{\mathrm{p}}$ identification power of the RICH detector will be very important in CLAS12 over the momentum range of 4.5 GeV/c to 8 GeV/c (see Section 1.4), and therefore these separation powers are promising for the prospects of the projected CLAS12 performance.

The equivalent unscaled and amplitude scaled histograms obtained with a beam momentum of 7 GeV/c are shown in Figs. 5.86 (a) and (b). The amplitude scale factor for the kaon distribution in this case was calculated as 78. The contribution from antiprotons remains present, however with a reduced amplitude compared to the result obtained at 8 GeV/c. Without scaling, the amplitude of the antiproton distribution, as extracted from a Gaussian fit, is returned

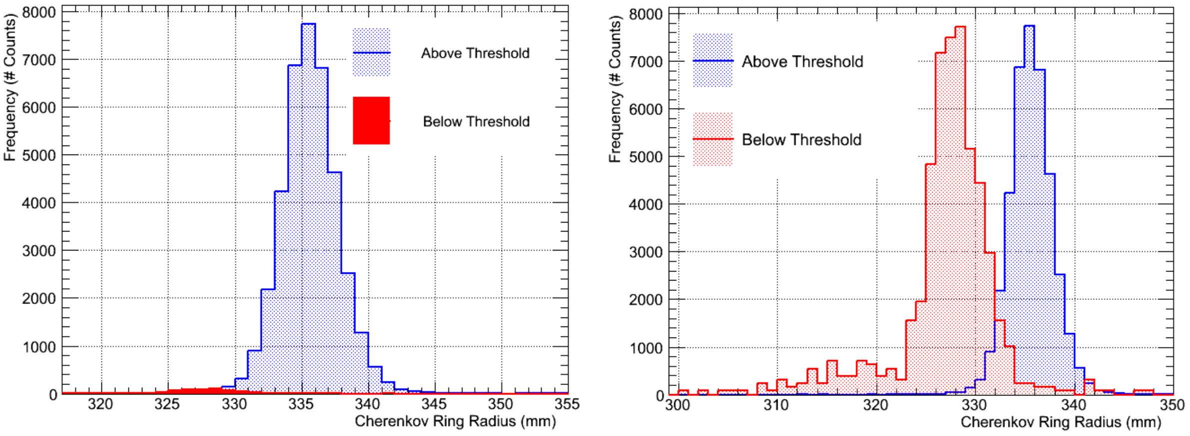

(a) (b)

Figure 5.86: (a) Un-scaled and (b) amplitude-scaled Čerenkov ring radius distributions for pions (beam Čerenkov counter above threshold) and kaons (beam Čerenkov counter below threshold) at 7 GeV/c.

as (5.37 ± 1.37) counts at 7 Gev/c and (42.87 ± 3.08) counts at 8 GeV/c. The results from a double Gaussian fit to the kaon and antiproton distribution and a double Gaussian fit to the pion distribution are given in Table 5.19. At 7 GeV/c the expected π/K and $K/\bar{\mathrm{p}}$ radius differences from theory and geometry are 8.04 mm and 24.01 mm respectively. The measured differences as returned from the fits to the Čerenkov ring radius distributions are 7.39 mm and 11.28 mm respectively. The agreement between expected and measured radius differences for pions and kaons is again close, however the equivalent comparison between the kaons and antiprotons is significantly worse than obtained at 8 GeV/c. With the fit results given in Table 5.19 a π/K separation of $(3.48 \pm 0.03)\,\sigma$ is obtained with the test-beam RICH prototype at 7 GeV/c, which is improved from the 8 GeV/c result, as expected, due to the larger difference in the β values of the particles at this momentum.

Table 5.19: Expected ring radii and measured radius distribution means and widths obtained for pions, kaons and what is postulated to be antiprotons. The results were obtained with a beam momentum of 7 GeV/c and the standard direct light imaging prototype case.

Particle Type	**Expected Radius [mm]**	**Measured Radius [mm]**	**Measured σ-width [mm]**
Pions	320.75	335.58 ± 0.16	1.8607 ± 0.0235
Kaons	312.75	328.19 ± 0.12	2.3852 ± 0.1009
Antiprotons	288.71	316.91 ± 1.49	5.2027 ± 2.3624

The π/K separation power of the prototype was expected to improve even further on the reduction of the beam momentum to 6 GeV/c, which was confirmed. The resulting unscaled and amplitude scaled histograms at 6 GeV/c are shown in Figs. 5.87 (a) and (b), where the amplitude scaling factor was found to be 77, in close agreement with the factor found at

7 GeV/c. At 6 GeV/c the antiproton contributions are no longer present, and the separation between the pion and kaon particle species is already visible in Fig. 5.87 (a) before application of the amplitude scaling factor. There does however appear to be some contamination from pions in the kaon distribution, which is accounted for in the double Gaussian fit to the kaon distribution. The fit results from both the pion and kaon distributions are given in Table 5.20. For the 6 GeV/c case a radius difference of 10.29 mm is obtained, which compares extremely well with the expected difference of 10.99 mm. The fit results correspond to a π/K separation power of $(4.81 \pm 0.02)\,\sigma$ at 6 GeV/c with the test-beam RICH prototype, which is significantly superior than the results obtained at 7 GeV/c and 8 GeV/c.

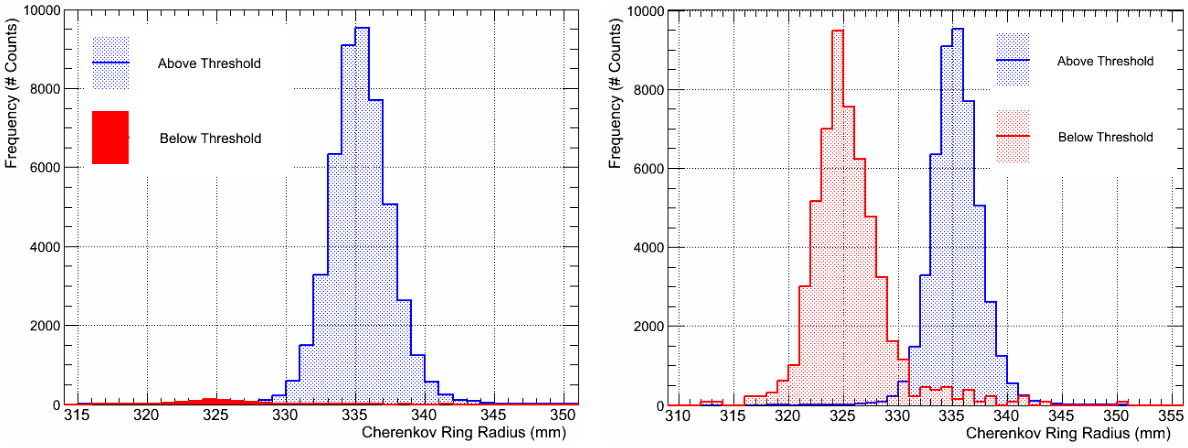

(a) (b)

Figure 5.87: (a) Un-scaled and (b) amplitude-scaled Čerenkov ring radius distributions for pions (beam Čerenkov counter above threshold) and kaons (beam Čerenkov counter below threshold) at 6 GeV/c.

Table 5.20: Expected ring radii and measured radius distribution means and widths obtained for pions and kaons. The results were obtained with a beam momentum of 6 GeV/c and the standard direct light imaging prototype case.

Particle Type	**Expected Radius [mm]**	**Measured Radius [mm]**	**Measured σ-width [mm]**
Pions	320.50	335.29 ± 0.01	1.8747 ± 0.0192
Kaons	309.51	325.00 ± 0.12	2.4018 ± 0.1037

The results from the separation power study prove that the spatial resolution and single photon efficiency obtained with the H8500 MAPMTs is adequate to provide π/K separation with the test-beam RICH prototype across the tested energies of 6 GeV/c, 7 GeV/c and 8 GeV/c. The results are summarised in Fig. 5.88, where the separation power increases with decreasing momentum, as expected, from $(2.73 \pm 0.02)\,\sigma$, to $(3.48 \pm 0.03)\,\sigma$ and finally $(4.81 \pm 0.02)\,\sigma$, at 8 GeV/c, 7 GeV/c and 6 GeV/c respectively. The value obtained at 8 GeV/c is slightly less

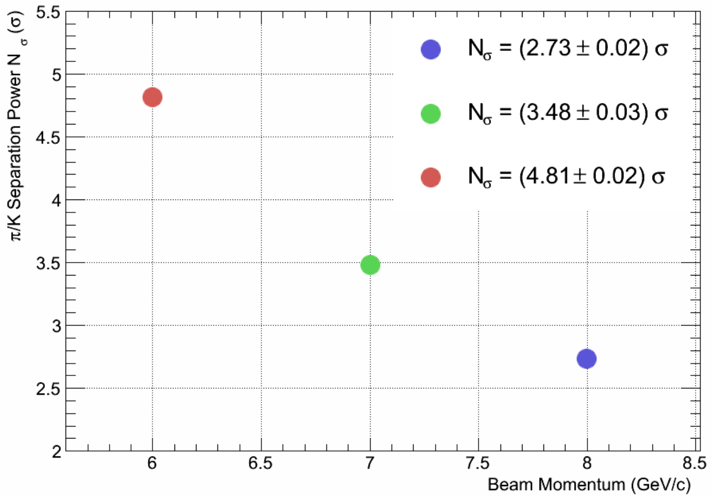

Figure 5.88: π/K separation powers obtained with the large-scale prototype with beam momenta of 6, 7, and 8 GeV/c.

than the required $3\,\sigma$ minimal value required in the CLAS12 RICH detector, however there are several manipulations of the data which may be performed to improve the result. For instance the fixing of ring centres in the Čerenkov event fitting step has been shown to improve the Čerenkov ring resolution by 10 %, which is likely to yield improved separation powers. Furthermore, there may still remain some contamination or background effects which are not accounted for in the simple Gaussian fits of the kaon distributions. The separation power result at 8 GeV/c is sufficiently close to $3\,\sigma$ considering such effects and the limitations of the test-beam setup. The Čerenkov ring coverage for the 8 GeV/c measurement provided by the 28 H8500 MAPMTs was 68.8 %, whereas in the final CLAS12 RICH detector a wall of H8500 MAPMTs will be incorporated, allowing for full ring coverage and increased Čerenkov yield measurements. The prototype also revealed $\pi/\bar{\text{p}}$ and $K/\bar{\text{p}}$ separation powers of $(7.38 \pm 0.02)\,\sigma$ and $(4.69 \pm 0.02)\,\sigma$ at 8 GeV, which will fulfill a required particle species separation in the final CLAS12 RICH detector. Further to this, at 7 GeV/c and 6 GeV the test-beam results already meet the projected demands for π/K separation in the CLAS12 RICH detector.

5.2.5 Summary: Large-Scale Prototype Studies

A large-scale prototype RICH detector was characterised in test-beam studies with a mixed hadron beam. This study furthered the investigations performed with the small-scale cosmic muon RICH prototype, in assessing the capabilities of the H8500 MAPMT to efficiently detect Čerenkov light and its corresponding applicability to the CLAS12 RICH detector. The results presented focussed on the direct light imaging case of the RICH prototype, and examined the

Čerenkov yields, ring resolutions and π/K separation powers achievable through use of the H8500 MAPMTs for imaging of the Čerenkov photons.

The technique of hit clustering was used in the analysis of Čerenkov ring events and revealed that the level of crosstalk signals present was $\leq 5\,\%$, in agreement with single photon level crosstalk studies performed previously with the laser characterisation tests of the H8500 MAPMT when the different readout electronics and higher noise environment of the test-beam facility are considered. Several comparisons between cluster size distributions confirmed that this noise is intrinsic to the MAPMT and readout, and does not depend on factors such as the radiator refractive index, the wavelength of the Čerenkov light, or the window type of the MAPMT. This confirms that the H8500 MAPMT is a suitably low-noise detector to provide single photon detection in the CLAS12 RICH application. Čerenkov yield results returned a value of (11.38 ± 0.02) clusters per event, where the event is equivalent to a Čerenkov ring with 69.74 % coverage. This value was obtained for a beam momentum of 8 GeV/c, aerogel refractive index of $\mathrm{n} = 1.05$ and $\mathrm{t} = 2\,\mathrm{cm}$, which was used as the standard test configuration for the setup, and also has not been corrected for the background due to dark counts which corresponds to 0.5 dark counts per event for the entire RICH prototype [201]. The yield measured with the H8500 MAPMTs therefore meets the yield requirements of the CLAS12 RICH proposed from simulation studies.

With the standard test-beam setup a Čerenkov ring radius resolution value approaching 2 mm was obtained through analysis of the signals extracted from the H8500 MAPMTs alone. This ring resolution could be further improved, for example, by the inclusion of particle track information from the GEM chambers. A study into the difference in the Čerenkov ring resolution obtained with either UV-extended or standard borosilicate glass window type H8500 MAPMTs revealed that the UV-extended window type MAPMT degrades the Čerenkov ring resolution by $\sim 10\,\%$. This is due to Rayleigh scattering of UV-wavelength Čerenkov light in the aerogel material. These dispersion effects are most severe in the aerogel material at shorter wavelengths. Despite the fact that the majority of the Čerenkov yield is produced and obtained at the UV-wavelengths, the outcomes of the test-beam studies imply that the standard window type H8500 MAPMTs will provide a superior Čerenkov ring resolution in the CLAS12 RICH.

The Čerenkov ring resolution and yields achieved with the test-beam prototype were sufficient, through use of a beam line threshold Čerenkov counter as an offline kaon veto and pion trigger, to provide π/K separations of $(2.73 \pm 0.02)\,\sigma$ to $(3.48 \pm 0.03)\,\sigma$ and finally $(4.81 \pm 0.02)\,\sigma$ at 8 GeV/c, 7 GeV/c and 6 GeV/c. The result at 8 GeV/c is limited by the 68.8 % ring coverage provided by the 28 H8500 MAPMTs, for instance if one re-scales the value for a full ring coverage then close to $4\,\sigma$ π/K separation is obtained. The result with 28 MAPMTs could also be improved through the inclusion of charged particle track information. Considering these factors and the level of analysis which looks only at the 28 MAPMTs and beam Čerenkov signals, the result is sufficiently close to the required minimal value of $3\,\sigma$ in the CLAS12 RICH detector, and at energies of 7 GeV and 6 GeV the test-beam prototype largely meets the detector requirements.

Chapter 6

Conclusions and Outlook

The CLAS12 upgrade will provide numerous opportunities to further explore nucleon structure, QCD and hadronic matter, enhancing our knowledge in these fields with unprecedented precision. For the full achievement of its physics program, a Ring Imaging CHerenkov (RICH) detector has been proposed for installation in the forward region of CLAS12 to allow for greatly improved $\pi/K/p$ identification in the momentum range of 3 - 8 GeV/c. Due to several constraints imposed on the RICH detector, a novel hybrid imaging design incorporating aerogel radiator materials, focussing mirrors and visible light photon detectors has been selected. Depending upon the incident particle track angle and momentum, the Čerenkov light will either be imaged directly in a proximity-like setup or undergo two reflections and passes through the aerogel radiator material before detection. The benchmark Particle IDentification (PID) goal for the CLAS12 RICH is $> 3\,\sigma$ π/K separation up to 8 GeV/c and simulation studies have shown that to achieve the required Čerenkov angle resolution for this in the direct light imaging case, 7 detected photons are required per Čerenkov ring event. Overall the time-scale for the research, development, construction and commissioning of the RICH detector is very short, with the first completed sector required to be ready in 2016 to coincide with the start of CLAS12 data taking.

This thesis was concerned with the selection of the photon detector for application to the CLAS12 RICH, which represents a crucial component of the RICH detector to guarantee its successful performance. The photon detector must provide an efficient active area with minimal deadspace, especially since numerous detectors must be tiled into large arrays of $\sim 1\,\mathrm{m} \times 1\,\mathrm{m}$ area to be used as imaging planes in the CLAS12 RICH. The spatial resolution provided by the photon detectors must be superior than $1\,\mathrm{cm} \times 1\,\mathrm{cm}$ and it is vital that the photon detectors be sensitive to single photons produced from the aerogel radiator material.

The spectral sensitivity of the photon detector must also span the entire visible wavelength range to reduce chromatic contributions to the Čerenkov angle resolution arising in the UV wavelength region. Since the CLAS12 RICH detector is a position sensitive photon counting application, the photon detector must also demonstrate minimal crosstalk and be sufficiently low-noise. Photon detection technologies which are currently available from the market were considered, due to the short time-scale of the RICH project, and after comparison between the different detector properties MultiAnode PhotoMultiplier Tubes (MAPMTs) were selected as the optimal detector type.

To confirm this selection a high-precision and ultra-stable laser scanning facility was developed to study the intrinsic performance of MAPMTs in detail and in terms of: single photon detection capabilities, spatial resolution, imaging plane homogeneity, noise and crosstalk behaviour. Three MAPMTs, consisting of the Hamamatsu H8500, H9500 and H7546 models, were subject to low and high resolution scans with the laser test facility. All three devices proved to be low noise and single photon sensitive, however, from an initial comparison between the design of the MAPMTs, the H8500 device was considered to be the optimal candidate and this choice was further validated through the laser tests. Through high resolution scans the H9500 MAPMT provided a deteriorated uniformity response at the single PhotoElectron (PE) level compared to the H8500 and H7546 devices. Moreover, the H9500 provides $4\times$ the number of readout channels than in the H8500 MAPMT, for the same area, and considering the required increase in number of electronics channels in the CLAS12 RICH, the H9500 was therefore not selected for further testing. The H7546 MAPMT exhibited sufficiently uniform surface sensitivity at the single PE level, however, to improve the high fraction of deadspace in the device it would require coupling with a lens or light catcher system and preliminary studies of an H7546 MAPMT demonstrated that this option is unfavourable given the large angular acceptance that the RICH must provide uniform response over.

The H8500 performed well throughout the low and high resolution scans. The device provided typical relative gain values over its 64 channels lying within the $1:4$ maximum value given by Hamamatsu. The device also proved to be single photon sensitive, as required for the CLAS12 RICH detector, although when operated at $1\,000\,\mathrm{V}$ an average single PE signal loss fraction of $\sim 20\,\%$ was recorded, and the efficiency of the MAPMT in response to single photons therefore required further study in Čerenkov prototype setups. Response scans of the H8500 MAPMT also demonstrated that its pixel sizes agree with the $5.8\,\mathrm{mm}\times 5.8\,\mathrm{mm}$ quoted by Hamamatsu, matching the demands for the CLAS12 RICH spatial resolution whilst maintaining a cost-effective solution for the required number of readout channels. The intrinsic crosstalk of the device was found to be on the level of $< 3\,\%$ at the single PE level, which is not a significant concern for the CLAS12 RICH detector, and the crosstalk was found to be strongest amongst side-sharing neighbours of an illuminated pixel. Hit clustering analysis methods in the final RICH configuration may offer a way of accounting for this behaviour. High resolution scans of the H8500 MAPMT response revealed signal response and crosstalk patterns which depend upon the dynode mesh construction of the MAPMT. A comparison between signal response and crosstalk results obtained from scans performed at 407.2 nm and 634.7 nm wavelengths indicated that this effect arises from unconverted photons which strike the opening face of the dynode mesh construction and reflect back to the photocathode for conversion and subsequent detection. At the single PE level, the uniformity of the H8500 surface sensitivity and the crosstalk magnitudes arising from these optical effects were found to be acceptable for the CLAS12 RICH application. The H8500 MAPMT also offers a common last dynode output signal, which may be used as a common logic OR amongst all pixels of the device for self-triggering purposes. This signal was also measured throughout a selection of laser scans and it is concluded that, when used with a fast $200\,\times$ amplifier, the strength and timing of this signal is suitable for use in the CLAS12 RICH detector to aid in offline rejection of background hits. As a result of the laser scans performed with the H8500 MAPMT the device was selected for further testing within prototype setups, to determine its capability in the detection of Čerenkov light produced from aerogel material and examine its performance in more realistic setups.

To study the response of the H8500 MAPMT to Čerenkov light, a small-scale proximity RICH prototype was designed and constructed. In the prototype one H8500 MAPMT was used to image Čerenkov rings produced by cosmic muons traversing aerogel radiator tiles directly, and the small-scale prototype study aimed to determine the number of Čerenkov photons detected by the H8500 MAPMT as a function of aerogel radiator tile thickness. A detailed Monte Carlo simulation of the cosmic muon RICH prototype was developed. Comparisons between simulation and data to describe the features of the Čerenkov light created by the cosmic muon hit in the MAPMT window were in close agreement, validating the simulated models for the H8500 MAPMT, for example its geometry, glass window and photocathode models. These models are therefore suitable and available for extraction and further use in the full-scale CLAS12 RICH detector simulation. Furthermore, simulation and data comparisons also revealed that the mean values of the Čerenkov yields extracted from data are reproduced well by the simulation, however there is a slight resolution mis-match in the widths of the distributions. It is postulated that this arises from the optical models used to describe the aerogel in the simulation and the comparison could be improved by inputting data from a full characterisation of the actual aerogel tile used in the cosmic muon prototype setup into the simulation. Another source of discrepancy may lie in the modeling of the single photon resolution of the MAPMT response in the simulation. The detection of Čerenkov light is extremely sensitive to the single photon resolution of the photon detector, and so it is possible that this quantity is not simulated accurately enough for the H8500 MAPMT. In the prototype simulation one resolution value is used for all pixels of the MAPMT, whereas results from low resolution laser scans demonstrate that the individual pixels display different resolutions depending upon their absolute gain variations. This effect is not observed when the muon hit in the MAPMT window is compared between simulation and data because of the high signal charges involved in that case. The results from two analysis algorithms were compared for cross-checking purposes and found to be in agreement within a 10 % scale uncertainty, which results from the absolute gain calibration of the MAPMT. The final Čerenkov ring event yields extracted for 1 cm and 2 cm of aerogel respectively, with the template analysis algorithm are (10.58 ± 1.06) PE and (15.40 ± 1.54) PE, where the background created from the muon hit in the MAPMT window has been removed and the geometrical loss factors have been corrected for. The results confirm that the H8500 MAPMT can successfully be used to detect Čerenkov rings in a proximity setup in accordance with the yield requirements of the direct light imaging case of the CLAS12 RICH detector.

Further to the cosmic muon RICH prototype, the performance of 28 H8500 MAPMTs in a large-scale prototype RICH detector was investigated through a preliminary analysis of data extracted from test-beam studies with a mixed hadron beam. The configuration of the large-scale prototype setup which was studied was matched closely to that expected in the direct-light imaging case of the final CLAS12 RICH detector. Studies with the large-scale prototype aimed to extract further Čerenkov event yield results, obtain the Čerenkov ring resolution provided by the H8500 MAPMTs alone and evaluate any possible separation of different Čerenkov ring radii extracted from π and K particle species.

The technique of hit clustering was used in the analysis of Čerenkov ring events and revealed that the level of crosstalk signals present was ≤ 5 %, which, considering the drastically different readout electronics used and the extremely different noise environment, was in rather close agreement with < 3 % value obtained from single photon level crosstalk studies performed during the laser characterisation tests of the H8500 MAPMT. This noise level was found to be intrinsic to the MAPMT and electronics readout system used, and did not depend on factors such as the radiator refractive index, the wavelength of the Čerenkov light, or the window type of the MAPMT. This result confirms that the H8500 MAPMT is a suitably low-noise detector to provide single photon detection in the CLAS12 RICH application. The standard large-scale prototype configuration and analysis case was defined as a beam momentum of 8 GeV/c, an aerogel refractive index of $n = 1.05$ and $t = 2$ cm. Čerenkov yield results with this configuration returned a value of (11.38 ± 0.02) clusters per event, where the event is equivalent to a Čerenkov ring with 69.74 % coverage provided by the 28 H8500 MAPMTs. The result has not been corrected for backgrounds arising from effects such as Rayleigh scattering of the Čerenkov light within the aerogel material, which must first be validated through simulation studies, or corrected for dark counts, which are estimated at a value of 0.5 dark counts per event for the entire RICH prototype [201]. If one scales the 2 cm result obtained from the cosmic-muon prototype results by a 69.74 % ring coverage factor, then the results between the two prototypes agree within the 10 % scale uncertainty of the cosmic-muon RICH prototype MAPMT calibration. The Čerenkov event yield results obtained with the large-scale prototype again represent promising results for the projected performance of the CLAS12 RICH detector.

With the standard test-beam setup a Čerenkov ring radius resolution value approaching 2 mm was obtained through analysis of the signals extracted from the H8500 MAPMTs alone. This ring resolution could be further improved by, for example, the inclusion of particle track information from the GEM chambers to fix the centre positions of the Čerenkov event ring fits. A study into the Čerenkov ring resolutions obtained with either UV-extended or standard borosilicate glass window type H8500 MAPMTs revealed that the UV-extended windows deteriorate the Čerenkov ring resolution by $\sim 10\,\%$, as a result of Rayleigh scattering of UV-wavelength photons within the aerogel material. Furthermore, dispersion effects are most severe in the aerogel material at shorter wavelengths, which was observed as shifts in the mean of the radii distributions extracted through the detection of different allowed wavelength bands of Čerenkov light. Despite the fact that the majority of the Čerenkov yield is produced at the UV-wavelengths, the large-scale prototype results indicate that standard window type H8500 MAPMTs will provide superior Čerenkov ring resolutions in the CLAS12 RICH.

Through the use of a beamline threshold Čerenkov counter as an offline kaon veto and pion trigger, the Čerenkov ring resolution and yields achieved with the MAPMTs of the test-beam prototype were sufficient to achieve π/K separations of $(2.73 \pm 0.02)\,\sigma$, $(3.48 \pm 0.03)\,\sigma$ and

$(4.81 \pm 0.02)\,\sigma$, at 8 GeV/c, 7 GeV/c and 6 GeV/c respectively. The result at 8 GeV/c is limited by the 68.8 % ring coverage provided by the 28 H8500 MAPMTs in the test-beam setup, and could be further improved through the inclusion of charged particle track information. Such a study has subsequently been performed by M. Mirazita [204], and such procedures as inclusion of information from GEM chambers improves the π/K separation to a value of $3.5\,\sigma$ at 8 GeV/c. Considering the preliminary analysis, using information only from the 28 H8500 MAPMTs to reconstruct the Čerenkov rings, and the limitations of the test-beam setup compared to the final RICH detector, a value of $(2.73 \pm 0.02)\,\sigma$ at 8 GeV/c does remain relatively close to the minimal quoted benchmark value for the CLAS12 RICH. A momentum of 8 GeV/c represents the most challenging case for the RICH, and in the final detector a high threshold Čerenkov counter will assist the PID measurement for momenta > 6 GeV/c. At beam momenta of 7 GeV/c and 6 GeV/c the π/K PID provided by the H8500 MAPMTs within the test-beam prototype surpassed the required minimum value of $3\,\sigma$. Such results from the large-scale prototype studies and their prospect for comparison with simulation studies will be important for the tuning of aerogel and MAPMT models used in the full-scale CLAS12 RICH simulation.

The current outlook foresees the start of the procurement process for the RICH detector components before 2014, including the photon detectors, which have been selected as the Hamamatsu H8500 MAPMT with the standard window type. Recently this year Hamamatsu unveiled a new upgraded version of the H8500 MAPMT, which is not yet released. The device promises an improved collection efficiency to enhance single photon detection, resulting from a slightly different dynode mesh and focussing electrode design. This new MAPMT may be subject to tests, using the equipment and standards successfully developed and described in this thesis, to investigate any benefit to the overall performance of the RICH detector. For the standard configuration and the beginnings of the procurement process for the CLAS12 RICH detector the current Hamamatsu H8500 is selected.

In summary, a rigorous evaluation of the H8500 MAPMT and its prospects for application to the CLAS12 RICH detector has been carried out. These studies have demonstrated that the device successfully meets the crucial demands for photon detection within the CLAS12 RICH by providing sufficient spatial resolution, single photon sensitivity, and low-level crosstalk behaviours. Further to this π/K separations were achieved through the use of H8500 MAPMTs to image Čerenkov rings. Given the short time-scale of the RICH project these studies have been critical for the selection of the photon detectors and realisation of the detector design, which are necessary for completion of the project on time.

Bibliography

[1] R.W. McAllister and R. Hofstadter. Elastic scattering of 188-MeV electrons from the proton and the alpha particle. *Phys. Rev.*, 102:851–856, 1956.

[2] Nuclear Physics Research Group. Research themes, University of Glasgow, 2013. http://nuclear.gla.ac.uk/research/themes/ [Last checked 01/07/12].

[3] C.W. Leemann, D.R. Douglas, and G.A. Krafft. The Continuous Electron Beam Accelerator Facility: CEBAF at the Jefferson Laboratory. *Annu. Rev. Nucl. Part. Sci.*, 51:413–50, 2001.

[4] B.A. Mecking. Physics program and instrumentation at CEBAF. *Prog. Part. Nucl. Phys.*, 34:53–67, 1995.

[5] A. Lung. 12 GeV Upgrade: future science at Jefferson Lab, project information, 2012. http://www.jlab.org/12GeV/ [Last checked 03/07/13]

[6] V.D. Burkert. The JLab 12GeV upgrade and the initial science program. *arXiv:1203.2373v1 [nucl-ex]*, 2012.

[7] B.A. Mecking. The CEBAF Large Acceptance Spectrometer (CLAS). *Nuclear Instruments and Methods in Physics Research A*, 503:513–553, 2003.

[8] The CLAS Collaboration. CLAS12 technical design report, revised version, version 5.1, 2008. http://www.jlab.org/Hall-B/clas12_tdr.pdf [Last checked 03/07/13].

[9] J. Dudek, R. Ent, R. Essig, K. Kumar, C. Meyer, R. McKeown, Z. Meziani, G. Miller, M. Pennington, D. Richards, L. Weinstein, and G. Young. Physics opportunities with the 12 GeV upgrade at Jefferson Lab. *arXiv:1208.1244v2 [hep-ex]*, 2012.

[10] S. Niccolai and The CLAS Collaboration. The physics program of CLAS12. *Nuclear Physics B (Proc. Suppl.)*, 210–211:119–124, 2011.

[11] D. Hasch *et al.* Probing strangeness in hard processes - the science case of a RICH detector for CLAS12. *arXiv:1202.1910v2 [hep-ex]*, 2012.

[12] J. Blümlein. The theory of deeply inelastic scattering. *Progress in Particle and Nuclear Physics*, 69:28–84, 2013.

[13] S.E. Kuhn. Experimental methods in polarized DIS and SIDIS. *Procedings of the International School of Physics "Enrico Fermi"*, 180:1–31, 2012.

[14] M. Guidal. Generalized parton distributions and deep virtual Compton scattering. *Progress in Particle and Nuclear Physics*, 61:89–105, 2008.

[15] X. Ji. Deeply virtual Compton scattering. *Physical Review D*, 55:11, 1997.

[16] M. Diehl. Generalized parton distributions. *Procedings of the International School of Physics "Enrico Fermi"*, 180:81–105, 2012.

[17] A. Prokudin. Phenomenology of transverse-momentum-dependent distributions. *Procedings of the International School of Physics "Enrico Fermi"*, 180:157–195, 2012.

[18] D. Hasch. Recent results from HERMES. Talk presented at RBRC Workshop on *Progress in high pT physics at RHIC*, BNL, USA, March 2010.

[19] S. Stepanyan. Hadron physics with CLAS12. *arXiv:1004.0168 [hep-ph]*, 2010.

[20] C. Grupen and B. Shwartz. *Particle detectors.* Cambridge University Press, Cambridge, United Kingdom, Second Edition, 2008.

[21] C. Lippmann. Particle identification. *arXiv:1101.3276v4 [hep-ex]*, 2011.

[22] C. Lippmann. Particle identification. *Nuclear Instruments and Methods in Physics Research A*, 666:148–172, 2012.

[23] V.D. Burkert. CLAS12 and its science program at the Jefferson Lab upgrade. *arXiv:0810.4718v2 [hep-ph]*, 2008.

[24] F. Hartmann. Silicon tracking detectors in high-energy physics. *Nuclear Instruments and Methods in Physics Research A*, 666:25–46, 2012.

[25] J. Ball *et al.* Micromegas tracker project for CLAS12. *Nuclear Instruments and Methods in Physics Research A*, 604:53–55, 2009.

[26] G. Charles. Micromegas detectors for CLAS12. *Nuclear Instruments and Methods in Physics Research A*, 718:414–415, 2013.

[27] E.S. Smith *et al.* The time-of-flight system for CLAS. *Nuclear Instruments and Methods in Physics Research A*, 432:265–298, 1999.

[28] P. Stoler *et al.* The CLAS Cherenkov detector. *Nuclear Instruments and Methods in Physics Research A*, 465:414–427, 2001.

[29] R.K. Bock and A. Vasilescu. *The particle detector brief book.* Springer-Verlag, Germany, 1998.

[30] G.F. Knoll. *Radiation detection and measurement.* Third Edition, John Wiley, United States of America, 1989.

[31] D.S. Carman *et al.* The CLAS drift chamber system. *Nuclear Instruments and Methods in Physics Research A*, 449:81–111, 2000.

[32] L.C. Smith *et al.* The CLAS forward electromagnetic calorimeter. *Nuclear Instruments and Methods in Physics Research A*, 460:239–265, 2001.

[33] A. El Alaoui *et al.* A RICH detector for CLAS12 spectrometer. *Physics Procedia*, 37:773–780, 2012.

[34] M. Contalbrigo *et al.* The CLAS12 large area RICH detector. *Nuclear Instruments and Methods in Physics Research A*, 639:302–306, 2011.

[35] V. Kubarovsky. Particle identification in CLAS12. Talk presented at CLAS12 RICH technical review, Jefferson Lab, June 2013.

[36] P.A. Čerenkov. Visible radiation produced by electrons moving in a medium with velocities exceeding that of light. *Phys. Rev.*, 52:378–379, 1937.

[37] T. Ypsilantis and J. Seguinot. Theory of ring imaging Cherenkov counters. *Nuclear Instruments and Methods in Physics Research A*, 343:30–51, 1994.

[38] J.V. Jelley. *Čerenkov radiation and its applications.* Pergamon Press, London, Great Britain, 1958.

[39] K. Kleinknecht. *Detectors for particle radiation.* Cambridge University Press, Cambridge, Great Britain, 1987.

[40] W.R. Leo. *Techniques for nuclear and particle physics experiments (second-revised edition)*. Springer-Verlag, Germany, 1994.

[41] J. Beringer *et al.* Review of particle physics. *Phys. Rev. D*, 86:010001, Jul 2012.

[42] J. Seguinot and T. Ypsilantis. Photo-ionization and Cherenkov ring imaging. *Nuclear Instruments and Methods in Physics Research A*, 142:377–391, 1977.

[43] T. Ypsilantis and J. Seguinot. A historical survey of ring imaging Cherenkov counters. *Nuclear Instruments and Methods in Physics Research A*, 343:1–29, 1994.

[44] B.N. Ratcliff. Imaging rings in ring imaging Cherenkov counters. *Nuclear Instruments and Methods in Physics Research A*, 502:211–221, 2003.

[45] D.M. Websdale. Review of Cherenkov imaging devices in particle and nuclear physics experiments. *Nuclear Instruments and Methods in Physics Research A*, 595:12–18, 2008.

[46] B.N. Ratcliff. Advantages and limitations of the RICH technique for particle identification. *Nuclear Instruments and Methods in Physics Research A*, 595:1–7, 2008.

[47] P. Glässel. The limits of the ring image Cherenkov technique. *Nuclear Instruments and Methods in Physics Research A*, 433:17–23, 1999.

[48] R. Sia. Performance of the LiF-TEA ring imaging Cherenkov detector at CLEO. *Nuclear Instruments and Methods in Physics Research A*, 553:323–327, 2005.

[49] P. Martinengo and the ALICE Collaboration. The ALICE high momentum particle identification system: an overview after the first Large Hadron Collider run. *Nuclear Instruments and Methods in Physics Research A*, 639:7–10, 2011.

[50] K. Zeitelhack *et al.* The HADES RICH detector. *Nuclear Instruments and Methods in Physics Research A*, 433:201–206, 1999.

[51] P. Glässel *et al.* The CERES RICH detector system. *Nuclear Instruments and Methods in Physics Research A*, 343:87–98, 1994.

[52] P. Križan *et al.* The HERA-B RICH. *Nuclear Instruments and Methods in Physics Research A*, 453:289–295, 2000.

[53] H.E. Jackson *et al.* The HERMES dual-radiator ring imaging Cherenkov detector. *Nuclear Instruments and Methods in Physics Research A*, 479:511–530, 2002.

[54] S. Dalla Torre *et al.* Design and construction of the fast photon detection system for COMPASS RICH-1. *Nuclear Instruments and Methods in Physics Research A*, 616:21–37, 2010.

[55] D.L. Perego. The LHCb RICH silica aerogel performance with LHC data. *Nuclear Instruments and Methods in Physics Research A*, 639:234–237, 2011.

[56] M. Contalbrigo. RICH project overview. Talk presented at CLAS12 RICH technical review, Jefferson Lab, June 2013.

[57] CLAS12 RICH Collaboration. CLAS12 RICH conceptual design report. *Un-published, Internal Document*, June, 2013.

[58] D. Orecchini and S. Tomassini. CLAS12 RICH design status-report. Talk presented at CLAS12 RICH technical review, Jefferson Lab, June 2013.

[59] N. Baltzell. RICH12 update: simulations (material properties, single photon resolution, photon counting). Talk presented at internal CLAS12 RICH meeting, Jefferson Lab, February 2012.

[60] M. Cantin *et al.* Silica aerogels used as Cherenkov radiators. *Nuclear Instruments and Methods in Physics Research A*, 118:177–182, 1974.

[61] M. Musy *et al.* Aerogel as Cherenkov radiator for RICH detectors. *Nuclear Instruments and Methods in Physics Research A*, 502:227–230, 2003.

[62] E. Nappi *et al.* Electronic detection of focused Cherenkov rings from aerogel. *Nuclear Instruments and Methods in Physics Research A*, 401:187–205, 1997.

[63] A.F. Daniluk *et al.* Recent results on aerogel development for use in Cherenkov counters. *Nuclear Instruments and Methods in Physics Research A*, 494:491–494, 2002.

[64] I. Adachi *et al.* Study of a silica aerogel for a Cherenkov radiator. *Nuclear Instruments and Methods in Physics Research A*, 595:180–182, 2008.

[65] E. Nappi. Aerogel and its applications to RICH detectors. *Nuclear Physics B (Proc. Suppl.)*, 61:270–276, 1998.

[66] I. Adachi *et al.* Study of a threshold Cherenkov counter based on silica aerogels with low refractive indices. *Nuclear Instruments and Methods in Physics Research A*, 355:390–398, 1995.

[67] H. Burkhardt *et al.* The TASSO gas and aerogel Cherenkov counters. *Nuclear Instruments and Methods in Physics Research A*, 184:319–331, 1981.

[68] A.J. Hunt. Light scattering for aerogel characterization. *Journal of Non-Crystalline Solids*, 225:303–306, 1998.

[69] I. Adachi *et al.* Study of highly transparent silica aerogel as a RICH radiator. *Nuclear Instruments and Methods in Physics Research A*, 553:146–151, 2005.

[70] T. Iijima *et al.* Aerogel Cherenkov counter for the Belle detector. *Nuclear Instruments and Methods in Physics Research A*, 453:321–325, 2000.

[71] R. De Leo. Long-term operational experience with the HERMES aerogel RICH detector. *Nuclear Instruments and Methods in Physics Research A*, 595:19–22, 2008.

[72] Y. Miyachi *et al.* The HERMES RICH aerogel radiator. *Nuclear Instruments and Methods in Physics Research A*, 502:222–226, 2003.

[73] R. Forty. The RICH system of LHCb. *Nuclear Instruments and Methods in Physics Research A*, 623:294–296, 2010.

[74] E.A. Kravchenko *et al.* Development of aerogel Cherenkov detectors at Novosibirsk. *Nuclear Instruments and Methods in Physics Research A*, 553:125–129, 2005.

[75] A.F. Danilyuk *et al.* Status of aerogel production in Novosibirsk. *Nuclear Instruments and Methods in Physics Research A*, 639:225–226, 2011.

[76] D. Casadei *et al.* Design and test results of the AMS RICH detector. *Nuclear Instruments and Methods in Physics Research A*, 125:303–307, 2003.

[77] R. Pereira *et al.* The AMS-02 RICH detector: performance during ground-based data taking at CERN. *Nuclear Instruments and Methods in Physics Research A*, 639:37–41, 2011.

[78] M. Buénerd *et al.* The RICH counter of the AMS experiment. *Nuclear Instruments and Methods in Physics Research A*, 502:158–162, 2003.

[79] R. Pestotnik *et al.* Proximity focusing RICH with flat-panel PMT (Hamamatsu H8500) as photon detector and aerogel radiator. *Nuclear Instruments and Methods in Physics Research A*, 525:158–162, 2004.

[80] D.L. Perego *et al.* Study of ageing effects in aerogel. *Nuclear Instruments and Methods in Physics Research A*, 527:319–328, 2004.

[81] T. Sumiyoshi *et al.* Silica aerogels in high energy physics. *Journal of Non-Crystalline Solids*, 225:369–374, 1998.

[82] R. Enomoto *et al.* Measurement of radiation damage on a silica aerogel Cherenkov radiator. *Nuclear Instruments and Methods in Physics Research A*, 382:441–446, 1996.

[83] S. Iwata *et al.* Development of ring imaging Cherenkov counter for Belle II experiment at super KEKB. *Physics Procedia*, 37:820–829, 2012.

[84] I. Adachi *et al.* Study of a 144 channel multi-anode hybrid avalanche photo-detector for the Belle II RICH counter. *Nuclear Instruments and Methods in Physics Research A*, 639:103–106, 2011.

[85] F. Tessarotto *et al.* The COMPASS RICH-1 photon detection system. *Nuclear Instruments and Methods in Physics Research A*, 595:23–26, 2008.

[86] A. Teufel *et al.* The characterisation of the multianode photomultiplier tubes for the RICH-1 upgrade project at COMPASS. *Nuclear Instruments and Methods in Physics Research A*, 595:177–179, 2008.

[87] F. Tessarotto *et al.* Studies for a fast RICH. *Nuclear Instruments and Methods in Physics Research A*, 553:53–57, 2005.

[88] P. Križan. Recent progress in ring imaging Cherenkov counters with vacuum-based photon counters. *Nuclear Instruments and Methods in Physics Research A*, 502:28–35, 2003.

[89] S. Korpar *et al.* HERA-B RICH. *Nuclear Instruments and Methods in Physics Research A*, 502:41–45, 2003.

[90] A. Kubarovsky. Magnetic field study for CLAS12 RICH detector. Talk presented at internal CLAS12 RICH meeting, Jefferson Lab, April 2013.

[91] T. Hakamata (Editor). *Photomultiplier tubes basics and applications (Third Edition).* http://www.hamamatsu.com/resources/pdf/etd/PMT_handbook_v3aE.pdf, Japan, 2006 [last checked 30/05/13].

[92] S-O. Flyckt and C. Marmonier (editors). *Photomultiplier tubes principles & applications.* Photonis, France.

[93] K. Arisaka. New trends in vacuum-based photon detectors. *Nuclear Instruments and Methods in Physics Research A*, 442:80–90, 2000.

[94] R. Barbier. Tutorial on photodetection, talk presented at *6th International Conference on New Developments in Photodetection NDIP2011*, http://ndip.in2p3.fr/ndip11/AGENDA/AGENDA-by-DAY/Presentations/Tuto/Tut2-barbier.pdf, Lyon, July, 2011 [Last checked 03/07/13].

[95] M.D. Eisaman, J. Fan, A. Migdall, and S.V. Polyakov. Single-photon sources and detectors. *Rev. Sci. Instrum.*, 82:071101, 2011.

[96] T. Gys. Status and perspectives of vacuum-based photon detectors for single photon detection. *Nuclear Instruments and Methods in Physics Research A*, 595:136–141, 2008.

[97] F. Piuz. CsI-photocathode and RICH detector. *Nuclear Instruments and Methods in Physics Research A*, 371:96–115, 1996.

[98] F. Piuz. Ring Imaging CHerenkov systems based on gaseous photo-detectors: trends and limits around particle accelerators. *Nuclear Instruments and Methods in Physics Research A*, 502:76–90, 2003.

[99] A. Breskin *et al.* Advances in gas avalanche photomultipliers. *Nuclear Instruments and Methods in Physics Research A*, 442:58–67, 2000.

[100] D. Mörmann *et al.* GEM-based gaseous photomultipliers for UV and visible photon imaging. *Nuclear Instruments and Methods in Physics Research A*, 504:93–98, 2003.

[101] E. Cabruja *et al.* Review of CMOS image sensors. *Microelectronics Journal*, 37:433–451, 2006.

[102] K. Inami *et al.* Lifetime of MCP–PMT. *Nuclear Instruments and Methods in Physics Research A*, 564:204–211, 2006.

[103] T. Mori *et al.* Lifetime-extended MCP-PMT. *Nuclear Instruments and Methods in Physics Research A*, 629:111–117, 2011.

[104] A. Lehmann *et al.* Significantly improved lifetime of micro-channel plate PMTs. *Nuclear Instruments and Methods in Physics Research A*, 718:535–540, 2013.

[105] J. Va'vra *et al.* A 30 ps timing resolution for single photons with multi-pixel Burle MCP-PMT. *Nuclear Instruments and Methods in Physics Research A*, 572:459–462, 2007.

[106] A. Lehmann *et al.* Studies of MCP properties. *Journal of Instrumentation*, 4:P11024, 2009.

[107] A. Lehmann *et al.* Systematic studies of micro-channel plate PMTs. *Nuclear Instruments and Methods in Physics Research A*, 639:144–147, 2011.

[108] K. Inami *et al.* MCP-PMT timing property for single photons. *Nuclear Instruments and Methods in Physics Research A*, 528:763–775, 2004.

[109] A. Ronzhin *et al.* Development of a 10 ps level time of flight system in the Fermilab Test Beam Facility. *Nuclear Instruments and Methods in Physics Research A*, 623:931–941, 2010.

[110] A. Lehmann *et al.* Performance studies of microchannel plate PMTs in high magnetic fields. *Nuclear Instruments and Methods in Physics Research A*, 595:173–176, 2008.

[111] F. Uhlig *et al.* Lifetime of MCP–PMT. *Nuclear Instruments and Methods in Physics Research A*, 695:68–70, 2012.

[112] S. Suzuki *et al.* Time-of-propagation Cherenkov counter for particle identification. *Nuclear Instruments and Methods in Physics Research A*, 440:124–135, 2000.

[113] T. Iijima *et al.* Development of RICH counters towards the KEKB/Belle upgrade. *Nuclear Instruments and Methods in Physics Research A*, 598:138–142, 2009.

[114] K. Inami. MCP-PMT development for Belle-II TOP counter. *Physics Procedia*, 37:683–690, 2012.

[115] K. Inami. TOP counter prototype R&D. *Nuclear Instruments and Methods in Physics Research A*, 639:298–301, 2010.

[116] K. Inami. Development of a TOP counter for the SuperB factory. *Nuclear Instruments and Methods in Physics Research A*, 595:96–99, 2008.

[117] J. Va'vra *et al.* FDIRC design for SuperB. *Nuclear Instruments and Methods in Physics Research A*, 639:282–286, 2011.

[118] J. Schwiening *et al.* Status of the fast focusing DIRC (fDIRC). *Nuclear Instruments and Methods in Physics Research A*, 595:104–107, 2008.

[119] P. Križan *et al.* Tests of the Burle 85011 64-anode MCP PMT as a detector of Cherenkov photons. *Nuclear Instruments and Methods in Physics Research A*, 567:124–128, 2006.

[120] T. Iijima *et al.* Studies of a proximity focussing RICH with aerogel radiator for future Belle upgrade. *Nuclear Instruments and Methods in Physics Research A*, 595:92–95, 2008.

[121] P. Križan *et al.* Photonis MCP PMT as light sensor for the Belle II RICH. *Nuclear Instruments and Methods in Physics Research A*, 639:162–164, 2011.

[122] S. Korpar *et al.* Proximity focussing RICH with TOF capabilities. *Nuclear Instruments and Methods in Physics Research A*, 572:432–433, 2007.

[123] Photonis. Planacon Photon Detector, Data Sheet. http://www.photonis.com/en/ism/63-planacon.html, 2012 [Last checked 03/06/13].

[124] Price of one Photonis Planacon MCPPMT from quotation. Private communication, Matthias Hoek (Johannes Gutenberg Universität Mainz), June 2013.

[125] Price of one Hamamatsu H8500 MAPMT from quotation. Private communication, Scott Lumsden (University of Glasgow), July 2013.

[126] D. Renker. Geiger-mode avalanche photodiodes, history, properties and problems. *Nuclear Instruments and Methods in Physics Research A*, 567:48–56, 2006.

[127] D. Renker *et al.* Advances in solid state photon detectors. *Journal of Instrumentation*, 4:P04004, 2009.

[128] B. Dolgoshein *et al.* Status report on silicon photomultiplier development and its applications. *Nuclear Instruments and Methods in Physics Research A*, 563:368–376, 2006.

[129] D. Renker. Geiger-mode avalanche photodiodes for Cherenkov detectors. *Journal of Instrumentation*, 5:P01001, 2010.

[130] SensL, The Low Light Level Sensing Company. An introduction to the silicon photomultiplier, technical note, revision 3.1. http://www.sensl.com/downloads/ds/TN - Intro to SPM Tech.pdf, 2011 [Last checked 03/07/13].

[131] SensL The Low Light Level Sensing Company. *SPMMini high gain APD data sheet*, 2008.

[132] B. Dolgoshein *et al.* Silicon photomultiplier and its possible applications. *Nuclear Instruments and Methods in Physics Research A*, 504:48–52, 2003.

[133] Hamamatsu Photonics K.K. MPPC (Multi-Pixel Photon Counters), http://www.hamamatsu.com/eu/en/product/category/3100/4004/4114/index.html, Hamamatsu Photonics K.K., 2013 [Last checked 03/07/13].

[134] Price of Hamamatsu MPPCs. Private communication with Richard Briggs (Hamamatsu Photonics K.K.), July 2013.

[135] E. Nappi. Trends in the development of large area photon detectors for Cherenkov light imaging applications. *Nuclear Instruments and Methods in Physics Research A*, 504:70–87, 2003.

[136] T. Iijima. Status and perspectives of vacuum-based photon detectors. *Nuclear Instruments and Methods in Physics Research A*, 639:137–143, 2011.

[137] N. Luth *et al.* The BABAR detector. *Nuclear Instruments and Methods in Physics Research A*, 479:1–116, 2002.

[138] J. Schwiening *et al.* The DIRC detector at the SLAC B-factory PEP-II: operational experience and performance for physics application. *Nuclear Instruments and Methods in Physics Research A*, 502:67–75, 2003.

[139] J. Engelfried *et al.* SELEX RICH performance and physics results. *Nuclear Instruments and Methods in Physics Research A*, 502:285–288, 2003.

[140] A. Stanovnik *et al.* Tests of a multianode PMT for the HERA-B RICH. *Nuclear Instruments and Methods in Physics Research A*, 394:27–34, 1997.

[141] R. Pestotnik *et al.* Multianode photomultipliers as position-sensitive detectors of single photons. *Nuclear Instruments and Methods in Physics Research A*, 442:316–321, 2000.

[142] B. Baret *et al.* In-beam tests of the AMS RICH prototype with 20 A GeV/c secondary ions. *Nuclear Instruments and Methods in Physics Research A*, 525:126–131, 2004.

[143] F. Barao *et al.* In-beam aerogel light yield characterization for the AMS RICH detector. *Nuclear Instruments and Methods in Physics Research A*, 614:237–249, 2010.

[144] S. Stone *et al.* Performance of a C_4F_8O gas radiator ring imaging Cherenkov detector using multi-anode photomultiplier tubes. *Nuclear Instruments and Methods in Physics Research A*, 558:373–387, 2006.

[145] T. Matsumoto *et al.* Studies of proximity focusing RICH with an aerogel radiator using flat-panel multi-anode PMTs (Hamamatsu H8500). *Nuclear Instruments and Methods in Physics Research A*, 521:367–377, 2004.

[146] P. Križan *et al.* Proximity focusing RICH with flat-panel PMT as photon detector and aerogel as radiator. *Nuclear Instruments and Methods in Physics Research A*, 553:58–63, 2005.

[147] T. Matsumoto *et al.* Studies of a proximity focusing RICH with aerogel radiator. *Nuclear Instruments and Methods in Physics Research A*, 518:582–585, 2004.

[148] C. Höhne *et al.* Development of a RICH detector for CBM: simulations and experimental tests. *Nuclear Instruments and Methods in Physics Research A*, 639:294–297, 2011.

[149] J. Eschke *et al.* Results from first beam tests for the development of a RICH detector for CBM. *Nuclear Instruments and Methods in Physics Research A*, 639:307–310, 2011.

[150] N. Dinu, T. Gys, C. Joram, S. Korpar, Y. Musienko, V. Puill, and D. Renker. Photodetection - principles, performance and limitations. Talk presented at *EDIT School*, CERN, 2011, http://indico.cern.ch/getFile.py/access?resId=1&materialId=11&confId=122157 [Last checked 03/07/13].

[151] Burle Industries Incorporated. *Photomultiplier handbook: theory, design, application*. Burle Industries, Lancaster (Pa), 1980.

[152] H. Kyushima, H. Shimoi, A. Atsumi, M. Ito, K. Oba, and Y. Yoshizawa. The development of flat panel PMT. *Nuclear Science Symposium Conference Record, 2000 IEEE*, 1:7/3–7/7, 2000.

[153] J. Va'vra. Novel photon detectors for RICH applications. *Nuclear Instruments and Methods in Physics Research A*, 502:172–182, 2003.

[154] Y. Yoshizawa and J. Takeuchi. The latest vacuum photodetector. *Nuclear Instruments and Methods in Physics Research A*, 387:33–37, 1997.

[155] Y. Enari *et al.* Cross-talk of a multi-anode PMT and attainment of a 10 ps TOF counter. *Nuclear Instruments and Methods in Physics Research A*, 547:490–503, 2005.

[156] SensL, The Low Light Level Sensing Company. SPMArray4 test sheet for SPMArray4 serial number 0950-SPMA39, 2010..

[157] Advanced Laser Diode Systems A.L.S. GmbH. Picosecond injection Laser (PiLas) owner's manual. Testsheet results for PiLas system, 2004.

[158] Thorlabs Ltd. NRT series motorised translation stage. User Guide.

[159] Edmund Optics Ltd. Absorptive neutral density filters. http://www.edmundoptics.com/optics/optical-filters/neutral-density-filters/absorptive-neutral-density-nd-filters/1945 [last checked 13/01/13].

[160] Rachel Ann Montgomery. *An investigation into the crosstalk of an H9500 multianode photomultiplier tube*. Master's thesis, Nuclear Physics Group, University of Glasgow, 2009.

[161] Hamamatsu Photonics K.K. *Flat panel type multianode photomultiplier tube assembly, H7546 series data sheet.*, 2007.

[162] Hamamatsu Photonics K.K. *Flat panel type multianode photomultiplier tube assembly, H8500 series data sheet.*, 2007.

[163] Hamamatsu Photonics K.K. *Flat panel type multianode photomultiplier tube assembly, H9500 series data sheet.*, 2008.

[164] Comparison between H7546 and H8500 MAPMT single photon sensitivities. Private communication, Richard Briggs (Hamamatsu Photonics K.K.), April 2011.

[165] M. Mirazita. Test of the CLAS12 RICH detector. Talk presented at CLAS Collaboration meeting, Jefferson Lab, October 2011.

[166] R. Perrino *et al.* Performances of the aerogel threshold Cherenkov counter for the Jefferson Lab Hall A spectrometers in the 1 - 4 GeV/c momentum range. *Nuclear Instruments and Methods in Physics Research A*, 457:571–580, 2001.

[167] Hamamatsu Photonics K.K. *H9500 Final Test Sheet, Serial Number BA0146*, 2006.

[168] M. Dracos *et al.* The OPERA experiment target tracker. *arXiv:physics/0701153v1 [physics.ins-det]*, 2007.

[169] P. Križan *et al.* Surface sensitivity of multianode photomultiplier tubes. *Nuclear Instruments and Methods in Physics Research A*, 478:391–391, 2002.

[170] Matthias Hoek. *Design and construction of a scintillating fibre tracker for measuring hard exclusive reactions at HERMES.* Ph.D. thesis, Physikalisches Institut der Justus-Liebig-Universität Gießen, Gießen, Germany, 2006.

[171] Cluster algorithm analysis and corresponding results obtained from the cosmic muon prototype. Private communication, Matthias Hoek (Johannes Gutenberg Universität Mainz), April 2013.

[172] Andrew Gordon. Cosmic muon detector: set up, calibration and data analysis. Master's thesis, Nuclear Physics Group, University of Glasgow, 2011.

[173] Runtime stability of the cosmic muon prototype. Private communication, Matthias Hoek (Johannes Gutenberg Universität Mainz), April 2013.

[174] Geometrical acceptance of the cosmic muon prototype. Private communication, Matthias Hoek (Johannes Gutenberg Universität Mainz), April 2013.

[175] J. Allison *et al.* Geant4 - a simulation toolkit. *Nuclear Instruments and Methods in Physics Research A*, 506:250–303, 2003.

[176] J. Allison *et al.* Geant4 developments and applications. *IEEE Transactions on Nuclear Science*, 53:270–278, 2006.

[177] Geant4 Collaboration. Geant4 user's guide for application developers, version: geant4 9.6.0, November 2012.

[178] Simulation of aerogel optical properties. Private communication, Nathan Baltzell (Argonne National Laboratory), February 2012.

[179] T. Bellunato *et al.* Refractive index dispersion law of silica aerogel. *Eur. Phys. J. C*, 52:759–764, 2007.

[180] R. De Leo *et al.* Chromatic aberration and forward scattering of light in silica aerogel. *Nuclear Instruments and Methods in Physics Research A*, 457:52–63, 2001.

[181] R. De Leo *et al.* Optical characterization of *n=1.03* silica aerogel used as radiator in the RICH of HERMES. *Nuclear Instruments and Methods in Physics Research A*, 440:338–347, 2000.

[182] ET Enterprises Limited. Photomultipliers. http://www.et-enterprises.com/files/file/Pmtbrochure11.pdf, United Kingdom, 2011 [last checked 03/07/13].

[183] R. Suykerbuyk *et al.* East area operations, the PS experimental area. http://psdata.web.cern.ch/psdata/www/eastareaop/index.html, 2000 [Last checked 29/04/13].

[184] CERN. The proton synchrotron, http://home.web.cern.ch/about/accelerators/proton-synchrotron, 2013 [Last checked 29/04/13].

[185] D.J. Simon *et al.* Secondary beams for tests in the PS east experimental area. *European Organisation for Nuclear Research, PS/PA Note 93-21, Revised version 4.8.93 (1993).*

[186] L. Durieu and O. Ferrando. Design of T9 (ATLAS/CMS) for ENHL. *European Organisation for Nuclear Research, PS/PA Note 96-39, (1996).*

[187] R. Turchetta *et al.* Design and results from the APV25, a deep sub-micron CMOS front-end chip for the CMS tracker. *Nuclear Instruments and Methods in Physics Research A*, 466:359–365, 2001.

[188] V. Lucherini. RICH prototype geometrical survey. Talk presented at internal CLAS12 RICH meeting, Jefferson Lab, April 2013.

[189] L. Derome *et al.* Characterization study of silica aerogel for Cherenkov imaging. *Nuclear Instruments and Methods in Physics Research A*, 614:184–195, 2010.

[190] S. Blin *et al.* MAROC, a generic photomultiplier readout chip. *Journal of Instrumentation*, 5:C12007, 2010.

[191] S. Blin and P. Barrillon. *MAROC3 datasheet.* Omega, 2010.

[192] N. Seguin-Moreau. Latest generation of ASICs for photodetector readout. *Nuclear Instruments and Methods in Physics Research A*, 718:173–179, 2013.

[193] S. Blin, P. Barrillon, and C. de La Taille. MAROC, a generic photomultiplier readout chip. *Nuclear Science Symposium Conference Record (NSS/MIC), 2010 IEEE*, pages 1690–1693, 2010.

[194] P. Musico *et al.* A multichannel compact readout system for single photon detection: design and performances. *Nuclear Instruments and Methods in Physics Research A*, 617:348–350, 2010.

[195] M. Mirazita. Analysis of alignment runs. Talk presented at internal CLAS12 RICH meeting, Jefferson Lab, April 2013.

[196] Event display for the large-scale RICH prototype test-beams. Private communication, Matthias Hoek (Johannes Gutenberg Universität Mainz), August 2012.

[197] Common noise subtraction algorithm for the large-scale RICH prototype test-beams. Private communication, Evaristo Cisbani (Istituto Superiore di Sanita section of the INFN) and Matteo Turisini (Federico Santa María Technical University), August 2012.

[198] L. Barion, M. Contalbrigo, and L.L. Pappalardo. Summary of transparency measurements of aerogel tiles used during the RICH prototype 2012 test-beam at T9 (CERN), verson 0.4. Internal report, INFN Ferrara, University of Ferrara, 2012.

[199] M. Contalbrigo. Rich test-beam: MC simulation. Talk presented at CLAS collaboration meeting, Jefferson Lab, February 2013.

[200] M. Contalbrigo. Rich GEMC simulations. Talk presented at internal CLAS12 RICH meeting, Jefferson Lab, April 2013.

[201] M. Hoek and A. Kubarovsky. Investigation of Hamamatsu H8500 MAPMT noise properties. CLAS12 Čerenkov Group internal technical report, April 2013.

[202] M. Mirazita. Gem tracking update. Talk presented at internal CLAS12 RICH meeting, Jefferson Lab, May 2013.

[203] G. Schepers *et al.* Particle identification at $\bar{\text{P}}$anda. Internal report of the PID TAG, March 2009.

[204] M. Mirazita. The RICH prototype. Talk presented at CLAS12 RICH technical review meeting, Jefferson Lab, June 2013.

Appendices

Appendix A

List of Abbreviations

A list of abbreviations used throughout the thesis, their corresponding definitions and references to their first use are given in Table A.1.

Table A.1: List of abbreviations used throughout the thesis.

Abbreviation	**Definition**	**First Use [Page]**
ADC	Analogue to Digital Converter	178
BP	Back Plane	179
CB	Control Board	179
CCD	Charge Coupled Device	41
CD	Central Detector	10
CE	Collection Efficiency	43
CEBAF	Continuous Electron Beam Accelerator Facility	2
CHL	Central Helium Liquefier	3
CLAS	CEBAF Large Acceptance Spectrometer	2
CTOF	Central Time-Of-Flight	12
DAC	Digital to Analogue Converter	178
DAQ	Data AcQuisition	65
DC	Drift Chamber	12
DIRC	Detector of Internally Reflected Čerenkov light	45
DIS	Deep Inelastic Scattering	5
DVCS	Deeply Virtual Compton Scattering	6

Continued on next page

Table A.1 – continued from previous page

Abbreviation	Definition	First Use (Page)
DVMP	Deeply Virtual Meson Production	6
EC	Electromagnetic Calorimeter	11
E-H	Electron-Hole	41
FD	Forward Detector	10
FE	Front-End	179
FTOF	Forward Time-Of-Flight	12
FWHM	Full Width Half Maximum	64
G-APD	Geiger-mode Avalanche PhotoDiode	45
GEM	Gaseous Electron Multiplier	172
GPD	Generalised Parton Distribution	6
GPS	General Particle Source	134
HTCC	High Threshold Cherenkov Counter	12
HV	High Voltage	65
INFN	Instituto Nazionale di Fisica Nucleare	105
JLab	Jefferson Laboratory	2
LINAC	LINear ACcelerator	3
LNF	Laboratori Nazionali di Frascati	105
LTCC	Low Threshold Cherenkov Counter	12
MAPMT	MultiAnode PhotoMultiplier Tube	2
MAROC	MultiAnode ReadOut Chip	177
MCP	MicroChannel Plate	44
MCPPMT	MicroChannel Plate PhotoMultiplier Tube	42
NDF	Neutral Density Filter	65
NPE	Number of detected PhotoElectrons	123
OD	Optical Density	65
PCAL	Pre-shower CALorimeter	17
PDE	Photon Detection Efficiency	42
PE	PhotoElectron	41
PID	Particle IDentification	2

Continued on next page

Table A.1 – continued from previous page

Abbreviation	Definition	First Use (Page)
PMT	PhotoMultiplier Tube	12
QCD	Quantum ChromoDynamics	1
QDC	Charge to Digital Convertor	65
QE	Quantum Efficiency	42
RICH	Ring Imaging CHerenkov	2
RMS	Root Mean Square	47
SIDIS	Semi-Inclusive Deep Inelastic Scattering	6
SiPM	Silicon PhotoMultiplier	43
SRF	Superconducting RadioFrequency	3
SVT	Silicon Vertex Tracker	11
TDC	Time to Digital Convertor	73
TMD	Transverse Momentum Dependent	6
TOF	Time-Of-Flight	11
TOP	Time-Of-Propagation	44
UV	Ultra-Violet	24

Appendix B

Muon Counter Calibration Stability

The muon counter of the cosmic muon RICH prototype, as described in Section 5.1.1, was calibrated weekly to monitor any drift in the correlation parameters used to convert time differences between signals from the readout PMTs of a scintillator bar into hit position of a muon along the bar.

The intercept, gradient and offset correlation parameters, as explained fully in Section 5.1.1, obtained from an example set of 26 calibrations with the bottom scintillator bar are shown in Figs. B.1 (a), (b) and (c) respectively. Despite the appearance of a slight increase in the intercept and gradient parameters, the magnitude of this is negligible and the extracted stabilities for all parameters are satisfactory. In particular the gradient parameter shown in Fig. B.1 (b), which is the crucial value for converting TDC time difference into position, is constant over the period of 26 weeks within fitting errors. Each graph has additionally been fitted with first order polynomials, the gradient values of which (denoted by the parameters p_1 in Figs. B.1 (a), (b) and (c)) indicate very consistent performance of the muon counter.

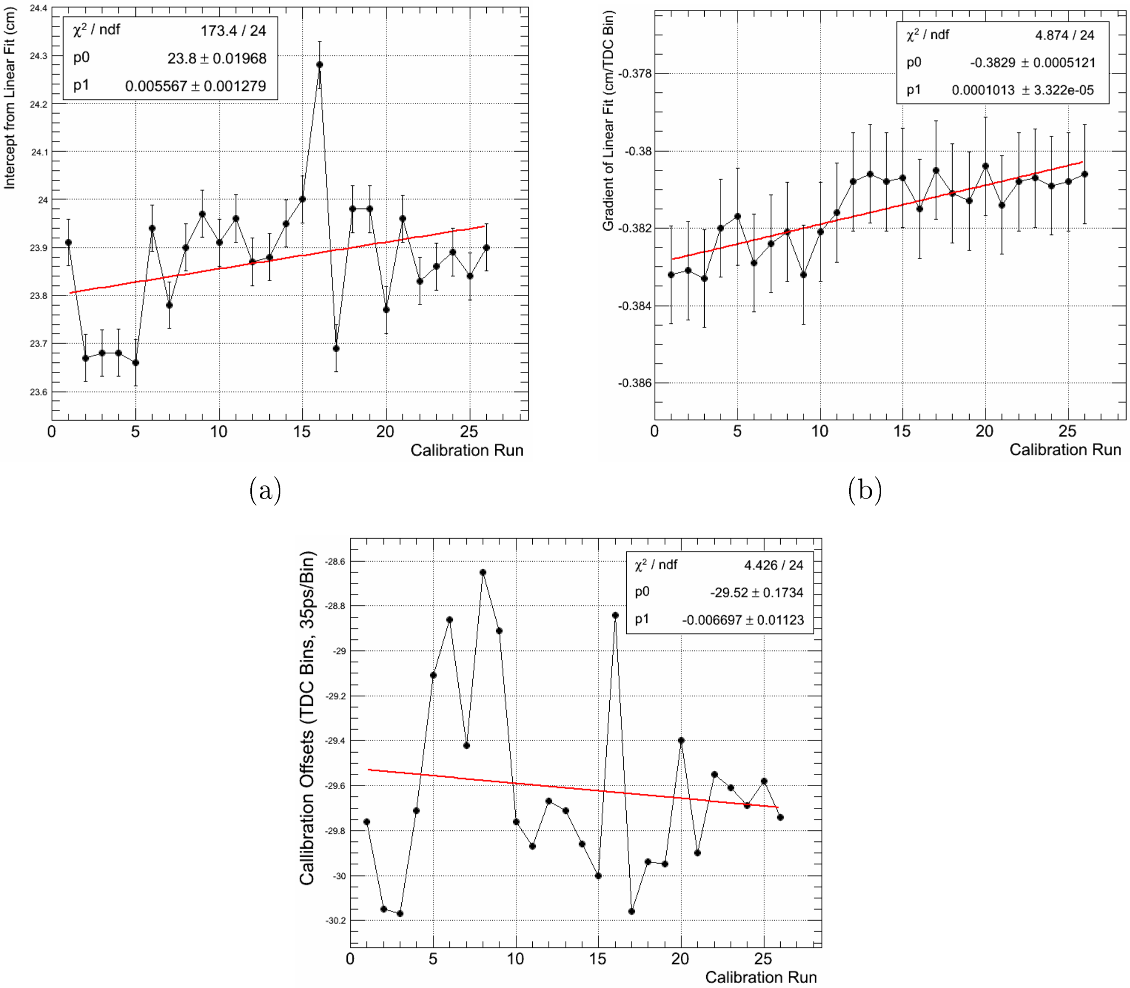

(a) (b)

(c)

Figure B.1: Calibration stability of the muon counter of the cosmic muon RICH prototype as monitored over a period of 26 weekly calibrations. Calibration parameters for the (a) intercept, (b) gradient and (c) offset parameters are shown.

Appendix C

Muon Counter Runtime Stability

Further to monitoring the muon counter calibration stability, its general signal and trigger characteristics were monitored throughout the runtimes for each configuration. The stability graphs show either the summed QDC signal from both readout PMTs of a scintillator bar against event ID, or the time between raw coincidences of the two readout PMTs of a scintillator bar against event ID. The results indicate an extremely stable performance of the tracking system.

C.1 1 cm Thickness Aerogel Setup

The results obtained throughout the runtime of the 1 cm aerogel thickness experimental setup are shown in figs. C.1 (a), (b), (c) and (d). Apart from a slight systematic jump in the QDC sum signal extracted from the top-bar readout PMTs, at the end of the runtime, very stable charge and timing responses are observed throughout the entire muon counter system.

C.2 2 cm Thickness Aerogel Setup

The results obtained throughout the runtime of the 2 cm aerogel thickness experimental setup are shown in figs. C.2 (a), (b), (c) and (d). As for with the 1 cm aerogel thickness runtime, strong stability of the muon counter system is observed, apart from slight systematic jumps at the start and end of the runtime with the top and bottom scintillator bar sum charge signals respectively.

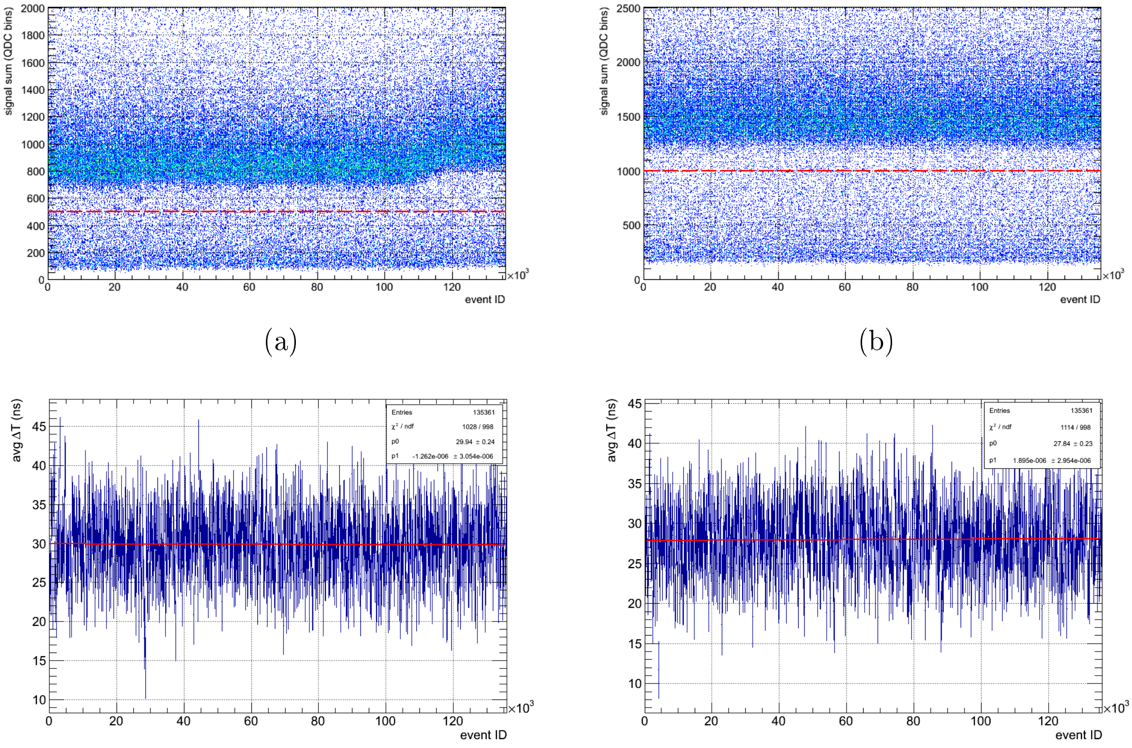

(a) (b)

(c) (d)

Figure C.1: Stability of muon counter during the 1 cm thickness aerogel setup data taking. Graphs show the summed QDC charge extracted from the two readout PMTs of (a) the top and (b) bottom scintillator bars, and the time between coincident signals of the readout PMTs for both the (c) top and (d) bottom scintillator bars.

C.3 Masked MAPMT Setup

The results obtained throughout the runtime of the masked MAPMT experimental setup are shown in figs. C.3 (a), (b), (c) and (d), which again demonstrate excellent stability of the muon counter system.

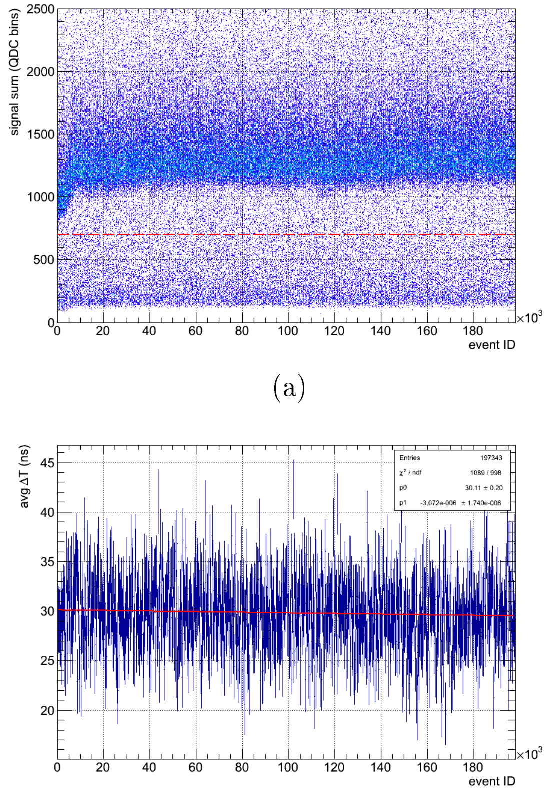

(a) (b)

(c) (d)

Figure C.2: Stability of muon counter during the 2 cm thickness aerogel setup data taking. Graphs show the summed QDC charge extracted from the two readout PMTs of (a) the top and (b) bottom scintillator bars, and the time between coincident signals of the readout PMTs for both the (c) top and (d) bottom scintillator bars.

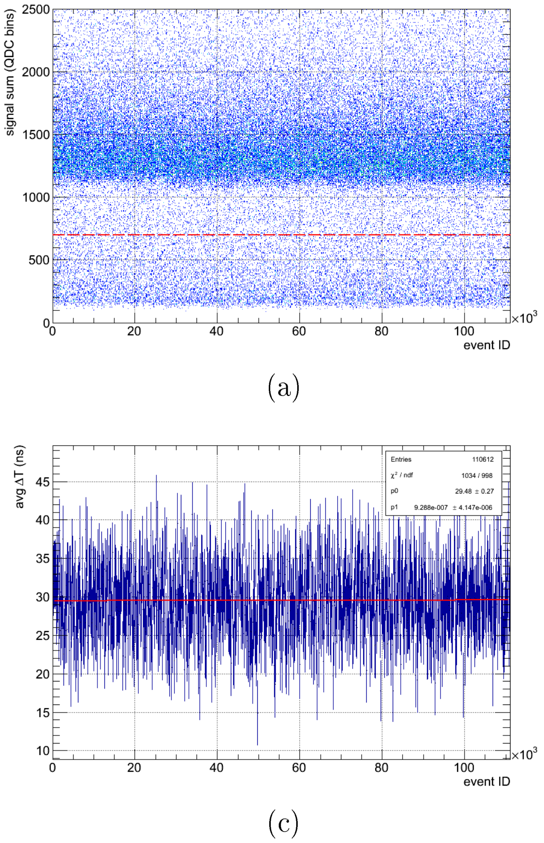

(a) (b)

(c) (d)

Figure C.3: Stability of muon counter during the masked MAPMT setup data taking. Graphs show the summed QDC charge extracted from the two readout PMTs of (a) the top and (b) bottom scintillator bars, and the time between coincident signals of the readout PMTs for both the (c) top and (d) bottom scintillator bars.

Appendix D

Electronics Modules used for the Small-Scale RICH Prototype

A list of the NIM and VME modules, including their manufacturers and model types, which were used for trigger generation and DAQ in the cosmic muon RICH prototype is given in Table D.1.

Table D.1: NIM and VME modules used in the cosmic muon RICH prototype.

Unit Description	**Manufacturer**	**Model**
Constant fraction discriminators	ORTEC	CF8000
Scaler	CAEN	C243
Analogue delays	CERN NP	N9053
Quad coincidence units (used for ANDs and ORs)	LeCroy	622
Dual timer	CAEN	N93B
Leading edge discriminator	LeCroy	621BL
Linear fan in/fan out	LeCroy	428F
HV	CAEN	N470
QDCs	CAEN	v792
TDC	CAEN	v775
CONET-VME Bridge	CAEN	v2718

Appendix E

Large-Scale Prototype Data-Sets: Dispersion Study

Table. E.1 gives a list of the data-sets used throughout the study performed into the dispersion of Čerenkov light within aerogel radiators. An accumulation of 40 000 events were studied for each filter setting, and the data was extracted from the November - December 2012 test-beam run.

Table E.1: Data-sets used for the Čerenkov light wavelength dependence study performed with the large-scale RICH prototype.

Wavelength Band (nm)	**Run ID**	**Number of Events**
All	1051	20 000
	1052	20 000
< 400	1070	20 000
	1071	20 000
$400 < \lambda < 450$	1073	20 000
	1074	20 000
$450 < \lambda < 500$	1076	20 000
	1077	20 000
$500 < \lambda < 550$	1080	20 000
	1081	20 000
$550 < \lambda < 600$	1083	20 000
	1084	20 000
> 600	1096	20 000
	1097	20 000

Appendix F

Large-Scale Prototype Data-Sets: π/K Separation Power Study

Table F.1 gives a list of the data-sets used throughout the π/K separation power study performed with the large-scale RICH test-beam prototype. Accumulations of 93 720 events, 40 000 events and 50 000 events were studied respectively for momenta of 8 GeV/c, 7 GeV/c and 6 GeV/c. The data was extracted from the November - December 2012 test-beam run.

Table F.1: Data-sets used for the separation power study performed with the large-scale RICH prototype.

Beam Momentum (GeV/c)	**Run ID**	**Number of Events**
8	1051	20 000
	1052	20 000
	1053	20 000
	1054	20 000
	1055	13 720
7	1141	20 000
	1142	20 000
6	1144	20 000
	1145	20 000
	1146	10 000